CDMRI'08

MICCAI
2008 NEW YORK

WORKSHOP ON
COMPUTATIONAL DIFFUSION MRI

September 10th, 2008
Kimmel Center, New York City, USA

http://picsl.upenn.edu/cdmri08

Editors:
Daniel Alexander (University College London, UK)
James Gee (University of Pennsylvania, USA)
Ross Whitaker (University of Utah, USA)

Preface

Over the last decade interest in diffusion MRI has exploded. The technique provides a unique insight into the microstructure of living tissue and enables in-vivo connectivity mapping of the brain. Tractography and connectivity mapping give fundamental new insights in neuroscience and neuroanatomy. Furthermore, microstructural changes or abnormalities are often the earliest signs of disease or tissue regeneration, and thus diffusion MRI promises to have an important clinical impact. The variety of clinical applications is expanding rapidly and includes detection of lesions and damaged tissue, prognosis of functional impairment and neurosurgical planning.

Computational techniques are critical to the continued success and development of diffusion MRI and to its widespread transfer into the clinic. New processing methods are essential for addressing issues at each stage of the diffusion MRI pipeline: acquisition, reconstruction, modeling and model fitting, image processing, fiber tracking, connectivity mapping, visualization, group studies and inference. This workshop, held under the auspices of the 11th International Conference on Medical Image Computing and Computer Assisted Intervention, MICCAI 2008, provides a snapshot of the current state of the art and gives some insight into the future of diffusion MRI analysis.

A highlight of the program is the invited presentations by two very promising young investigators in the field, Thomas Fletcher and Saad Jbabdi, to whom we are grateful for their participation. We are also indebted to members of the Program Committee for ensuring the quality of the presented work, as well as chairing sessions, at the meeting. Gary Hui Zhang deserves particular recognition for his management of the workshop website and production of the electronic proceedings.

It is our distinct pleasure to welcome participants to CDMRI'08, and to provide this record of the exciting work represented at the workshop.

September 2008

Daniel Alexander
James Gee
Ross Whitaker

Table of Contents

Organization

Workshop Organizers

Daniel Alexander	University College London, UK
James Gee	University of Pennsylvania, USA
Ross Whitaker	University of Utah, USA

Program Committee

Andrew Alexander	University of Wisconsin, USA
Philip Batchelor	King's College London, UK
Philip Cook	University of Pennsylvania, USA
Rachid Deriche	INRIA, France
Maxime Descoteaux	CEA, France
Lawrence Frank	University of California, San Diego, USA
Pierre Fillard	CEA, France
Thomas Fletcher	University of Utah, USA
Hubert Fonteijn	University College London, UK
Guido Gerig	University of Utah, USA
Matt Hall	University College London, UK
Saad Jbabdi	University of Oxford, UK
Gordon Kindlmann	Harvard Medical School, USA
Jean-Francois Mangin	CEA, France
Susumu Mori	Johns Hopkins University, USA
Xavier Pennec	INRIA, France
Baba Vemuri	University of Florida, USA
Hui Zhang	University of Pennsylvania, USA

Oral Session I: Modeling and Measuring Microstructure

Estimation of the axonal radius from diffusion MR data in directionally heterogeneous tissues

Rosario Sance[1], Andrés Santos[1], María J. Ledesma–Carbayo[1], Timothy Behrens[2], and Saad Jbabdi[2]

[1] Department of Electronic Engineering, Universidad Politécnica de Madrid, Madrid (Spain)
[2] Center for Functional Magnetic Resonance Imaging of the Brain, Oxford, UK

Abstract. Diffusion-weighted Magnetic Resonance imaging is sensitive to self–diffusion of water molecules, which in turn is influenced by tissue geometry and composition. Recent models have attempted to relate the former to the latter, by including microstructural properties such as axonal radius in the signal equation, but the orientation of the axonal bundles was assumed to be known a priori. This restriction limits the application of such models to locations where white matter orientation is well defined, such as in the spinal cord. We present an extension of a previously proposed model that includes directional heterogeneity in the distribution of axonal orientations, using a spherical harmonic decomposition. We prove on simulations the feasibility of estimating the model parameters, including axonal radius, both in directionally homogenous and heterogeneous tissue configurations.

Key words: Diffusion imaging, tissue modelling, spherical harmonics, axon radius.

1 Introduction

Accessing micro-structural information about the in-vivo brain is crucial to our understanding of normal brain function, and its breakdown in disease. Diffusion weighted Magnetic Resonance Imaging (dMRI) has the potential to provide access to some interesting features of the microstructure. For example, the sensitivity of the diffusion MR signal to tissue orientation has enabled neuroscientists to infer the orientation of white matter fibre tracts from the in-vivo brain, and use this information to virtually dissect cerebral large-scale connections [1]. Other local structural parameters influence the diffusion signal. For example, the degree of myelination, the caliber or the packing of axonal fibre bundles all are thought to influence the diffusion signal, by creating barriers that *hinder* the random walk of water molecules [2]. The diffusion tensor model [3] captures some of these features. For instance, the local orientation of white matter tracts is captured by the principal eigenvector of the diffusion tensor. This property made the tensor model extremely popular in the early days of tractography, the technique of tracing white matter tracts in vivo using diffusion MR data. Other models have since then been adopted to overcome some of the limitations of the tensor model for representing fibre orientations, such as partial volume effects [4–6] or accounting for the uncertainty in the estimate of the fibre orientations [7].

The *shape* of the diffusion tensor has also provided useful information about the local structure. The most common measures that are calculated from the diffusion tensor, fractional anisotropy (FA) and mean diffusivity (MD) are so sensitive to clinical pathology that dMRI is now the most popular technique for in-vivo research into white matter diseases. Changes in FA and MD have been reported in numerous neurological and psychiatric disorders (e.g. [8] for a review of applications in Multiple Sclerosis), as well as in studies of brain plasticity in healthy subjects [9, 10]. However diffusion tensor-derived measures are not very *specific*, as one may conclude from the plethora of different diseases that show similar variations in diffusivity. Changes in MD and FA are thought to be due to various biophysical features, but it is not clear to which extent. When researchers witness a change in FA, they cannot specifically relate this change to an underlying tissue parameter such as axonal geometry, or myelination. The ability to measure such biophysical parameters in-vivo would clearly have an impact on clinical research. This is the main motivation behind the current effort to develop models to infer biophysical parameters directly from the dMRI data, taking the signal models a step further.

Models for restricted diffusion in various tissue geometries have been proposed since the early days of diffusion imaging [11–13], relating the measured MR signal to geometrical characteristics of the medium. The most interesting model for the diffusion in white matter was the model for restricted diffusion in cylinders (e.g. [12]). Assaf and colleagues [14] transposed this model to diffusion in brain tissues. They proposed a model where diffusion within a brain voxel was a mixture of hindered (tensor-like) and cylindrically restricted diffusion, including thereby the axonal radius in the signal model. They have shown on ex-vivo data that the axonal radius can be estimated with a great degree of accuracy. A recent analysis in [15] has shown the feasibility of such experiments in-vivo, provided an optimised choice of the scanning parameters.

A crucial assumption in Assaf's model was that the orientation of the tissues (axon bundles) was *fixed* and known *a priori*. This meant that their experiments could only be made on locations where white matter bundles had a known homogenous orientational structure, such as in the spinal cord. Here we propose to extend this approach to account for variability in the orientation of axonal fibres. We used a spherical harmonic (SH) decomposition to model the distribution of axonal orientations whitin a voxel [16]. This is an important advance since it would potentially allow us to estimate axonal diameter distributions throughout the whole brain white matter, where orientation is a priori unkown, or heterogenous within a voxel (i.e. crossing fibres), or even within the grey matter.

2 Methods

2.1 Two-compartments model

The diffusion model proposed in [14] consists of two non-exchanging compartments related to two different diffusion processes occurring within a voxel: an extra–cellular compartment with hindered diffusion and an intra–cellular compartment with cylindrical restricted diffusion. The overall signal is the sum of the contributions from both compartments:

$$S = S_0\left[(1-\nu)S_h + \nu S_r\right], \tag{1}$$

where ν is the intra-cellular volume fraction, S_0 is the diffusion signal value when no pulsed gradient is applied.

As in [17], we model hindered diffusion in the extra-cellular compartment as an isotropic gaussian diffusion, i.e. a mono-exponential diffusion signal with scalar diffusivity d. Hinderance in this compartment reflects the tortuosity of the extracellular matrix, as well as increased viscosity inside glial cells or the imposed by cell membranes. In the case of a standard spin-echo experiment, the signal equation writes:

$$S_h = \exp\left\{-td|\mathbf{q}|^{\mathbf{2}}\right\}, \tag{2}$$

where $t = \mathit{\Delta} - \delta/3$ is the effective diffusion time, $\mathbf{q} = \gamma\mathbf{G}\delta$ is the diffusion wave vector when a gradient $\mathbf{G} = G\hat{\mathbf{n}}$ of duration δ is applied, and $\mathit{\Delta}$ is the diffusion time. The second compartment models diffusion within infinite cylinders with equal radii R and impermeable walls. Restricted diffusion within a single cylinder decomposes into the product of parallel and perpendicular diffusion components:

$$S_c = S_{c\perp}S_{c\|}, \tag{3}$$

We use the same expressions for $S_{c\perp}$ and $S_{c\|}$ as in [15], which we rewrite here for clarity:

$$\begin{aligned} S_{c\|} &= \exp\{-tdq_{\|}^2\} \\ S_{c\perp} &= \exp\{-2\frac{q_{\perp}^2}{\delta^2}\mathcal{F}(d,R,\delta,\mathit{\Delta},G)\}, \end{aligned} \tag{4}$$

where $q_\perp$ and $q_\|$ are the components of the wave vector $\mathbf{q}$ across and along the cylinder axis respectively. $\mathcal{F}(d,R,\delta,\mathit{\Delta},G)$ is a function that accounts for cylinder geometry (through R), medium effective diffusivity (d), and NMR experimental parameters ($\delta,\mathit{\Delta},G$) to create the restricted component of the signal [12]. Intuitively, it results from an analytical derivation of the Fourier transform of a truncated gaussian diffusion profile, when the truncation occurs within a cylindrical geometry.

2.2 Spherical convolution

Finally, the contributions of each cylinder are summed up to give the signal from the restricted compartment. Denoting $f(\theta,\phi)$ the spherical distribution of axonal orientations, the restricted component writes:

$$S_r(\mathbf{q}) = \iint f(\theta,\phi)S_c(\mathbf{q})\sin(\theta)d\theta d\phi. \tag{5}$$

In order to estimate the distribution of axon orientations $f(\theta,\phi)$, we represent it using a –truncated– spherical harmonic decomposition:

$$f(\theta,\phi) = \sum_{l=0}^{L}\sum_{m=-L}^{L} f_{lm}Y_{lm}(\theta,\phi). \tag{6}$$

Estimating the distribution $f(\theta, \phi)$ will then simply consist of estimating the coefficients f_{lm} in the spherical harmonics basis. Following developments similar to [17], equation (5) writes:

$$S_r(\theta', \phi') = \pi e^{-\frac{2|q|^2\mathcal{F}}{\delta^2}} \sum_{lm} f_{lm} C_l \left(|q|^2 (td - 2\mathcal{F}/\delta^2) \right) Y_{lm}(\theta', \phi'). \tag{7}$$

In the above equation, (θ', ϕ') indicate the orientation of the diffusion gradient $\mathbf{G}$, and C_l is a function that results from convolving the signal from a single cylinder with one basis function. A formula for $C_l(x)$ can be found in [17].

2.3 Inference

Model parameters were estimated using Bayesian inference. We used Metropolis Hastings, a variation on Markov Chain Monte Carlo (MCMC) algorithms, to get samples from the posterior distributions on all model parameters. The noise model was considered to be Rician with unknown variance that was also estimated from the data. We used uniform priors on S_0, R and ν and broad gamma priors for d and the noise variance. MCMC was run for 80000 iterations, with a sampling rate or one every 400 after a burn–in period of 40000 jumps to attain convergence, yielding 100 samples from the marginal posterior distribution on model parameters.

3 Results and discussion

3.1 Simulated signals

We have simulated data that could potentially be acquired in vivo, i.e. constrained by the limits of the current hardware in MR scanners and acquisition time. Gradient strength was set to G=70mT/m, and the duration of the diffusion gradients to δ=12ms. We used a combination of diffusion factor values *b-values* and diffusion gradient orientations in order to have a good balance between capturing the features of the signal related to tissue orientation on the one hand, and to cylindrical restriction on the other hand. The latter results in a non-exponential decay that can be captured if one uses a range of *b-values*. One hundred and twenty data points were generated, consisting of ten data points with no diffusion weighting, and eleven sets data points with diffusion weighting. Each of these sets consisted of ten data points with a diffusion gradient oriented along one of ten random orientations. The full set of 110 orientations was chosen to yield an even coverage of the sphere. The *b-values* were gradually increased from 1000 to 5000 s/mm^2, by increasing the diffusion time Δ. Figure 1 pictures this scheme, representing each gradient orientation with a stick in a sphere. The length of the sticks is proportional to the *b-value* applied along this orientation.

Data were simulated using a Rician noise with a SNR of 30. Three tissue configurations were simulated, by varying the fibre orientation distribution $f(\theta, \phi)$: isotropic, single fibre and crossing fibres. Moreover, the experiment was repeated with five different axon radius values ranging from $1\mu m$ to $20\mu m$. We chose a diffusivity value of $d = 10^{-3}$mm^2/s and a intra-cellular volume fraction of $\nu = 0.7$.

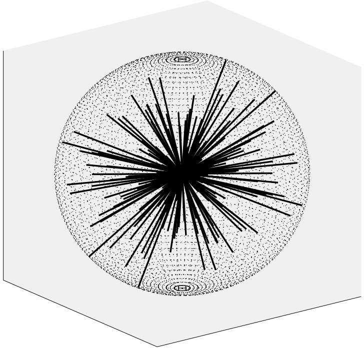

Fig. 1. Representation of the diffusion gradient scheme used for the simulated data. Each stick shows the diffusion of a diffusion gradient. The length of the sticks is proportional to the applied diffusion factor value *b*.

3.2 Posterior distributions

Figure 2 shows the histograms of the marginal posterior distributions on model parameters given by MCMC sampling. Overall, the estimation of the axon radius is very accurate for all tissue configurations, except for small radii (as predicted also by the simulations made in [15]). We note also that the estimation is overall more accurate, i.e. the variance of the posterior distribution is smaller, for the crossing fibre scenario than for an isotropic tissue model.

4 Conclusions and future work

Many publications have previously dealt with ex–vivo experiments and excised tissue for estimating brain tissue microstructural features. We tackle here the same problem with simulations mimicking in–vivo protocols. We extended a previous white matter diffusion model by implementing the orientation distribution function of the cylinders modeling the axons. A single value for the axon radius has been assumed per voxel. In the future, this can easily be extended to a distribution of axonal radii.

Our inference results based on simulated datasets with realistic SNR illustrate the potential of such a method in estimating microstructural tissue parameters like the axon radius and orientation in the whole brain, including crossing fibre areas and grey matter. In order to extend these results to the clinical practice, further work on real data is required for validation, e.g. via a direct comparison with histology.

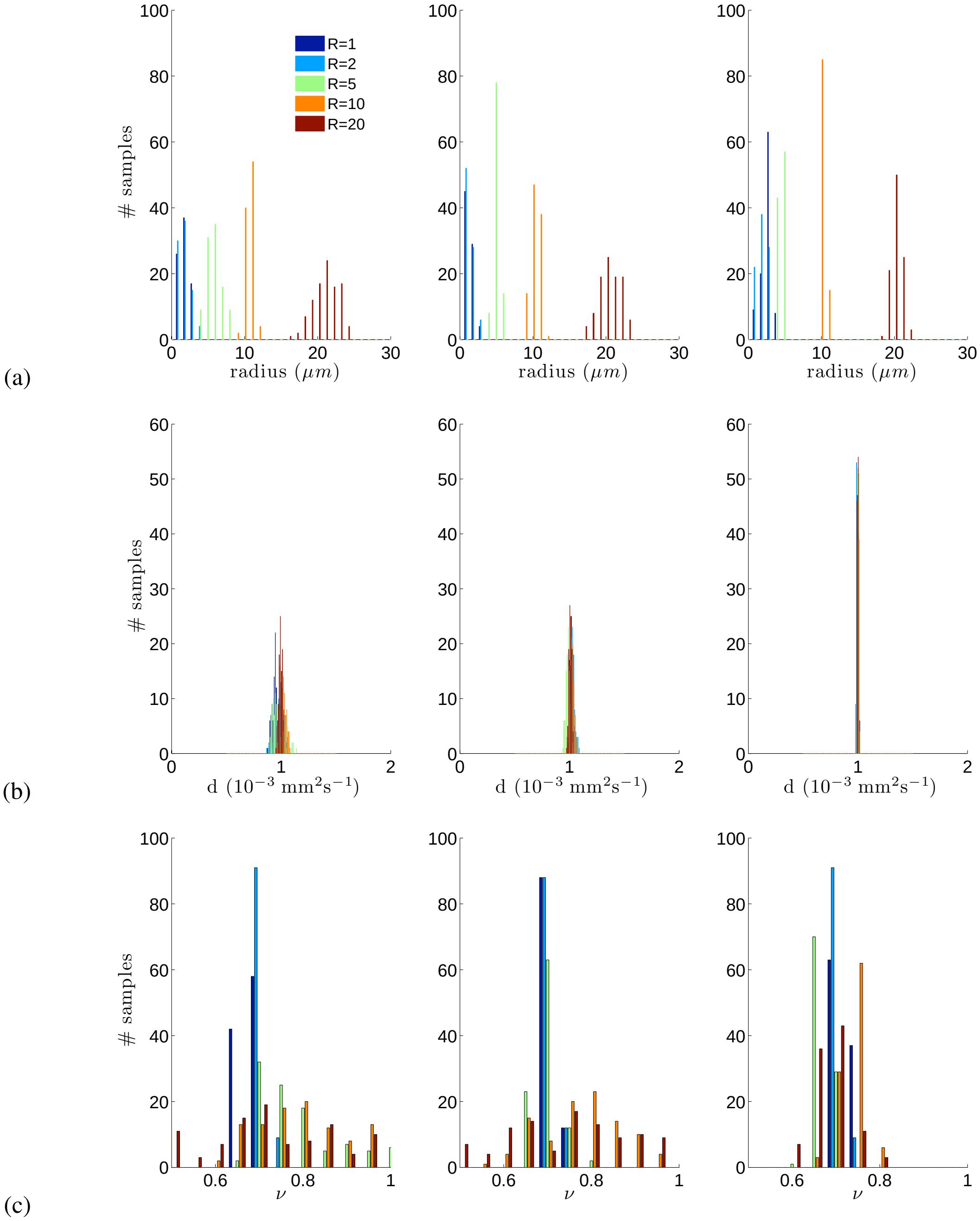

Fig. 2. Histograms of the posterior distribution on model parameters using MCMC sampling. (a) axon radius, (b) diffusivity, (c) relative size of the restricted compartment. Colours indicate different axon radii. Columns from left to right: isotropic, single fibre and crossing fibres.

References

1. Marco Catani, Robert J Howard, Sinisa Pajevic, and Derek K Jones. Virtual in vivo interactive dissection of white matter fasciculi in the human brain. Neuroimage, **17**, 77–94. (2002).
2. C Beaulieu. The basis of anisotropic water diffusion in the nervous system - a technical review. **15**, 435–455. (2002).
3. PJ Basser, J Mattiello, and D Le Bihan. Estimation of the effective self-diffusion tensor from the NMR spin echo. Journal of Magnetic Resonance, **103**, 247–254. (1994).
4. A L Alexander, K M Hasan, M Lazar, J S Tsuruda, and D L Parker. Analysis of partial volume effects in diffusion-tensor mri. Magn Reson Med, **45**, 770–780. (2001).
5. GJM Parker and DC Alexander. Probabilistic anatomical connectivity derived from the microscopic persistent angular structure of cerebral tissue. Philisophical Transactions of the Royal Society B, **360**, 893–902. (2005).
6. Timothy E J Behrens, Mark W Woolrich, Mark E Walton, and Matthew F S Rushworth. Learning the value of information in an uncertain world. Nat Neurosci, **10**, 1214–1221. (2007).
7. T E J Behrens, M W Woolrich, M Jenkinson, H Johansen-Berg, R G Nunes, S Clare, P M Matthews, J M Brady, and S M Smith. Characterization and propagation of uncertainty in diffusion-weighted mr imaging. Magn Reson Med, **50**, 1077–1088. (2003).
8. Marco Rovaris and Massimo Filippi. Diffusion tensor mri in multiple sclerosis. J Neuroimaging, **17 Suppl 1**, 27S–30S. (2007).
9. Heidi Johansen-Berg, Valeria Della-Maggiore, Timothy E J Behrens, Stephen M Smith, and Tomas Paus. Integrity of white matter in the corpus callosum correlates with bimanual coordination skills. Neuroimage, **36 Suppl 2**, T16–21. (2007).
10. David S Tuch, David H Salat, Jonathan J Wisco, Alexandra K Zaleta, Nathanael D Hevelone, and H Diana Rosas. Choice reaction time performance correlates with diffusion anisotropy in white matter pathways supporting visuospatial attention. Proc Natl Acad Sci U S A, **102**, 12212–12217. (2005).
11. J. S. Murday and R. M. Cotts. Self-diffusion coefficient of liquid lithium. The Journal of Chemical Physics, **48**, 4938–4945. (1968).
12. C. H. Neuman. Spin echo of spins diffusing in a bounded medium. The Journal of Chemical Physics, **60**, 4508–4511. (1974).
13. J. E. Tanner and E. O. Stejskal. Restricted self-diffusion of protons in colloidal systems by the pulsed-gradient, spin-echo method. The Journal of Chemical Physics, **49**, 1768–1777. (1968).
14. Yaniv Assaf, Raisa Z Freidlin, Gustavo K Rohde, and Peter J Basser. New modeling and experimental framework to characterize hindered and restricted water diffusion in brain white matter. Magn Reson Med, **52**, 965–978. (2004).
15. Daniel C Alexander. Axon radius measurements in vivo from diffusion mri: a feasibility study. In Computer Vision, 2007. ICCV 2007. IEEE 11th International Conference on, pages 1–8, (2008).
16. J-Donald Tournier, Fernando Calamante, David G Gadian, and Alan Connelly. Direct estimation of the fiber orientation density function from diffusion-weighted mri data using spherical deconvolution. Neuroimage, **23**, 1176–1185. (2004).
17. Sune N Jespersen, Christopher D Kroenke, Leif Ostergaard, Joseph J H Ackerman, and Dmitriy A Yablonskiy. Modeling dendrite density from magnetic resonance diffusion measurements. Neuroimage, **34**, 1473–1486. (2007).

A tissue model of white matter undergoing tissue swelling

Matt G Hall[1] and Daniel C Alexander[1]

Centre for medical image computing (CMIC)
Department of Computer Science.
University College London, Gower Street, London, WC1E 6BT, UK.
`m.hall@cs.ucl.ac.uk`

Abstract. We describe a model of oedema in white matter. White matter is modeled as parallel cylinders with radii chosen from a gamma distribution fitted to histological images. Cylinders expand due to the onset of oedema and are allowed to deform due to pressure from neighbours. Cylinders that would overlap are deformed along the chord of intersection, which allows cylinder deformation and abutment to be handled explicitly. Diffusion is modeled as a set of spins executing Brownian motion and reflected by the walls of the cylinders.

We synthesise diffusion-weighted measurements and compare them to the predictions of an analytical model of diffusion in parallel cylinders based on the CHARMED model. We find that the diffusion-weighted signal increases more rapidly when the effects of abutting cylinders are taken into account and that the effect is of sufficient magnitude potentially to be detectable in vivo.

1 Introduction

Diffusion-weighted MR Imaging (DWI) measures the diffusive motion of water in vivo in the direction of an applied magnetic field gradient. Particle scattering depends on the tissue microstructure, and diffusion MRI supports inferences about the underlying microstructure. For example, diffusion tensor imaging (DTI) [1] fits a diffusion tensor to six or more diffusion-weighted images on the assumption of Gaussian-distributed water-molecule displacements. The principle direction of the diffusion tensor provides an estimate of white-matter fibre orientations. Tractography techniques follow the principle direction point-to-point through the image to reconstruct macroscopic fibre trajectories and infer brain connectivity. These techniques have emerged as powerful tools for probing both anatomy [2, 3] and pathology [4].

One of the first and most successful clinical applications of DWI is the diagnosis of ischemic stroke. In the long term, ischemic insults result in a loss of structure in tissue and an increase in the observed diffusivity in the region of the lesion [4]. This change in diffusion contrast had been shown to be more sensitive than other forms of imaging [5]. The model presented here can be applied to any type of white matter oedema, but we will concentrate on comparisons with acute ischemia.

Interestingly, the short term behaviour of the diffusivity in the region of the lesion is markedly different to the longer term. In the first 4 hours after ischemic insult, the diffusivity falls, indicating reduced diffusion during this period [5]. The reason for this reduction in diffusivity is not clear, and one mechanism that has been suggested is that tissue swelling leads to a reduced extracellular volume fraction, and hence a reduced contribution to the overall signal from the less restricted extracellular compartment.

Benveniste et al [6] and VanGelderan et al [7] model the changes using a fast-exchange two compartment model:

$$ADC = V_I D_I + (1 - V_I) D_E \tag{1}$$

where V_I is the intracellular volume fraction and D_I and D_E are the intra- and extracellular diffusivities respectively.

Halpern [8] proposed a tissue model of periodic array of cell membranes in which membrane permeability decreases in the aftermath of ischemia, although Szafer [9] points out that this model overestimates the influence of these membranes on observed ADC. They point out that at long diffusion times the extracellular space can be modeled using a tortuosity approximation. The effect of tissue swelling leading to increased tortuosity in the extra cellular space was explored by Norris [10] and Latour [11].

Synthetic diffusion weighted data provides the facility to explore the effects of various pathological scenarios on the measured diffusion-weighted signals. Here we model swelling white matter tissue and explore the changes in diffusion signal as swelling occurs.

We generate synthetic data in two ways: using an analytical model similar to the CHARMED model [12] in which white matter is modeled as a collection of parallel cylinders with controlled volume fraction, and also in a Monte-Carlo model. In the Monte-Carlo model tissue is modeled as parallel cylinders with distributed radii, but here cylinders are allowed to deform and abut when their edges touch.

As cylinders increase in size, clusters of mutually abutting cylinders begin to form. As swelling continues these clusters join together and rapidly form a system-spanning cluster that segments the extracellular space into two, greatly increasing restriction to diffusion. This effect is known as the percolation threshold and we observe that the formation of such clusters has a large effect on the observed diffusion-weighted signal over and above that due to reduced extracellular volume fraction due to cell swelling.

The rest of this paper is structured as follows. Section 2 discusses previous data synthesis models (section 2.1). Section 3 discusses the tissue models used here in detail. Section 4 describes the experiment performs and presents results, which are discussed in section 5.

2 Background

This section briefly reviews diffusion imaging as well as previous work on generating synthetic diffusion-weighted MR data.

2.1 Models of diffusion-weighted MR data

Models of the diffusion process in various tissues have been used to gain insight into tissue structure by providing ground truths to validate diffusion MR analyses, or fitting to a set of experimental results to measure a parameter of interest. Models in the literature fall into two broad categories: analytical, in which some solution or approximate solution of the diffusion equation in an environment reflecting tissue structure is used to generate diffusion-weighted signals, and numerical whereby either the diffusion process is simulated directly with a chosen tissue model or numerical solutions to the diffusion equation are obtained.

Analytic models typically use either an assumed form for diffusion particle displacement profile such as a Gaussian or mixture of Gaussians (e.g. [13][14] [15]) or a solution or approximate solution of the diffusion equation in restricted geometries [16][17][18] to generate diffusion-weighted measurements. More complex models use a combination of these to construct a more complex tissue model [12][19].

Numerical approaches allow more complex tissue models. Lipinski [20] uses a two-dimensional Monte-Carlo diffusion simulation with a tissue model derived from light microscopy images. Hackney and coworkers [21][22] construct three-dimensional tissue models by extruding a segmentation of a 2D light-microscope image and obtain synthetic data in a different way by solving the diffusion equation within the model using a finite-difference approach.

In the current work we construct and compare two models of data synthesis: an analytical model, which incorporates a scheme for generating synthetic measurements that takes finite gradient pulse widths into account, and a Monte-Carlo model of spins executing Brownian motion in the presence of reflecting barriers.

3 Models of white matter tissue

This section describes the numerical tissue model and the analytical model used for comparison.

3.1 Swelling white matter tissue with deformation and abutment

We model diffusion in an environment where fibre radius increases due to tissue swelling. The initial, unswollen, substrate contains 100 cylinders with radii drawn from a gamma distribution

$$P(x;k,\theta)=\frac{x^{k-1}e^{-x/\theta}}{\Gamma(k)\theta^{k}} \tag{2}$$

with scale parameter $k = 6.91 \times 10^{-6}$m and shape parameter $\theta = 2.331$. These values are obtained by fitting a gamma distribution to the histograms of axon radii in Aboitz et al [23] (fig-4, mid-body). The cylinders are positioned within a cubic region of space 3.65×10^{-5}m on each side. Initially, (i.e. prior to swelling) cylinders are guaranteed not to touch. In order achieve the desired positioning, the algorithm for placing cylinders proceeds as follows:

1. Draw 100 radii from the gamma distribution
2. Sort them into descending order
3. Starting with the largest, for each cylinder
    - (a) Choose a random position for the cylinder on the substrate
    - (b) If the cylinder position overlaps the edges of the voxel, create copies that overlap the opposing edge(s) to ensure periodicity of substrate (see fig-1)
    - (c) If the new cylinder or any of the copies touches or overlaps any other cylinder that has been already placed, discard and return to 3(a)
4. Add new cylinder plus copies to the substrate

Care must be taken when cylinders overlap the edges of the substrate. In this case (step 3(b)), duplicates of the placed cylinder are added on the opposite side(s) of the substrate. These duplicates are also checked for overlaps with other cylinders and are included in checks for subsequently placed cylinders. This ensures that the substrate is periodic. Fig-1 shows the periodic unit cell (square) and the positions of the cylinders and copies ensuring periodicity at the boundaries.

Using this procedure it is possible to achieve biologically relevant intracellular volume fraction $V_I \simeq 0.7$ [24].

Tissue swelling is simulated by iteratively enlarging the cylinders on the substrate. Cylinder radii are enlarged by an amount proportional to their volume (in line with Boyle's Law). Since their positions are not altered, larger radii will inevitably lead to overlaps between cylinders. Overlapping cylinders are deformed along the chord of intersection in the plane of cross section so that they abut. The substrate is updated in each swelling iteration as follows:

1. Generate a radius increment $\Delta\mathbf{r}_j$ for each cylinder proportional to initial volume
2. For each cylinder position j:
    - (a) Using the cylinder positions obtained in the initial placement phase, replace the cylinders at each position with an new one of radius $\mathbf{r}_j = \mathbf{r}_{0,j} + i\Delta\mathbf{r}_j$ where i is the swelling iteration number, $i = 0, ..., 9$ or the current radius if cylinder has stopped expanding.
    - (b) Check if the new cylinder intersects any that are already placed. If yes, find the chord of intersection and use it as the deformed surface of the two cylinders (See fig-2).
    - (c) If the angle of intersection (i.e. the angle subtended by the chord of intersection, see fig-2) between two cylinders is greater than 90° in either one, stop both from expanding in subsequent iterations.

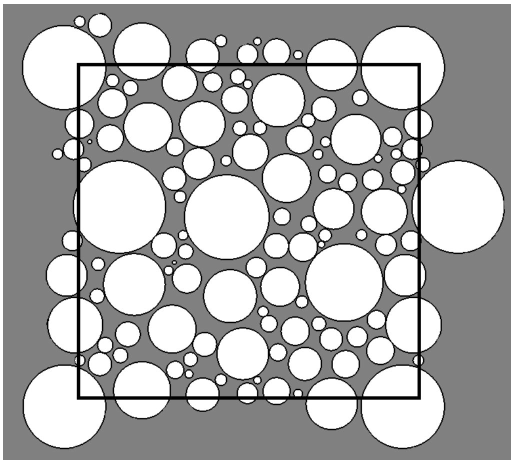

Fig. 1. Cross-section of non-overlapping parallel cylinders with gamma distributed radii. Additional cylinders are added to ensure periodic boundaries to the voxel. The square illustrates the boundaries of the voxel. Within the square, the pattern of cylinders tiles exactly in the plane.

Fig-3 shows the cross section of a substrate with cylinders positioned using this method, and the changes that occur as the cylinders swell. Rapidly, the extracellular space becomes divided by a continuous barrier of deformed circles. This is known in the statistical mechanics literature as the percolation threshold [25].

As swelling continues, the extracellular space becomes increasingly segmented into smaller and smaller regions in which diffusion is restricted rather than hin-

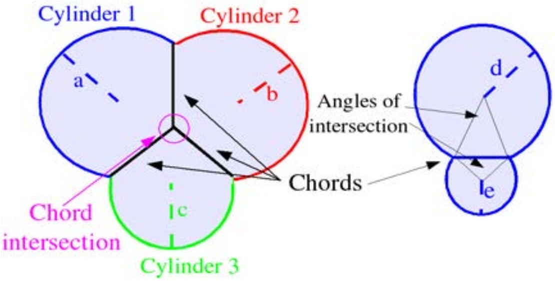

Fig. 2. Cylinder deformation scheme. Cylinders that would otherwise intersect are deformed along the chord of intersection (left). Chords that intersect each other are shortened accordingly. Cylinder swelling is limited by the angle of intersection (right). If either angle is greater than 90° both cylinders stop expanding.

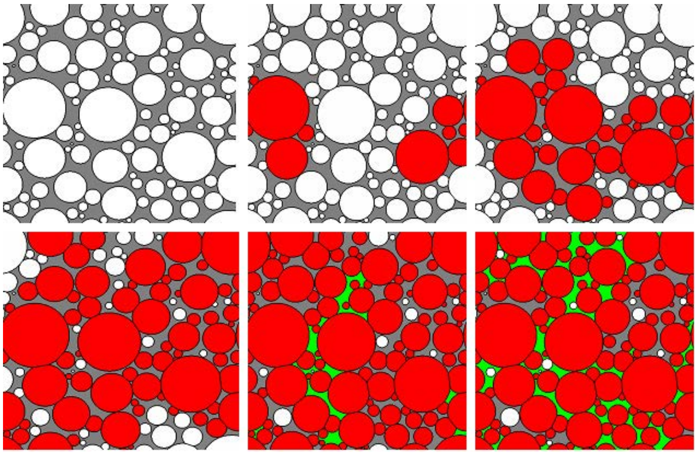

Fig. 3. Cross-section of cylinders, degree of swelling increases across rows. As cylinders swell, number of cylinders deformed due to overlaps increases (these abutting cylinders are shown in red). At the third iteration the intersections form a complete barrier, segmenting the external space. As swelling continues to increase, the extracellular space becomes highly restricted (green). Eventually green regions become very widespread.

dered. This additional restriction leads to a more rapid decrease in ADC (i.e. increase in diffusion-weighted signal) than would be the case for a simple increase in V_I.

The segmenting effect of overlapping cylinders is not captured in the analytical model and so any differences in predictions of the two models will be an indication of the importance of this mechanism.

3.2 Analytical model

Similar to the CHARMED model [12], this model treats the diffusion environment as a two-compartment system: an intracellular compartment for which the signal is synthesised using the solution of diffusion in a cylinder from [26] and an extra cellular compartment with a tortuosity factor that models hinderence from the presence of cylinders.

Cylinder radii are gamma-distributed using the same parameters as in the main tissue model. Cylinders walls are of zero thickness and permeability is set to zero. We assume free diffusivity parallel to cylinders. Diffusion in the extracellular compartment perpendicular to cylinders is modeled using a tortuosity approximation. The tortuosity approximation uses a model from Szafer et al [27] for diffusion around randomly placed cylinders. It sets an effective diffusion constant

$$D_E = \frac{d}{\lambda^2} \tag{3}$$

where d is the free diffusivity and λ^2 is the tortuosity given by

$$\frac{1}{\lambda^2} = \begin{cases} (1 - V_I) & \text{perpendicular to fibre direction} \\ 1 & \text{parallel to fibre direction} \end{cases} \tag{4}$$

The total analytic synthetic signal is

$$\mathcal{S} = V_E S_E + V_I S_I \tag{5}$$

where

$$S_E = \exp\left(-bD_E\right) \tag{6}$$

is the signal from the external compartment, S_I is the signal from inside the cylinders and $V_E = 1 - V_I$ is the extracellular volume fraction.

There is no explicit notion of cylinder overlap in the intracellular compartment. Cylinder radius and volume fraction may increase, but the tortuosity approximation assumes that the extracellular space remains completely connected (i.e. every location in the extracellular space is reachable from every other, albeit via a tortuous path).

4 Experiments and Results

Diffusion-weighted measurements are synthesised using the Monte-Carlo simulation method outlined in [28]. A simulation of 100000 spins and 1000 updates at each iteration of the tissue model. We repeat this 30 times with different substrate realisations and random number generator seeds. Spin positions are initially drawn from a uniform distribution across the unit cell defined by the tissue model.

We compare the Monte-Carlo synthesised data with that from the analytic model from section 3.2. Fig-4 shows the normalised diffusion-weighted signal predicted by each model accompanied by the number of abutting cylinders in each iteration of the tissue model. We see that in the first iteration in which cylinders are well-separated there is good agreement between the models. As the number of intersections increases and the extracellular space is increasingly segmented the signal predicted by the Monte-Carlo model increases more quickly than that from the analytical model.

5 Conclusions

The tissue model presented here captures the effect of a segmented extracellular space due to cylinder swelling. This is difficult to capture analytically, and is an example of how a detailed numerical model can be useful.

We observe that the differences in the predictions of the two models is of a magnitude that should be detectable in vivo. Since the segmenting of the extracellular space leads to regions aligned with the cylinder axis, it should also introduce additional anisotropy into the diffusion signal, and the reduction

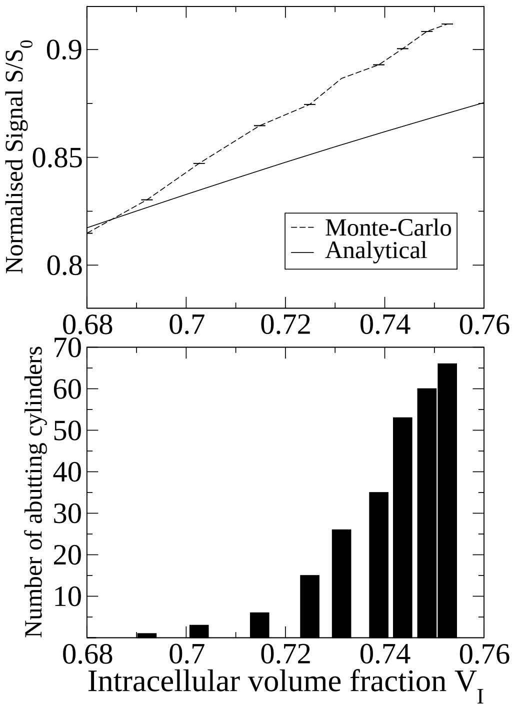

Fig. 4. Normalised diffusion-wighted signals perpendicular to cylinder axes as a function of intracellular volume fraction and number of abutting cylinders. We observe good agreement between more in the absence of abutments, with the signal from the Monte-Carlo model increasing faster than that from the analytical model, which does not include abutting cylinders

in diffusivity (i.e. increase in normalised diffusion-weighted signal) should be accompanied by an increase in fractional anisotropy. It would be interesting to see if this is observed in patients.

One shortcoming of the current framework is that there is no notion of time between successive swelling iterations (although time is well-defined within each simulation and the substrate is assumed to be static during the diffusion simulation), hence it is not possible to make predictions regarding the timescales of swelling. However it is possible to predict that FA should be maximum when normalised diffusion-weighted signal is maximum, and indeed a sharp peak in FA occurring at the same time as the minimum in diffusivity is observed by Sotak [5] in white matter tissue.

In future work, we hope to increase the complexity of the tissue model by incorporating tissue models based on confocal laser microscopy image stacks of excised white matter tissue and emulating tissue swelling in the images. By performing an ex vivo DWI acquisition prior to microscopy, this also provides a powerful way to validate the results of the simulation on the derived tissue model.

Acknowledgments

MGH is funded by EPSRC grant EP/E056938/1.

References

1. Basser P J, Matiello J and Le Bihan D 1994 MR diffusion tensor spectroscopy and imaging *Biophysical Journal* **66** 259–67
2. Mori S, Crain BJ, Chackoand PJ, van Zijl PCM 1999 Three dimensional tracking of axonal projections in the brain by magnetic resonance imaging *Annals of Neurology* **45** 265–269
3. Catani M, Howard RJ, Pajevic S and Jones DK 2002 Virtual *in vivo* Interactive dissection of white matter fasciculi in the human brain *NeuroImage* **17** 77–94
4. Kucharczyk J, Mintorovitch J, Asgari H and Moseley M 1991 Diffusion/perfusion MR imaging of acute cerebral ischemia *Magnetic Resonance in Medicine* **19** 311–315
5. Sotak CH 2002 The role of diffusion tensor imaging in the evaluation of ischemic brain injury – a review *NMR in Biomedicine* **15** 561–569
6. Benveniste H, Hedlun LW and Johnson GA 1992 A mechanism of detection of acute cerebral ischemia in rats by diffusion-weighted magnetic resonance microscopy *Stroke* **23** 746–754
7. van Gelderan P, Vleeschouwer MHM DesPres D, Pekar J, vanZijl PCM and Moonen CTW 1994 Water diffusion and acute stroke *Magnetic Resonance in Medicine* **31** 154–163
8. Helpern JA, Ordidge RJ and Knight RA 1992 The effect of cell-membrane water permeability on the apparent diffusion coefficient of water *In: Proc. SMRM 11th annual meeting* 1201
9. Szafer A, Zhong J, Anderson AW and Gore JC 1995 Diffusion-weighted imaging in tissues: theoretical models *NMR in Biomedicine* **8** 289–296

10. Norris DG, Niendorf T and Leibfritz D 1994 Healthy and infacted brain tissues studied at short diffusion times: the origins of apparent restriction and the reduction of apparent diffusion coefficient *NMR in Biomedicine* **7** 304–310
11. Latour LL, Svoboda K, Mitra p and Sotak CH 1994 Time-dependent diffusion of water in a biological model system *Proc. Natn. Acad. Sci USA* **91** 1229–1233
12. Assaf Y and Basser P J 2005 Composite hindered and restricted model of diffusion (CHARMED) MR imaging of the human brain *NeuroImage* **30** 1100–1111
13. Tuch D S, Reese T G, Wiegell M R and Wedeen V J 2003 Diffusion MRI of complex neural architecture *Neuron* **40** 885–895
14. Tournier J-D, Calamante F, Gadian D G and Connelly A 2004 Direct estimation of the fiber orientation density function from diffusion-weighted MRI data using spherical deconvolution *NeuroImage* **23** 1176–1185
15. Alexander D C 2005 Multiple fibre reconstructions for diffusion MRI *Annals of the New York Academy of Sciences* **1046** 113–133
16. Neuman C H 1974 Spin echo of spins diffusing in a bounded medium *Journal of Chemical Physics* **60** 4508–4511
17. Callaghan P T 1995 Pulsed-gradient spin-echo NMR f'or planar, cylindrical and spherical pores under conditions of wall relaxation *Magnetic Resonance in Medicine* **113** 53–59
18. Soderman O and Jonsson B 1995 Restricted diffusion in cylindrical geometry *Journal of Magnetic Resonance A* **117** 94–97
19. Stanisz G J, Szafer A, Wright G A and Henkelman M 1997 An analytical model of restricted diffusion in bovine optic nerve *Magnetic Resonance in Medicine* **37** 103–111
20. Lipinski H-G 1990 Monte-Carlo simulation of extracellular diffusion in brain tissues *Physics in Medicine and Biology* **35** 441–447
21. Chin C-L, Wehrli FW, Hwang SN, Takahashi M and Hackney DB 2002 Biexponential diffusion in the rat spinal cord: Computer simulations based on anatomical images of axonal architecture *Magnetic Resonance in Medicine* **47** 455–460
22. Hwang SN, Chin C-L, Wehrli FW and Hackney DB 2003 An image-based difference model for simulating restricted diffusion *Magnetic Resonance in Medicine* **50** 373–382
23. Aboitz F, Scheibel A B, Fisher R S and Zaidel E 1992 Fiber composition of the human corpus callosum *Brain Research* **598** 143–153
24. Ford JC and Hackney DB 1997 Numerical model for calculation of apparent diffusion coefficients (ADC) in permeable cylinders–Comparison with measured ADC in rat spinal cord white matter *Magnetic Resonance in Medicine* **37** 387–394
25. ben-Avraham D and Havlin S 2000 *Diffusion and reactions in fractals and disordered systems* (Cambridge University Press)
26. Murday JS and Cotts RM 1968 Self-diffusion coefficient of liquid lithium *Journal of Chemical Physics* **48** 4938–4945
27. Szafer A, Zhong J and Gore J C 1995 Theoretical model for water diffusion in tissues *Magnetic Resonance in Medicine* **33** 697–712
28. Hall MG and Alexander DC 2008 Agreement and Disagreement in two models of synthetic diffusion MR data *Proc. ISMRM, Toronto, Canada* **abstract 1780**

The Influence of Microscopic Shape Invariants in Diffusion MRI and on Time Correlations

P. G. Batchelor and D. C. Alexander
philip.batchelor@kcl.ac.uk

King's College London and University College London

1 Introduction

Diffusion MRI makes measurements on a relatively large voxel scale ($\sim$5–20 mm^3) compared to the underlying mechanism which takes place at a microscopic level ($\sim$ μm). However, the measurements are sensitive to features of tissue microstructure that is consistent over the macroscopic voxel. For example, the microscopic observations show a clear orientation dependence in tissue with anisotropic microstructure, such as white matter in the brain. Although the exact transition from microscopic to macroscopic is not perfectly understood [1], it is clear that the local cellular structure plays an important role [2]. Models of the microstructure can help the interpretation of diffusion MRI measurements and allow inferences of important microstructural features such as cell size and density [3,4,5].

Here, we investigate the influence of pore shape on particle scattering through diffusion. In particular, we derive a general framework to compute the displacement probability density function and related quantities such as time correlations of functions, which lead to models for the diffusion MRI signal from particles restricted in these environments. We reduce most quantities to arrays of shape invariants. Most of these shape invariants can be related to classical computations, often going back to the 19th century, on eigenmodes of shapes [6,7,8]. Our approach has strong links with Codd and Callaghan's work on matrix descriptions for spin echo experiments with general gradient waveforms [9]. We generalise these matrix terms and show that most correlations can be expressed as elegant functions of generalised centroids.

According to Einstein's relation, the observed diffusion tensor components, in free space, are proportional to time correlations of spatial coordinates. In a restricted space, the time dependence will change, and will depend on the restriction properties. If we are able to sample this function at different diffusion times, and we know the theoretical time and shape dependence, we may be able to fit the observations, and thus deduce shape parameters. These ideas have lead to the recent trend in diffusion MRI towards estimating direct features of microstructure, such as cell size and density, see for example [3,10,5]. The framework we develop here provides a general method to obtain models for future techniques of this type.

2 Theory

Notations and Background We consider idealised cells, or pores, denoted Ω. These are domains in D-dimensional space. In general $D = 3$, but for cylindrical domains $D = 2$ is also of interest. A point in Ω is denoted $\mathbf{r}$, and we consider diffusion processes of water molecules in Ω, $P(\mathbf{r}_0, \mathbf{r}, t_0)$ is the probability of starting at $\mathbf{r}_0$ and reaching $\mathbf{r}$ at time t.

Without restrictions, the water molecules bounce against each other, with a kinetic energy dependent on temperature. Under no external influence, the average position as function of time should not change. Einstein's relation gives a formula for the mean squared distance, and the main result is that $\langle \mathbf{r}^2 \rangle(t)$ is proportional to t. The proportionality constant is the *diffusion* constant D. In an anisotropic substrate, we would have $\langle x_i x_j \rangle(t) =: D_{ij} t$, which defines the *diffusion tensor* in free space.

By *microscopic*, we mean effects (spatial and temporal) which take place inside Ω without being affected by the boundary. At a *mesoscopic* scale, some molecules having started at $\mathbf{r}_0$ will reach the boundary. Depending on the type of boundary, some will be reflected, some absorbed. Consider for example a perfectly reflecting boundary. In this case, the molecules will be more likely to be near the centre, and the mean position drifts towards the centre. At a *macroscopic* scale the effect of the starting position will have been forgotten, and in the long time limit the mean position will be the centre of the domain. In our computations below we show how to establish an exact time and shape-dependent formula for this function. This also takes into account the boundary permeability.

We define the *apparent diffusion functions* $\mathbb{D}_{ij}(t, \Omega) := \langle x_i x_j \rangle_\Omega (t_0, t_0 + t)/t$. Thus, when Ω is the entire space, $\mathbb{D}_{ij}$ is independent of t. In a Diffusion MRI context, we want to extract information on Ω by sampling this function at different times, see also [5,10] for more details on the MRI foundations of this idea. Here, we make the shape dependence of general correlation functions explicit, by writing them in terms of shape invariants. In particular we show how most terms can be written in terms of 'generalised centroids' for reflecting boundary conditions. This gives us a flexible and intuitive way to incorporate shape informations. The shape invariants are related to eigenmodes of the Laplace operator for that shape (as in [9]), and these define natural time-scales. Our method generalises and explains the formulas provided by Neuman [11]. We provide some explicit formulas for basic important shapes where this is possible to illustrate further the power of the method.

2.1 Time Correlations

Solution of Diffusion Equation Let

$$\partial_t P(\mathbf{r}, \mathbf{r}_0, t) = D \Delta P(\mathbf{r}, \mathbf{r}_0, t) \quad \text{on } \Omega \tag{1}$$

$$P(\mathbf{r}, \mathbf{r}_0, 0) = \delta_{\mathbf{r}_0}(\mathbf{r}) \quad \text{Start at } \mathbf{r}_0 \tag{2}$$

$$\mathcal{B} P|_{\partial \Omega} = 0 \tag{3}$$

$\mathcal{B}$ is the boundary condition operator. Standard boundary conditions are $\mathcal{B}P|_{\partial\Omega} = P|_{\partial\Omega}$ for *Dirichlet* boundary condition (absorbing boundary), or $\mathcal{B}P|_{\partial\Omega} = \partial_{\mathbf{n}}P|_{\partial\Omega}$ for *Neumann* boundary condition (reflecting boundary). *Robin* boundary conditions $P + p\partial_{\mathbf{n}}P = 0$ are a mixture of both, which may model semi-permeable boundaries.

A classical result (see e. g. [7] and references therein) is

$$P(\mathbf{r}, \mathbf{r}_0, t) = \sum_k w_k(\mathbf{r}_0) w_k(\mathbf{r}) e^{D\lambda_k t}.$$

where w_k is the $k - th$ eigenfunction of the Laplace operator on Ω, and λ_k the k-th eigenvalue [7,8,12]. The eigenfunctions form an orthonormal basis of $L^2(\Omega)$.

Expectations We pick functions $\phi_i(\mathbf{r})$ $i = 0 \dots N$ on Ω. These functions are assumed to be measurements performed on the tissue. They could be coordinates, or $q-$space harmonics. We are interested in the time correlations $\langle \phi_0 \cdots \phi_N \rangle_\Omega (t_0, \dots, t_N)$, which model the temporal behaviour of these measures, where as model experiment we could have for example a DT-MRI experiment interpreted as sampling second order spatial correlations as function of diffusion time Δ. We have

$$\begin{aligned}
:= &\int_\Omega d\mathbf{r}_0 \phi_0(\mathbf{r}_0) \int_\Omega P(\mathbf{r}_1, \mathbf{r}_0, t_1) \phi_1(\mathbf{r}_1)\, d\mathbf{r}_1 \cdots \int_\Omega P(\mathbf{r}_N, \mathbf{r}_{N-1}, t_N) \phi_N(\mathbf{r}_N)\, d\mathbf{r}_N \\
= &\sum_{k_0,\dots,k_N} e^{-\sum_{j=0}^N \lambda_{k_j} t_j} \int_\Omega \phi_0(\mathbf{r}_0) w_{k_0}(\mathbf{r}_0) d\mathbf{r}_0 \int_\Omega w_{k_0}(\mathbf{r}_1) w_{k_1}(\mathbf{r}_1) \phi_1(\mathbf{r}_1)\, d\mathbf{r}_1 \cdots \\
&\int_\Omega w_{k_N}(\mathbf{r}_N) w_{k_N}(\mathbf{r}_{N-1}) \phi_{N-1}(\mathbf{r}_{N-1})\, d\mathbf{r}_{N-1} \int_\Omega w_{k_N}(\mathbf{r}_N) \phi_N(\mathbf{r}_N)\, d\mathbf{r}_N \\
&= \sum_{k_0,\dots,k_N} e^{-\sum_{j=0}^N \lambda_{k_j} t_j} S_{k_0}(\phi_0) A_{k_0 k_1}(\phi_1) \cdots A_{k_{N-1} k_N}(\phi_{N-1}) S_{k_N}(\phi_N)
\end{aligned}$$

where we have introduced the arrays $A_{kl}(\phi) = \int_\Omega w_k(\mathbf{r}) w_l(\mathbf{r}) \phi(\mathbf{r})\, d\mathbf{r}$ and $S_k(\phi) = \int_\Omega w_k(\mathbf{r}) \phi(\mathbf{r}) = (\phi, w_k)_\Omega$. These shape invariants are the fundamental tools of our computations. The array S is the array of L^2 coefficients of the measurements in the L^2-orthonormal basis of eigenmodes. We chose this notation so as to be consistent with Codd and Callaghan, where they treat the special case where measurements are spatial modes $\phi(\mathbf{r}) = e^{-2\pi i \mathbf{q}^t \mathbf{r}}$. The time correlation can thus be written in terms of these arrays using standard linear algebraic operations (traces, matrix products etc).

It is possible to make some generic statements from *spectral geometry*:

1. Only for reflecting boundary condition, 0 is an eigenvalue for the constant function $1/|\Omega|$ where $|\Omega|$ is the area or volume of Ω. It follows that $\int w_k = 0$ for $k > 0$. Otherwise all terms decay exponentially with time.
2. For $k \to \infty$, we have *Weyl's* asymptotic formula [7]: $\lambda_k \sim 2\pi k/|\Omega|$. Here λ_k means the k-th eigenvalue when they are sorted by magnitude. Thus for large k the eigenvalues give information on the area.

3. Eigenfunctions have symmetries associated to that of the domain. Special symmetric shapes are extremal among classes of domains, and eigenvalues usually multiplicity larger than 1, and alternate numbering systems may be used.

Special Cases. We are now in position to answer more exactly the questions raised in the introduction. We first go back to the first order averages:

1. The average position $\langle \mathbf{r} \rangle_\Omega(t)$ for a starting distribution $\phi_0(\mathbf{r}_0)$ satisfies
$$\langle \mathbf{r} \rangle_\Omega(t) = \sum_k e^{-\lambda_k t} S_k(\phi_0) S_k(\mathbf{r})$$
For a uniform starting distribution, and reflecting walls, $w_k = \delta_{k0}/\sqrt{|\Omega|}$, and we confirm the intuition that $\langle \mathbf{r} \rangle_\Omega(t) = \bar{\mathbf{r}}$, the centroid, independently of time. If the starting position is known to be $\mathbf{p}_0$, the starting distribution is $\delta_{\mathbf{p}_0}(\mathbf{r}_0)$, and $\langle \mathbf{r} \rangle_\Omega = \sum_k e^{-\lambda_k t} \bar{\mathbf{r}}_k w_k(\mathbf{p}_0)$. Here $\bar{\mathbf{r}}_k := S_k(\mathbf{r}) = \int_\Omega \mathbf{r} w_k(\mathbf{r})$ is the weighted centroid using the k-th eigenmode, let us call it the k-mode centroid. We see how the different eigenmodes contribute to the time dependent shift from the centroid. Note that the w_k are *not* pure probability distributions.
2. The average second order correlation $\langle \mathbf{r} \cdot \mathbf{r} \rangle_\Omega(t_1, t_2)$ is $\sum_{kl} S_k A_{kl} e^{-(\lambda_k t_1 + \lambda_l t_2)} \bar{S}_l$. For reflecting boundary conditions and uniform starting estimates, we can simplify further to
$$\mathbb{D}(t, \Omega) = \sum_l e^{-\lambda_l t} \bar{\mathbf{r}}_l \bar{\mathbf{r}}_l. \tag{4}$$
3. The k-mode centroids are related to derivatives at zero of q-space measurements: $\partial_\mathbf{q}|_{\mathbf{q}=0} \int w(\mathbf{r}) e^{-2\pi i \mathbf{q}^t \mathbf{r}} \propto \int w(\mathbf{r}) \mathbf{r}$.

These computations confirm the intuitions for zero or very large time, but are particularly of interest for the mid-range in highlighting how via the eigenmodes the shape and boundary conditions influence the time behaviour. The formulas are valid for any domain shape. Thus, for each shape, we just need to compute the shape invariants $S_k, A_{kl}, \bar{r}_k$.

2.2 Eigendecomposition of Δ on some domains

Here, we want to investigate how the shape explicitly influences the shape invariants cited above. It is possible to give explicit or semi-explicit formulas for eigenmodes in some cases. We essentially use results from *spectral geometry* for our own purposes [8,7].

The general idea is again of separation, as the general diffusion equation was solved by separation in eigenmodes. By separation of variables, the PDE is transformed in multiple ODEs which have standard solutions. The variables can usually be found by a transformation in *orthogonal curvilinear coordinates* (see Appendix). We consider two and three-dimensional examples, the two dimensional ones also represent cylinders. Usually this results in a different indexing than the standard one by eigenvalue magnitudes, and the multiplicity of eigenvalues is related to the symmetry.

1. Rectangles, parallelepipeds: we use Cartesian coordinates such that the rectangle with side length a, b has boundaries at $x = 0, a$ and $y = 0, b$. Writing $w(x, y) =: u(x)v(y)$ the eigenmode equation can be transformed into $vu'' + uv'' + \lambda uv = 0$ and for reflecting boundary condition $u'(0) = u'(a) = 0 = v'(0) = v'(b)$. The eigenmodes are then $w_{mn}(x, y) := \frac{2}{\sqrt{ab}} \cos(\pi n/a) \cos(\pi m/b)$ with eigenvalues $\pi^2(n^2/a^2+m^2/b^2)$. The standard magnitude based indexing is replaced by a more appropriate. From this we easily get that generalised centroids are

$$\bar{x}_{mn} = -\frac{4}{\pi^2}\frac{\delta_{n,0}\delta_{m|2,1}}{m^2}\frac{a^2}{\sqrt{ab}} \quad \bar{y}_{mn} - \frac{4}{\pi^2}\frac{\delta_{m,0}\delta_{n|2,1}}{n^2}\frac{b^2}{\sqrt{ab}} \tag{5}$$

   From this by using the general formulas above, we get an explicit expression for the mean position as function of time, as well as for the second order correlations. From this we recover formulas for P such as the ones in [11].
2. Disks, spheres: the Laplace operator in spherical coordinates is

$$\partial_r^2 + \frac{D-1}{r}\partial_r + \frac{1}{r^2}\mathit{\Delta}_S$$

   where $\mathit{\Delta}_S$ is the angular Laplace-Beltrami operator. We separate into radial and angular variables: $w(r, \mathbf{e}) = u(r)v(\mathbf{e})$ where $\mathbf{e}$ is a point on the sphere or circle. Then the eigenvalue equation becomes

$$\left(\partial_r^2 + \frac{D-1}{r}\partial_r + \frac{1}{r^2}\mathit{\Delta}_S\right) uv = \lambda uv \tag{6}$$

$$\tag{7}$$

   the right hand side depends only on r, meaning that $\frac{\mathit{\Delta}_S v}{v}$ must be independent of $\mathbf{e}$, thus $\mathit{\Delta}_S v = \mu v$, in other words v is an eigenfunction on the sphere or circle. These are the spherical harmonics in 3D, or $cosq\theta, \sin q\theta$ in 2D, the periodicity imposes $\mu = q$ an integer. In 3D, the constants are $\mu = l(l + 1)$. The equation in u

$$u'' + \frac{1}{r}u' + (\frac{1}{r^2}(q^2 - r^2\lambda)u = 0 \quad (D = 2) \tag{8}$$

$$u'' + \frac{2}{r}u' + (\frac{1}{r^2}(l(l+1)) - r^2\lambda)u = 0 \quad (D = 3) \tag{9}$$

   is *Bessel*'s differential equation D=2, Eq. 8spherical differential equation D=3, Eq. 9. The solutions are *spherical Bessel functions* $j_n(r)$, which are standard Bessel functions weighted by $1/\sqrt{r}$ (hence the terms in [11]). For the generalised centroids, we need integrals such as $\int_0^R r^2 J_p(z_{pq}r)\, dr \int P_n(\cos\theta)\cos\theta\sin\theta\, d\theta = \int_{-1}^1 P_n(y)y\, dy$ etc, which can be found in standard integral tables, for which we refer to the appendix for some (see also [13], p. 516–518). We give here explicit formulas for the 2D example, as three dimensional formulas would take too much space, and the cylindrical cases are of special interest. Again, eigenmodes are re-indexed in terms of pairs of indices, the angular index q, and the radial index p, z_{qp} is the p-th zero of the qth Bessel function J_q (see Fig. 1).

$$\lambda_{qp} = \frac{z_{qp}^2}{R^2}; \quad c_{qp}(r,\theta) = \frac{2}{\pi^{1/2} R J_{q+1}(z_{qp})} \cos(q\theta) \cdot J_n(z_{qp}\frac{r}{R}); \tag{10}$$

$$\lambda_{qp} = \frac{z_{qp}^2}{R^2}; \quad s_{qp}(r,\theta) = \frac{2}{\pi^{1/2} R J_{q+1}(z_{qp})} \sin(q\theta) \cdot J_q(z_{qp}\frac{r}{R}) \tag{11}$$

The generalised centroids are thus

$$\bar{x}_{qp} = \frac{2\pi}{\sqrt{\pi}} \frac{J_1(z_{1p})}{J_2(z_{1p})} \frac{R^2}{z_{1p}^2} \delta_{q1} \qquad \bar{y}_{qp} = \frac{2\pi}{\sqrt{\pi}} \frac{J_1(z_{1p})}{J_2(z_{1p})} \frac{R^2}{z_{1p}^2} \delta_{q1} \tag{12}$$

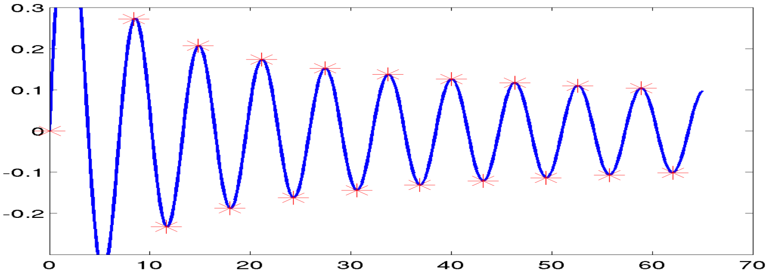

Fig. 1. Zeros of $J_1'(z)$, as computed from [14] `http://iris-lee3.ece.uiuc.edu/~jjin/routines/routines.html` converted to Matlab (The MathWorks) `http://www.mathworks.com/matlabcentral/fileexchange/loadFile.do?objectId=6218` routine `mjdzo.m`. Blue line shows $J_1(z)$ and the red stars are $J_1(z_{1p})$

3. Ellipses and Ellipsoids. In two dimensions, we can introduce elliptical coordinates, and the equation again separates in a 'radial' and and 'angular' part (see Appendix). Both equations are *Mathieu* equations. As for the disk, the periodicity conditions on the radial part imposes that solutions exist only for integer-indexed characteristic values. These are not anymore separated from the radial constant. A noticeable feature of these eigenmodes is the existence of different types, called 'whispering gallery' modes which concentrate around the boundary Details are described for example in [6,15]. In three dimensions, we can use *ellipsoidal* coordinates. This leads to Lamé equations, and *ellipsoidal harmonics* see for example [16]. These have found applications in MRI shimming [17], but again formulas for them would run beyond the allocated space.

3 Numerical Results

In this section we show explicit eigenmodes, and the derived quantities.

Simulation on a disk. Here we perform a simple simulation of a random walk inside a disk with reflecting boundaries (1 mio time steps, starting position $[5/6, 0]$, fixed spatial steps $R/100$), and record the average position of the centroid of the points as function of time. We also plot the second order correlations. Results are shown for different time-scale. With this experiment we aim to demonstrate the shape dependent behaviour of the time curves. The disk was chosen for its simplicity. Reflecting boundaries are easy to compute, and the shape depends on a unique parameter. Note that we have one experiment, from a fixed starting position $\mathbf{p}_0$ (Fig. 2).

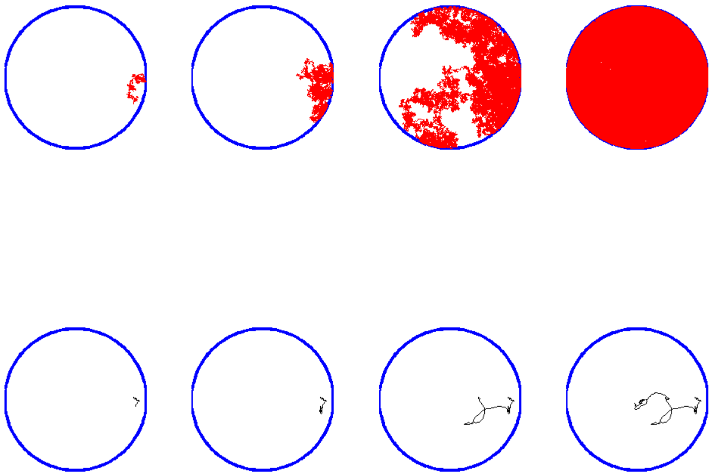

Fig. 2. Random walk starting at $\mathbf{p}_0 := (5/6, 0)$ inside a disk of radius 1 (above), with their centroids (below). From left to right, after 10^N steps, for $N = 3, 4, 5, 6$

Comparisons of spectra. Here we compare the spectra of some symmetric and less symmetric shapes, and show how they characterise the geometry (see Fig. 3).

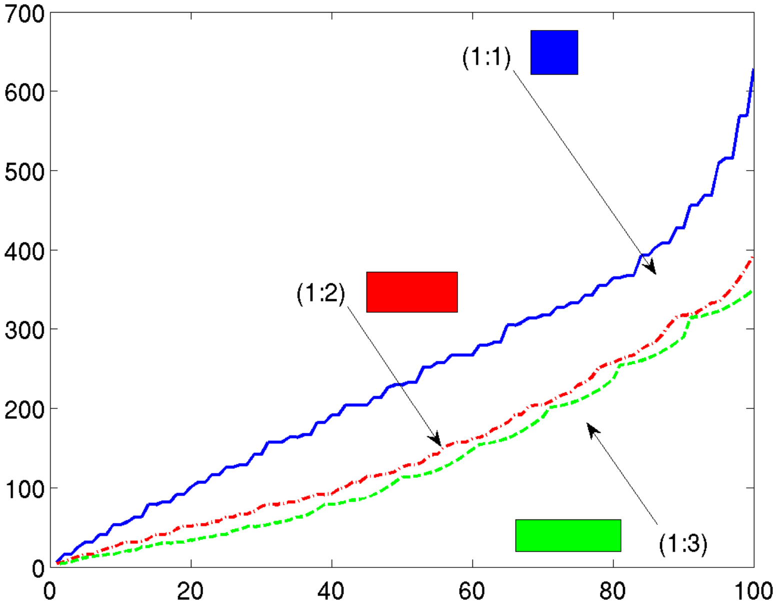

Fig. 3. Spectra of rectangular shapes for different side-lengths a, b: blue-(1,1), red– (1,2), green-. (1:3).

Apparent Diffusion Functions Here we illustrate second order correlations. Fig. 4 shows the values computed purely numerically from the simulations above.

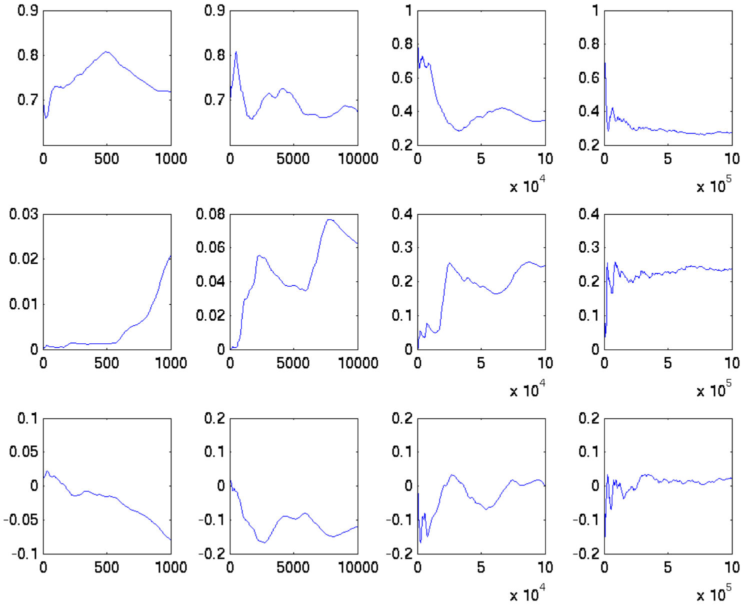

Fig. 4. Second order correlations from the simulations Fig. 2. First row $\mathbb{D}_{xx}(t)t = \langle xx \rangle$, second row $\mathbb{D}_{yy}(t)t = \langle yy \rangle$ third row $\mathbb{D}_{xy}(t)t = \langle xy \rangle$, at the same time scales as Fig. 2.

4 Discussion

Our analysis describes a method to investigate microscopic shapes via the time behaviour of some correlation functions. Of course, for a practical application, this will require making some assumptions. For example, if we assume that the pores are disks of a fixed radius R_0 with reflecting boundaries, a few values of an apparent diffusion function at different diffusion times (such as Δ in a spin-echo pulsed gradient diffusion experiment). would enable us to compute R_0. Another example would be that only perfectly reflecting boundaries give eigenvalue 0, and the porosity is likely to control how small the main eigenvalue is. The main eigenmode is for relatively large time the only remaining one, thus we could attempt to investigate wall porosity by considering the temporal decay rate as function of Δ.

If we want to make statements about the microscopic shapes, we need to agree on a vocabulary for these shapes, for example assuming that they can be parametrised in some ways. Furthermore, the exact mechanism for the transition to macroscopic measures is more complex, as here we have described the effect of measuring one single cell. Nevertheless, the shape dependence of the spectrum reduces most of the problems to the eigenmodes for suitable boundary conditions, and a good understanding of them is thus a stepping stone in the understanding of apparent diffusion coefficients.

Future work. We plan more extensive work in particular in three dimensions, and more general boundary conditions including permeability. In order to best incorporate multiple compartments, we would also generalise the PDEs to coupled PDEs.

Appendix: Properties of Bessel functions

1. $x^{q+1}J_q(x) = (x^q J_q(x))'$. Thus $\int_0^R x^{q+1} J_q(ax)\,dx = \frac{R^q}{a^2} J_q(aR)$.
2. $\int_0^R x J_q(z_{qn}\frac{x}{R}) J_q(z_{qm}\frac{x}{R})\,dx = \frac{R^2}{2} J^2_{q+1}(z_{qn})\delta_{nm}$. This reflects the orthogonality of eigenfunctions of self-adjoint operators.
3. Zeros for J_q and J_{q+1} alternate, there is an infinity of them. We note $J_q'(z_{qp}) = 0$ for the zeros of derivatives, these numbers are tabulated.
4. The MacMahon expansion gives asymptotics for z_{qp}: $\beta_{qp} := (p + \frac{q}{2} - \frac{3}{4})\pi$

$$z_{qp} \sim \beta_{qp} + \frac{4q^2+3}{\beta_{qp}} + \frac{112q^4 + 328q^2 - 9}{\beta_{qp}^3} + \cdots .$$

See also Fig. 1 which confirms that the zeros are well approximated by integer multiples.

Appendix: Centroids for Legendre functions For this we need the following formula

$$\int_{-1}^{1} y P_L(y) P_N(y) = \begin{cases} \frac{2(L+1)}{(2L+1)(2L+3)} & N = L+1 \\ \frac{2L}{(2L+1)(2L+1)} & N = L-1 \end{cases}$$

[18] (which cites Arfken 1985, p. 700, Ch. 12 in *Math. Methods for Physicists 3rd ed*). It follows that $\int_{-1}^{1} y P_1(y)\,dy = 2/3$.

Appendix: Elliptic coordinates Let $x(\mu,\theta) = \frac{R}{2}a(\mu)\cos\theta$ and $y(\mu,\theta) = \frac{R}{2}b(\mu)\sin\theta$. Fix a 2 dimensional anisotropy (eccentricity) $f = a/b$ for an ellipse. Let $\mu_0 = \mathrm{atanh}(f)$. Then $\mu = \mu_0$ in these coordinates defines an ellipse with this shape. Ellipsoidal coordinates are defined similarly (see [6,19,15,20,21]).

Appendix: Orthogonal Coordinate Systems This is a coordinate system $x(\xi,\eta,\zeta), y(\xi,\eta,\zeta), z(\xi,\eta,\zeta)$ for which $ds = \sqrt{dx^2+dy^2+dz^2} = (h_1 d\xi)^2 +$

$(h_2 d\eta)^2+(h_3 d\zeta)^2$. This means that the lines ξ =const are orthogonal to η=constant and ζ=constant. The Laplace-Beltrami operator is

$$\frac{1}{h_1 h_2 h_3}\left(\frac{h_2 h_3}{h_1} f_{\xi\xi} + \frac{h_1 h_3}{h_2} f_{\eta\eta} + \frac{h_2 h_3}{h_1} f_{\zeta\zeta}\right)$$

Cartesian, polar and spherical, and elliptical and ellipsoidal coordinates are examples of orthogonal coordinate systems (see [16]).

References

1. J. Nicholson. Diffusion and related transport mechanisms in brain tissue. *Rep. Prog. Phys*, 64:815–884, 2001.
2. C. Nicholson and E. Syková. Extracellular space structure revealed by diffusion analysis. *Trends in Neurosciences*, 21(5):207–215, 1998.
3. G. J. Stanisz, A. Szafer, G. A. Wright, and M. Henkelman. An analytical model of restricted diffusion in bovine optic nerve. *Magnetic Resonance in Medicine*, 37:103–111, 1997.
4. Y. Assaf, T. Blumenfeld-Katzir, Y. Yovel, and P. J. Basser. AxCaliber: A method for measuring axon diameter distribution from diffusion MRI. 59:1347–1354, 2008.
5. D. C. Alexander. A general framework for experiment design in diffusion mri and its application to measuring direct tissue-microstructure features. *Magnetic Resonance in Medicine*, In Press, 2008.
6. E. Mathieu. Mémoire sur le mouvement vibratoire d'une membrane de forme elliptique. *Liouville's Journal*, XIII, 1868.
7. M. Kac. Can one hear the shape of a drum? *The American Mathematical Monthly*, pages 1–23, 1966.
8. M. Berger, P. Gauduchon, and E. Mazet. *Le spectre d'une variété Riemannienne*, volume 194 of *Lecture Notes in Mathematics*. Springer (Berlin), 1971.
9. S. L. Codd and P. T. Callaghan. Spin echo analysis of restricted diffusion under generalized gradient waveforms: Planar, cylindrical, and spherical pores with wall relaxivity. *J of Magn. Res.*, pages 358–372, 1999.
10. Y. Assaf, R. Z. Freidlin, and P. J. Basser. The measurement of the axon diameter distribution in white matter using diffusion MR methods. In *Proc. ISMRM*, page 842, Miami, 2005. ISMRM.
11. C. H. Neuman. Spin echoes of spins diffusing in a bounded medium. *J. of Chem. Phys.*, 60:4508–4511, 1974.
12. S. Rosenberg. *The Laplacian on a Riemannian Manifold*. London Mathematical Society, 1997.
13. *Equations of Mathematical Physics (translated from Russian)*. Pergamon Press, 1963.
14. S. Zhang and J. Jin. *Computation of Special Functions*. Wiley, 1996.
15. G. Chen, P. T. Morris, and J. Zhou. Visualization of special eigenmode shapes of a vibrating elliptical membrane. *SIAM Review*, 36:453–469, 1994.
16. William Elwood Byerly. *An Elementary Treatise on Fourier Series And Spherical, Cylindrical, And Ellipsoidal Harmonics: With Applications To Problems In Mathematical Physics*. Kessinger, First published 1893 (Dover 1959).
17. S. Crozier, L. K. Forbes, and M. Brideson. Ellipsoidal harmonic (Lamé) MRI shims. *IEEE Trans. on Appl. Superconductivity*, 12(4):1880–1885, 2002.

18. E. W. Weinstein. ”Legendre Polynomial.”. [Online] MathWorld–A Wolfram Web Resource. `http://mathworld.wolfram.com/LegendrePolynomial.html`.
19. J. C.-E. Sten. Ellipsoidal harmonics and their application in electrostatics. *J. of Electrostatics*, 64:647–654, 2006.
20. H. B. Wilson and R. W. Scharstein. Computing elliptic membrane high frequencies by mathieu and galerkin methods. *J Eng Math*, 57:41–55, 2007.
21. J. C. Gutierrez-Vegáa, R. M. Rodríguez-Dagnino, M. A. Meneses-Nava, and S. Chavéz-Cerda. Mathieu functions, a visual approach. *Am. J. Phys.*, 71(3):233–242, 2003.

Gene Effects Mapped Using Fractional and Geodesic Anisotropy in Diffusion Tensor Images of 92 Monozygotic and Dizygotic Twins

Agatha D. Lee[1], Natasha Leporé[1], Marina Barysheva[1], Yiyu Chou[1], Caroline Brun[1],
Sarah K. Madsen[1], Katie McMahon[2], Greig I. de Zubicaray[2], Margaret J. Wright[3],
Arthur W. Toga[1], Paul M. Thompson[1]

[1] Laboratory of Neuro Imaging, Department of Neurology.
UCLA School of Medicine, Los Angeles, USA
[2]Functional MRI Laboratory, Centre for Magnetic Resonance,
University of Queensland, Brisbane, Australia
[3]Queensland Institute of Medical Research, Brisbane, Australia

Abstract. We used tensor-derived measures to map the extent of genetic effects on brain fiber microstructure, in 23 monozygotic and 23 dizygotic twin pairs. All 92 DTI volumes were fluidly registered to a geometrically-centered template via a high-dimensional mapping of co-registered structural-MRI. After tensor re-orientation, we computed three scalar DTI measures: the fractional anisotropy (FA), geodesic anisotropy (GA), and the hyperbolic tangent of GA (tGA); GA measures the geodesic distance between tensors on the symmetric positive-definite tensor manifold. Spatial maps of intraclass correlations between MZ and DZ twins were compared to compute maps of Falconer's heritability statistics. We also performed a maximum likelihood estimation of genetic influences using path analysis. The manifold-based measure, tGA, was marginally more powerful than FA for detecting genetic influences, and improved the fit of quantitative genetic models relative to FA and GA. The pattern of genetic influences was remarkably consistent with the neurodevelopmental sequence, with strong occipital genetic effects and strong frontal environmental effects.

Keywords: DTI, Fractional Anisotropy, Geodesic Anisotropy, Twins, quantitative genetics, path analysis.

1 Introduction

Diffusion tensor (DT) MRI is sensitive to the magnitude and directional properties of local water diffusion in biological tissues. DT imaging of the brain provides vital information on fiber connectivity and composition; water diffuses preferentially along fiber tracts, but diffusion is restricted in directions orthogonal to the dominant fiber orientation. In clinical research, the fractional anisotropy (FA), computed from the eigenvalues of the local diffusion tensor, is sensitive to the effects of aging and neurodegenerative disease, and is commonly used to assess white matter fiber integrity. A related scalar quantity, the Geodesic Anisotropy (GA) [**1**] is an alternative to

FA. GA measures the intrinsic distance between positive-definite symmetric matrices on the manifold. GA may be transformed to hyperbolic tangent form of GA (tGA), making its range comparable to that of FA, [0, 1), and easing comparisons of the two values.

Intersubject variation of DTI signals is not yet well understood. There is great interest in finding which factors (e.g., genetic versus environmental) influence fiber characteristics, and ultimately which genes influence fiber structure. Two key steps in addressing this question are: (1) finding DTI-derived anisotropy measures that are most sensitive for detecting genetic effects; and (2) determining the relative proportion of genetic versus environmental control over DTI signals in different brain regions. Here we examine these two questions using a DTI dataset of 92 healthy young adult twins.

Several twin studies have examined how genes influence brain structure. A structural MRI study of twins [**2**] found that genetic factors strongly influence several aspects of brain morphometry, including cortical thickness and regional gray and white matter volumes. A neurodevelopmental study [**3**] found that brain tissue maturation rates differ by region, with those involved in primary sensory function (e.g., occipital lobes) maturing prior to those involved in sensory integration and behavioral control (e.g., frontal and parietal lobes). We hypothesized that fiber integrity in brain regions that develop earlier would be more heavily influenced by genetics while those developing over a more protracted period would be more heavily influenced by environmental factors. In [**2**], genetic influences on DTI were studied using FA, in a small sample of subjects, revealing that the proportion of genetic versus environmental control varied regionally in the corpus callosum.

Here we extend the work in [**2**] by creating 3D maps of heritability (the proportion of intersubject variance attributable to individual genetic differences) for FA, GA and tGA. We use DTI-derived maps of FA and GA to compute the intraclass correlation (*r*), or resemblance, for MZ and DZ twins at each voxel. This enables us to assess genetic effects on white matter microstructure and to visualize the 3D profile of genetic influences. Extending our work in [**4**], we computed the relative proportion of variance attributable to genetic versus environmental factors using the A/C/E quantitative genetic model. Lobar measures of FA and tGA were computed and structural equation models were fitted to the lobar mean data, using chi-squared statistics to rank models [**5**].

We also compared the power of 3 DTI-derived scalar measures for detecting genetic effects on fiber microstructure. The suitability of different DT signals for fitting genetic models depends on (1) empirical factors, e.g., the noise in each channel of the matrix-valued signals, and (2) mathematical factors such as the correct combination of the tensor components using statistics on associated Lie groups such as the symmetric tensor manifold [**6**]. Most clinical DTI studies use FA as a measure of fiber integrity, but GA exploits more of the multivariate information in the diffusion tensor. We determined how strongly genetic factors determine the normal population variability for each of these DTI parameters.

2 Methods

2.1. Subjects and image acquisition.

3D structural brain MRI scans and DT-MRI scans were acquired from 92 subjects: 23 pairs of monozygotic twins (MZ; 22 males/24 females; 25.1±1.4SD years old) and 23 pairs of dizygotic twins (DZ; all same-sex pairs; 20 males/26 females; 23.5±2.1 years) on a 4T Bruker Medspec MRI scanner with an optimized diffusion tensor sequence [**7**]. Imaging parameters were: 21 axial slices (5 mm thick), FOV = 23 cm, TR/TE 6090/91.7 ms, 0.5 mm gap, with a 128×100 acquisition matrix. 30 directional gradients were applied: three scans with no diffusion sensitization (i.e., T2-weighted images) and 27 diffusion-weighted images for which gradient directions were evenly distributed on the hemisphere [**7, 8**]. The reconstruction matrix was 128×128, yielding a 1.8x1.8 mm^2 in-plane resolution. Total scan time was 3.05 minutes.

3D T1-weighted images of corresponding subjects were also acquired with an inversion recovery rapid gradient echo sequence using 4T Bruker Medspec MRI scanner. Acquisition parameters were as follows: TI/TR/TE= 1500/2500/3.83 msec; flip angle=15 degrees; slice thickness = 0.9 mm, with an acquisition matrix of 256x256x256. The study was approved by the Institutional Review Boards at the University of Queensland and at UCLA.

2.2. Image Preprocessing and Registration.

Non-brain tissues were removed from the 3D structural MRIs using the Brain Surface Extraction software (BSE) [**9**] followed by manual editing. Edited scans were linearly registered to a high resolution single-subject brain template image, the Colin27 template, using the FLIRT software [**10**]. A Minimal Deformation Target (MDT) was generated from the 92 subjects, and each 3D structural image was warped using a 3D fluid registration algorithm that allows large deformations while guaranteeing diffeomorphisms [**11, 12**]. Jacobian matrices were calculated from the deformation fields for each subject.

From the DT-MR images, voxel-wise diffusion tensors (3x3 positive symmetric matrices; DT) were generated with the MedINRIA software (http://www.sop.inria.fr/asclepios/software/MedINRIA). Log-Euclidean tensor de-noising was used to eliminate singular, negative definite, or rank-deficient tensors. A diagonal component image (D_{xx}) was used as a template to eliminate extracerebral tissues. Masked images were linearly registered to the corresponding 3D structural images in the standard template space using FLIRT software [**10**].

2.3. Handling orientation information.

One issue with DT registration is that tensor orientations do not remain consistent with the anatomy after nonrigid image transformation. We used transformation parameters from the linear and nonlinear registrations to rotationally reorient the tensors at each voxel to ensure consistent tensor orientations after image registration [**12, 8**]. To compute the tensor rotations, we used the Finite Strain (FS) method on the affine transformation matrix *M*. We then applied a preservation of principal direction (PPD) algorithm on the higher-order transformation, as in [**13**] and [**14**].

The rotational component R_r, of the affine transformation, was found from [**13**] and [**14**]:

$$R_r = \arg\min_{Q'} \| Q' - M \| = \frac{M}{\sqrt{MM^T}} \tag{1}$$

We then computed reorientation components for the nonlinear transformation (R_n) using the Jacobian matrix (J) from the 3D fluid registration step for the structural MR images. The dominant orientation eigenvector (e_1) and the secondary eigenvector (e_2) were computed from DT images, as in [**13**]:

$$R_n = R_{n1} \cdot R_{n2}, \;\; R_{n1}e_1 = \frac{Je_1}{\| Je_1 \|}, \;\; R_{n2}e_2 = \frac{Je_2 - (Je_2 \cdot Je_1)Je_1}{\| Je_2 - (Je_2 \cdot Je_1)Je_1 \|}. \tag{2}$$

2.4. Scalar statistics in the Log-Euclidean space.

Positive-definite, symmetric DT matrices do not form a vector space under standard Euclidean algebraic operations, so we used the ‘Log-Euclidean framework’ [**15**] to simplify computations of tensor statistics, as illustrated in **Fig. 1.** The tensor manifold was projected by log-transformation to its tangent plane at the origin, allowing standard vector space operations such as addition or multiplication to be performed [**8, 15**]. **Fig. 1** illustrates the difference between the geodesic (intrinsic) distance (*green solid line on the manifold*) and the Euclidean (extrinsic) distance between tensors (*olive colored dotted line*).

We used the conventional definition of FA :

$$FA = \frac{\sqrt{3}}{\sqrt{2}} \frac{\sqrt{(\lambda_1 - <\lambda>)^2 + (\lambda_2 - <\lambda>)^2 + (\lambda_3 - <\lambda>)^2}}{\sqrt{\lambda_1{}^2 + \lambda_2{}^2 + \lambda_3{}^2}}, \tag{3}$$

with $<\lambda> = \frac{\lambda_1 + \lambda_2 + \lambda_3}{3}$. FA is a simple comparison of eigenvalues, and is an extrinsic measure on the manifold of symmetric positive definite tensors. The intrinsic measure, GA, was derived from the tensor manifold metric [**11**]. Here, we computed GA using the Log-Euclidean metric [**15**] as an alternative scalar measure to compare with FA. We used the following definition of GA:

$$GA(S) = \sqrt{Trace(\log S - <\log S> I)^2}, \tag{4}$$

with $<\log S> = \frac{Trace(\log S)}{3}$, the distance between the tensor and the “nearest” isotropic tensor in the associated Log-Euclidean metric. GA is a geodesic distance on the tensor manifold. We also transformed GA into tGA as in [**1**], to map the GA values to a convenient range [0, 1); FA values already fall in the range [0, 1].

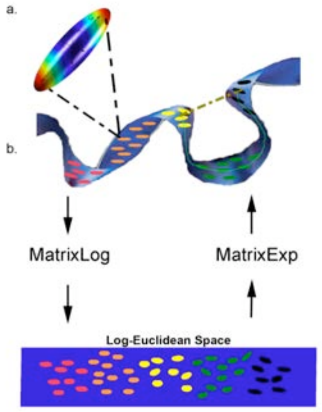

Fig. 1. **(a)** is an ellipsoidal representation of the DT at one voxel; the relative rates of diffusion (distance of boundary points to the origin) are represented by colors. The axes denote the 3 eigenvectors, and the eigenvalues are incorporated into the magnitude of each axis. **(b)** shows positive definite symmetric DTs in a non-linear manifold in R^6. The geodesic distance between tensors in the manifold is indicated by the green curve. Euclidean distances between tensors are shown by the olive dotted line. The dotted line does not lie on the manifold and thus is not an ideal distance measure between tensors. The tensors are projected to the tangent plane at the origin as in the Log-Euclidean framework, as displayed in the bottom panel **(b)**.

2.5. Statistics for heritability analyses in twins.

Voxel-wise FA, GA and tGA values were computed for each subject, and voxel-wise intraclass correlations (r) were computed separately for the MZ group (r_{MZ}) and for the DZ group (r_{DZ}) to assess the similarity within pairs. To provide a basic estimate of the proportion of variance in the FA (and GA) values attributable to genetic differences, we used Falconer's heritability estimate [**16**]:

$$h^2 = 2(r_{MZ} - r_{DZ}). \qquad \textbf{(5)}$$

This heritability estimate, ranging from 0 (no genetic effect) to 1 (total genetic control), is expected to vary across brain regions and across different DTI measures. This allows inferences about how much of the population variance is attributable to genes, environmental factors, measurement errors, or inter-subject registration errors.

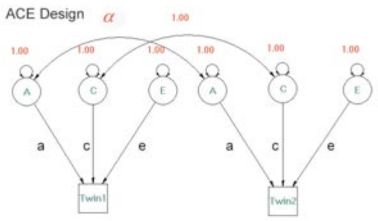

Fig. 2. Structural equation model for the classical A/C/E design. Each of three circles represents A (additive genetic), C (common environment), and E (unique environment) and the squares represent each phenotype. Causal paths are shown as single-headed arrows, correlational paths as double-headed arrows and the double-headed arrow to the same variable (circle) indicates a variance. α denotes the genetic correlation between twin pairs (1 for MZ and 0.5 for DZ).

We then used maximum likelihood estimation (MLE) to estimate a standard quantitative genetic model (the A/C/E model, Mx software (version 1.7.03)) [**5**], which estimates the proportion of the intersubject variance in the four major lobes of the brain (frontal, parietal, temporal, occipital) as well as within white matter and gray matter, attributable to each of 3 factors – additive genetic effects (a^2), common environmental effects (c^2), and individual-specific environmental effects (e^2). All variance components combine to create the observed inter-individual variance, such that $a^2+c^2+e^2=1$. The weights θ = (a, c, e) were estimated by comparing the covariance matrix implied by the model, $\Sigma(\theta)$, and the sample covariance matrix of the observed variables, **S**, using maximum-likelihood fitting:

$$F_{ML,\theta} = \log\left|\Sigma(\theta)\right| + trace(\Sigma^{-1}(\theta)\mathbf{S}) - \log\left|\mathbf{S}\right| - p, \tag{6}$$

where $p = 2$ is the number of observed variables. By convention, $p<0.05$ indicates that the model is a poor fit to the data and the model is rejected. The Akaike Information Criterion (AIC) is the difference between the χ^2 goodness of fit and twice the number of degrees of freedom, and measures of the goodness of fit of the variance component model, adjusted for the model complexity. **Fig. 2** shows the path diagram for the ACE twin model.

3 Results & Discussion

Fig. 3a, b, c, and g, h, i show intraclass correlation (r) maps between MZ pairs and DZ pairs for FA, GA and tGA measures. In MZ twins, who share the same genes, all deep white matter regions show high intra-pair correlations, reaching signficance in a broadly distributed deep white matter region, including the corpus callosum. This pattern of correlations is very similar for all three anisotropy measures (FA, GA and tGA) among the MZs pairs; as would be expected for a genetically influenced trait, the correlation is weaker in the DZ maps. Maps of Falconer's heritability (h^2) are also shown in **Fig. 3m, n** and **o**. Heritability values are high for all the anisotropy measures in the corpus callosum and almost all subcortical white matter regions. This is not unreasonable, as these are heavily myelinated white matter tracts with high FA (and GA). The correlation maps for tGA (**Fig. 3a, e**) show marginally higher effect sizes than those for FA (**Fig. 3b**, **f**). **Fig**. **3c, d, g** and **h** show significance value maps for these correlations, based on the computed r values; significance was assigned using a permutation test at each voxel for both FA and tGA, to establish a non-parametric null distribution for the statistics at each voxel. The correlation is strongest in the corpus callosum and medial frontal regions (not shown).

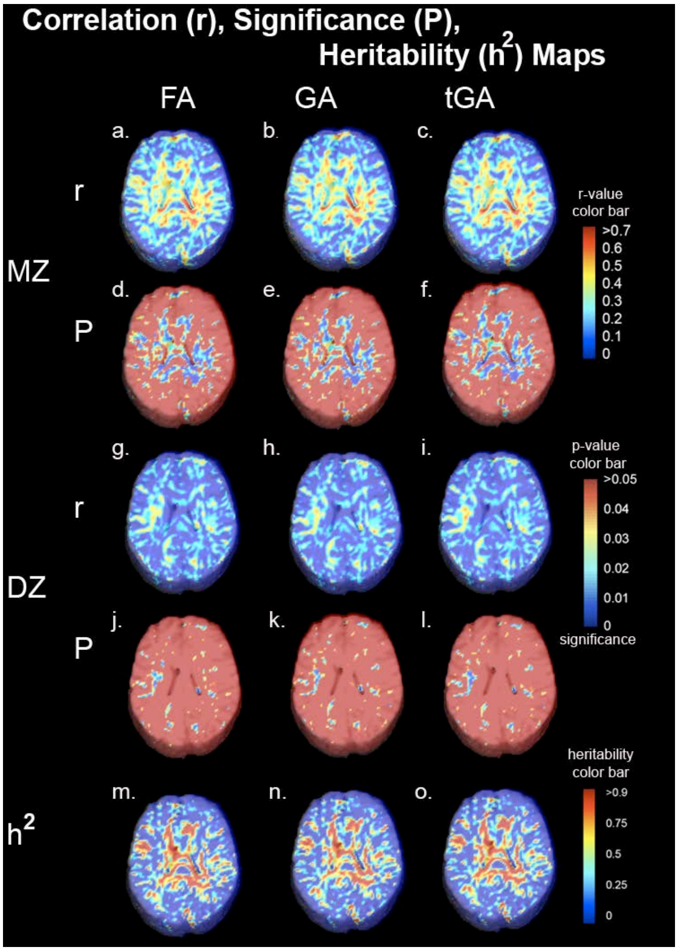

Fig. 3. (**a, b, c, g, h, i)** show intraclass correlation (ICC) maps for FA, GA and tGA in MZ and DZ twins. **(m, n, o)** show heritability maps for FA, for GA, and for tGA. **(c, d, g, h)** show non-parametric permutation based *P*-values at each voxel, based on *r* values for tGA and FA for MZ and DZ groups.

Percentage measures for a^2, c^2 and e^2 derived from the A/C/E model using both FA and tGA are displayed in **Fig. 4**. These estimate the effects of genetic, common and unique environmental factors on brain fiber parameters, suggesting that the relative magnitude of these effects may vary by region. **Table1** shows model parameters including goodness-of-fit (χ^2), degrees of freedom (df), *p*-values and AIC values for selected regions. *p*-values greater than 0.05 and low χ^2 values indicate that the model is a *good* fit to the data (note that this convention for structural equation models is the opposite of the typical range of significance values when rejecting a null hypothesis). Both FA and tGA measures show strong effects of A (genetic factors) and C (common environment) in the frontal lobes and effects of A (genetic factors) and E (individual environment) in the occipital lobes. Common environmental effects are only detected in the frontal lobes. The detection of a genetic effect is consistent with many other studies (e.g., [**17**]) that have detected strong genetic influences on brain morphology, but the mapping of genetic effects on fiber architecture here is novel. Occipital regions are among the first to mature, and their fiber characteristics may be already heavily genetically determined at an early age. Frontal regions develop over a much more protracted period, perhaps making them more susceptible to environmental influences. Our findings somewhat support our *a priori* hypothesis that genetic influences may vary depending on time-course sequence of white matter development, although this requires further testing.

Lobar Region	Model fit							Variance attributable to each factor (%)					
	χ^2		p		AIC		df	A		C		E	
	FA	tGA	FA	tGA	FA	tGA		FA	TGA	FA	tGA	FA	tGA
Frontal -Left	6.20	6.46	0.10	0.09	0.20	0.46	3	46.25	42.83	34.54	38.09	19.21	19.08
Frontal -Right	3.00	3.04	0.39	0.39	-3.00	-2.96	3	40.06	38.16	37.79	39.56	22.15	22.28
Occip.- Left	1.36	1.43	0.72	0.70	-4.64	-4.57	3	37.55	39.74	0.00	3.93	62.45	56.33
Occip.- Right	2.22	2.30	0.53	0.51	-3.78	-3.70	3	72.10	71.57	0.00	0.00	27.90	28.43

Table 1. Left: Fit of the genetic twin models for different DTI measures, averaged for the frontal and occipital lobes. Right: Variance attributable to each of a^2, c^2, and e^2 factors as a percentage of the overall variance in the sample of subjects. tGA denotes hyperbolic tangent of GA.

Table 2 compares values for GA and tGA, in frontal and occipital regions. *p*-values were below 0.05 for GA for both left and right frontal lobes, implying *rejection* of the model. Thus the use of tGA, rather than GA values, leads to a better fit of the model.

Lobar region	Model fit					
	χ^2		p		AIC	
	GA	tGA	GA	tGA	GA	TGA
Frontal-Left	30.40	6.46	0.00	0.09	24.40	0.46
Frontal-Right	34.26	3.04	0.00	0.39	28.26	-2.96
Occpital-Left	32.03	1.43	0.00	0.70	26.03	-4.57
Occpital-Right	3.27	2.30	0.35	0.51	-2.73	-3.70

Table 2. Comparison of goodness-of-fit for GA and tGA in the ACE genetic model. The table displays χ^2, *p*-values, and AIC. Model fit is generally poorer when GA is used, but improves when tGA is used.

p-values for tGA were greater than those for GA (**Table 1** and **Fig. 4**) in all brain regions, indicating that tGA marginally outperforms GA in detecting genetic influences on fiber architecture.

Anisotropy Measure	Corrected P-value based on Permutation	
	DZ	MZ
FA	***0.046***	***0.014***
GA	0.144	*0.054*
tGA	***0.042***	***0.0056***

Table 3. Overall *P*-values, corrected for multiple comparisons, using the entire brain as a region of interest, based on permutation testing. Both FA and tGA measures show significant patterns of correlation in both types of twins (MZ and DZ).

We also obtained global *P*-values, corrected for multiple comparisons, for the maps, to assess the likelihood that such a pattern of correlations might be observed by chance. We computed these corrected *P*-values based on permutation testing (on the suprathreshold count of voxels with correlations exceeding the p=0.05 threshold at the voxel level). In such a test, the number of voxels in the brain with significant correlations is computed for a large number of randomly permuted datasets, and the corrected *P*-value is the quantile at which the true maps fall in the overall empirical null distribution for the suprathreshold volume. Permutation tests verifying the significance of the maps were significant for FA and tGA in both MZ and DZ twins, but for GA they were borderline in MZ twins (p=0.054) and not significant for DZ twins (**Table 3**). This suggests that the hyperbolic tangent transformation is beneficial in normalizing the statistical distribution of GA. While both MZ and DZ pairs show high correlation, the lower effect sizes for the correlations in DZ pairs in comparison to MZ pairs - who share identical genes - is expected, and points to a genetic effect. At least in our sample of 92 twins, tGA slightly outperformed FA for detecting twin correlations, although effect sizes for both measures were strong. This sample will expand ten-fold to 1150 subjects over 5 years, with the aim of increasing statistical power sufficiently to detect stronger effect sizes for twin correlations and quantitative genetic models.

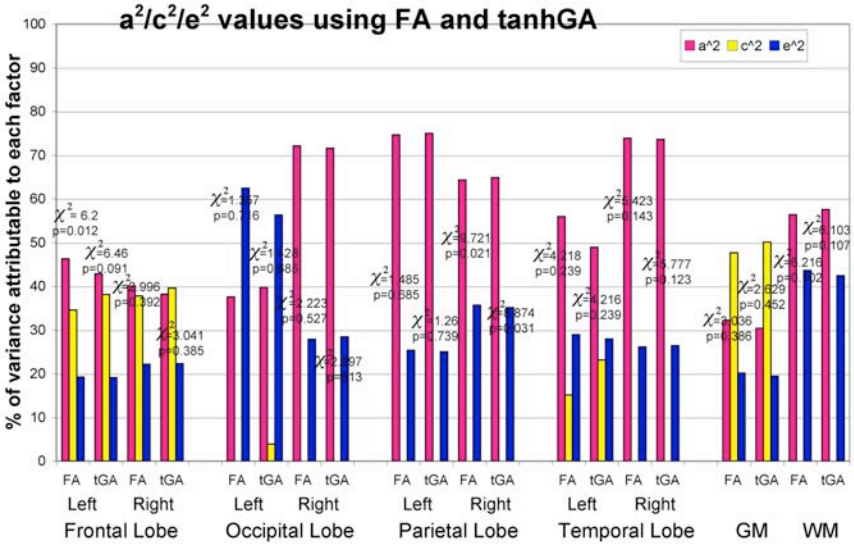

Fig. 4. Variance components, expressed as a percentage of the overall variance, attributable to each of the A/C/E factors, which respectively denote genetic, common and unique environmental effects. Results for FA and tGA are compared for each lobar region, and are highly consistent. An influence of common environment on brain fiber integrity is detected in the frontal lobes only, consistent with the notion that white matter maturation in this region has the most protracted developmental time-course. The χ^2 and *p*-values of each model are overlaid on the bar graphs. Note that, contrary to conventional statistics for testing group difference, *p*-values higher than 0.05 in these structural equation models denote that the model terms provide a good fit to the observed data.

4 References

1. P. Batchelor, Moakher, M., Atkinson, D., Calamante, F., Connelly, A., *A rigorous framework for diffusion tensor calculus,* Magn Reson Med. **53** (2005), 221-226.
2. A. Pfefferbaum, Sullivan,E.V., Carmelli,D., *Genetic regulation of regional microstructure of the corpus callosum in late life*, Neuroreport **12** (2001), 1677-1681.
3. N. Gogtay, Giedd, J.N., Lusk, L., Hayashi, K.M., Greenstein, D., Vaituzis, A.C., Nugent, T.F. 3rd, Herman, D.H., Clasen, L.S., Toga, A.W., Rapoport, J.L., Thompson, P.M., *Dynamic mapping of human cortical development during childhood through early adulthood.*, Proceedings of the National Academy of Sciences of the United States of America **101** (2004), no. 21, 8174-8280.
4. anonymous.
5. M. C. Neale, Boker, S.M., Xie, G., Maes, H.H., *Mx: Statistical modeling,* (1999).
6. A. D. Lee, Lepore, N., Lepore, F., Alary, F., Voss, P., Brun, C., Chou, Y-Y., Barysheva, M., Toga, A.W., Thompson, P.M., *Brain differences visualized in the blind using tensor manifold statistics and diffusion tensor imaging*, Frontiers in the Convergence of Bioscience and Information Technologies (2007), 470-477.
7. G. Christensen, Rabbitt, R., Miller, M. , *Deformable templates using large deformation kinematics,* IEEE Trans. Image Process **5** (1996), 1435-1449.
8. D. K. Jones, Horsfield, M. A., Simmons, A., *Optimal strategies for measuring diffusion in anisotropic systems by magnetic resonance imaging,* Magn Reson Med. **42** (1999), 515-526.
9. D. W. Shattuck, Leahy, R.M., *Brainsuite: An automated cortical surface identification tool*, Medical Image Analysis **8** (2001), no. 202, 129-142.
10. M. Jenkinson, Smith, S., *A global optimisation method for robust affine registration of brain images*, Med Image Anal **5** (2001), 143-157.
11. N. Lepore, Brun, C., Chiang, M.C., Chou, Y., Dutton, R.A., Hayashi, K.M., Lopez, O.L., Aizenstein, H. J., Toga, A.W., Becker, J.T., Thompson, P.M., *Multivariate statistics of Jacobian matrices in tensor based morphometry and their application to HIV/AIDS*, MICCAI (2006).
12. N. Lepore, Chou, Y-Y., Lopez, O.L., Aizenstein, H.J., Becker, J.T., Toga, A.W., Thompson, P.M., *Fast 3D fluid registration of brain magnetic resonance images*, Proceedings, SPIE conference on Physiology, Function and Structure from Medical Images (2008).
13. D. C. Alexander, Pierpaoli, C., Basser, P. J., Gee, J. C., *Spatial transformations of diffusion tensor magnetic resonance*, IEEE-TMI **20** (2001), 1131-1140.
14. H. Zhang, Yushkevich, P.A., Alexader, D.C., Gee, J.C., *Deformable registration of diffusion tensor MR images with explicit orientation optimization,* Medical Image Analysis **10** (2006), 764-786.
15. V. Arsigny, Fillard, P., Pennec, X., Ayache, N. , *Fast and simple calculus on tensors in the log-Euclidean framework,* Int Conf Med Image Comput Comput Assist Interv. **8** (2005), 115-123.
16. D. S. Falconer, *Introduction to quantitative genetics,* (1981).
17. A. W. Toga, and Thompson, P.M, *Genetics of brain structure and intelligence* Annu. Rev. Neurosci **28** (2005), 1-23.

Oral Session II: Tractography and Segmentation

Evaluation of Classification Trees for Fast Segmentation of White Matter Fiber Tracts

Arnaldo Mayer, Gali Zimmerman-Moreno, and Hayit Greenspan

Medical image processing lab, Tel-Aviv University, Ramat-Aviv, Israel
arnakdom@post.tau.ac.il, zimer@post.tau.ac.il, hayit@eng.tau.ac.il

Abstract. A method is proposed for modeling and classification of White Matter fiber tracts in the brain. The presented scheme uses Classification Trees in conjunction with spatial representation of the individual fibers, in order to capture the characteristic behavior of fibers belonging to a specific anatomical structure. The method is characterized by high classification speed, under 3 seconds for all the fibers in a typical DTI brain. The model has the ability to represent complex geometric structures and has an intuitive interpretation. The method is validated on 15 real DTI brains. Encouraging results are presented and analyzed.

Key words: MRI, DTI, brain, classification, supervised, classification trees

1 Introduction

In the last ten years Diffusion Tensor Imaging (DTI) has changed the way we perceive White Matter (WM) in MRI imaging of the brain [1]. A set of Diffusion Weighted Images (DWI) is acquired using non-colinear field gradients and is used to compute a distinct diffusion tensor for each voxel. The principal directions of the tensor were shown to generally coincide with the local orientation of sub-voxel WM axon bundles [2]. Deterministic and stochastic algorithms have been developed to propagate the principal direction of diffusion from seed voxels to the whole brain WM [2], leading to impressive in-vivo reconstructions of major WM tracts [3]. Software tools can be found on the web for tensor computation and tractographic reconstruction on DWI data [4] [5]. With these tools, a specific group of WM fibers or bundles can be identified using a set of two-dimensional regions of interest (ROI) defined on different slices of the brain. The fibers that obey a set of logical conditions involving these ROI's are extracted from the whole brain tractography. The process of extracting a specific group of WM fibers is schematically illustrated in Figure 1(a), where the fibers that pass through the regions $ROI1, ROI2$ and $ROI3$ but do not pass through the region $ROI4$ are displayed. In Figure 1(b) and Figure 1(c), we illustrate, the steps required for the extraction of the left-Uncinate tract, using a sequence of ROI's to define the tract path. In this case the selected fibers are required to pass through the regions R1 to R3 that are marked on different slices of the brain (Figure 1, column (c), rows (1)-(3)) while avoiding the last ROI, R4 (Figure 1, column (c), row (4)). The specificity of the selected fibers increases as more regions-of-interest are applied. This manual process per tract is clearly time-consuming. It becomes rapidly impractical when many distinct tracts have to be segmented from many brains, as in population studies.

Previously published works on fiber tracts segmentation can be divided into two main approaches, namely voxel and fiber based. Both require registration to an atlas. In the first approach, a set of probabilistic atlases has recently become available from the web site of Johns Hopkins Medical MRI Laboratory [6]. Each tract atlas is the voxel average of many co-registered instances of the same tract across several brains. Atlas based tract segmentation using these voxel-based Atlases requires non-linear alignment of the considered brain's tractography with the atlas space. For this purpose an atlas template, e. g. a Fractional Anisotropy volume, is aligned with the considered brain and the same transformation is applied to its fiber tracts.

In the second approach, clustering based methods (both parametric and non-parametric), have been proposed for the modeling of fiber tracts. In [7], the tracts are modeled by a Mixture of Gaussians Atlas learned by Expectation Maximization. In a non-parametric approach [8], normalized cuts are used to generate a high-dimensional atlas that is manually labeled following the clustering. New data is segmented by projecting the Atlas on the considered brain tractography. Registration with the atlas template is also required but a linear affine model is now sufficient. Both methods ([7], [8]) rely on an initial unsupervised clustering step that partitions the fibers into groups. A cluster that is not separated during this step can not receive a distinct classification label. In order to avoid this limitation, we adopt a supervised approach for fibers classification.

The method proposed in the current study is inspired by the manual procedure for tract extraction described above (Figure 1) in which a given tract is defined by a sequence of spatial ROIs that impose its course through the brain. The idea is to learn the sequence automatically from a set of sample fibers for the considered tract. At the same time, we need to discriminate between several tracts in order to enable multiple anatomical tracts segmentation. In this work, we show that Classification Trees [9] provide an adequate framework for the representation and segmentation of anatomical fiber tracts. The method is fast and powerful while easy to implement. The rest of this paper is organized as follows: In Section 2 we describe the proposed method that is validated experimentally in Section 3. Conclusions and future research directions follow in Section 4.

2 Methods

The proposed approach belongs to the supervised classification methods, characterized by a training and classification phase. In a training phase the classification tree is created. The training set contains manually labeled examples, in our case these are fibers belonging to the different fiber tracts.

This tree is later used in the classification step in order to label each fiber according to the fiber tract to which it belongs. Before the training and the

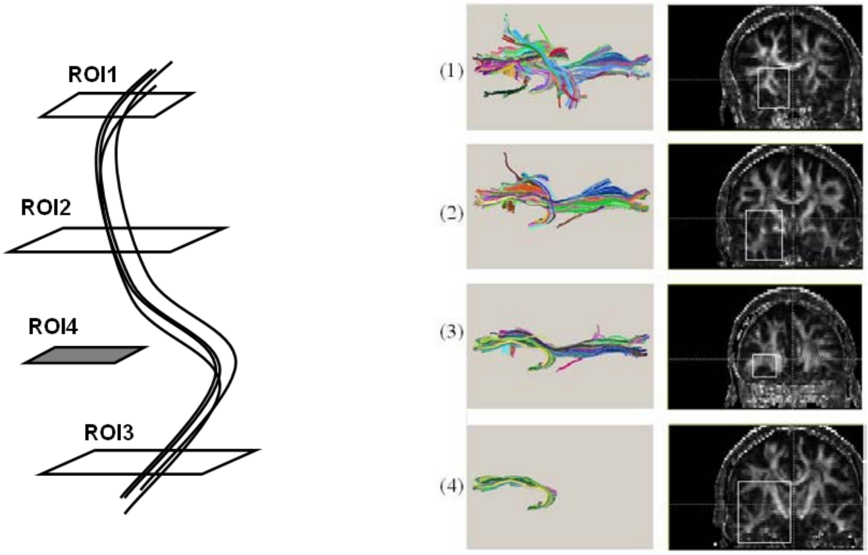

(a) (b) (c)

Fig. 1. Defining a fiber tact via a series of 2D ROIs: general description of the marking process (a); The steps of marking the left-Uncinate using a sequence of regions-of-interest marked on different slices of the brain ((b), (c)). The selected fibers are required to pass through regions R1 to R3 (rows (1)-(3)), while avoiding the last ROI, R4 (row (4), column (c)). The fibers satisfying the markings in column (c) are shown in column (b).

classification can begin, all the data sets involved are to be pre-processed in order to make them comparable. In our case, this entails spatial normalization or registration of the sets of fibers originating from different brains (Section 2.2).

2.1 Fiber Representation

The input data for the proposed scheme consists of brain WM fibers generated by DTIStudio [4]. Each fiber is a discrete three dimensional curve (Figure 2). For the purpose of the analysis a fiber is represented by a fixed length feature vector, containing the coordinates of the sampled points along the curve. Each feature vector f has $3N$ values $f = \{x_1, y_1, z_1, , x_N, y_N, z_N\}$, where (x_i, y_i, z_i) are the sequence of spatial coordinates at N equidistant points along the fiber (Figure 2).

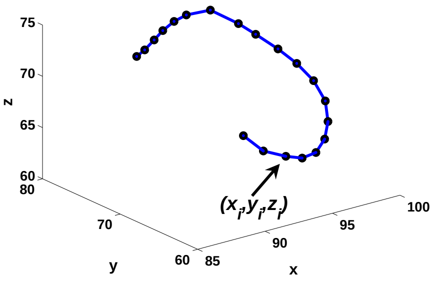

Fig. 2. Representation of a single fiber by equidistant points sampled along the fiber.

2.2 Spatial Normalization

The fibers used for training and for classification must be brought to a common brain space. In order to preserve anatomical variability between the same tracts in different brains, we choose to perform an affine normalization. The idea is to build a training set where inter-subject anatomical variability is well represented for each tract so that it can be properly learned and generalized. All the tractographies in the training and testing sets are affinely aligned to one of the brains in a pre-processing step. This can be achieved with standard registration tools [10]. In that case the transformation is first computed by aligning the corresponding Fractional Anisotropy volumes. This transformation is subsequently applied to the fibers.

In this work, we use a recently proposed scheme, termed the Iterative Closest Fiber (ICF) algorithm [11]. The ICF performs direct registration between tractographies without requiring classical voxel registration. It is based on an efficient extension of the iterative closest point algorithm [12] to the closest feature point in a high dimensional feature space. Here, each feature point corresponds to a DTI fiber according to the representation defined in section 2.1 and the nearest feature point is efficiently approximated by the locality sensitive hashing framework [13].

2.3 Training a Decision Tree

Classification trees perform pattern classification through an ordered sequence of questions. The choice of the next question in the sequence depends on the answer to the current question. Each question is represented as a node in a directed graph. In this work, binary classification trees are used for modeling the different groups of fibers. The trees are trained using the generic CART [9] (Classification and Regression trees) approach, the relevant part of which is reviewed here.

The tree model is built simultaneously for all the classes, using a representative training set in which each fiber has a manual label affiliating it with one of the considered tracts. Each fiber is treated as a data point in a M-dimensional feature space, where M is the number of features by which a fiber is described. We consider binary and monothetic trees, meaning that each non leaf node has two splits, and each split criterion is based on one feature only.

A tree is grown by a recursive process: given the data represented in a node, either declare that node to be a leaf (and assign a category), or split the data further. The splitting query T is chosen so that the data reaching the immediate descendent nodes is as *pure* as possible. The term *pure* refers here to a set of points that mostly have the same class labels. Often the notion of impurity is used in order to mathematically define the criterion for choosing the node query. The measure of impurity $i(N)$ at a node N may be defined in several ways. The definition used here is the classical Gini's impurity (Equation 1):

$$i(N) = \sum_{i \neq j} P(w_i)P(w_j) = 1 - \sum_{j} P^2(w_j) \tag{1}$$

where $P(w_j)$ is the fraction of data points at node N that belongs to category w_j. It can be seen that if all the points at node N belong to the same category, then $i(N)$ for this node equals zero, which is an ideal outcome (a perfectly pure node). In case that there is an equal representation of two categories in a node population, the impurity is maximal and equals 0.5.

When a node N is split so that the fraction P_L of its points goes to the left descendent node N_L and the rest of the points goes to the right descendant N_R, the impurity is reduced by the amount $\Delta i(N)$, which is defined as follows (Equation 2):

$$\Delta i(N) = i(N) - P_L i(N_L) - (1 - P_L) i(N_R) \tag{2}$$

The query T for the node N is chosen such that the decrease in the impurity is maximized.

Different criteria exist for deciding when to stop the tree development. The simplest of all continues splitting each node as long as the impurity measure keeps decreasing. Such a method produces an unbalanced tree (with leaves at different depth levels). The deeper branches describe the more complex classes. This is an advantage in our case since the different White Matter fiber tracts have varying geometric complexity, as can be seen in Figure 3.

2.4 Using the Tree

Once the tree is formed, a single label is assigned to each terminal node. The chosen label corresponds to the category that has the largest representation in the node. Classification of unlabeled data using a finalized tree is straightforward. Each new data point is propagated from the root node towards one of the leaves, according to the queries in each node. The data point is then assigned the label of the leaf that is reached.

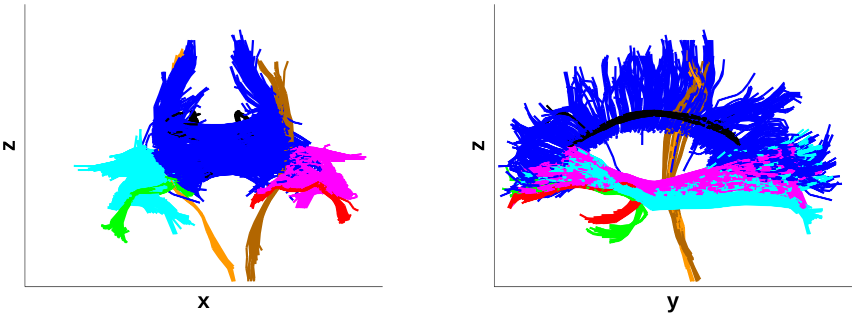

(a) (b)

Fig. 3. Two views of the fiber tracts from one of the brain data sets used in this work. Blue-Corpus Callosum, Green-Left Uncinate, Red-Right Uncinate, Cyan-Left IOF, Magenta-Right IOF, Orange-CST-Right, Brown-CST-left, Black-Cingulum

3 Experiments and Results Analysis

The suggested training and classification scheme was tested on a data set obtained from the Johns Hopkins Medical MRI Laboratory website [6]. It contains fifteen normal brains, each represented by $50 - 55$ axial slices with a voxel size of 1x1x2.6 mm in the x, y, z directions respectively. For each brain, the WM fibers were generated by DTIStudio [4]. The brains in the set contain a normal anatomical variability in the shape of the different tracts, that should be well described by the tree model. For example, the differences in the appearance of one of the tracts (Right Uncinate) in two of the the brains are illustrated in Figure 4.

The following tracts were modeled: Corpus Callosum (CC), right and left Uncinate (Unc.r and Unc.l), right and left Inferior Occipitofrontal Fascicle (IOF.r, IOF.l), right and left Cortico-Spinal Tract (CST.r, CST.l) and Cingulum. The different tracts belonging to one of the brains are presented in Figure 3. In each of the brains the eight fiber tracts were manually marked by successive Regions of Interest, as described in Section 1. As a result of the manual marking procedure, each fiber in a set received a class label $ml \in \{l_c\}$ where

$$l_c = \{CC, Unc.r, Unc.l, IOF.r, IOF.l, CST.r, CST.l, Cing, others\} \qquad (3)$$

where $others$, is the class of the WM fibers that do not belong to one of the modeled tracts. Subsets of the manually marked fibers were used for the experiment.

First, the fibers from the different brains were spatially aligned relatively to one of the brains (Section 2.2). A leave-one-out methodology was used in order to assess the tree classifier performance on various data sub-sets. Fifteen training-testing trials were conducted. In each trial, i, one brain ($brain_i$) was used as

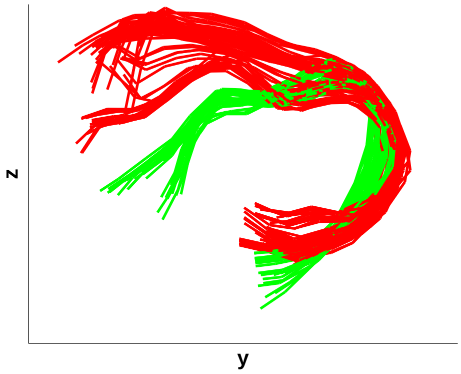

Fig. 4. Fibers belonging to the Right Uncinate tracts in two different brains from the experimental set. The different colors represent fibers belonging to the different brains.

the testing set, and the other fourteen were used as a training set. A classification tree, T_i was created using $\{brain_1, \ldots, brain_{i-1}, brain_{i+1}, \ldots, brain_{15}\}$. The training procedure (Section 2.3) produced unbalanced binary trees, with 78 up to 89 levels. The fibers from the remaining $brain_i$ were then classified using T_i (Section 2.4). Each fiber was propagated from the root of the tree, downward, and assigned the label of the final leaf.

Two examples of automatic classifications of fibers into the eight tracts of interest are presented in figure 5. The colors correspond to the different tracts, as classified by our trees.

For the evaluation of the classifier performance, two standard quality measures were selected: *recall* (also termed *accuracy*) and *precision* (also termed *purity*) of classification, defined as follows: for a given brain, $brain_j$, each fiber f_i is manually labeled by the class label ml_i. The classification procedure generates for this fiber the automatic classification label al_i, that receives one of the values of the class labels (where $l_1 = CC$, $l_2 = Unc.l$, etc.). In our case there are nine possible class labels, eight corresponding to defined anatomical tracts and one for all the remaining WM fibers. The amount of true positive classifications (TP_j) is then defined as the number of fibers for which the automatic label equals the manual label, or as written in Equation 4:

$$TP_j = \left| \left\{ i \middle| \; ml_i = l_c \; AND \; al_i = l_c \right\} \right| \tag{4}$$

In a similar manner, the true negatives (TN_j), false positives (FP_j) and the false negatives (FN_j) for $brain_j$ are defined as follows:

$$TN_j = \left| \left\{ i \middle| \; ml_i \neq l_c \; AND \; al_i \neq l_c \right\} \right| \tag{5}$$

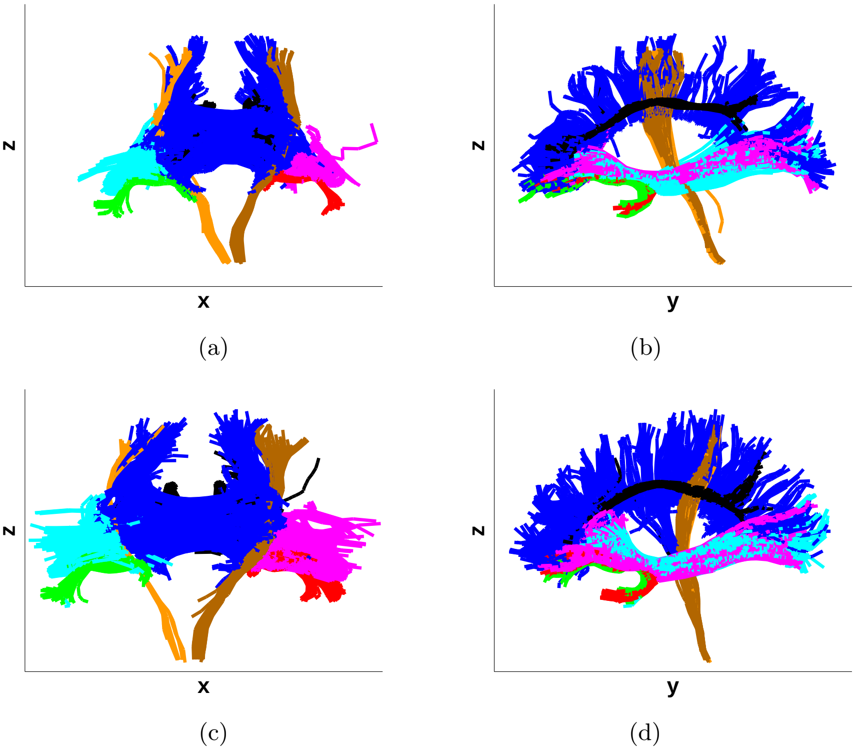

Fig. 5. Automatically classified fibers in two different brains: (a), (b) $brain_4$; (c), (d) $brain_2$. The colors correspond to the automatic classifications: Blue-Corpus Callosum, Green-Left Uncinate, Red-Right Uncinate, Cyan-Left IOF, Magenta-Right IOF, Orange-CST-Right, Brown-CST-left, Black-Cingulum

$$FP_j = \left|\left\{\, i \middle|\; ml_i \neq l_c \; AND \; al_i = l_c \,\right\}\right| \tag{6}$$

$$FN_j = \left|\left\{\, i \middle|\; ml_i = l_c \; AND \; al_i \neq l_c \,\right\}\right| \tag{7}$$

Finally, the *recall* and the *precision* classification measures are defined as follows:

$$recall = \frac{TP}{TP + FN}; precision = \frac{TP}{TP + FP} \tag{8}$$

The *recall* describes the capture rate of the classifier. It will take on a maximal value, 1, when the amount of False Negative classifications is zero, meaning that all of the fibers belonging to the class C are indeed classified with the label l_c. *Recall* will be zero if none of the fibers belonging to class C are captured by the automatic classifier and labeled as l_c. *Precision* shows how many of the fibers that were assigned the class label l_c, truly belong to this class.

Table 1. Summary of performance measures for each tract, based on fifteen leave-one-out trials.

Tract name	CC	Unc.r	Unc.l	IOF.r	IOF.l	CST.r	CST.l	Cing
recall, mean %	91.8	83.7	87.4	97	96.2	72.5	77.9	86.4
recall, std %	4.5	26.7	18.7	7.6	4.5	36.8	35.9	17.7
precision, mean %	93.1	96.8	96.2	98.7	99	94.8	95.2	97.2
precision, std %	3.7	4.3	6.1	1.6	1.1	1.3	11.6	4.5

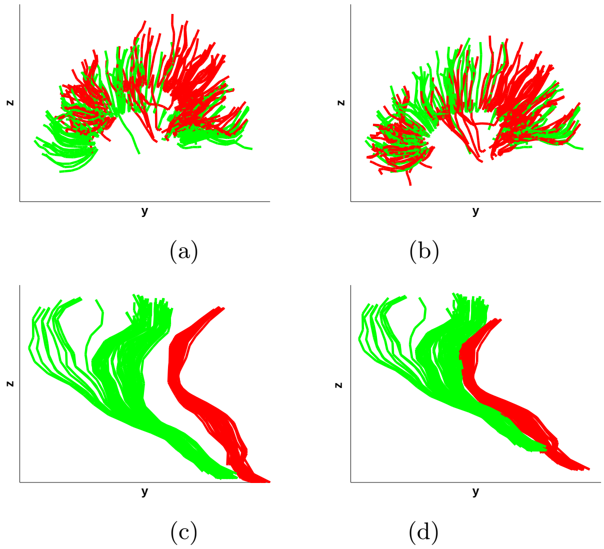

Fig. 6. The effect of spatial normalization on two different tracts from one of the brains. Fibers from the model brain (green). Fibers from the current brain, $brain_{14}$, (red). (a) CC tract before the registration; (b) CC tract after the registration; (c) CST.r tract before the registration; (d) CST.r after the registration.

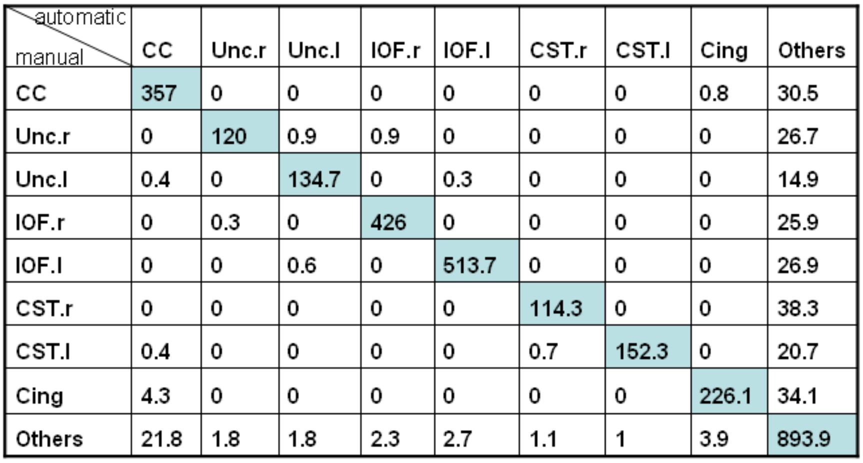

automatic manual	CC	Unc.r	Unc.l	IOF.r	IOF.l	CST.r	CST.l	Cing	Others
CC	357	0	0	0	0	0	0	0.8	30.5
Unc.r	0	120	0.9	0.9	0	0	0	0	26.7
Unc.l	0.4	0	134.7	0	0.3	0	0	0	14.9
IOF.r	0	0.3	0	426	0	0	0	0	25.9
IOF.l	0	0	0.6	0	513.7	0	0	0	26.9
CST.r	0	0	0	0	0	114.3	0	0	38.3
CST.l	0.4	0	0	0	0	0.7	152.3	0	20.7
Cing	4.3	0	0	0	0	0	0	226.1	34.1
Others	21.8	1.8	1.8	2.3	2.7	1.1	1	3.9	893.9

Fig. 7. Mean confusion matrix: rows correspond to the manual classifications. Columns correspond to the automatic classifications. The location (i, j) contains the number of fibers that were manually classified as class number i and automatically classified as class number j. The counts of true positive classifications reside on the diagonal of the confusion matrix.

The recall and precision measures for each tract in the 15 leave-one-out experiments are summarized Table 1. Mean and standard deviation values are presented. The mean precision values are high for all tracts, ranging from 93.1% to 99%. The standard deviations are reasonably low, for all of the tracts except for the left CST. The mean recall values vary between 72.5% (for right CST) to 96.2%. The largest standard deviations here are received for the left and right CST tracts. The variation in the mean values reveals that the performance for some of the tracts is more stable then for others. For example, the IOF right and left receive extremely high mean precision and recall measures together with a very small variation in values throughout the trials.

Further investigation of the performance on the CST tract reveals that most of the trials achieve good results, however there are few trials for which the *recall* is significantly reduced. One of the reasons is that this tract has in some cases very few fibers, so that each fiber that is missed reduces considerably the overall *recall*. Some of the cases of low *recall* were caused by a misalignment of a particular tract relatively to the training set, even after the spatial normalization, as can be seen in Figure 6. In this figure we examine closely the test set from one of the trials. In this trial there was a very good performance on the CC tract, but a poor *recall* on the right CST. In Figure 6(c) the CST from brain 14 is shown (red) overlayed on the CST from the model brain (green). Note that the model brain is the one to which all other brains were aligned in the pre-processing stage. Figure(d) shows the same fibers, after registration. It can be seen that the large shift that was present in (c) is not sufficiently corrected in (d), which caused the relatively large number of false negative classifications thus reducing the overall *recall* of this trial for the CST tract. Figure 6 (a) and (b) show the fibers of CC, before (a) and after (b) normalization, relative to the model fibers in green. It is seen that a very precise alignment was achieved in this case, and indeed both the *recall* and the *precision* measures are high. This leads to the conclusion that the problem with the CST classification originates in the pre-processing stage, and not in the classification scheme itself.

One of the accepted methods of examining a classifier performance is by constructing a class confusion matrix. In the confusion matrix the location (i, j), contains the number of fibers that were manually classified as class number i and automatically classified as class number j. The counts of true positive classifications reside on the diagonal of the confusion matrix. Such a confusion matrix was computed for each of the 15 trials. A mean confusion matrix (Figure 7) reveals that the amount of confusion between the marked tracts is very small. For instance, on average 114 right CST fibers were classified correctly out of 152, but in fact the missed fibers were not confused with the other tracts, but were affiliated with the *others* class, that is the mixture of all the unmarked fibers.

In addition to providing satisfactory performance, the classification process is very quick, with a complexity that is linear with respect to the tree depth. In this work the data was processed with $Matlab7.1$ (the Mathworks, Inc.,USA), running on a standard PC (Intel Core 2 Duo, 2.67GHz). The average time for a single fiber classification is $8\mu sec$. A typical full set of WM fibers from a single brain containing $300,000$ fibers can therefore be classified in less then 2.5 seconds.

4 Discussion and Future Work

This work presents a proof of concept and a feasibility test for a very simple and fast approach to classification of individual WM fibers in the brain, using Classification Trees. A method is proposed for training a supervised tree model that describes the different fiber tracts present in a training set. The model provides an intuitive and easy way to interpret the description of the different fiber tracts. In essence, for each fiber a series of questions is asked, each question addresses one of the coordinates of the points along this fiber. A sequence of characteristic answers to these questions identifies a spatial behavior associated with a specific tract. This method of classification is very fast, even when applied to large multidimensional data sets such as the fiber sets addressed here. The performance of the classifier was evaluated on a set of 15 brains, and 8 anatomical tracts in a leave-one-out experiment. The *precision* and *recall* aspects of the performance were assessed relatively to manual classifications. The tracts that were modeled vary in their geometrical complexity from reasonably simple (IOF) to very complex (CC). The presented results are very encouraging. We conclude that classification trees of the type described here can cope with the variety of challenges presented by the WM fiber tracts in the brain.

Future work entails testing the scheme on additional fiber tracts and a larger brain database, with and without abnormalities. In addition, various alternative representations of the fibers will be tested, with the purpose of reducing the dependence on the initial alignment and inherent tractography noise.

References

1. Basser, P., Pierpaoli, C.: Microstructural and physiological features of tissues elucidated by quantitative diffusion tensor MRI. Journal of Magn Reson B **111**(3) (1996) 209–219
2. Mori, S., Zijl, P.: Fiber tracking: principles and strategies-a technical review. NMR Biomed **15**(7)
3. Wakana, S., Jiang, H., Nagae-Poetscher, M., van Zijl, P., Mori, S.: A fiber-tract based atlas of human white matter anatomy. Radiology **230**(1) (2004) 77–87
4. Jiang, H., van Zijl, P., Kim, J., Pearlson, G., Mori, S.: Dtistudio: Resource program for diffusion tensor computation and fiber bundle tracking. Comp. Meth. and Prog. Biomed. **81**(2) (2006) 106–116
5. Fillard, P., Toussaint, N., Pennec, X.: Medinria: DT- MRI processing and visualization software. Guest paper at the Similar Tensor Workshop, Las Palmas, Spain
6. site, J.H.I.: http://lbam.med.jhmi.edu/
7. Maddah, M., Grimson, W.E.L., Warfield, S.: Statistical modeling and EM clustering of white matter fiber tracts. S. 3rd IEEE International Symposium on Biomedical Imaging: Macro to Nano (ISBI) (2006) 53–56
8. O'Donnell, L., Westin, C.F.: A high-dimensional fiber tract atlas. International Society of Magnetic Resonance in Medicine (ISMRM) (2006)
9. Breiman, L., J.H.Friedman, Olshen, R., Stone, C.J.: Classification and regression trees. (1993) Chapman Hall, New York.
10. Hellier, P., Ashburner, J., Corouge, I., Barillot, C., Friston, K.J.: Inter subject registration of functional and anatomical data using SPM. MICCAI **2** (2002) 590–597
11. A.Mayer, H.Greenspan: Bundles of interest based registration of white matter tractographies. ISBI (2008) 919–922
12. Besl, P., Mckay., N.: A method for registration of 3d shapes. IEEE Trans. Patt. Anal. Mach. Intell. **14**(2) (1992) 239–256
13. Darrell, T., Indyk, P., (eds.), G.S.: Nearest neighbor methods in learning and vision: Theory and practice. MIT Press (2006)

Probabilistic diffusion tractography with spatial priors

Anastasia Yendiki[1], Allison Stevens[1], Saad Jbabdi[2], Jean Augustinack[1], David Salat[1], Lilla Zollei[1], Tim Behrens[2], and Bruce Fischl[1]

[1] HMS/MGH/MIT Athinoula A. Martinos Center for Biomedical Imaging,
149 13th St., Charlestown, MA 02129, USA
`ayendiki@nmr.mgh.harvard.edu`,
[2] Centre for Magnetic Resonance Imaging of the Brain,
University of Oxford, John Radcliffe Hospital, Oxford OX3 9DU, UK

Abstract. We propose a Bayesian approach to the reconstruction of white-matter pathways from diffusion MR data that utilizes prior information on the pathways of interest from a set of training subjects. This method is fully automated and preliminary results indicate that it increases robustness to end-point ROI size, enhances test-retest reliability, and yields solutions that agree with expert-drawn manual labels of the pathways of interest.

1 Introduction

Diffusion tractography uses MR imaging data representing the diffusion of water molecules through the brain to infer the location and shape of white-matter fiber bundles. This is a challenging problem for several reasons. First, the imaging process introduces uncertainty in the data in the form of noise and distortions. Second, there is inherent uncertainty in the white-matter pathways that tractography seeks to identify due to multiple fiber bundles intersecting in many locations in the brain. Finally, the high dimensionality of the solution space results in additional computational difficulty.

Conventional approaches to tractography use a deterministic and local model of the diffusion process to step along a white-matter pathway a few voxels at a time [1]. Such methods are often confounded by the aforementioned sources of uncertainty in diffusion MR data. Consequently probabilistic approaches that attempt to address these issues have been proposed in recent years [2–5]. However, most methods often require manual intervention to produce reliable results, especially for weaker connections, making them less practical for large studies.

In this work we build upon a Bayesian approach to tractography proposed recently that uses a global model of white-matter pathways [6]. To eliminate reliance on manual intervention and reduce sensitivity to initialization and end point selection, we incorporate prior models of the unknown pathways based on a set of training subjects. The resulting method is fully automated and produces tract solutions that correspond well with expert manual labelings of the same pathways.

2 Background

Streamline approaches to diffusion tractography utilize the local properties of the diffusion data to determine the orientation of the unknown white-matter pathway at every step. As a result, in areas of high local uncertainty in the data, these methods may be unable to step in the right direction and suffer from error propagation issues. Global models of the underlying pathways integrate the information in the diffusion data along the entire path and are thus less sensitive to areas of local uncertainty.

2.1 Global Bayesian tractography

In this work we adopt the Bayesian global pathway model proposed in [6]. In this framework, we seek to estimate the posterior probability of the unknown path $\boldsymbol{\mathcal{F}}$ given the measured diffusion-weighted (DW) images $\boldsymbol{Y}$,

$$p(\boldsymbol{\mathcal{F}}, \boldsymbol{\Omega}|\boldsymbol{Y}) \propto \; p(\boldsymbol{Y}|\boldsymbol{\mathcal{F}}, \boldsymbol{\Omega})\, p(\boldsymbol{\mathcal{F}}, \boldsymbol{\Omega}), \tag{1}$$

where $\boldsymbol{\Omega}$ are the other unknown parameters in the model.

The data likelihood is assumed to be Gaussian,

$$p(\boldsymbol{Y}|\boldsymbol{\mathcal{F}}, \boldsymbol{\Omega}) = p(\boldsymbol{Y}|\boldsymbol{\Theta}, \boldsymbol{\Phi}, \boldsymbol{s}_0, \boldsymbol{d}, \boldsymbol{f}, \boldsymbol{\Sigma}) \sim \boldsymbol{\mathcal{N}}(\boldsymbol{\mu}; \boldsymbol{\Sigma}), \tag{2}$$

and utilizes a multiple-compartment model of the water diffusion process at each voxel, described in [7]. This model represents the expected intensity value of the jth voxel in the DW image acquired with the ith diffusion-encoding gradient direction as

$$\begin{aligned}\mu_{ij} = s_{0j} \Big\{ & \big(1 - \sum_{i=1}^{n_F} f_j^l\big) \exp(-b_i d_j) \\ & + \sum_{i=1}^{n_F} f_j^l \exp\big(-b_i d_j \boldsymbol{r}_i^T \boldsymbol{R}(\theta_j^l, \phi_j^l) \boldsymbol{A} \boldsymbol{R}^T(\theta_j^l, \phi_j^l) \boldsymbol{r}_i\big) \Big\},\end{aligned} \tag{3}$$

where the first summand inside the braces represents an isotropic diffusion compartment and the remaining n_F summands represent perfectly anisotropic fiber components with orientations defined by the angles (θ_j^l, ϕ_j^l). The diffusion-encoding weight and direction, b_i and $\boldsymbol{r}_i$ respectively, are known acquisition parameters. The non-DW image intensity s_{0j}, the diffusivity d_j, the anisotropic compartment volume fractions f_j^l, $l = 1, \ldots, n_F$, and the anisotropic compartment orientations (θ_j^l, ϕ_j^l), $l = 1, \ldots, n_F$, are unknown parameters to be estimated. Finally, $\boldsymbol{A}$ is the outer product of a unit vector along the left-right axis and $\boldsymbol{R}(\theta_j^l, \phi_j^l)$ is the rotation matrix that applies a rotation by θ_j^l around the anterior-posterior axis and by ϕ_j^l around the inferior-superior axis.

The prior term in (1) is given by

$$p(\boldsymbol{\mathcal{F}}, \boldsymbol{\Omega}) = p(\boldsymbol{s}_0) p(\boldsymbol{d}) p(\boldsymbol{\Sigma}) p(\boldsymbol{f}|\boldsymbol{\mathcal{F}}) p(\boldsymbol{\Theta}, \boldsymbol{\Phi}|\boldsymbol{\mathcal{F}}) p(\boldsymbol{\mathcal{F}}). \tag{4}$$

As detailed in [6], the observed DW image intensities $\boldsymbol{Y}$ are assumed independent and the unknown variances on the diagonal of $\boldsymbol{\Sigma}$ are nuisance parameters whose prior distribution is integrated out of the posterior. The diffusivities $\boldsymbol{d}$ and non-DW image intensities $\boldsymbol{s}_0$ are assigned non-informative priors (uniform over all positive values). The diffusion compartment volume fractions $\boldsymbol{f}$ are assigned an automatic relevance determination (ARD) prior, which allows the number of compartments at every voxel to be determined from the data. The fiber orientation angles $\boldsymbol{\Theta}$ and $\boldsymbol{\Phi}$ are specified completely by the path $\boldsymbol{\mathcal{F}}$ at any voxel that is traversed by the paths. At all remaining voxels, the orientation angles are assumed to be uniformly distributed.

2.2 Spatial path priors

The path $\boldsymbol{\mathcal{F}}$ is modeled as a piece-wise cubic Catmull-Rom spline with a small number of control points to make the problem tractable. Even with this constraint, however, the space of all possible paths $\boldsymbol{\mathcal{F}}$ between two brain regions is very large, making the estimation of the posterior difficult unless prior information on the path is incorporated in the posterior via $p(\boldsymbol{\mathcal{F}})$.

In [6] the only prior information on the path is assumed to be whether the two brain regions of interest (ROIs) are connected to each other or not. When the two ROIs (referred to as the seed and target ROI, although they are interchangeable) are known *a priori* to be connected, all paths that connect them are assumed to be equally probable. In this work we depart from the model of [6] in that we estimate the prior distribution of $\boldsymbol{\mathcal{F}}$ from a set of training subjects. To this end, we use path labels defined manually by an expert for each of these subjects.

Formally, let $\boldsymbol{\mathcal{F}}_1, \ldots, \boldsymbol{\mathcal{F}}_n$ be splines generated by the manually labeled control points from the n training subjects. By computing a histogram of the number of times that a given voxel j belongs to a path from the training set, we estimate the probability that voxel j belongs to the path $\boldsymbol{\mathcal{F}}$ given the paths of the training subjects. Assuming spatial independence, the path prior $p(\boldsymbol{\mathcal{F}})$ is simply the product of the probabilities corresponding to each voxel j along the path.

$$p(\boldsymbol{\mathcal{F}}) = \prod_j p(j \in \boldsymbol{\mathcal{F}} | \boldsymbol{\mathcal{F}}_1, \ldots, \boldsymbol{\mathcal{F}}_n). \tag{5}$$

For the study presented here an expert drew control points along each of the tracts of interest in a set of training subjects. To perform this labeling the expert viewed fractional anisotropy and primary eigenvector maps, which were obtained via a simple tensor reconstruction on the spatially normalized DW images of the training subjects. Note that these maps were used only as visual aids in the manual labeling stage; they were not used in any way by the tractography algorithm, which utilizes the multi-compartment diffusion model described above instead of a tensor model.

We used the manually drawn control points to fit a spline, representing the true path $\boldsymbol{\mathcal{F}}_k$, for each of the training subjects, $k = 1, \ldots, n$. We computed a histogram of these splines to estimate the prior $p(\boldsymbol{\mathcal{F}})$ in (5). An alternative approach would be to run the tractography algorithm on the training subjects, with the manually drawn points as initialization, and use the resulting posteriors to estimate $p(\boldsymbol{\mathcal{F}})$. We will compare this to our current approach in future work.

2.3 Control point initialization

As in [6], the path posterior (*i.e.*, the posterior on the control points of the spline) is estimated via a Markov chain Monte Carlo (MCMC) algorithm. The initialization of the control points is a very important issue, as a good initial guess is essential for the algorithm to converge to a reasonable solution. The existence of the training set provides us with an effective means to find such an initialization. Specifically, in addition to using the manually labeled control points to estimate path priors, we also use their centroids over all training subjects to initialize the MCMC algorithm for the test subject.

2.4 Automatic generation of seed/target ROIs

Finally, we also use centroids of the manually labeled end points of the path from the training subjects to generate the target and seed ROI for the test subject. Since an important issue with the original method is poorer performance as the seed and target ROIs get larger, we use gradually dilated versions of these end points to assess the reliability of the prior-based approach.

3 Preliminary results

We performed tractography on a data set provided by the Mental Illness and Neuroscience Discovery (MIND) Institute [8]. The data set, which was acquired to facilitate test-retest reliability studies on MRI-derived measures, included 10 healthy volunteers scanned twice. The scans were performed in a 3T Siemens Trio at the Massachusetts General Hospital. They were repeated on two visits that were separated by less than a month for each subject. The scans included diffusion-weighted images acquired at 2x2x2 mm resolution with 60 gradient directions. Using each subject's fractional anisotropy and primary eigenvector maps, an expert labeled the corticospinal tract (CST) and the three branches of the superior longitudinal fasciculus (SLF1, SLF2, SLF3).

For each subject, we used the other nine subjects as a training set. In particular, we used centroids of the manually labeled control points from the nine training subjects to initialize the control points of the test subject for the MCMC algorithm. We also used splines fitted to the manually labeled points from the nine training subjects to generate a path prior for the test subject. We applied the Bayesian global tractography method described above in three ways:

- No control point initialization and no path prior from the training subjects. (In this case the initializing control points for the MCMC algorithm were found by a search on a set of rotating planes, as described in [6].)
- Control point initialization from the training subjects but no path prior.
- Control point initialization and path prior from the training subjects.

No information from the manual labeling of the test subject was used in any of the three approaches. In all cases we modeled the paths as Catmull-Rom splines with 5 control points. In the future we plan to use the training set to perform model selection on the number of control points needed for each tract.

3.1 Reliability with respect to ROI size

We obtained the seed and target ROIs for all studies by finding the centroids of the corresponding manually labeled end points of the nine training subjects. To assess the robustness of the three methods described above to ROI size, we dilated the seed and target ROIs simultaneously and repeated the posterior estimation with ROIs of diameter equal to 1, 3, 5, 9, 17, and 33 voxels.

Figure 1 shows the results of this comparison. We assessed reliability by computing the modified Hausdorff distance of the path posteriors produced by each of the three methods to the "ground truth," represented by a spline that we generated from the manually labeled points of the test subject itself. We define the modified Hausdorff distance between two sets of points as the mean of the minimum distance from a given point in the first set to any point in the second set. We obtained one such distance measure for each subject and ROI size combination. We used only the data from the first of the subjects' two visits for this study.

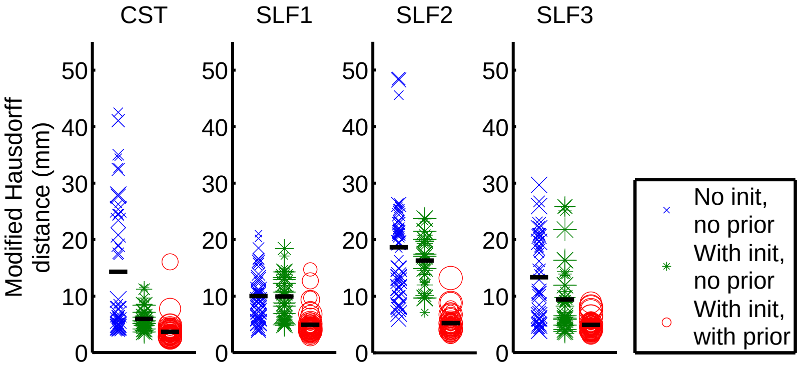

Fig. 1. Modified Hausdorff distance between the path posteriors produced by tractography and the spline defined by the manually labeled points. The scatter plots show individual subject/ROI size combinations and the black horizontal lines correspond to their mean. Larger markers correspond to larger ROIs. For each of the four tracts, the three methods compared are global Bayesian tractography with (i) No prior info from training subjects, (ii) Initialization of control points from training subjects, and (iii) Initialization of control points and path prior from training subjects.

3.2 Test-retest reliability

To assess test-retest reliability of the three estimation methods, we also computed the modified Hausdorff distance, as defined above, between the path posterior estimated from the data of each subject's first visit and that estimated from the data of the same subject's second visit. Figure 2 shows the results. Once again, we obtained one distance measure for each subject and ROI size combination.

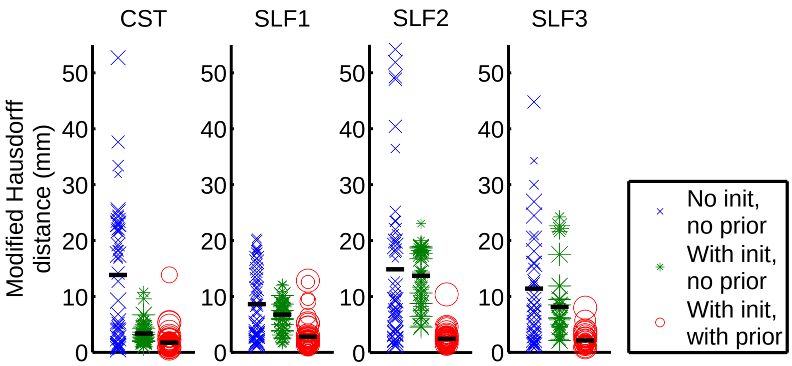

Fig. 2. Modified Hausdorff distance between the path posteriors produced by tractography from diffusion scans of the same subject acquired on two different visits. The scatter plots show individual subject/ROI size combinations and the black horizontal lines correspond to their mean. Larger markers correspond to larger ROIs. For each of the four tracts, the three methods compared are global Bayesian tractography with (i) No prior info from training subjects, (ii) Initialization of control points from training subjects, and (iii) Initialization of control points and path prior from training subjects.

Figure 3 shows the CST path posteriors estimated from one subject's data by each of the three methods we compared. Figure 4 shows the same for the three branches of the SLF. The paths shown are 2-D projections of the maximum value of each posterior along the left-right direction. They are superimposed on a maximum intensity projection of a white-matter mask obtained from a T1-weighted scan of the same subject.

4 Discussion and future work

Our preliminary studies show the utility of including prior information from training subjects in probabilistic diffusion tractography. As seen in figures 1 and 2, the nine training subjects used here were enough to yield significant improvements in terms of robustness to seed/target ROI selection and test-retest reliability. In future work we plan to investigate the appropriate size for the training set further.

The results indicate that using the manual labels from the training subjects only to initialize a prior-free estimation results in some but less significant improvement. The algorithm explores a large enough solution space to sometimes find solutions that are far from the ground truth and even anatomically implausible. The prior improves results by constraining the solution space. The benefits of using the information from the training subjects for both initialization and path priors vs. simple initialization were greater for the SLF, which is a weaker connection and more difficult to trace than the CST.

As seen in figures 3 and 4, the path posteriors estimated using path priors from the nine training subjects match the labels drawn manually on the test subject quite well. However, some mismatch remains, particularly near the cortex. For the studies shown here, the ten subjects' diffusion-weighted images were aligned in Talairach space

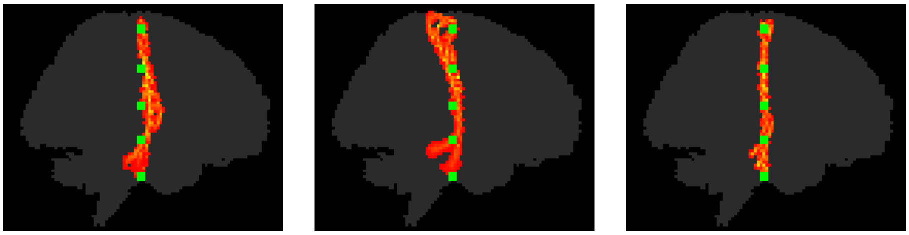

(a) CST, visit 1
(no init, no prior)

(b) CST, visit 1
(with init, no prior)

(c) CST, visit 1
(with init, with prior)

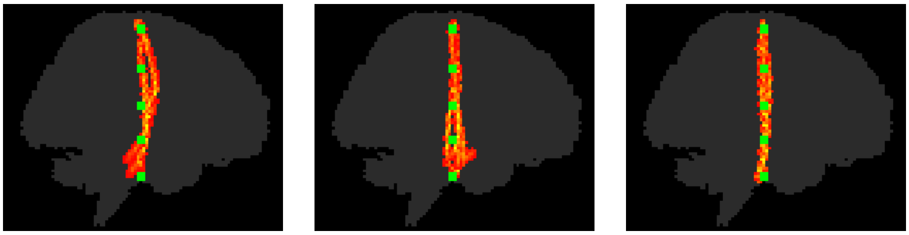

(d) CST, visit 2
(no init, no prior)

(e) CST, visit 2
(with init, no prior)

(f) CST, visit 2
(with init, with prior)

Fig. 3. CST path posteriors generated from test-retest data of a single subject acquired at separate visits. Paths generated with seed/target ROI diameters of 1, 3, 5, 9, 17, and 33 voxels are superimposed. The green squares show the locations of the manually labeled points for the same subject.

by linear registration. We are currently investigating the use of an elastic registration method that achieves better alignment of the subjects' cortical surfaces. We expect that this approach will drive the Hausdorff distances for the prior-based method even lower than the values shown in figure 1.

In the proposed method manual labeling is needed only to estimate the path prior, which is done only once on a set of training subjects. This atlas of manually labeled tracts can then be used to perform tractography for new studies in a completely automated manner, without any manual intervention on the new subjects' data. The rationale behind the use of a path prior is that the paths have a similar shape in different subjects. This is not an unreasonable assumption, especially among healthy individuals, where white-matter pathways are typically well-predicted by the surrounding anatomy.

An important concern in this regard is the applicability of the prior-based approach to patient populations. We are in the process of evaluating the methods described here on data from patients with neurodegenerative disorders. If the priors derived from healthy subjects prove unreliable for use on patient data, we will investigate the inclusion of patients in our training sets.

Finally, we are extending our priors to take advantage of anatomical context obtained from segmentations of T1-weighted images of the training and test subjects. We expect this to be beneficial in tracing paths that are well-constrained by the surrounding anatomy, *e.g.*, constraining the CST lateral to thalamus and medial to pallidum.

(a) SLF, visit 1
(no init, no prior)

(b) SLF, visit 1
(with init, no prior)

(c) SLF, visit 1
(with init, with prior)

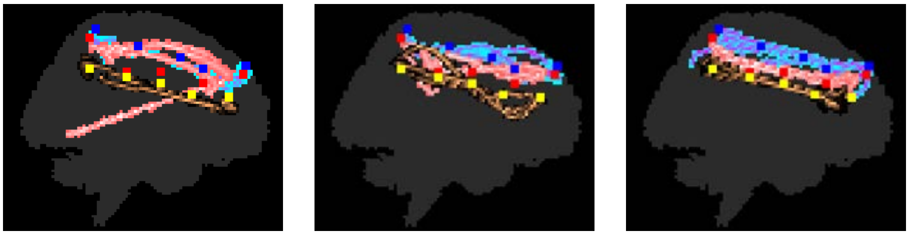

(d) SLF, visit 2
(no init, no prior)

(e) SLF, visit 2
(with init, no prior)

(f) SLF, visit 2
(with init, with prior)

Fig. 4. SLF path posteriors generated from test-retest data of a single subject acquired at separate visits. The SLF1, SLF2, and SLF3 paths are shown in blue, pink, and copper color maps respectively. Paths generated with seed/target ROI diameters of 1, 3, 5, 9, 17, and 33 voxels are superimposed for each case. The blue, red, and yellow squares show the locations of the manually labeled points for the SLF1, SLF2, and SLF3 of the same subject respectively.

References

1. Mori, S., Crain, B.J., Chacko, V.P., van Zijl, P.C.: Three-dimensional tracking of axonal projections in the brain by magnetic resonance imaging. Ann. Neurol. 45, 265–9 (1999).
2. Behrens, T.E.J., Woolrich, M.W., Jenkinson, M., Johansen-Berg, H., Nunes, R.G., Clare, S., Matthews, M., Brady, J.M., Smith, S.M.: Characterization and propagation of uncertainty in diffusion-weighted MR imaging. Magn. Reson. Med. 50, 1077–88 (2003).
3. Hagmann, P., Thiran, J.P., Jonasson, L., Vandergheynst, P., Clarke, S., Maeder, P., Meuli, R.: DTI mapping of human brain connectivity: statistical fibre tracking and virtual dissection. NeuroImage 19, 545–54 (2003).
4. Parker, G.J.M., Alexander, D.C.: Probabilistic anatomical connectivity derived from the microscopic persistent angular structure of cerebral tissue. Philos. Trans. R. Soc., B 360, 893–902 (2005).
5. Friman, O., Farneback, G., Westin, C.F.: A Bayesian approach for Stochastic White Matter Tractography. IEEE Trans. Med. Imag. 25, 965–78 (2006).
6. Jbabdi, S., Woolrich, M.W., Andersson, J.L., Behrens, T.E.J.: A Bayesian framework for global tractography. NeuroImage 37, 116–29 (2007)
7. Behrens, T.E.J., Johansen-Berg, H., Jbabdi, S., Rushworth, M.F.S., Woolrich, M.W.: Probabilistic diffusion tractography with multiple fibre orientations: What can we gain? NeuroImage 34, 144–155 (2007)
8. Mental Illness and Neuroscience Discovery Institute. http://themindinstitute.org/

A Fiber Tracking Method for Building Patient Specific Dynamic Musculoskeletal Models from Diffusion Tensor Data

David I.W. Levin[1], Benjamin Gilles[1], Burkhard Mädler[2,3], and Dinesh K. Pai[1]

[1] Department of Computer Science
The University of British Columbia
Vancouver, British Columbia, Canada
[2] Philips Healthcare
[3] Department of Physics and Astronomy
The University of British Columbia
Vancouver, British Columbia, Canada

Abstract. A new musculoskeltal simulation primitive, the strand, can provide an efficient way of simulating complicated muscle fiber architectures [1]. In this paper we present a new fiber tracking algorithm based on an energy minimizing active curve that is well suited for building these strand type models from diffusion tensor imaging data. We present fiber tracking results for the Brachioradialis muscle in the left forearm of a male subject. The algorithm produces a space filling arrangement of fibers that are uniformly distributed throughout the muscle and aligned with the underlying muscle fiber direction.

Key words: musculoskeletal simulation, fiber tracking, diffusion tensor imaging

1 Introduction

Subject specific dynamic models of muscle can provide invaluable tools for the diagnosis of movement disorders [2] as well as for the study of the neurological control of movement [3]. Previous muscle simulations have focused on approaches such as line-of-force models and Finite Element Methods (FEM). However, line-of-force models overly simplify muscle fiber arrangement by treating muscles as straight lines and FEM models are complex to construct and time intensive to simulate. Recently a new simulation primitive, the muscle strand, has been developed for simulating musculotendon systems [1]. Strands are based on cubic spline curves with inertia. They allow contractile forces to be propagated along complex trajectories. By using strands to represent the arrangement of muscle fibers within a muscle we plan to construct accurate, efficient simulations which take into account subject specific fiber architectures. One major hurdle in building these strand-based models is the extraction of muscle fiber fields from subjects and the fitting of a number of strands to this data. In this paper we present preliminary results of a semi-automatic technique for solving this problem using Diffusion Tensor Imaging (DTI) data from human muscle. Instead of relying on random seeding of the muscle volume to produce fiber paths we present an algorithm which seeks to fit a collection of energy minimizing, curves to the fiber field. Each of these contours could then be used as a strand in a musculoskeletal simulation.

2 Related Work

Musculoskeletal DTI has been previously used on human leg muscles. Sinha *et al.* [4] developed a tetrahedral gradient encoding scheme to perform fast DTI of human calf muscles. Lansdown *et al.* [5] used musculoskeletal DTI in order to measure pennation angle of muscle fibers in the human leg and compared the results to ultrasound (US) measurements. Lansdown found that the measurements acquired from the DTI data were statistically comparable to those from the US data.

Most fiber tracking approaches focus on seeding the DTI volume and using a numerical integration scheme to follow the primary eigenvector of the DTI tensor field to create a fiber path [6]. Probabilistic approaches have been used to deal with more complex fiber arrangements. Mori and Zijl have provided a summary of recent developments in fiber tracking [6]. Blemker and Delp presented a method for use with FEM muscle models that maps templated fiber geometries to anatomical meshes in order to include fiber data in the simulation. However these fiber templates are defined mathematically using tunable parameters, not from subject specific data [7].

3 Methods

Our pipeline for generating muscle geometry and patient specific strands begins with imaging the appropriate area of the body using MRI. Both anatomical and diffusion weighted scans are acquired. Muscle and bone surfaces are extracted from the anatomical scans while a muscle fiber field is computed from a DTI volume constructed from the diffusion weighted data. Below we present the details of each of these steps.

3.1 MRI Data Acquisition

Imaging for this study was performed on a 3T Philips Achieva MRI Scanner with dual nova gradients ($80mT/m$ maximum gradient strength, $200T/m/s$ maximum slewrate) and scanner software release 2.1.3.

During image acquisition the subject lay prone in the scanner with the left arm raised straight overhead to be placed as optimally as possible in the magnet's centre. The subject's forearm was secured in an 8-element phased array knee coil with $15cm$ inner diameter.

The imaging protocol consisted of a fast gradient echo T1W localizer for positioning and planning followed by low and high resolution T2W fast spin echo (FSE) scans for reconstruction of bone and muscle/fat surface boundaries. The session was concluded with a high resolution Diffusion Tensor Imaging (DTI) scan for muscle fiber orientation and segmentation.

Quick low resolution anatomical FSE-scans were acquired with an in-plane resolution of 1.5x1.5 mm^2 and a slice thickness of $4mm$ covering the entire lower arm (Fig.1).

The high resolution FSE was designed to match the Diffusion Tensor Imaging (DTI) scan in location, orientation and anatomy coverage with the following parameters: FSE-factor 12 with asymmetric profile order to give an effective echo time of TE=$50ms$; field of view (FOV):120x120x150 mm^3 with an in-plane resolution of 0.65x0.65 mm^2 and a slice thickness of $2mm$.

The lower resolution T2W-scan was used for segmenting bones and muscles that passed out of the field of view of the high resolution scan. Important parameters such as origin/insertion locations and bone coordinate systems could thus be obtained. Note that these two scans were run sequentially with the DTI scan and that the subject was immobilized. Therefore all volumes were closely aligned.

Diffusion Tensor Imaging (DTI) was performed with a single shot diffusion sensitized spin-echo Echo Planar Imaging (EPI) sequence involving 16 different gradient encoding directions at a maximum diffusion b-value of $500s/mm^2$. We used a reduced FOV of 120x120x150mm^3, SENSE-factor of 2.0 and enhanced gradient performance to shorten the echo train length of the EPI-readout as much as possible for better compensation of susceptibility induced artifacts. Fat suppression was performed with a spectral spatial inversion prepared fat suppression technique. Further imaging parameters were as follow: TE=$48ms$, TR=$6000ms$, acquisition matrix 80x80 leading to an effective acquisition voxel size of 1.5x1.5x2.0 mm^3 and a scan time of 5 minutes.

3.2 Segmentation of Bone and Muscle Surfaces

Given the high complexity of the forearm structure and the fuzzy muscle boundaries on MRI (e.g. because of thin intermuscle fat), surfaces are not reconstructed based on a slice-by-slice segmentation. Instead, the subject-specific model is obtained from the registration of a template surface onto the individual MRI. This prior model was constructed from the Ultimate Human Dataset (Snoswell Design, Adelaide).

Musculoskeletal registration is particularly challenging because it involves a large number of interrelated components undergoing large non-linear deformations with large anatomical variations in the population. Hence allowable deformations need to be carefully parameterized to avoid falling into one of the numerous local solutions, *and* to present sufficient degrees of freedom [8, 9].

Our surface-to-image registration method is based on discrete deformable models evolving under internal forces (e.g., elastic forces) and external forces (e.g., image forces, user constraints). Our internal forces enforce a spatially coherent evolution and consistent shapes by minimizing non-rigid local transformations between the model and the template. Our method is derived from a fast deformation technique called *shape matching* developed in the computer graphics community [10, 11], to efficiently approximate large soft-tissue elastic deformations. In [12], we show that quasi automatic inter-patient registration can be achieved when the template is built from a reference image dataset (external forces locally match icons around the surface). In this present work, we do not have any prior appearance model, so external forces are based on user constraints (for each bone/ muscle, the user places internal/ external/ frontier points on MRI slices) and local gradient maximization. The model ($\sim 20k$ particles) can be deformed in real time, so the adaptation is done interactively while putting constraint points.

3.3 DTI Data Processing and Fiber Tracking

In order to reduce distortion in the diffusion weighted images, eddy correction was performed using FMRIB's Diffusion Toolbox (FDT) [13]. Image volumes were converted from DICOM to Analyze format in order to perform the correction. MedINRIA's DTI Track [14] was used to compute a tensor image from the diffusion weighted data. MATLAB was used to compute the primary eigenvector of each tensor in order to facilitate fiber tracking.

The fiber tracking performed in this study differs from typical tractography algorithms because of the end use of the data. We are seeking to build a strand-based dynamic model from the diffusion tensor data (DTI). The algorithm seeks to evenly distribute a user-specified number of strands within the segmented muscle surface. In order to accomplish this we utilize a deformable contour for fiber tracking and segmentation. In general this method shares similarities with active contours used for image segmentation [15]. However instead of segmenting the boundary of the muscle we seek a space filling arrangement of curves which lie both on and inside the muscle surface. The algorithm is semi-automatic in that it requires the user to specify the insertion and origin of the muscle to which tracking will be applied. A template strand is initialized between the insertion and origin points and the user can move control points on the template to ensure that the template strand is entirely enclosed by the muscle surface. Once this initialization step is complete, the required number of strands are initialized to be identical to the template strand. Each strand is discretized using linear elements.

The energy for this i^{th} element is

$$E^i = \alpha \|\mathbf{x}_1^i - \mathbf{x}_0^i\|^2 - \beta \left(|\mathbf{e}^i \cdot \mathbf{t}\left(\mathbf{x}_m^i\right)| \right) + \gamma E_r^i, \tag{1}$$

where $\mathbf{x}_j^i$ are the end points of element i, $\mathbf{e}^i$ is the normalized element tangent vector, $\mathbf{t}\left(\mathbf{x}_m^i\right)$ is value of the underlying primary eigenvector evaluated at the midpoint of the element and E_r^i is a repulsion energy.

The initial term in the energy equation is a stiffness term and prevents unnecessary elongation of the strand during tracking. The second term causes each element of the strand to align with the underlying DTI fiber field. The final term is a repulsion term that is computed between a strand and all other neighboring strands. This term forces the strands away from each other thus seeking a space filling configuration within the muscle surface.We seek the minimum energy configuration of all strands subject to the constraints that each node of a strand must lie inside or on the muscle surface. The constraints that arise in such a problem are quite complicated. Formulating the minimization at the velocity level is easier because the constraints can be locally linearized. The following equation is arrived at by linearizing equation (1) and adding a kinetic energy term.

$$Q\left(\dot{\mathbf{x}}\right) = h\dot{\mathbf{x}} \cdot \bigtriangledown E^{s} + \dot{\mathbf{x}} \cdot \dot{\mathbf{x}}, \tag{2}$$

where h is the algorithm time step, $\bigtriangledown E^{s}$ is the negative force acting on strand s and can be computed from the sum of the gradients of E^{i} and $\dot{\mathbf{x}}$ is a vector of the strands nodal velocities.

We minimize Q subject to the constraints in order to obtain a feasible velocity, and step the solution forward in time. An initial perturbation is applied to each strand to prevent the repulsion term from being infinite. In this implementation the force term is evaluated using an explicit trapezoidal type sum. Nodal velocities are computed from these forces using QL, a robust program for solving quadratic programming problems subject to equality and inequality constraints [16]. The computed nodal velocities are then applied to the nodal positions and the process is repeated until the strands reach a steady state.

Equality constraints are used to fix the insertion and origin points of each strand in space, and inequality constraints are used to keep strand nodes inside the muscle surface. Ray-triangle intersection is used to detect if a node has violated the muscle surface constraint. If so the node is moved back to the surface and an inequality constraint is added to prevent the node from moving in a direction normal to the triangle that it passed through.

4 Results and Discussion

In this section we present the preliminary results of muscle segmentation and fiber fitting for the Brachioradialis muscle of the left arm of the subject.

Despite a careful placement of constraint points, the anatomical segmentation is not perfect, because of fuzzy edges and partial volume effects. We also expect small misalignments between the different volumes due to slight movements of the subject. Although more validation and cross-comparison between different manual segmentations will be required, we presume for the moment that our segmentation lies within a $3mm$ error bound in terms of distance to the surfaces. Fig. 1 also shows how the segmentation of the Brachioradialis is constrained by the boundaries of other forearm muscles.

An initial example (Fig. 2) demonstrates how the deformable curves take muscle fiber vector field information into account during the fiber tracking process. Without vector field information the curves fill the entire muscle shape.

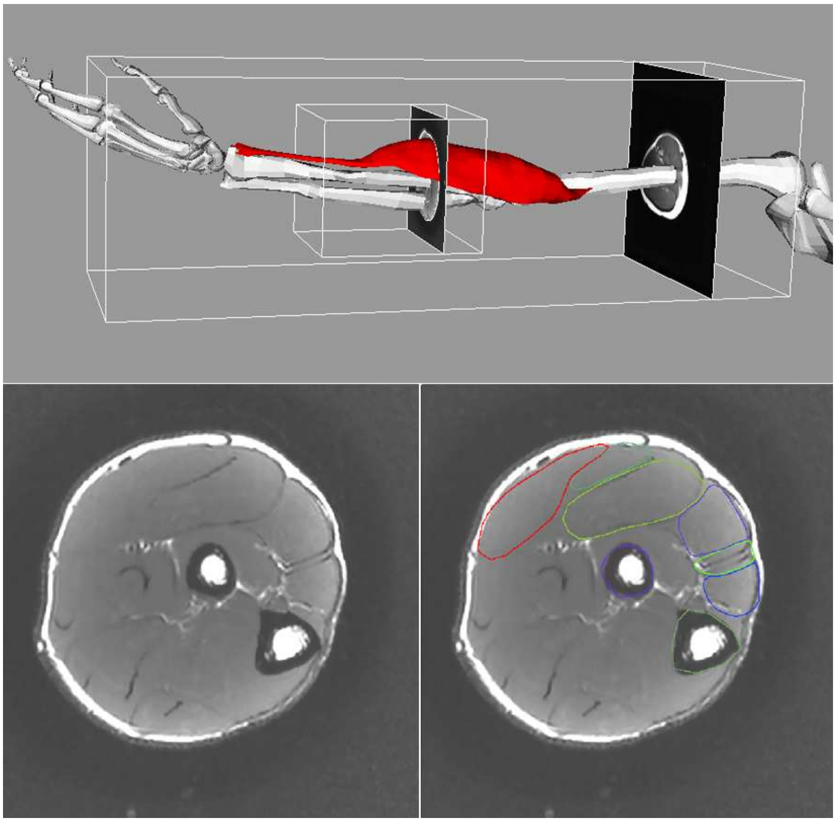

Fig. 1. Left: High/ low resolution MRI volumes and reconstructed models (bones and Brachioradialis muscle) of the arm. Bottom: High resolution sample slice with and without superimposed models. Note that the Brachioradialis is shown in red while other muscles in the forearm are shown as contours of different colours.

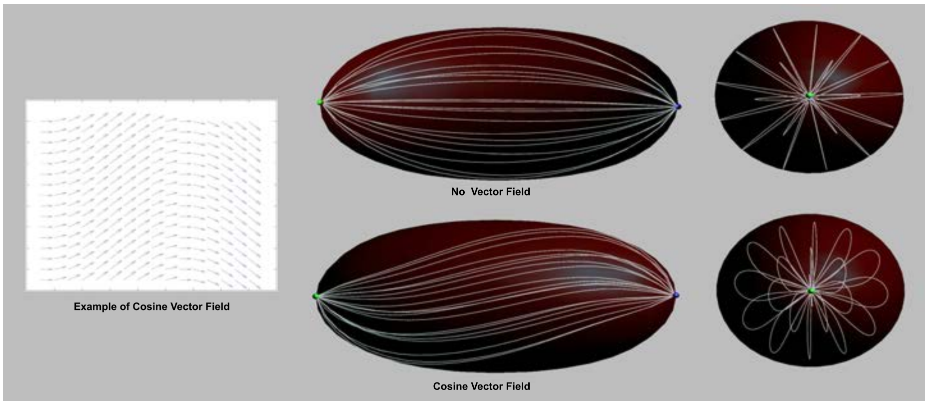

Fig. 2. A simple example showing how the curves respond to vector data. The upper images show an ellipsoidal shape filled with curves using no muscle vector field information. The lower images show the same curves under the influence of a cosine vector field.

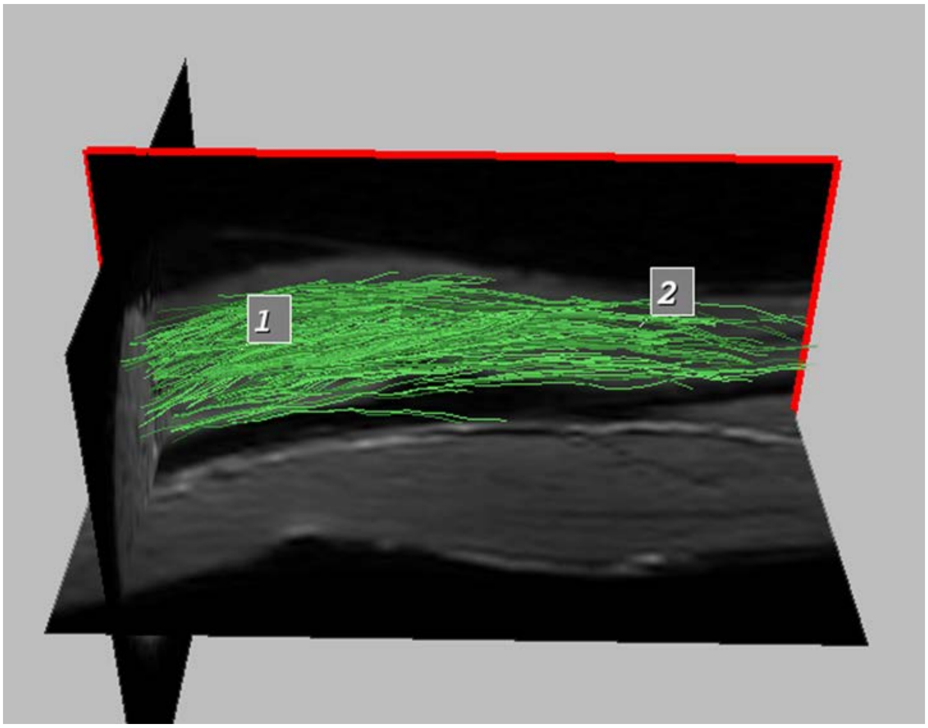

Fig. 3. DTI Fiber Tracking of the Brachioradialis muscle.

Incorporating vector field information still leads to a uniform distribution of strands within the muscle but their configuration is altered noticeably.

Next we show the results of tractography performed using the Stanford DTI Query tool (Fig. 3). The pathway shown was segmented using two volumes-of-interest positioned in the region of the Brachioradialis muscle. The primary eigenvectors of the DTI data used to compute this pathway were used to build the muscle vector field for the strand fiber tracking algorithm.

Parameters for the strand tracking algorithm were adjusted manually until we could achieve a space filling configuration of strands for which the average dot product between a strand element and the muscle fiber direction vector was 0.9 or greater. This led to parameter values of 0.5 for α, 20 for β and 300 for γ. We used a time step (h) of 0.01. Fig. 4 shows the output of the strand fiber tracking algorithm. The top left image shows the segmented muscle mesh of the Brachioradialis muscle and the template strand. The insertion and origin of the muscle are shown as green and blue spheres respectively. Notice that as the algorithm progresses that the strand arrangement (shown by the white lines) progresses from being tightly packed along the medial axis of the muscle to being evenly distributed throughout the whole muscle geometry. Also note that despite the extreme narrowing of the muscle the strands remain constrained inside the muscle shape. Fig. 5 shows the fiber field matching behavior of one strand from the fiber tracking result. Each colored line shows the direction of the muscle fiber field at the midpoint of each strand midpoints. Notice that once the strand reaches its final configuration all the vectors are virtually parallel with the elements (average dot product with the fiber field equal to 0.95) showing that the contour does align itself with the underlying fiber field.

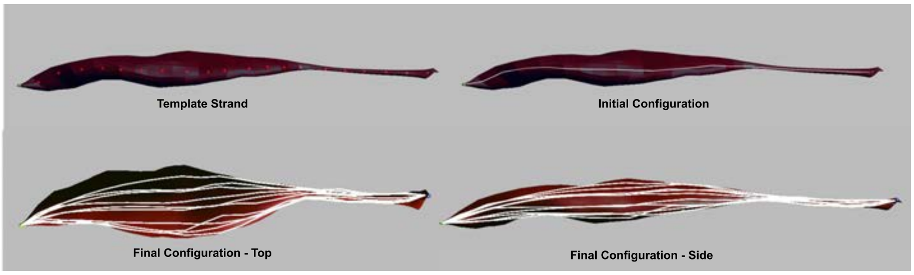

Fig. 4. The progression of the fiber tracking algorithm from the initial template strand (top left) to the completed strand configuration (bottom).

In terms of future work, parameter optimization for the energy term needs to be performed in order to find values that fit a wide range of fiber configurations accurately. Also necessary is the modification of the algorithm so that it can be used on non-fusiform muscles. Furthermore, though our preliminary results are encouraging, rigorous validation of the algorithm needs to be conducted using

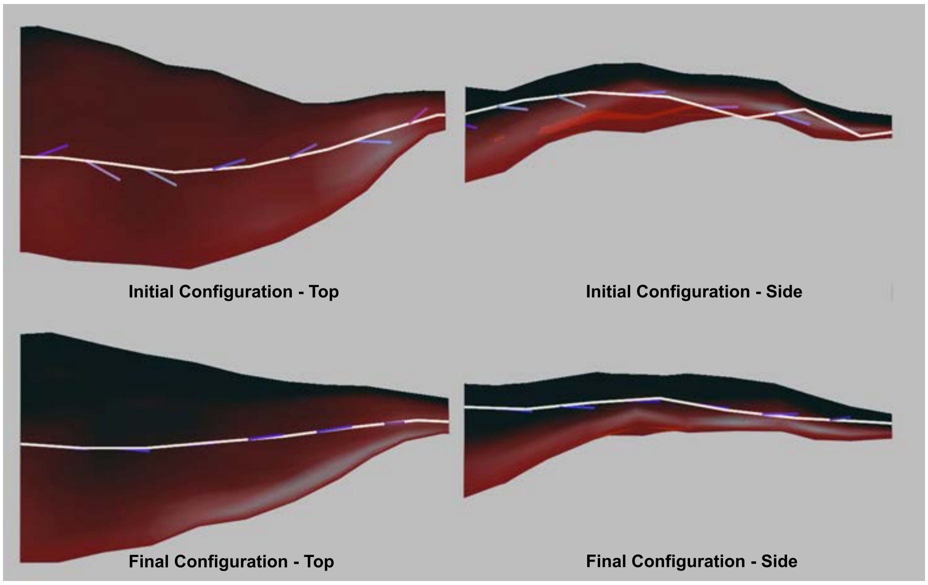

Fig. 5. The fiber field matching behavior of one of the strands from the muscle fiber tracking. Colored lines show the direction of the fiber field at each element midpoint.

more subjects. Ultimately we hope to build numerous dynamic muscle models and explore the effect that differing fiber architecture has on behavior of muscles.

5 Conclusion

We have developed a fiber tracking algorithm which fits a finite number of muscle strands to a muscle fiber field using an energy minimizing approach. Unlike previous tractography approaches, this algorithm allows more careful control of the number of muscle strands produced by the algorithm and is thus well suited for building patient specific, strand-based dynamic muscle models.

6 Acknowledgements

The authours would like to thank Danny Kaufman and Shinjiro Sueda for help with this work. This work was supported in part by the Canada Research Chairs Program, NSERC, Peter Wall Institute for Advanced Studies, Canada Foundation for Innovation, and BC KDF.

7 References

References

1. Sueda, S., Kaufman, A., Pai, D.K.: Musculotendon simulation for hand animation. ACM Trans. Graph. (Proc. SIGGRAPH) **27**(3) (2008) 83:1–83:8
2. Piazza, S.J., Delp, S.L.: The influence of muscles on knee flexion during the swing phase of gait. Journal of Biomechanics **29**(6) (1996) 723–733
3. Thelen, D.G., Anderson, F.C., Delp, S.L.: Generating dynamic simulations of movement using computed muscle control. Journal of Biomechanics **36**(3) (2003) 321–328
4. Sinha, S., Sinha, U., Edgerton, V.R.: In vivo diffusion tensor imaging of the human calf muscle. Journal of Magnetic Resonance Imaging **24**(1) (2006) 182–190
5. Lansdown, D.A., Ding, Z., Wadington, M., Hornberger, J.L., Damon, B.M.: Quantitative diffusion tensor MRI-based fiber tracking of human skeletal muscle. J Appl Physiol **103**(2) (2007) 673–681
6. Mori, S., van Zijl, P.C.M.: Fiber tracking: principles and strategies - a technical review. NMR in Biomedicine **15**(7) (2002) 468–480
7. Blemker, S.S., Delp, S.L.: Three-dimensional representation of complex muscle architectures and geometries. Annals of Biomedical Engineering **33** (2005) 661–673
8. Maintz, J., Viergever, M.: A survey of medical registration. Medical image analysis **2**(1) (1998) 1–36
9. Blemker, S., Asakawa, D., Gold, G., Delp, S.: Image-based musculoskeletal modeling: Applications, advances, and future opportunities. Journal of Magnetic Resonance Imaging **25**(2) (2007) 441–451
10. Müller, M., Heidelberger, B., Teschner, M., Gross, M.: Meshless deformations based on shape matching. Proc. of SIGGRAPH'05 (2005) 471–478
11. Rivers, A., James, D.: Fastlsm: Fast lattice shape matching for robust real-time deformation. Proc. of SIGGRAPH'07, ACM Transactions on Graphics **26**(3) (2007)
12. Gilles, B., Pai, D.K.: Fast musculoskeletal registration based on shape matching. Proc. of MICCAI'08 (2008) 822–829
13. FMRIB: Fmrib's diffusion toolbox - fdt v2.0. Webpage: `http://www.fmrib.ox.ac.uk/fsl/fdt/index.html` (2007)
14. INRIA: MedINRIA. Webpage: `http://www-sop.inria.fr/asclepios/software/MedINRIA/` (2006)
15. Kass, M., Witkin, A., Terzopoulos, D.: Snakes: Active contour models. International Journal of Computer Vision **1**(4) (1988) 321–331
16. Schittkowski, K.: QL: A fortran code for convex quadratic programming - user's guide. Report for the Department of Mathematics, University of Bayreuth (2003)

Oral Session III: High Angular Resolution Methods

Robust Variational Estimation of PDF functions from Diffusion MR Signal

Haz-Edine Assemlal, David Tschumperlé, and Luc Brun

GREYC (CNRS UMR 6072), 6 Bd Maréchal Juin, 14050 Caen Cedex, France *

Abstract. We address the problem of robust estimation of tissue microstructure from Diffusion Magnetic Resonance Imaging (dMRI). On one hand, recent hardware improvements enable the acquisition of more detailed images, on the other hand, this comes along with a low Signal to Noise (SNR) ratio. In such a context, the approximation of the Rician acquisition noise as Gaussian is not accurate. We propose to estimate the volume of PDF-based characteristics from data samples by minimizing a nonlinear energy functional which considers Rician MR acquisition noise as well as additional spatial regularity constraints. This approach relies on the approximation of the MR signal by a series expansion based on Spherical Harmonics and Laguerre-Gaussian functions. Results are presented to depict the performance of this PDE-based approach on synthetic data and human brain data sets respectively.

1 Introduction

Water molecules exhibit Brownian motion which might be constraint by internal micro-structure of the brain white matter. Diffusion-Weighted Imaging (DWI) measures this local displacement using the pulse gradient spin echo sequence [1] in each voxel and thus provides images of the architecture of the brain. These images provide valuable information to diagnose early stages of stroke, brain diseases or neurological disorders [2]. However, this molecular displacement is not directly measured. Indeed, when the diffusion gradient pulse duration δ is negligible compared to diffusion time Δ, the MR signal E defined in Q-Space is related to the average displacement probability P by the Fourier transform [3]

$$P(\mathbf{p}) = \int_{\mathbf{q}\in\mathbb{R}^3} E(\mathbf{q}) \exp(-2\pi i \mathbf{q}\mathbf{p}^T) d\mathbf{q}, \quad \text{with } E(\mathbf{q}) = \frac{S(\mathbf{q})}{S_0}, \tag{1}$$

where $\mathbf{p}$ is the displacement vector and $\mathbf{q}$ stands for the diffusion wave-vector of the Q-Space. The symbols $S(\mathbf{q})$ and S_0 respectively denote the diffusion signal at gradient $\mathbf{q}$ and the baseline image at $\mathbf{q} = 0$.

Eq.(1) naturally suggests to use the Fourier transform to numerically estimate the PDF (Probability Density Function). This technique known as Diffusion Spectrum Imaging (DSI) [4] is not clinically feasible due to the huge acquisition time required to retrieve the whole Q-Space coefficients. As a result of DSI

---

* We are thankful to Cyceron for providing data and the fruitful technical discussions.

constraints, High Angular Resolution Diffusion Imaging (HARDI) [5] comes as an interesting alternative and suggests to sample the signal on a single sphere of the Q-Space.

Prior methods of the literature based on HARD images [6–10] use a single shell acquisition and have thus to assume strong priors on the radial behavior of the signal, *i.e. mono*-exponential decay. Nonetheless, sampling schemes on several spheres in the Q-Space have been proposed recently [10–14]. Since the number of samples still remains too low to allow a precise Fourier transform, some methods rather consider computed tomography methods [14] or an approximation of the MR signal radial attenuation by a multi-exponential function [10, 12]. Note that these methods use a larger set of data but are still based on a priori models of the radial behavior of the input signal.

Nonetheless, a recent method [15] tackles this problem with a continuous representation of data from multiple shells and a fast method for computation of functions of the PDF. It involves a damped least square estimation of the best-fitting coefficients in the Spherical Polar Fourier basis. However magnitude MR data are corrupted by a Rician noise not a Gaussian one, and consequently introduces a bias in intensity at low Signal-to-Noise Ratio (SNR) which reduces the tissue contrast. This arises from complex Gaussian noise in the original frequency domain measurements named K-Space [16–19]. In this study we propose to extend the previous approach to robustness to Rician noise within a variational framework.

In section 2, we overview the mathematical background of the method introduced in [15]. Then, we present an variational framework extension of previous method for a robust estimation in section 3. Section 4 shows validation results on both numerical and real human data-sets. Finally, we draw conclusions of the proposed approach in section 5.

2 Mathematical background

To be as self-contained as possible, we briefly overview the method introduced in [15] using the Spherical Polar Fourier (SPF) expansion. In order to be able to reconstruct the PDF from Eq.(1) even with few samples, we seek a basis in which the acquired signal is sparse. For convenience, a list of common notations used in this paper is reminded in Table 1.

2.1 Spherical Polar Fourier Expansion

Let E be the MR signal attenuation, we propose to express it as a serie in a spherical orthonormal basis named Spherical Polar Fourier (SPF) [20]

$$E(\mathbf{q}) = \frac{S(\mathbf{q})}{S(0)} = \sum_{n=0}^{\infty}\sum_{l=0}^{\infty}\sum_{m=-l}^{l} a_{nlm} R_n(||\mathbf{q}||) y_l^m\left(\frac{\mathbf{q}}{||\mathbf{q}||}\right), \qquad (2)$$

where a_{nlm} are the expansion coefficients, y_l^m are real Spherical Harmonics (SH), and R_n is an orthonormal radial basis function.

Table 1. A list of major notations used in this paper

Symbol	Description	Symbol	Description
PDF	Probability Density Function	$\mathbf{p}, \mathbf{k}$	Displacement vectors in $\mathbb{R}^3$
ODF	Orientation Density Function	$P(\mathbf{p})$	Average displacement probabilities
FRT	Funk-Radon Transform	$\mathbf{q}$	Diffusion space vector in $\mathbb{R}^3$
SH	Spherical Harmonics	$S(\mathbf{q})$	MR signal at diffusion gradient $\mathbf{q}$
SPF	Spherical Polar Fourier	$E(\mathbf{q})$	MR signal attenuation $S(\mathbf{q})/S(0)$
a_{nlm}	SPF expansion coefficient	$\mathcal{G}(\mathbf{k})$	PDF characteristic at point $\mathbf{k}$
	at order n, l and m	$h_{\mathbf{k}}(\mathbf{p})$	projection function of $\mathcal{G}(\mathbf{k})$

The angular part of the signal E is reconstructed by the complex SH Y_l^m which form an orthonormal basis for functions defined on the single sphere. For this reason, they have been widely used in diffusion MRI [21, 22]. Indeed, as the diffusion signal exhibits real and symmetry properties, the use of a subset of the complex basis made of real and symmetric SH y_l^m strenghten the robustness of the reconstruction to signal noise and reduces the number of required coefficients [21, 22].

The radial part of the signal E is reconstructed by the elementary radial functions R_n. A sparse representation of the radial signal should approximate it in a few radial order N. Based on these observations, we propose to estimate E using the normalized generalized Gaussian-Laguerre polynomials basis R_n [20, 23]:

$$R_n\left(||\mathbf{q}||\right) = \left[\frac{2}{\gamma^{3/2}}\frac{n!}{\Gamma\left(n+3/2\right)}\right]^{1/2} \exp\left(-\frac{||\mathbf{q}||^2}{2\gamma}\right) L_n^{1/2}\left(\frac{||\mathbf{q}||^2}{\gamma}\right), \quad (3)$$

where γ denotes the scale factor and $L_n^{(\alpha)}$ are the generalized Laguerre polynomials. The Gaussian decay arises from the normalization of the Laguerre polynomials in spherical coordinates.

The SPF forms an orthonormal basis on Spherical Harmonics (SH) and Gaussian-Laguerre polynomials. Consequently a low order truncation assumes a radial Gaussian behavior as in [10, 12] and a high order truncation provides a model-free estimation. Besides, the square error between a function and its expansion in SPF to order $n <= N$ and $l <= L$ converges to zero as N and L go to infinity.

2.2 Fast Computation of Characteristics on the PDF

As we have a continuous representation of E from the SPF coefficients, let $\mathcal{G}(\mathbf{k}) = \int P(\mathbf{p}) h_{\mathbf{k}}(\mathbf{p}) d\mathbf{p}$ be a characteristic $\mathcal{G}$ of the PDF at point $\mathbf{k}$, where $h_{\mathbf{k}}$ denotes a projection function at point $\mathbf{k}$. Table 2 represents several popular characteristics $\mathcal{G}$ which can be evaluated using this computational scheme. A natural way to retrieve $\mathcal{G}$ would be to reconstruct E from the SPF coefficients, compute a Fast Fourier Transform (FFT) and finally calculate $\mathcal{G}$ on the PDF

Table 2. A non-exhaustive list of some PDF characteristics $\mathcal{G}$ and their projection function $h_{\mathbf{k}}$ at point $\mathbf{k}$. FRT stands for the Funk-Radon Transform used in QBI, where J_0 is the Bessel function of the first kind and $||\mathbf{q}'||$ is the radius of the q-ball shell. ISO stands for isoprobability profiles. SD and FD respectively stands for slow and fast diffusion, where $||\mathbf{p}'||$ is the radius limit between intra and extra cellular diffusion.

$\mathcal{G}$	ODF	FRT	ISO	SD	FD
$h_{\mathbf{k}}(\mathbf{p})$	$\delta(1 - \frac{\lvert\mathbf{p}\cdot\mathbf{k}\rvert}{\lvert\lvert\mathbf{p}\rvert\rvert \lvert\lvert\mathbf{k}\rvert\rvert})$	$J_0(2\pi\lvert\lvert\mathbf{q}'\rvert\rvert\lvert\lvert\mathbf{p}\rvert\rvert)$	$\delta(\mathbf{k})$	ODF if $\lvert\lvert\mathbf{p}\rvert\rvert < \lvert\lvert\mathbf{p}'\rvert\rvert$ 0 if $\lvert\lvert\mathbf{p}\rvert\rvert > \lvert\lvert\mathbf{p}'\rvert\rvert$	0 if $\lvert\lvert\mathbf{p}\rvert\rvert < \lvert\lvert\mathbf{p}'\rvert\rvert$ ODF if $\lvert\lvert\mathbf{p}\rvert\rvert > \lvert\lvert\mathbf{p}'\rvert\rvert$

volume; however such a scheme would induce cumbersome computations and raise numerical accuracy issues. So, any characteristic $\mathcal{G}$ defined from Eq.(4) can alternatively be computed directly from the SPF coefficients. Indeed, since the SPF are an orthonormal basis the following relation holds:

$$\mathcal{G}(\mathbf{k}) = \int_{\mathbf{p}\in\mathbb{R}^3} P(\mathbf{p})h_{\mathbf{k}}(\mathbf{p})d\mathbf{p} = \int_{\mathbf{q}\in\mathbb{R}^3} E(\mathbf{q})H_{\mathbf{k}}(\mathbf{q})d\mathbf{q} = \sum_{nlm}^{\infty} a_{nlm} b^{\mathbf{k}}_{nlm} \tag{4}$$

where $H_{\mathbf{k}}$ is the inverse Fourier transform of $h_{\mathbf{k}}$ and $a_{nlm}, b^{\mathbf{k}}_{nlm}$ respectively denote the SPF expansion of E and $H_{\mathbf{k}}$. Therefore, the numerical computation of $\mathcal{G}(\mathbf{k})$ which is an integration over an entire volume simply turns into a very fast dot product between two vectors of SPF coefficients.

We seek the SPF coefficients that represent the best the MR data samples E. However, E is strongly corrupted by noise and may lead to distortion of computed characteristics on the PDF.

3 Robustness to noise

Since the acquisition noise on the MR signal is not Gaussian, a least square fit is definitely not the best choice for such an estimation process. This issue arises especially when dealing with low SNR data as this is the case for very high-q values. Furthermore, independent voxel estimation does not reflect the spatial regularity of the diffusion function. We propose to tackle these issues with a variational framework which is adaptable to noise distribution and is able to use valuable information given by the neighbour voxels.

3.1 Variational Framework

The key idea is to estimate *and* regularize the whole volume of voxels at the same time. Indeed, it enables to take into account correlation between all parts of the processing pipeline instead of doing the different parts separately. Let E be the acquired dMRI volume corrupted by Rician noise, we seek the SPF coefficients A of the filtered dMRI volume $\hat{E} = MA$, where the symbol $M = (R_n(||\mathbf{q}_j||)y_l^m(\frac{\mathbf{q}_j}{||\mathbf{q}_j||}))_{nlm \times j \in \mathbb{N}^3 \times \mathbb{N}}$ denotes the SPF basis matrix. We propose to robustly estimate and regularize the SPF coefficients field from the dataset volume simultaneously by minimizing the following nonlinear functional energy:

$$\min_{A}\left\{\int_{\Omega_E}\left[\sum_{k}^{n_s}\psi(\hat{E}_k)\right]+\alpha_r\varphi(||\nabla A||)d\Omega_E\right\} \tag{5}$$

where $\Omega_E \subset \mathbb{R}^3$ is the domain of datasets voxels. The likelihood term $\psi(E_k)$ measures the dissimilitudes at voxel $\mathbf{x} \in \Omega_E$ between E and its reconstruction $\hat{E}$ at gradient direction k, $\psi : \mathbb{R} \rightarrow \mathbb{R}^+$ and $\varphi : \mathbb{R} \rightarrow \mathbb{R}^+$ are real and positive functions, $\alpha_r \in \mathbb{R}$ is the regularization weight and $||\nabla A||$ the gradient norm defined as

$$||\nabla A|| = \sum_{nlm} ||\nabla A_{nlm}|| \tag{6}$$

Note that if $\psi(s) = s^2$ and $\alpha_r = 0$ in Eq.(5), we minimize the least square criterion. As the minimization cannot be computed straightforwardly, the gradient descent coming from the Euler-Lagrange derivation of Eq.5 leads to a set of multi-valued Partial Differential Equation (PDE) as described in Eq.(7). In practice, we first set $A_{(t=0)}$ to U_0, an initial estimate of SPF coefficients. In order to estimate a solution, SPF coefficients velocity $\frac{\partial A}{\partial t}$ giving the direction from the current A to a solution is computed. The latter is done several times until convergence (typically when $\varepsilon \in \mathbb{R}^+, \varepsilon \rightarrow 0, \frac{\partial A}{\partial t} < \varepsilon$),

$$\begin{cases} A_{t=0} = U_0 \\ \frac{\partial A_j}{\partial t} = \sum_k^{n_s} M_{k,j}\psi'(\hat{E}_k) + \alpha_r \operatorname{div}(\varphi(||\nabla A||)) \end{cases} \tag{7}$$

The initial estimate U_0 is computed either by considering a random field or a more structured one. A good choice is to start from an initial set which is not so far from the global minimum; so the linear least square estimation seems to be an adequate alternative. Indeed, least square minimization is the global minimum when $\psi(s) = s^2$ and $\alpha_r = 0$. One can expect the minimum to be close enough to the least square minimum through variations of ψ and φ; and should consequently bring down the number of iterations required to converge.

3.2 Likelihood function ψ

The diffusion MR magnitude images are corrupted by noise and the best ψ function is the one specific to the MR scanners, that is to say the Rice distribution whose probability density function is:

$$p(E|\hat{E},\sigma) = \frac{E}{\sigma^2}\exp\left(\frac{-(E^2+\hat{E}^2)}{2\sigma^2}\right) I_0\left(\frac{E\cdot\hat{E}}{\sigma^2}\right) \tag{8}$$

where σ is the standard deviation of the noise and I_0 is the modified zeroth-order Bessel function of the first kind. We adapt the Rician bias correction

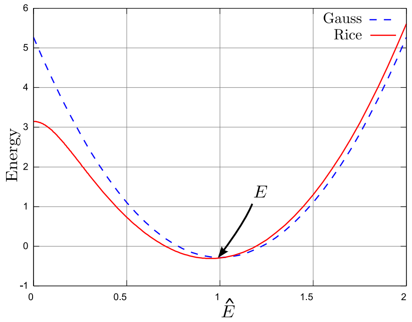

Fig. 1. Energy associated to respectively Gaussian and Rician likelihood ψ functions. Note the bias introduced by the Rician function on low SNR data. $E = 1$ and $\sigma = 0.5$.

filter introduced in [24] from 2nd-order DTI to the SPF basis. It is based on a *maximum a posteriori* approach so we construct the filtered volume $\hat{E}$ that maximizes the log-posterior probability:

$$\log p(\hat{E}|E) = \log p(E|\hat{E}) + \log p(\hat{E}) - \log p(E) \tag{9}$$

where $p(E|\hat{E})$ is the likelihood term, $p(\hat{E})$ is the prior or the regularization term and $p(E)$ is the normalizing constant. We are interested in the likelihood term, thus combining Eq.(8) and Eq.(9) the pointwise log-likelihood becomes

$$\log p(E|\hat{E},\sigma) = \log \frac{E}{\sigma^2} - \frac{(E^2 + \hat{E}^2)}{2\sigma^2} + \log I_0\left(\frac{E \cdot \hat{E}}{\sigma^2}\right) = \psi(\hat{E}) \tag{10}$$

Fig.3.2 illustrates variation of the opposite function with scalar values of $\hat{E}$ when $E = 1$ and $\sigma = 0.5$. The energy is low when $E \approx \hat{E}$ and increases with their dissimilitudes. Note that σ has to be known *a priori* and can be either retrieved as a parameter specific to the MR scanner, or can be either computed from a uniform area as described in [19]. Combining Eq.(7) and the derivative of Eq.(10) with respect to A_j gives the PDE adapted to Rician noise,

$$\frac{\partial A_j}{\partial t} = \frac{\sum_k^{n_s} M_{k,j}}{\sigma^2}\left(-\hat{E}_k + E_k\left[\frac{I_1\left(\frac{E_k \cdot \hat{E}_k}{\sigma^2}\right)}{I_0\left(\frac{E_k \cdot \hat{E}_k}{\sigma^2}\right)}\right]\right) + \alpha_r \operatorname{div}(\varphi(||\nabla A||)) \tag{11}$$

3.3 Regularization function φ

Regarding the spatial regularization, various functions φ of the image processing literature can be proposed as long as it preserves important features of the image. Indeed, regularization should be strong on homogeneous area (low $||\nabla A||$), and preserve contours not only between isotropic and anisotropic regions but also among voxels with different number of fibers (large $||\nabla A||$). We drop the angular and radial regularization step of Eq.4 in [15] since the spatial regularization puts sufficient constraints on the diffusion signal to be estimated. Our experiments have confirmed that combining these regularization to the spatial one is useless.

4 Experiments

In this section, we present results of our method on both synthetic simulations and real human brain data-sets. We first focus on a comparison between the damped least square estimation introduced in previous work and the robust variational framework introduced in this paper. Then we illustrate the flexibility of the proposed approach with a comparison of ODF computed with QBI method as proposed in [25] and with our method [15] on an in-vivo dataset.

4.1 Numerical Simulations

We have applied the above scheme to the simulations of a single fiber and crossing fiber configurations. The following synthetic multi-exponential model was used to generate data, $E(\mathbf{q}) = \sum_{k=1}^{N_b} f_k \exp\left(-\mathbf{q}^T D_k \mathbf{q}\right)$ where $\sum_{k=1}^{N_b} f_k = 1$. The symbol N_b stands for the number of fibers and D_k is a 3×3 symmetric definite positive matrix defining the diffusion anisotropy. Diffusion images were synthesized following 3 sampling protocols: low resolution (1 shell $b = 3000\,\mathrm{s/mm}^2$), medium resolution (2 shells $b = \{1000\,,3000\}\,\mathrm{s/mm}^2$) and high resolution (5 shells $b = \{500\,,1000\,,1700\,,2400\,,3000\}\,\mathrm{s/mm}^2$) along with a single baseline image acquired at $b = 0\,\mathrm{s/mm}^2$. Each shells is composed of 42 directions along the edges of a subdivided icosahedron. Estimation parameters were chosen empirically for each sampling protocol: low resolution $\{N = 0,\, L = 4,\, \gamma = 100,\, \lambda_N = 0,\, \lambda_L = 6 \times 10^{-5}\}$, medium resolution $\{N = 1,\, L = 4,\, \gamma = 70,\, \lambda_N = \lambda_L = 0\}$, high resolution $\{N = 4,\, L = 4,\, \gamma = 50,\, \lambda_N = \lambda_L = 0\}$.

In order to assess the robustness to noise of our proposed variational framework, we produced a synthetic phantom of crossing fibers (horizontal and vertical networks) surrounded by water regions (upper left area) (*c.f.* Fig.3a). To simulate dMRI acquisitions, we added Rician noise of variance σ to the signal E which was then sampled using medium resolution protocol as described above.

Fig.2 shows the results of a comparison between the reconstruction of E with Gaussian and the Rician likelihood functions on a noisy dataset (Fig.2b). A post-processing contrast enhancement with the same parameters was applied to all images (a-f) to highlight artifacts. Although the Gaussian function is classically used in the least square minimization [15], it is not robust to noise and creates undesirable radial oscillations at high q values (Fig.2c). On the contrary, the Rician likelihood function strongly attenuate this drawback and gives a correct estimation of E (Fig.2d).

The Generalized Fractional Anisotropy (GFA) measure [5] in Fig.3 is a generalization of the fractional anisotropy (FA) measure of DTI. Each image was normalized independently to enhance visualization contrast. This qualitative comparison highlights the need for spatial regularization within the estimation

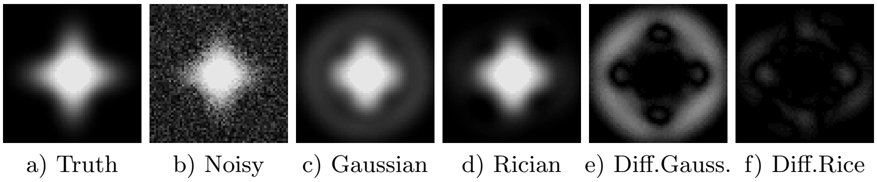
a) Truth b) Noisy c) Gaussian d) Rician e) Diff.Gauss. f) Diff.Rice

Fig. 2. Qualitative comparison between Gaussian and Rician likelihood functions influence on reconstruction of an noisy dataset. PSNR(noisy,original)=18.5. Graphics (e,f) are the absolute difference between respectively (c,d) and (a).

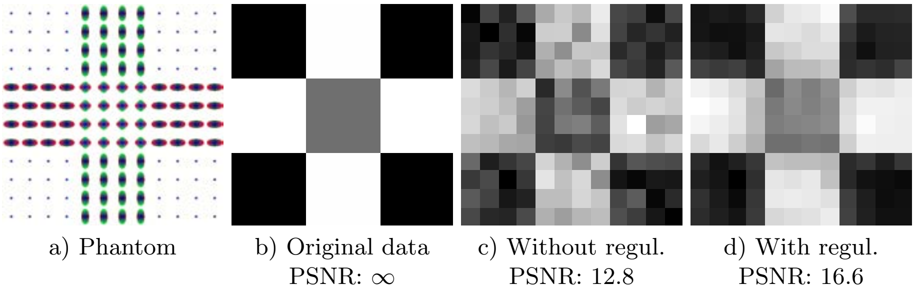
a) Phantom b) Original data PSNR: ∞ c) Without regul. PSNR: 12.8 d) With regul. PSNR: 16.6

Fig. 3. Effects of spatial regularization on the GFA [5]. Isotropic area are black, anisotropic area are white. PSNR(noisy,original)=18.5. (a) The ODF of the synthetic phantom which is composed of two groups of fiber, horizontal and vertical, and surrounded by water. (b) GFA of the perfect dataset. (c) GFA of the LS estimation on a noisy dataset (without regularization). (d) GFA of the PDE estimation on the same noisy dataset (with regularization).

process. Indeed, GFA is an adequate measure to have insight on the global coherence of the dataset volume estimation since every voxel is summarized by a scalar value. When it comes to noisy input data, regularization greatly improves the spatial coherence of the volume estimation as illustrated in Fig.3(c,d). It is worth noting that the gradient norm $||\nabla A||$ is an adequate measure to set apart isotropic area from anisotropic area and subsequently, divergence $\text{div}(\varphi||\nabla A||)$ performs well in regularizing homogeneous area without degrading the contours.

We computed statistics on the performance of the PDE estimation with various likelihood and regularization functions ψ and φ. The PSNR (Peak Signal to Noise Ratio) between the reconstruction and the original data stands for the PSNR between the ground truth dataset *volume* E and its estimation $\hat{E}$. Values of $\hat{E}$ were restricted to $[0, 1]$ in order to reflect the signal attenuation properties. Fig.4a, illustrates the PSNR(E,$\hat{E}$) of the reconstruction versus the quality of input datasets. Out of the results, the Rician likelihood function outperforms the Gaussian function and greatly improves the PSNR of the estimation. This gap can be explained by a more robust radial fit thanks to the Rician likelihood function as shown in Fig.2(c,d). Indeed, the number of radial sample in this

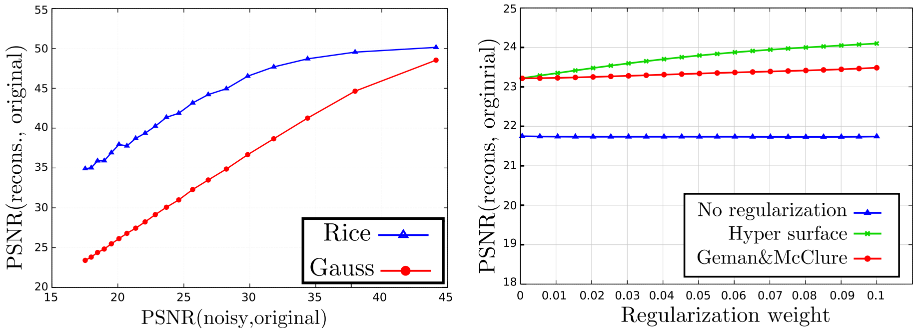

a) Comparison of likelihood functions. b) Comparison of regularization functions.

Fig. 4. Synthetic phantom of networks of crossing fibers (*c.f.* Fig.3a). a) Performances of likelihood functions on increasing levels of noise. b) Performances of regularization functions on increasing regularization strength α_r.

experiment is very limited (2 shells) whereas the number of angular samples is sufficient (42 directions).

Fig.4b shows influence of regularization function φ on the PSNR of the reconstruction $\hat{E}$. Although this brings modest improvements, the spatial regularization ensures numerical stability of the estimation by adding constraints when there are only very few samples available. Besides, this also brings stability to the fiber-tracking algorithms and helps to better estimate the white matter nerve fibers tracks [26].

4.2 In vivo experiments

Diffusion-weighted images were acquired in two shells along 32 directions at $b = 1000\,\mathrm{s/mm}^2$ and $b = 3000\,\mathrm{s/mm}^2$, and a single image at $b = 0\,\mathrm{s/mm}^2$. Thus, there were a total of 65 images acquired in a sequence of 15 minutes on a 3 T Philips scanner. The SENSE parallel imaging protocol was used with a factor of acceleration set to 2; and only 80% of the k-space was acquired. Matrix size was $112 \times 112 \times 60$ and the image resolution was $2 \times 2 \times 2\,\mathrm{mm}^3$. Repetition time was TR=11490 ms, echo time was TE=85 ms. Time between two pulses and time of diffusion gradients were respectively $\Delta = 42.2\,\mathrm{ms}$ and $\delta = 26.3\,\mathrm{ms}$. Terms up to $N = 1$ and $L = 4$ were used in the calculations. Computations were done in less than an hour on a 3 Ghz processor, and includes calculations of SPF coefficients and projections along the 642 directions for the whole data-set $112 \times 112 \times 60$ volume.

Representative images of GFA on the data are presented in Fig.5 and reveals microstructures around the genu of the corpus callosum. The first line of Fig.5 are the results from previous work [15] and shows how it compares to standard dMRI methods. DTI performs well in corpus callosum but fails in voxel with orientational heterogeneity as shown in Fig.5b. QBI can successfully retrieve multiple fibers orientations using the analytical stable ODF reconstruction de-

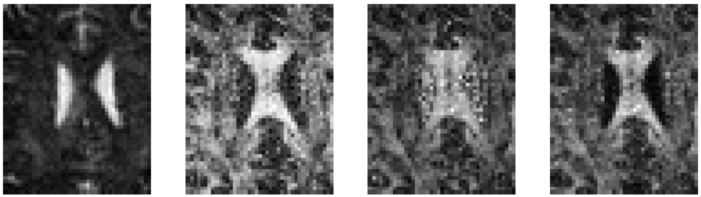

a) S_0 b) DTI [27] c) QBI [25] d) $\mathcal{G}$=ODF [15]

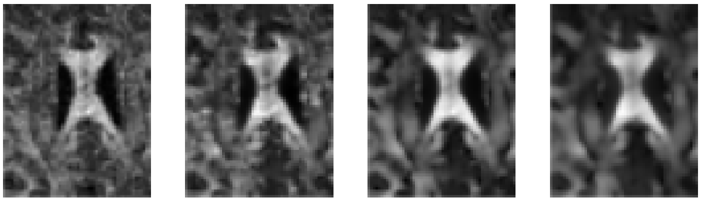

e) Rice f) Soft Reg. g) Med. Reg. h) Strong Reg.

Fig. 5. Comparison of GFA [5] on region of corpus callosum and lateral ventricles. (a) Baseline image, $\mathbf{q} = 0$. (b) DTI anisotropy map. (c) Q-Ball Imaging. (d) Previous work using damped least-square estimation. (e) Variational approach using Rician likelihood function. (f-g) Variational approach using Rician likelihood function + Hyper Surface regularization function.

scribed in [25] but is sensitive to noise, especially in region of cerebrospinal fluid (*c.f.* Fig.5c). On the contrary, the ODF obtained by the SPF estimation approach does not fall into this pitfall (Fig.5d), it successfully retrieves anisotropic shapes in brain white matter fibers regions and isotropic shape in cerebrospinal fluid area (*c.f.* Fig.5d). The second line of Fig.5 shows the performances of the proposed variational framework. Out of the results, Rician likelihood function does not modify much the GFA map computed on ODF (*c.f.* Fig.5(d,e)). It was expected as artifacts on $\hat{E}$ are mostly radial distortion and GFA focuses on angular variations. However, spatial regularization strongly influence results, depending on the regularization strength α_r as illustrated in Fig.5(f-h).

5 Discussion and conclusion

In this paper, we proposed a variational approach which robustly estimates at a stretch the whole volume of PDF functions as a set of Spherical Polar Fourier (SPF) coefficients. This is done by minimizing an energy that simultaneously considers the Rician model of the MRI noise and the regularization on spatial constraints. Results demonstrate that the ability to reconstruct a voxel taking the whole neighborhood information into account strongly improve the spatial coherence of the reconstruction. Besides, fiber-tracking is unstable on noisy datasets and this last property may greatly improve the ability to recover reliable and accurate intra-voxel fibers distributions within the human brain.

References

1. Stejskal, E., Tanner, J.: Spin diffusion measurements: spin echoes in the presence of a time-dependent field gradient. Journal of Chemical Physics **42** (1965) 288–292
2. LeBihan, D., Breton, E., Lallemand, D., *et al.*: Mr imaging of intravoxel incoherent motions: Application to diffusion and perfusion in neurologic disorders. Radiology (1986) 401–407
3. Callaghan, P.: Principles of Nuclear Magnetic Resonance Microscopy. Oxford University Press, USA (1991)
4. Wedeen, V., Reese, T., Tuch, D., *et al.*: Mapping fiber orientation spectra in cerebral white matter with fourier transform diffusion mri, ISMRM (2000) 82
5. Tuch, D., Weisskoff, R., Belliveau, J., Wedeen, V.: High angular resolution diffusion imaging of the human brain. (1999) 321
6. Tuch, D.: Q-ball imaging. Magn Reson Med **52** (2004) 1358–1372
7. Yablonskiy, D.A., Bretthorst, G.L., Ackerman, J.J.: Statistical model for diffusion attenuated mr signal. Magn Reson Med **50** (2003) 664–669
8. Jian, B., Vemuri, B.C., Özarslan, *et al.*: A novel tensor distribution model for the diffusion-weighted mr signal. NeuroImage **37** (2007) 164–176
9. Liu, C., Bammer, R., Acar, B., Moseley, M.: Characterizing non-gaussian diffusion by using generalized diffusion tensors. Magn Reson Med **51** (2004) 924–937
10. Özarslan, E., Sherperd, T.M., Vemuri, B.C., *et al.*: Resolution of complex tissue microarchitecture using the diffusion orientation transform (dot). NeuroImage **31** (2006) 1086–1103
11. Cercignani, M., Alexander, D.: Optimal acquisition schemes for in vivo quantitative magnetization transfer mri. Magn. Reson. Med. **56** (2006) 803–810
12. Assaf, Y., Basser, P.J.: Composite hindered and restricted model of diffusion (charmed) mr imaging of the human brain. NeuroImage **27** (2005) 48–58
13. Wu, Y.C., Alexander, A.L.: Hybrid diffusion imaging. NeuroImage **36** (2007)
14. Pickalov, V., Basser, P.J.: 3d tomographic reconstruction of the average propagator from mri data, ISBI (2006)
15. Assemlal, H.E., Tschumperlé, D., Brun, L.: Efficient computation of pdf-based characteristics from diffusion mr signal, MICCAI (2008)
16. Granlund, G., Knutsson, H.: Signal Processing for Computer Vision. Kluwer Academic Publish. (1995)
17. Gudbjartsson, H., Patz, S.: The rician distribution of noisy mri data. Magn. Reson. Med. **34** (1995) 910–914
18. Henkelman, R.: Measurement of signal intensities in the presence of noise in mr images. Med. Phys. **12** (1985) 232–233
19. Sijbers, J., den Dekker, A., van Audekerke, J., *et al.*: Estimation of the noise in magnitude mr images. Magn. Reson. Imag. **16** (1998) 87–90
20. Ritchie, D.W.: High-order analytic translation matrix elements for real-space six-dimensional polar fourier correlations. J. Appl. Cryst. **38** (2005) 808–818
21. Alexander, D., Barker, G., Arridge, S.: Detection and modeling of non-gaussian apparent diffusion coefficient profiles in human brain data. Magn Reson Med **48** (2002) 331–340
22. Frank, L.: Characterization of anisotropy in high angular resolution diffusion-weighted mri. Magn Reson Med **47** (2002) 1083–1099
23. Biedenharn, L.C., Louck, J.D.: Angular momentum in quantum physics. Addison-Wesley Publishing Co., Reading, Mass. (1981)

24. Basu, S., Fletcher, T., Whitaker, R.: Rician noise removal in diffusion tensor mri. MICCAI (2006) 117–125
25. Descoteaux, M., Angelino, E., Fitzgibbons, S., Deriche, R.: Regularized, fast and robust analytical q-ball imaging. Magn Reson Med **58** (2007) 497–510
26. Assemlal, H.E., Tschumperlé, D., Brun, L.: Fiber tracking on hardi data using robust odf fields, ICIP (2007) 133–136
27. Basser, P.J., Mattiello, J., LeBihan, D.: Estimation of the effective self-diffusion tensor from the nmr spin echo. J. Magn Reson **103** (1994) 247–254

Two Canonical Representations for Regularized High Angular Resolution Diffusion Imaging

Luc Florack and Evgeniya Balmashnova

Eindhoven University of Technology, Mathematics and Computer Science,
Den Dolech 2, 5600 MB Eindhoven, The Netherlands
`{L.M.J.Florack,E.G.Balmashnova}@tue.nl`

Abstract. Two canonical representations for regularization of unit sphere functions encountered in the context of high angular resolution diffusion imaging (HARDI) are discussed. One of these is based on spherical harmonic decomposition, and its one-parameter extension via Tikhonov regularization. This case is well-established, and is mainly reviewed for the sake of completeness. The second one is new, and is based on a higher order diffusion tensor decomposition. A homogeneous representation of this type has been proposed in the literature, but we show that this is inconvenient for the purpose of regularization. We instead construct a heterogeneous representation that can be regarded as "canonical", to the extent that its behaviour under regularization mimics that of spherical harmonics.

Key words: Tikhonov regularization, higher order diffusion tensors, spherical harmonics, high angular resolution diffusion imaging (HARDI), diffusion tensor imaging (DTI), scale space.

1 Introduction

High angular resolution diffusion imaging (HARDI)—and, as a special case, diffusion tensor imaging (DTI)—has the potential to provide unprecedented insight into the microstructure of fibrous tissue such as muscle and brain white matter. It is to date the only in vivo technique for studying the microstructure of such tissues. Since tissue degeneration may occur as a precursor of certain diseases, it holds the promise to become an essential diagnostic tool. In addition it may further our insight in anatomy and brain connectivity, cf. Alexander et al. in the context of neurotherapeutic applications of brain DTI [1].

In order to model the a priori unconstrained number of point measurements in HARDI, one is naturally led to an infinite-dimensional Hilbert space framework. Apart from the obvious risk of overfitting, lack of control on the overwhelming number of degrees of freedom greatly complicates analysis and visualization.

Regularization provides a way to control data complexity and to ensure manifest robustness. We will review some finite-order Tikhonov regularization schemes from the literature, as well as a recently introduced infinite-order scheme [2–8]. It has appeared natural in all cases to employ a basis of spherical harmonics [9, 10], and this is indeed the typical procedure followed in practice. (The main reason for this review is to make the paper self-contained; the reader is referred to cited literature for details.)

However, an alternative but equally interesting decomposition has been put forward by Özarslan and Mareci [11]. Instead of spherical harmonics the authors propose to use *homogeneous* polynomials confined to the unit sphere, as a generalization of DTI. The "higher order diffusion tensors" constructed accordingly are in principle capable of modeling raw HARDI data to any prescribed accuracy. Although there is some implicit regularization in the act of truncating the polynomial expansion at some finite order, akin to the regularizing effect of fitting acquisition data to a second order DTI tensor, the intention is primarily to capture *raw* data to any desired level of detail. Indeed, the higher order diffusion tensor model of Özarslan and Mareci is best appreciated as a DTI generalization.

However, unlike with DTI, which by construction has only six independent degrees of freedom per point [12–14], there is no explicit regularization of a general HARDI signal. The question thus presents itself whether the tensor model of Özarslan and Mareci admits regularization in a "natural" way, similar to the case of the spherical harmonic description. The answer is no, in the sense that the employed basis functions are not eigenfunctions of standard regularization operators. This implies that there exists no "simple" way of adapting the raw data coefficients in their polynomial expansion so as to obtain a corresponding regularized expansion. We therefore modify their scheme by instead considering a *heterogeneous* polynomial on the sphere, and exploiting intrinsic redundancy so as to make each homogeneous term an eigenfunction under regularization. As a result, our alternative higher order diffusion tensor model reconciles the tensor rationale championed by Özarslan and Mareci with the regularization rationale, without sacrificing the niceties exhibited by the spherical harmonic description in this context. The "trick" is basically to extract from a homogeneous polynomial representation of order N, say, all those degrees of freedom that can be expressed in terms of spherical harmonics of lower orders, which can then be reformatted into lower order polynomial terms, ultimately producing an equivalent, heterogeneous polynomial. This will be operationalized in the next section.

For simplicity we will collectively refer to various related representations that employ functions on the unit sphere simply as "HARDI". These include Tuch's orientation distribution function (ODF) [15], the higher order diffusion tensor model and the diffusion orientation transform (DOT) by Özarslan et al. [11, 16], Q-Ball imaging [2], and the diffusion tensor distribution model by Jian et al. [17]. Considerations in this paper pertain to all such representations.

2 Theory

2.1 Notation

Let $S : \Omega \to \mathbb{R}$ denote a raw HARDI (or HARDI-related, v.s.) signal confined to the unit sphere $\Omega : \|x\| = 1,\ x \in \mathbb{R}^3$. Ω may be parameterized using two coordinates, ξ^μ, $\mu = 1, 2$, say. The components of the Riemannian metric for the unit sphere Ω embedded in Euclidean 3-space $\mathbb{R}^3$ are then given by[1]

$$g_{\mu\nu} = \frac{\partial x^i}{\partial \xi^\mu} \eta_{ij} \frac{\partial x^j}{\partial \xi^\nu} \,, \tag{1}$$

in which η_{ij} are the components of the Euclidean metric of the embedding space (in Cartesian coordinates $\eta_{ij} = 1$ iff $i = j$, otherwise zero). With D_μ we denote the covariant derivative with respect to x^μ induced by the metric $g_{\mu\nu}$. Recall that by construction we have $D_\rho g_{\mu\nu} = 0$, whence also $D_\mu g = 0$, in which we have used the shorthand notation $g = \det g_{\mu\nu}$. This "covariant constancy" of the metric tensor in fact defines the covariant derivative [18], and plays a key role in partial integration in covariant variational formulations of regularization.

The spherical geometry of the problem naturally suggests the use of spherical coordinates ($\xi^1 = \theta, \xi^2 = \phi$):

$$\Omega : (x^1, x^2, x^3) = (\sin\theta\cos\phi, \sin\theta\sin\phi, \cos\theta)\,. \tag{2}$$

2.2 Regularization via Spherical Harmonic Decomposition

We now consider regularization of a raw HARDI signal S. To this end, consider the following functional, in which $S_T : \Omega \to \mathbb{R}$ is a Tikhonov regularization of $S : \Omega \to \mathbb{R}$, viz. such that

$$E(S_T) = \int_\Omega (S(\xi) - S_T(\xi))^2 + \sum_{k \geq 1} t_k D_{\mu_1} \ldots D_{\mu_k} S_T(\xi)\, D^{\mu_1} \ldots D^{\mu_k} S_T(\xi)\, D\xi \tag{3}$$

is minimal. The subscript T refers to a sequence of nonnegative regularization parameters, $T = \{t_k\}_{k \in \mathbb{N}}$, on which the solution depends. D^μ is shorthand for $g^{\mu\nu}(\xi) D_\nu$, and $D\xi = \sqrt{g(\xi)}\, d\xi^1 d\xi^2$, denotes the invariant measure on Ω (in spherical coordinates $D\xi = \sin\theta\, d\theta\, d\phi$). The parameters $t_k \in T$ need to be chosen so as to ensure convergence of the integral. An obvious choice is to set all but one of them equal to zero. Examples of this are first and second order Tikhonov regularization as proposed by Hess et al. [4] ($t_1 = t \in \mathbb{R}^+$, remaining ones zero), and Descoteaux et al. [2,3] ($t_2 = t \in \mathbb{R}^+$, remaining ones zero). The resulting Euler-Lagrange equations are finite-order PDEs, and are easily

---

[1] Index summation applies to pairs of identical upper and lower indices.

solved relative to the basis of spherical harmonics, using conventional spherical coordinates, Eq. (2), by virtue of the property

$$\Delta_\Omega Y_\ell^m(\theta,\phi) = -\ell(\ell+1) Y_\ell^m(\theta,\phi)\,, \tag{4}$$

in which $\Delta_\Omega = D_\mu D^\mu$ is the Laplace-Beltrami operator on the unit sphere Ω, and Y_ℓ^m denote the spherical harmonics[2]

$$Y_\ell^m(\theta,\phi) = \sqrt{\frac{(2\ell+1)(\ell-m)!}{4\pi(\ell+m)!}}\, e^{im\phi}\, P_\ell^m(\cos\theta)\,, \tag{5}$$

with P_ℓ^m the associated Legendre polynomials:

$$P_\ell^m(z) = \frac{(-1)^m}{2^\ell \ell!} \left(1-z^2\right)^{\frac{m}{2}} \frac{d^{\ell+m}}{dz^{\ell+m}} \left(z^2-1\right)^\ell \quad (\text{with } -1 \le z \le 1)\,. \tag{6}$$

With the help of polar coordinates and spherical harmonics, setting

$$S(\theta,\phi) = \sum_{\ell,m}^{*} c_{\ell m}(0)\, Y_\ell^m(\theta,\phi)\,, \tag{7}$$

in which the asterisk indicates summation over the effective indices $\ell \in \mathbb{Z}_0^+$, $m \in \{-\ell, -\ell+1, \ldots, \ell-1, \ell\}$, and

$$c_{\ell m}(0) = \int_0^{2\pi} \int_0^{\pi} S(\theta,\phi)\, Y_\ell^{-m}(\theta,\phi)\, \sin\theta d\theta d\phi\,, \tag{8}$$

minimizers of Eq. (3) can generically be written as

$$S_T(\theta,\phi) = \sum_{\ell,m}^{*} c_{\ell m}(T)\, Y_\ell^m(\theta,\phi)\,. \tag{9}$$

In the first order Tikhonov regularization scheme by Hess et al. [4] we have, using a self-explanatory change of function prototype for the coefficients,

$$c_{\ell m}(t) = \frac{c_{\ell m}(0)}{1 + t\,\ell(\ell+1)}\,. \tag{10}$$

In the second order scheme by Descoteaux et al. [2, 3] we have

$$c_{\ell m}(t) = \frac{c_{\ell m}(0)}{1 + t\,\ell^2(\ell+1)^2}\,, \tag{11}$$

and so forth. Another scheme that leads to convergence of Eq. (3) is obtained by taking

$$t_k = \frac{t^k}{k!}\,, \tag{12}$$

---

[2] Cf. functions.wolfram.com for further properties of Y_ℓ^m and P_ℓ^m.

yielding the spherical scale space representation

$$c_{\ell m}(t) = e^{-t\ell(\ell+1)}\, c_{\ell m}(0)\,, \tag{13}$$

which is the analogue of the $e^{-t\|\omega\|^2}$-attenuation of frequencies of scalar images in the Euclidean plane under Gaussian blurring[3] [19]. This scheme is particularly interesting for its connection to an abelian semigroup, since one may write

$$S_t(\theta,\phi) = e^{t\Delta_\Omega}\, S(\theta,\phi)\,. \tag{14}$$

It reproduces the first order scheme by a Laplace transform over $t \in \mathbb{R}_0^+$, cf. Florack et al. [8].

We end this brief review with the remark that all one-parameter regularization schemes of the types discussed above are qualitatively similar, and identical in their asymptotics. Let us now turn to the tensor formalism.

2.3 Regularization via Higher Order Diffusion Tensor Decomposition

Instead of Eq. (7) we now consider a decomposition of raw HARDI data into "higher order diffusion tensors", recall Eq. (2),

$$S_N(x) = \sum_{k=0}^{N} \mathscr{D}^{i_1\ldots i_k}\, x_{i_1}\ldots x_{i_k} \quad \text{with } N \in \mathbb{N}\cup\{0,\infty\} \text{ and } S_\infty(x) \equiv S(x). \tag{15}$$

It should be realized that the collection of polynomials on the sphere,

$$\mathscr{B} = \bigcup_{k\in\mathbb{N}\cup\{0\}} \mathscr{B}_k \quad \text{with} \quad \mathscr{B}_k = \{x_{i_1}\ldots x_{i_k} \mid k \in \mathbb{N}\cup\{0\} \text{ fixed}\}\ , \tag{16}$$

is complete, but redundant. In fact, any order monomial of fixed parity can be obtained from a given higher order one of the same parity via contractions. There is no way to remove such redundancies from the *full* expansion, i.e. when $N = \infty$ in Eq. (15). However, if, following Özarslan and Mareci [11], one considers only the *approximation* corresponding to *finite* N, then mutual dependencies can be removed by setting all coefficients equal to zero except $\mathscr{D}^{i_1\cdots i_N}$. The resulting homogeneous polynomial can then be fitted to the raw HARDI data as described by Özarslan and Mareci [11]. One then ends up with a representation of the form

$$S_N^{\text{Ö.M.}}(x) = D^{i_1\ldots i_N}\, x_{i_1}\ldots x_{i_N} \quad \text{with } N \in \mathbb{N}\cup\{0\}, \tag{17}$$

as a generalization of the rank-2 DTI tensor. (By symmetry of the HARDI profile only even N are relevant.) By construction, this polynomial representation is equivalent to the spherical harmonic decomposition, Eqs. (7–8), if the latter is constrained to include terms of orders $\ell \leq N$ only.

---

[3] Koenderink's argument generalizes to Riemannian spaces without major difficulties.

Following the same rationale as in the context of a spherical harmonic decomposition, we would like to regularize the data representations of Eq. (15). That is, we seek corresponding regularized representations of the form[4]

$$S_N(x,t) = \sum_{k=0}^{N} \mathscr{D}^{i_1 \dots i_k}(t)\, x_{i_1} \dots x_{i_k} \quad \text{with } N \in \mathbb{N} \cup \{0, \infty\} \text{ and } S_\infty(x,t) \equiv S(x,t). \tag{18}$$

Of course, Eq. (17) *in principle* admits regularization in formally the same way:

$$S_N^{\text{Ö.M.}}(x,t) = D^{i_1 \dots i_N}(t)\, x_{i_1} \dots x_{i_N} \quad \text{with } N \in \mathbb{N} \cup \{0\}, \tag{19}$$

which is just the tensorial counterpart of Eq. (9) (for the one-parameter case, and inclusion of terms $\ell \leq N$ only). However, whereas the spherical harmonics of fixed ℓ are eigenfunctions of the Laplace-Beltrami operator $\varDelta_\varOmega$, recall Eq. (4), this is *not* the case for any of the monomials in $\mathscr{B}_k$, Eq. (16). Consequently it is a nontrivial task to establish the coefficients $D^{i_1 \dots i_N}(t)$ as a function of t in Eq. (19). Another drawback of the tensor representation in the form of Eq. (17) is that the coefficients depend on the truncation order N. Thus as soon as one alters N, *all* data information (as far as captured by the available degrees of freedom) will have to migrate to new tensor coefficients of corresponding rank.

In the formulation of our *Ansatz*, Eq. (15), we anticipate that only *residual* information is encoded in the higher order part of the heterogeneous polynomial, i.e. additional structure that cannot be revealed by a lower order polynomial. In fact we will construct the coefficients $\mathscr{D}^{i_1 \dots i_k}$ such that (i) they do not depend on N, and (ii) they transform upon regularization in a way quite similar to the coefficients $c_{\ell m}(t)$ in Eqs. (10), (11), or (13), depending on one's preferred choice of regularization paradigm. We are now in a position to formulate our main results. Detailed derivations and proofs can be found elsewhere [7].

We construct the coefficients according to the following algorithm.

Algorithm 1 *Suppose we are in possession of* $\mathscr{D}^{i_1 \dots i_k}$ *for all* $k = 0, \dots, N-1$, *then minimization of the function*

$$E_N(\mathscr{D}^{j_1 \dots j_N}) = \int_\varOmega \left(S(x) - \sum_{k=0}^{N} \mathscr{D}^{i_1 \dots i_k} x_{i_1} \dots x_{i_k} \right)^2 d\varOmega\,,$$

yields the following linear systems:

$$\varGamma_{i_1 \dots i_N j_1 \dots j_N} \mathscr{D}^{j_1 \dots j_N} = \int_\varOmega S(x)\, x_{i_1} \dots x_{i_N}\, d\varOmega - \sum_{k=0}^{N-1} \varGamma_{i_1 \dots i_N j_1 \dots j_k} \mathscr{D}^{j_1 \dots j_k}\,,$$

with symmetric covariant tensor coefficients $\varGamma_{i_1 \dots i_k} = \int_\varOmega x_{i_1} \dots x_{i_k}\, d\varOmega$.

---

[4] We henceforth restrict our attention to the scheme of Eqs. (12–13), but the other one-parameter schemes discussed can be handled in a similar fashion.

The appearance of the second inhomogeneous term on the r.h.s. of the linear systems, absent in the scheme proposed by Özarslan and Mareci, reflects the fact that in our scheme higher order coefficients encode residual information only. The last integral is the tensorial counterpart of a well-known closed-form multi-index representation, cf. Folland [20] and Johnston [21], viz.:

$$\int_{\Omega} x_1^{\alpha_1} \dots x_n^{\alpha_n} \, d\Omega = \frac{2}{\Gamma(\frac{1}{2}|\alpha| + \frac{n}{2})} \prod_{i=1}^{n} \Gamma(\frac{1}{2}\alpha_i + \frac{1}{2}) \,, \tag{20}$$

if all α_j are even (otherwise the integral vanishes). Here $|\alpha| = \alpha_1 + \dots + \alpha_n$ denotes the norm of the multi-index, and

$$\Gamma(t) = \int_0^{\infty} s^{t-1} \, e^{-s} \, ds = 2 \int_0^{\infty} r^{2t-1} \, e^{-r^2} \, dr \tag{21}$$

is the gamma function. Recall $\Gamma(\ell) = (\ell - 1)!$ and $\Gamma(\ell + \frac{1}{2}) = (\ell - \frac{1}{2}) \, \dots \, \frac{1}{2} \sqrt{\pi} = (2\ell)! \sqrt{\pi}/(4^{\ell} \, \ell!)$ for $\ell \in \mathbb{N} \cup \{0\}$. A translation from multi-index to tensor-index notation provides us with the closed-form of $\Gamma_{i_1 \dots i_k}$:

Result 1 *Cf. Algorithm 1 and Eqs. (20–21). In* n *dimensions* $\Gamma_{i_1 \dots i_{2k+1}} = 0$*, and*

$$\Gamma_{i_1 \dots i_{2k}} = \frac{2 \, \Gamma(k + \frac{1}{2}) \Gamma(\frac{1}{2})^{n-1}}{\Gamma(k + \frac{n}{2})} \, \eta_{(i_1 i_2} \dots \eta_{i_{2k-1} i_{2k})} \,.$$

Parentheses denote complete symmetrization of indices. For $n = 3$ *we obtain*

$$\Gamma_{i_1 \dots i_{2k}} = \frac{2\pi}{k + \frac{1}{2}} \, \eta_{(i_1 i_2} \dots \eta_{i_{2k-1} i_{2k})} \,.$$

Some examples ($n = 3$):

$$\Gamma = 4\pi \,, \quad \Gamma_{ij} = \frac{4\pi}{3} \, \eta_{ij} \,, \quad \Gamma_{ijk\ell} = \frac{4\pi}{15} \, (\eta_{ij} \, \eta_{k\ell} + \eta_{ik} \, \eta_{j\ell} + \eta_{i\ell} \, \eta_{jk}) \,. \tag{22}$$

It is straightforward to sequentially solve the linear systems in Algorithm 1. It follows that the scalar $\mathscr{D}$ is just the average value over the unit sphere:

$$\mathscr{D} = \frac{\int_{\Omega} S(x) \, d\Omega}{\int_{\Omega} d\Omega} \,. \tag{23}$$

The constant vector $\mathscr{D}^i$ vanishes identically, as it should. For the rank-2 tensor coefficients we find the *traceless* matrix

$$\mathscr{D}_{ij} = \frac{15 \int_{\Omega} S(x) \, x_i \, x_j \, d\Omega - 5 \int_{\Omega} S(x) \, d\Omega \, \eta_{ij}}{2 \int_{\Omega} d\Omega} \,, \tag{24}$$

and so forth. If, instead, we fit a homogeneous second order polynomial to the data (by formally omitting the second term on the r.h.s. of the linear systems in Algorithm 1), as proposed by Özarslan and Mareci, we obtain the following rank-2 tensor coefficients:

$$D_{ij}^{\text{Ö.M.}} = \frac{15 \int_\Omega S(x)\, x_i\, x_j\, d\Omega - 3 \int_\Omega S(x)\, dx\, \eta_{ij}}{2 \int_\Omega d\Omega}\,, \tag{25}$$

which is clearly different. However, Özarslan and Mareci's homogeneous expansion should be compared to our heterogeneous expansion. Indeed, if we compare the respective second order expansions in this way we observe that $S_2^{\text{Ö.M.}}(x) = S_2(x)$. The difference in coefficients, in this example, is explained by the contribution already contained in the lowest order term of our polynomial, which in Özarslan and Mareci's scheme has migrated to the second order tensor. In fact equality holds for any order N:

Theorem 1 *Recall Eqs. (15) and (17). We have* $S_N^{\text{Ö.M.}}(x) = S_N(x)$*.*

The following theorem shows in which precise sense our new expansion can be called "canonical".

Theorem 2 *If* Δ_Ω *denotes the Laplace-Beltrami operator on the unit sphere, then for any* $N \in \mathbb{N} \cup \{0, \infty\}$*,*

$$S_N(x,t) \equiv e^{t\Delta_\Omega}\, S_N(x) = \sum_{k=0}^{N} \mathscr{D}^{i_1 \ldots i_k}(t)\, x_{i_1} \ldots x_{i_k}\,,$$

with $\mathscr{D}^{i_1 \ldots i_k}(t) = e^{-k(k+1)t}\, \mathscr{D}^{i_1 \ldots i_k}$*.*

The proof of Theorems 1–2 is presented elsewhere [7].

It seems somewhat miraculous that the t-scaling behaviour of the coefficients in Theorem 2 is identical to that in the spherical harmonic decomposition, Eq. (13). This is quite nontrivial, since the monomials $x_{i_1} \ldots x_{i_k}$ are themselves not eigenfunctions of the Laplace-Beltrami operator. In fact, what happened is that, by considering the *specific* linear combinations $\mathscr{D}^{i_1 \ldots i_k}(t)\, x_{i_1} \ldots x_{i_k}$ according to the recipe of Algorithm 1, we have effectively disposed of the degrees of freedom in the monomials $x_{i_1} \ldots x_{i_k}$ that live in eigenspaces spanned by the spherical harmonics Y_ℓ^m of orders $\ell < k$. The span of the resulting homogeneous polynomials coincides with the degenerate eigenspace of the k-th order spherical harmonics, $\text{span}\,\{Y_k^m \,|\, m \in \{-k, -k+1, \ldots, k-1, k\}\;,\; k \in \mathbb{N} \cup \{0\} \text{ fixed}\}$.

Heuristically, the significance of Theorem 2 is that it segregates degrees of freedom in the polynomial expansion in such a way that we may interpret each homogeneous higher order term as an incremental refinement of detail relative to that of the lower order expansion. The linear combinations $\mathscr{D}^{i_1 \ldots i_k}\, x_{i_1} \ldots x_{i_k}$, unlike the monomials $x_{i_1} \ldots x_{i_k}$ themselves, apparently constitute *self-similar* *polynomials on the sphere* under the act of blurring by the regularization operator $\exp(t\Delta_\Omega)$, recall Eq. (14), or any of the other bounded one-parameter regularization operators previously reviewed, which are all of the form $f(t\Delta_\Omega)$ for suitably defined analytical function f. The parameter t determines the angular resolution of the regularized data.

As a final observation we note that the classical rank-2 DTI representation, defined via the Stejskal-Tanner formula [11, 22]:

$$\Sigma(x) = \Sigma_0 \exp\left(-bS(x)\right) , \tag{26}$$

arises not merely as an approximation under the assumption that the diffusion attenuation can be written as

$$S(x) \approx S_{\mathrm{DTI}}(x) = D^{ij}_{\mathrm{DTI}}\, x_i\, x_j , \tag{27}$$

but, according to Theorem 2, expresses the *exact* asymptotic behaviour of $S(x,t)$ as $t \to \infty$:

$$S(x,t) = \underbrace{\left(\mathscr{D}\,\eta^{ij} + e^{-6t}\,\mathscr{D}^{ij}\right)\, x_i\, x_j}_{S_{\mathrm{DTI}}(x,t)\, =\, D^{ij}_{\mathrm{DTI}}(t)\, x_i\, x_j} + \mathcal{O}(e^{-20t}) \quad (t \to \infty) . \tag{28}$$

This example shows that the higher order tensors constructed by Özarslan and Mareci in general, and the classical DTI tensor in particular, are not self-similar, but have a multimodal (respectively bimodal) resolution dependence, i.e. they contain multiple self-similar terms with different scaling behaviour under regularization. The actual limit of vanishing resolution is of course given by a complete averaging over the sphere, recall Eq. (23), noting that $\eta^{ij}\, x_i\, x_j = 1$ on Ω:

$$\lim_{t\to\infty} S(x,t) = \lim_{t\to\infty} S_{\mathrm{DTI}}(x,t) = \mathscr{D} . \tag{29}$$

See Figs. 1–2 for an illustration of Theorem 2 for $N = 8$ on a synthetic image.

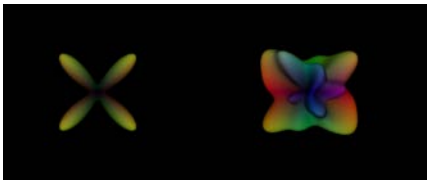

Fig. 1. Left: Synthetic noise-free profile induced by two crossing fibers at right angle. Right: Same, but with Rician noise.

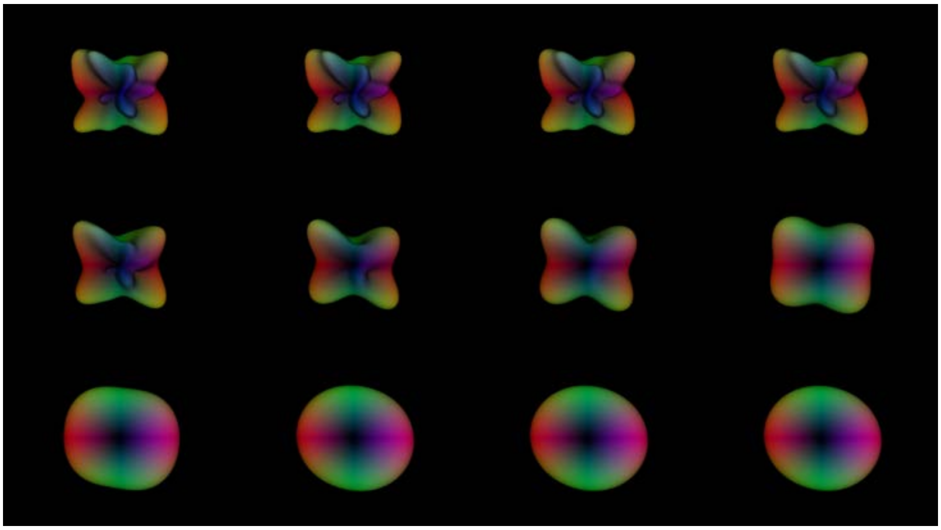

Fig. 2. Regularized profiles produced from the right image in Fig. 1 using Theorem 2 for $N = 8$. The regularization parameter t increases exponentially from top left to bottom right over the range 0.007–1.0. For low t-values spurious peaks prevent correct detection of underlying fiber orientations. Peaks are gradually removed as t increases. In the range $t \in [0.05, 0.15]$ we find two nearly correct peak locations intersecting at a stable angle of $82.5^\circ \pm 0.8^\circ$. For larger t overregularization sets in as we enter the classical DTI regime, which is incapable of unconfounding crossing fibers.

3 Summary and Conclusion

We have considered two alternative representations for scalar functions on the sphere in the context of high angular resolution diffusion imaging (HARDI). One employs spherical harmonics, the second "higher order diffusion tensors".

The spherical harmonic representation is ideally suited for the application of various Tikhonov regularization schemes, associated with operators of the form $f(t\Delta_\Omega)$, in which Δ_Ω is the Laplace-Beltrami operator on the sphere Ω, and f a suitably defined analytical function. This is a result of the fact that the spherical harmonics have a natural arrangement into orthogonal subsets of degenerate eigenfunctions of this operator, such that the closure of the direct sum of these subsets makes up $L_2(\Omega)$. This representation thus provides a natural ("canonical") framework for regularization.

If one wishes to employ a tensorial representation (or polynomials on the unit sphere), regularization becomes in general a highly nontrivial matter if one declines from an explicit projection onto the spherical harmonic basis. We have argued that the homogeneous tensorial representation proposed in their seminal paper by Özarslan and Mareci [11] is inconvenient in this respect. We have operationally constructed an alternative, heterogeneous tensorial representation, which does mimic the "canonical" behaviour of the spherical harmonics.

Although all representations—spherical harmonics, higher order diffusion tensors by Özarslan and Mareci, and our newly constructed ones—are equivalent, there may be good reasons for preferring or excluding a particular one, as we have demonstrated in the context of regularization. A case where tensors may be preferred over spherical harmonics is in generalizing the differential geometric rationale for tractography and connectivity analysis via geodesics and geodesic congruences (Hamilton-Jacobi framework). For instance, it is most straightforward to construct a Finsler metric using a higher order diffusion tensor description, as a generalization of the DTI induced Riemannian metric, cf. Melonakos et al. [23].

In any case, regularization is an important procedure in HARDI, and so it is quite convenient to be able to carry it out irrespective of one's preferred paradigm. It remains an open question how to combine codomain regularization, as proposed here, with regularization in the spatial domain, cf. [24] in the context of DTI.

Acknowledgments. We thank Vesna Prckovska for conducting the experiments that have led to Figs. 1–2. The Netherlands Organisation for Scientific Research (NWO) is gratefully acknowledged for financial support.

References

1. Alexander, A.L., Lee, J.E., Lazar, M., Field, A.S.: Diffusion tensor imaging of the brain. Neurotherapeutics: The Journal of the American Society for Experimental NeuroTherapeutics **4**(3) (July 2007) 316–329
2. Descoteaux, M., Angelino, E., Fitzgibbons, S., Deriche, R.: Regularized, fast, and robust analytical Q-ball imaging. Magnetic Resonance in Medicine **58**(3) (2007) 497–510
3. Descoteaux, M., Angelino, E., Fitzgibbons, S., Deriche, R.: Apparent diffusion coefficients from high angular resolution diffusion imaging: Estimation and applications. Magnetic Resonance in Medicine **56**(2) (2006) 395–410
4. Hess, C.P., Mukherjee, P., Tan, E.T., Xu, D., Vigneron, D.B.: Q-ball reconstruction of multimodal fiber orientations using the spherical harmonic basis. Magnetic Resonance in Medicine **56** (2006) 104–117
5. Pennec, X., Fillard, P., Ayache, N.: A Riemannian framework for tensor computing. International Journal of Computer Vision **66**(1) (January 2006) 41–66
6. Tikhonov, A., Arseninn, V.Y.: Solution of Ill-Posed Problems. John Wiley & Sons, New York (1977)
7. Florack, L., Balmashnova, E.: Decomposition of high angular resolution diffusion images into a sum of self-similar polynomials on the sphere. In Bayakovsky, Y., Moiseev, E., eds.: Proceedings of the Eighteenth International Conference on Computer Graphics and Vision, GraphiCon'2008, Moscow, Russia, June 23–27, 2008, Moscow State University (2008) 26–31 (invited paper).

8. Florack, L.M.J.: Codomain scale space and regularization for high angular resolution diffusion imaging. [25] Digital proceedings.
9. Frank, L.R.: Characterization of anisotropy in high angular resolution diffusion-weighted MRI. Magnetic Resonance in Medicine **47**(6) (2002) 1083–1099
10. Alexander, D.C., Barker, G.J., Arridge, S.R.: Detection and modeling of non-Gaussian apparent diffusion coefficient profiles in human brain data. Magnetic Resonance in Medicine **48**(2) (2002) 331–340
11. Özarslan, E., Mareci, T.H.: Generalized diffusion tensor imaging and analytical relationships between diffusion tensor imaging and high angular resolution imaging. Magnetic Resonance in Medicine **50** (2003) 955–965
12. Basser, P.J., Mattiello, J., Le Bihan, D.: Estimation of the effective self-diffusion tensor from the NMR spin echo. Journal of Magnetic Resonance **103** (1994) 247–254
13. Basser, P.J., Mattiello, J., Le Bihan, D.: MR diffusion tensor spectroscopy and imaging. Biophysics Journal **66**(1) (1994) 259–267
14. Le Bihan, D., Mangin, J.F., Poupon, C., Clark, C.A., Pappata, S., Molko, N., Chabriat, H.: Diffusion tensor imaging: Concepts and applications. Journal of Magnetic Resonance Imaging **13** (2001) 534–546
15. Tuch, D.S.: Q-ball imaging. Magnetic Resonance in Medicine **52** (2004) 1358–1372
16. Özarslan, E., Shepherd, T.M., Vemuri, B.C., Blackband, S.J., Mareci, T.H.: Resolution of complex tissue microarchitecture using the diffusion orientation transform (DOT). NeuroImage **31** (2006) 1086–1103
17. Jian, B., Vemuri, B.C., Özarslan, E., Carney, P.R., Mareci, T.H.: A novel tensor distribution model for the diffusion-weighted MR signal. NeuroImage **37** (2007) 164–176
18. Spivak, M.: Differential Geometry. Volume 1–5. Publish or Perish, Berkeley (1975)
19. Koenderink, J.J.: The structure of images. Biological Cybernetics **50** (1984) 363–370
20. Folland, G.B.: How to integrate a polynomial over a sphere. The American Mathematical Monthly **108**(5) (May 2001) 446–448
21. Johnston, T.W.: Cartesian tensor scalar product and spherical harmonic expansions in Boltzmann's equation. Physical Review **120** (1960) 1103–1111
22. Stejskal, E.O., Tanner, J.E.: Spin diffusion measurements: Spin echoes in the presence of a time-dependent field gradient. Journal of Computational Physics **42** (1965) 288–292
23. Melonakos, J., Pichon, E., Angenent, S., Tannenbaum, A.: Finsler active contours. IEEE Transactions on Pattern Analysis and Machine Intelligence **30**(3) (2008) 412–423
24. Florack, L.M.J., Astola, L.J.: A multi-resolution framework for diffusion tensor images. [25] Digital proceedings.
25. Aja Fernández, S., de Luis Garcia, R., eds.: CVPR Workshop on Tensors in Image Processing and Computer Vision, Anchorage, Alaska, USA, June 24–26, 2008. In Aja Fernández, S., de Luis Garcia, R., eds.: CVPR Workshop on Tensors in Image Processing and Computer Vision, Anchorage, Alaska, USA, June 24–26, 2008, IEEE (2008) Digital proceedings.

A Study of Information Gain in High Angular Resolution Diffusion Imaging (HARDI)

A.D. Leow[1,3], S. Zhu[2], L. Zhan[3], K. McMahon[4], G.I. de Zubicaray[4], M. Meredith[4], M. Wright[4], P.M. Thompson[3]

[1] Neuropsychiatric Institute, UCLA
[2] Department of Mathematics, UCLA
[3] Laboratory of Neuroimaging (LONI), UCLA
[4] Functional MRI Laboratory, University of Queensland and Queensland Institute of Medical Research, Brisbane, Australia

Abstract. Diffusion weighted magnetic resonance (MR) imaging is a powerful tool to investigate white matter microstructure, by mapping local 3D displacement profiles of water molecules in brain tissue. High-angular resolution diffusion imaging (HARDI) schemes have been employed to resolve fiber crossing and more complex diffusion geometries. Most recently, the tensor distribution function (TDF) has been proposed as a novel technique for multi-tensor reconstruction by representing the diffusion profile as a probabilistic mixture of tensors. Here, we propose a TDF-based framework for studying the amount of information in HARDI. To illustrate the proposed method, we compared a 94-direction HARDI scheme to its optimally sub-sampled schemes with 20, 40, 60 and 80 directions. We quantified the information gain when more gradient directions are used, as measured by the Shannon entropy of the recovered TDF. Our results showed an absence of significant gain beyond 60 directions, while anisotropy estimates of the recovered fibers stabilized with around 40 directions, suggesting asymptotic but clear advantages of HARDI over conventional DTI.

1 Introduction

In the past decade, diffusion magnetic resonance imaging (MRI) has become a powerful tool for studying the structure of fibrous materials. By applying diffusion-sensitized magnetic field gradients, diffusion MRI characterizes the water diffusivity profile in various tissues. When the duration of the applied diffusion sensitization δ is much smaller than the time between the two pulses, the MR signal attenuation is related to the displacement probability function using a Fourier integral relationship with respect to a wave vector q [1].

In brain imaging, diffusion MRI is particularly advantageous over conventional non diffusion-weighted MRI as it can reveal the configuration and orientation of fiber tracts in white matter. Diffusion Tensor MRI (DT-MRI), proposed in [2], models the water displacement probability function using a zero-mean 3D Gaussian distribution whose covariance matrix, a second-order positive-definite symmetric tensor, represents the principal directions of diffusion and orientation of local fiber tracts. Although extremely powerful and easy to compute, DT-MRI has some disadvantages. For example, any Gaussian probability distribution function has at most one orientational mode (principal direction), and thus cannot resolve fiber crossing, or more complex diffusion geometries.

More recently, several different approaches have been developed to address this issue, involving sets of diffusion gradients with high angular resolution, and by sampling the q-space on one or more shells with fixed radii. Methods such as the Persistent Angular Structure (PAS) technique [3], spherical deconvolution techniques [4], and the q-ball imaging technique [5] have been proposed to recover partial information on the displacement probability function, while still allowing underlying fiber orientations to be inferred.

If more angular detail is available, fiber orientation distribution functions (ODFs) can be reconstructed from the raw HARDI signal using deconvolution methods, yielding mathematically rich models of fiber geometries using fields of von Mises-Fisher mixtures [6], or higher-order tensors (e.g., 3x3x3 tensors) [7]). Recent fluid registration and stochastic tractography methods have also exploited HARDIs increased angular detail, aligning ODFs using specialized metrics on densities (e.g., Fisher-Rao) from information theory [8].

The tensor distribution function (TDF), which we first proposed in [9], offers a new way to resolve intra-voxel fiber crossing by solving for a probability distribution, defined on the tensor manifold, that optimally reconstructs the observed diffusion-weighted images (also see [10] where a continuous mixture using Wishart distributions was first introduced to model HARDI data). Moreover, the TDF approach also provides a novel way to compute the eigenvalues of each individual crossing fiber (for more details, please refer to the Theory section).

In this paper, we use the TDF concept and compare the information content of HARDI acquisition schemes with 20, 40, 60, 80, and 94 directions. The 94-direction scheme is currently used as a standard protocol in our lab, while the rest of the acquisition schemes are generated by optimally sub-sampling this 94-direction scheme as described in [11].

2 Theory

2.1 The tensor distribution function

In standard diffusion-weighted MRI, images are acquired using the Stejskal-Tanner pulsed gradient spin-echo method. With some simplifications (rectangular pulse profiles), measured image intensities S are linked to p, the displacement probability function of water molecules, via a Fourier transform relationship: $S(q) = S(0) \int p(x) \exp(iq \cdot x) dx$ (here, the wavenumber $q = r\delta G$; r, δ, and G are the gyromagnetic ratio, the duration of the diffusion sensitization, and the applied magnetic gradient vector). Without loss of generality, we assume the constant S(0) is 1.

Assuming a simple one-tensor Gaussian diffusion model, the displacement probability function evaluated at position x (given diffusion tensor D, and diffusion time t) is

$$p(x) = ((4\pi t)^3 \det(D))^{-\frac{1}{2}} \exp\Big(- \frac{x^t D^{-1} x}{4t} \Big) \tag{1}$$

Thus, the measured diffusion MR image intensities in this one-tensor case are simply $S(q) = \exp(-tq^t Dq)$. In the TDF approach, a probability density function P defined on $\mathbb{D}$, the space of symmetric positive definite 3-by-3 matrices, is computed to explain the observed data:

$$S(q) = \int_{D \in \mathbb{D}} P(D) \exp\Big(- tq^t Dq \Big) dD \tag{2}$$

To solve for an optimal TDF P^*, the least-squares principle is used

$$P^* = \text{argmin}_P \sum_i \Big(S_{obs}(q_i) - S_{calculated}(q_i) \Big)^2 \tag{3}$$

Here, different gradient directions are indexed by i. The numerical solution as proposed in [9] is obtained from the following gradient descent equation:

$$\frac{dR}{d\tau}(D) = \sum_i E(q_i) \exp(R(D)) F(D, q_i) + L \exp(R(D)) \tag{4}$$

where the Lagrange multiplier L is

$$L = - \frac{\int_{D \in \mathbb{D}} \exp(R(D)) \sum_i E(q_i) \exp(R(D)) F(D, q_i) dD}{\int_{D \in \mathbb{D}} \exp(R(D))^2 dD}$$

Here, $P(D) = \exp(R(D))$, $E(q_i) = S_{obs}(q_i) - S_{calculated}(q_i)$, τ is an artificial time, and $F(D, q_i) = \exp\big(- tq_i^t Dq_i \big)$. To reduce the dimensionality of the TDF model, every tensor D is assumed to be cylindrical, and thus may be expressed using $D(\lambda, \theta)$, where the eigenvalues $\lambda = (\lambda_1, \lambda_2)$ (with λ_2 the repeated eigenvalue), and $\theta = (\theta_1, \theta_2)$ the azimuthal and polar angles associated with λ_1. The dominant fiber directions can then be determined by examining the local maxima (that exceed a certain threshold, set to 0.2 in this paper) of the Tensor Orientation Distribution Function (TOD). In the case of one dominant fiber direction, we have:

$$\theta^* = argmax_\theta \text{TOD}(\theta) = argmax_\theta \int_\lambda P(D(\lambda, \theta)) d\lambda \tag{5}$$

Once the dominant direction is determined, one can estimate the eigenvalues of dominant fibers (λ^*) by computing the expected values of λ along this direction.

$$\lambda^* = \frac{\int P(D(\lambda, \theta^*)) \lambda d\lambda}{\int P(D(\lambda, \theta^*)) d\lambda} \tag{6}$$

Notice that Eq. (6) offers advantages over deconvolution methods, in which eigenvalues for a single fiber tract are usually pre-determined and fixed. Lastly, we can also compute the orientation distribution function (ODF) from the TDF by analytically evaluating the following radial integral:

$$ODF(\tilde{x}) = C \int_{r=0}^{\infty} p(r\tilde{x})dr$$

$$= C \int_{D\in\mathbb{D}} P(D)\Big(\det(D)\tilde{x}^t D^{-1}\tilde{x}\Big)^{-\frac{1}{2}} dD \tag{7}$$

Here C is a normalizing constant.

2.2 Shannon entropy as a measure of information and the exponential isotropy

Given any TDF P, we observe that its Shannon entropy (H) measures the randomness of this probabilistic ensemble, and thus inversely measures how certainly we can estimate dominant fibers.

$$\mathrm{H}(P(D)) = -\int_{D\in\mathbb{D}} P(D)logP(D)dD \tag{8}$$

Thus, we propose that the amount of information can be measured by the negative of H. Moreover, by taking the exponential of H, we may define the exponential isotropy (EI), which quantifies the overall isotropy of any given voxel.

$$\mathrm{EI}(P(D)) = e^{-\int_{D\in\mathbb{D}} P(D)logP(D)dD} \tag{9}$$

To motivate the concept of EI, we observe that in an ideal one-fiber system (i.e., P(D)=0 everywhere except for one point in the tensor space $\mathbb{D}$), the Shannon entropy is 0 and the EI is 1. For an ideal two-fiber system with equal weights (P(D)=0 everywhere except for two points in the tensor space $\mathbb{D}$, each of which takes a value of 0.5), the Shannon entropy is $ln2$ and the EI is 2. Thus, in general, we expect EI to take a value that is proportional to the number of dominant fibers. As indicated by its name (and opposite to the fractional anisotropy (FA) or the generalized FA (GFA)), the EI is a measure of isotropy instead of anisotropy, and thus takes greater values in gray matter tissue than white matter. As will be shown in the results section, EI is the equivalent of FA or GFA in the TDF framework.

3 Results

In this section, we present experimental results to illustrate the proposed framework for measuring information gain in HARDI. An individual subject was scanned using a diffusion-sensitized gradient protocol on a Bruker Medspec 4

Tesla MRI scanner, with a transverse electromagnetic (TEM) headcoil. The timing of the diffusion sequence was optimized for SNR according to the scheme proposed in [12].

The protocol used 94 diffusion-sensitized gradient directions, and 11 baseline scans with no diffusion sensitization (b-value: 1159 s/mm^2; TE/TR: 92.3/8250 msec; FOV=230x230; in-plane resolution: 1.8mmx1.8mm; 55 x 2mm contiguous slices; acquisition time 14.5 minutes). The area shown in the left panel of Fig. 1, which mainly consists of white matter, was chosen for comparison (the GFA and EI plots of this windowed region are shown in the middle and right panels of Fig. 1). Visually, we notice that the EI plot nicely separates gray matter from white matter, and thus may be useful for tissue segmentation or tractography purposes. The full 94 gradient directions were optimally sub-sampled, as in [11], to determine subsets of 20, 40, 60, and 80 gradient directions. The TDF was computed voxel-wise by using the full 94-direction HARDI and the four sub-sampled schemes. For each voxel, we then computed the TOD, ODF, GFA, and EI of its TDF. To correctly identify dominant fibers and estimate their eigenvalues using Eq. 6, both voxel-wise GFA and TOD peaks are thresholded at a value of 0.2.

Fig. 2 shows, for each scheme, the voxel-wise TOD, ODF, GFA, and EI plots. Here, GFA plots are scaled relative to their contrast. Visually, 60, 80, and 94 directions yield very similar results. Statistics of the estimated eigenvalues and the Shannon entropy are summarized in Table 1. We found that there is an overall increase in λ_1, and a decrease of entropy (i.e., information gain) as the number of gradient directions increases. This is consistent with prior reports [13] that diffusion anisotropy may be underestimated when angular sampling is low, and eigenvalue estimates may be biased. The trend for λ_2 is less clear, although both estimated λ_1 and λ_2 values are consistent with those reported in the literature.

To formally test if these trends are statistically significant, paired t-tests, with respect to the full 94-direction HARDI, were conducted on the estimated eigenvalues λ_1, λ_2, and the Shannon entropy of the recovered TDF (Table 2). Notice that estimations of both eigenvalues do not change significantly beyond 40 directions, while entropy continues to decrease until around 80 directions. Even so, the effect size for entropy decrease or information gain from 60 directions to 94 directions, using Cohen's d, is 0.17, indicating that this statistically significant information gain is of less practical value (the usual cut-off point for a significant effect size using Cohen's d is 0.2).

4 Conclusion

In this paper, we introduced a tensor distribution function-based framework and its mathematical formulations for assessing the amount of information in high angular resolution diffusion imaging. We also proposed the exponential isotropy as a natural measure of isotropy (i.e, inverse measure of anisotropy). In the TDF framework, the exponential isotropy replaces GFA or FA. Borrowing ideas from

Table 1. Means and standard deviations for estimated eigenvalues of dominant fibers (λ_1, λ_2) and for the mean Shannon entropy of the TDF, for the white matter voxels highlighted in Fig. 1, from the four subsampled and full 94-direction HARDI. The FA values computed using these mean eigenvalues are also given.

	20	40	60	80	94
λ_1	1.061 (0.324)	1.049 (0.431)	1.142 (0.435)	1.154 (0.438)	1.169 (0.449)
λ_2	0.308 (0.145)	0.269 (0.155)	0.243 (0.118)	0.255 (0.156)	0.246 (0.122)
FA	0.6565	0.6990	0.7538	0.7436	0.7568
Entropy	6.884 (0.624)	6.070 (1.005)	5.794 (1.056)	5.734 (1.036)	5.743 (1.011)

Table 2. Paired t-tests, with respect to the full 94-direction HARDI, for estimated eigenvalues of dominant fibers (λ_1, λ_2), and the Shannon entropy of the TDF (with n degrees of freedom). The numbers shown in the table are Student's T statistics. Those with a significant p value less than 0.05 are in bold. Notice that eigenvalues do not change significantly beyond 40 directions, while entropy continues to decrease until around 80 directions (however, the effect size for entropy improvement or information gain from 60 directions to 94 directions, using Cohen's d, is 0.17, indicating that this statistically significant information gain may have less practical value.

	20	40	60	80	n
λ_1	**-3.32**	**-3.95**	-0.92	-0.62	255
λ_2	**5.31**	**2.18**	-0.30	1.04	255
Entropy	**26.13**	**14.76**	**2.61**	-0.52	244

probability and information theory, we argued that the ability to accurately estimate dominant fiber eigenvalues and their orientations, as well as to resolve fiber crossing, can be measured by computing and comparing the randomness or Shannon entropy in the corresponding tensor distribution function. In other words, one would expect that, ideally, randomness in the TDF should decrease as the number of gradient directions increases in HARDI acquisition schemes. However, due to the presence of noise and other problems in acquiring HARDI (e.g., motion artifacts), it is likely that the amount of additional information would become negligible once a certain number of gradient directions is reached. This hypothesis is supported by our results, where we demonstrated that the information contained in HARDI is not linearly correlated with the number of gradient directions, and plateaus around 60 to 80 gradient directions in our simulation studies using the 94-direction protocol currently employed in our lab. This finding is also supported by comparing the expected values of eigenvalues along dominant fiber directions. Even so, the issue of whether greater numbers of gradients may still be beneficial for tractography applications (which rely heavily on the orientational information in the ODFs) remains unsolved. In future studies, we plan to apply this framework to systemically investigate the effect of scanner field strength, spatial resolution, and other acquisition parameters in HARDI, as well as how these may affect tractography and its related applications.

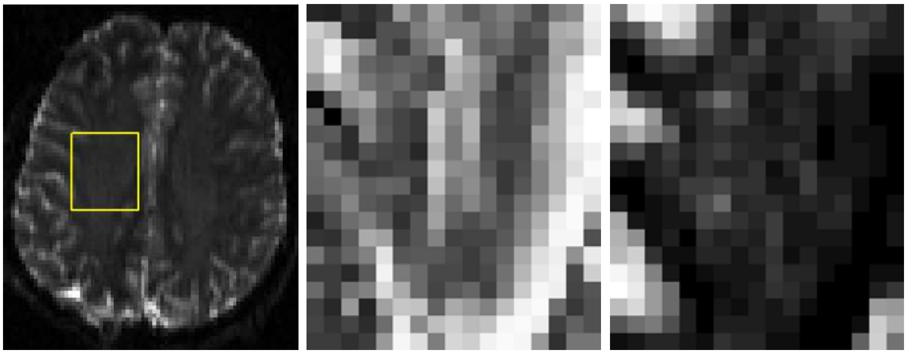

Fig. 1. This figure shows the T2 weighted MRI of a normal human subject derived from the non-difsion sensitized HARDI gradient images. The region over which the patient data was extracted is marked in yellow, with its GFA and EI plots shown in the middle and right panels respectively. Visually, we notice that the EI plot nicely separates gray matter from white matter. Unlike GFA, gray matter has greater EI values than white matter.

References

1. Stejskal, E. O. and Tanner, J. E. ”Spin diffusion measurements: spin echoes in the presence of a time-dependent field gradient.” *J. Chem. Phys.* 42, 288-292, 1965
2. Basser, P. J. ”Inferring microstructural features and the physiological state of tissues from diffusion-weighted images.” *NMR Biomed* 8, p. 333-344, 1995.
3. Kalvis M Jansons and Daniel C Alexander. ”Persistent Angular Structure: New Insights from Diffusion Magnetic Resonance Imaging Data.” *Inverse Problems* 19, p. 1031-1046, 2003.
4. J.-D. Tournier, F. Calamante, D. Gadian, and A. Connelly. ”Direct estimation of the ber orientation density function from diffusion-weighted MRI data using spherical deconvolution.” NeuroImage, 23:1176-1185, (2004)
5. David S. Tuch. ”Q-Ball Imaging.” *Magnetic Resonance in Medicine* 52, p. 1358-1372, 2004.
6. McGraw, T.; Vemuri, B. C.; Yezierski, B.; Mareci, T. ”Von Mises-Fisher mixture model of the diffusion ODF.” Biomedical Imaging: Nano to Macro, 3rd IEEE International Symposium on Biomedical Imaging: 65-68. (2006)
7. A. Barmpoutis, and B. C. Vemuri. ”Exponential Tensors: A framework for efficient higher-order DT-MRI computations.” In Proceedings of ISBI07: IEEE International Symposium on Biomedical Imaging: Page(s): 792-795. (2007)
8. Chiang MC, Barysheva M, Lee AD, Madsen SK, Klunder AD, Toga AW, McMahon KL, de Zubicaray GI, Meredith M, Wright MJ, Srivastava A, Balov N, Thompson PM. ”Mapping Genetic Influences on Brain Fiber Architecture with High Angular Resolution Diffusion Imaging (HARDI).” ISBI 2008.
9. Alex D. Leow, Siwei Zhu, Liang Zhan, Katie McMahon, Greig I. de Zubicaray, Matthew Meredith, Margaret Wright, Paul M. Thompson ”Tensor distribution function” To appear in Magnetic Resonance in Medicine

10. Bing Jian, Baba C. Vemuri, Evren Ozarslan, Paul R. Carney, and Thomas H. Mareci. ”A novel tensor distribution model for diffusion-weighted MR signal.” NeuroImage 37: 164-176. (2007)
11. Zhan L, Chiang MC, Barysheva M, Toga AW, McMahon KL, de Zubicaray GI, Meredith M, Wright MJ, Thompson PM ”How Many Gradients are Sufficient in High-Angular Resolution Diffusion Imaging (HARDI)?” 13th Annual Meeting of the Organization for Human Brain Mapping (OHBM), Melbourne, Australia, June 15-19, 2008.
12. Jones, D.K., Horsfield, M.A., Simmons, A. ”Optimal strategies for measuring diffusion in anisotropic systems by magnetic resonance imaging.” *Magn. Reson Med.* 42(3), p. 515-525, 1999.
13. B. A. Landman, J. A., S. A. Smith, S. Mori, and J. L. Prince. ”Tradeoffs between tensor orientation and anisotropy in DTI: Impact of Diffusion Weighting Scheme.” 15th ISMRM Meeting, Berlin. (2007)

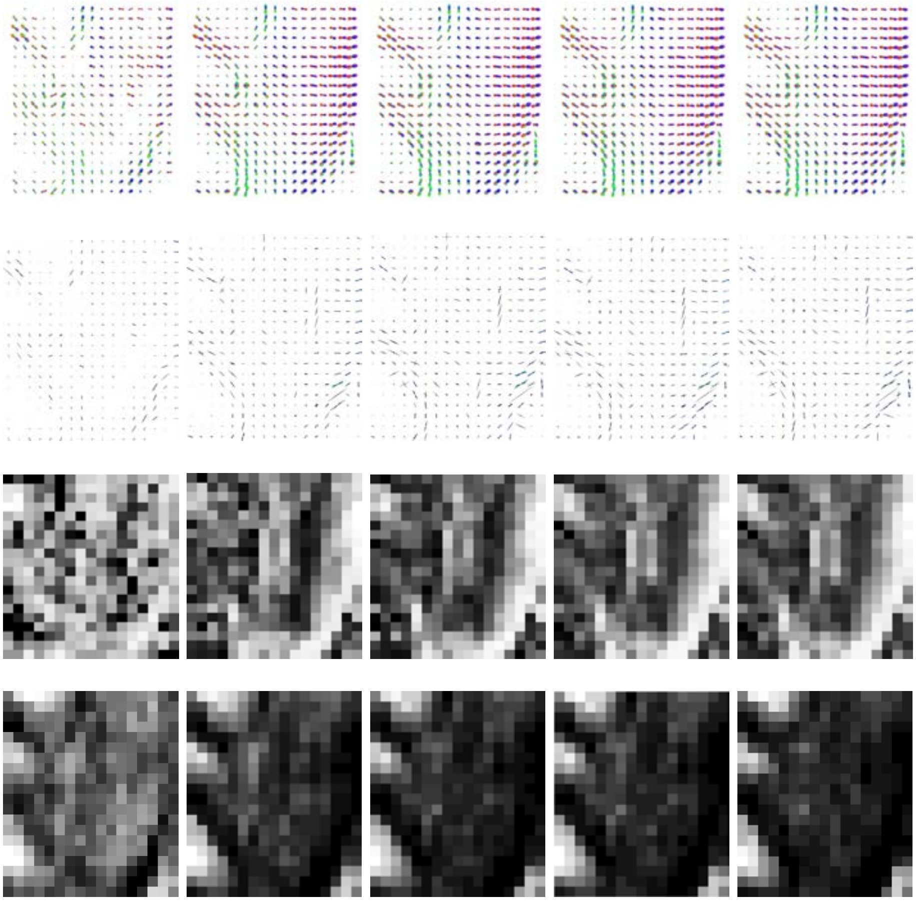

Fig. 2. Top: ODF plots for HARDI sequences with 20, 40, 60, 80, and 94 directions. Second row: respective TOD plots. Third Row: respective GFA maps. Bottom: respective EI plots. Visually, 60, 80 and 94 directions yield very similar results for all four plots.

Oral Session IV: Pre and Post Processing

Comparison of B_0 field mapping method and B-spline image registration method in EPI distortion correction in Diffusion Tensor MRI

Minjie Wu[1,2], Lin-Ching Chang[3], Lindsay Walker[1], Herve Lemaitre[4], Alan S. Barnett[4], Stefano Marenco[4], Carlo Pierpaoli[1]

[1]National Institute of Child Health and Human Development, National Institutes of Health, Bethesda, MD, USA
[2]Dept. of Bioengineering, University of Pittsburgh, Pittsburgh, PA, USA
[3]Dept. of Electrical Engineering and Computer Science, Catholic University of America, Washington, D.C., USA
[4]Clinical Brain Disorders Branch, Genes Cognition and Psychosis Program, National Institute of Mental Health Intramural Research Program, National Institutes of Health, Bethesda, MD, USA
minjiewu@gmail.com, cp1a@nih.gov

Abstract. Diffusion weighted images (DWIs) are commonly acquired with Echo-planar imaging (EPI). B_0 inhomogeneities affect EPI by producing spatially nonlinear image distortions. Several strategies have been proposed to correct EPI distortions including B_0 field mapping (B_0M) and image registration. In this study, an experimental framework is proposed to evaluation the performance of different EPI distortion correction methods in improving DT-derived quantities. A deformable registration based method with mutual information metric and cubic B-spline modeled constrained deformation field (BSP) is proposed as an alternative when B_0 mapping data are not available. BSP method is qualitatively and quantitatively compared to B_0M method using the framework. Both methods can successful reduce EPI distortions and significantly improve the quality of DT-derived quantities. Overall, B_0M was clearly superior in infratentorial regions including brainstem and cerebellum, as well as in the ventral areas of the temporal lobes while BSP was better in all rostral brain regions.

Keywords: DTI, EPI distortion, B_0 field mapping, B-spline image registration

1 Introduction

Clinical diffusion MR studies use almost exclusively single-shot echo-planar imaging (EPI) acquisitions. EPI is very sensitive to static magnetic field (B_0) inhomogeneities that produce nonlinear geometric distortion primarily along the phase-encoding direction. Artifacts are most pronounced at air-tissue interfaces and are clearly evident in the ventral portions of the frontal and temporal lobes, particularly in areas near the sphenoid sinus and the temporal petrous bone. These artifacts become more severe at higher magnetic field strengths.

Different techniques have been reported to correct geometric distortions originating from B_0 inhomogeneities in EPI images [1-4]. The field map based method is a popular method, in which the B_0 field inhomogeneity is computed from phase images acquired at different echo times [1, 4]. Another field map based method proposed by Chen and Wyrwicz utilizes the field maps derived from multi-echo gradient-echo images, which avoids complicated phase unwrapping procedures, but is computationally more demanding [2, 3]. Another method proposed by Kybic, et al [**5**] uses image registration techniques for EPI spatial distortion correction. The distorted EPI image is registered to a corresponding anatomically correct MR image with an intensity-based least-squares similarity metric and the B-spline modeled deformation field. Or log-intensity metric is used in the registration to improve the sensitivity in areas of low EPI signal [**6**].

The above EPI distortion correction methods remain virtually unused in the context of DTI, partly because there are no objective tests for establishing whether the improvement in the quality of the computed DTI data justifies the additional scan time and/or computational complexity. The main goals of this study are 1) to propose an experimental framework that would enable evaluating the performance of different EPI distortion correction methods in terms of improving the quality of DTI results; 2) to propose an image registration-based correction method as an alternative when B_0 mapping data are not available; 3) to compare the image registration-based correction method and the standard B_0 mapping correction method in their ability to improve the DT-MRI results.

2 Methods

2.1 Methodological framework for evaluating the performance of EPI distortion correction strategies

Given that EPI distortions occur in the phase encode direction, one can obtain DT-derived quantities that are differently corrupted by EPI distortions, with datasets of diffusion-weighted images (DWIs) acquired with different phase encoding directions. A simple approach to evaluate the effect of EPI distortion on DT-MRI data is to measure, on a voxel by voxel basis, the variability of DT-derived quantities from these co-registered DWI datasets. Significantly higher variability will appear in regions that are most significantly affected by EPI distortions. An effective EPI distortion method should reduce the misalignment between these DTI datasets due to different EPI distortions and lead to a reduction in the variability of the DTI quantity.

In this study, four replicate DWI datasets were acquired for each subject as shown in Fig. 1, with acquisition protocols differing only in the phase-encoding direction: along the right-left (RL) and anterior-posterior (AP) direction with either negative (-) or positive (+) sign of the phase encoding blips respectively. The positive or negative blips will result in either compression or expansion distortion of the image along the phase-encoding direction.

The local variability of DT-MRI derived quantities (for example, fractional anisotropy (FA)) was assessed by the standard deviation map (SD) of the FA maps computed from the four DWI datasets, as in equation (1)

$$SD_{FA} = std(FA_{RL+}, FA_{RL-}, FA_{AP+}, FA_{AP-}) \quad \textbf{(1)}$$

2.2 Subjects and imaging methods

Five young subjects (2 males; mean age = 35.95, range 24-48 years old) participated in this study. Written informed consent was obtained. Data were acquired on a 1.5 Tesla scanner (GE Medical Systems, Milwaukee, WI) equipped with an 8-channel RF coil. Diffusion weighted images were acquired with a single-shot spin-echo EPI sequence (FOV = 24x24cm, slice thickness = 2.5mm, no gap, matrix = 96x96, 60 axial slices). Each DTI dataset consisted of 2 images with b=0s/mm^2 and 12 images with b=1100s/mm^2 with different orientations of diffusion sensitization. An undistorted T2 weighted scan (T2WFSE) was acquired with a fast spin echo sequence. For B_0 field mapping, two gradient-echo images with different echo times (TE= 7 and 11.5 ms, FOV= 22cm, TR= 1300ms, slice thickness= 2.0mm) were collected.

2.3 EPI distortion correction methods

Image Registration based correction method: The distorted EPI image (the first b=0 image in the DWI dataset) was registered to the anatomically undistorted T2WFSE image using a deformable registration algorithm with mutual information (MI) metric and cubic B-spline modeled deformation field. In the remainder of the paper we refer to this approach as the BSP method. The deformation was constrained to be only in the phase-encoding direction. The mutual-information based metric enables the registration of images with different modalities such as T1-weighted or T2-weighted images and the anatomically undistorted T2WFSE image is used as the target image for EPI correction in this study. The registration algorithm was implemented in C++ using the registration library in the Insight Segmentation and Registration Toolkit (ITK, www.itk.org)[**7**].

Field map based method: This method uses several tools provided by the Oxford Center for Functional Magnetic Resonance Imaging of the Brain (FMRIB. FSL, http://www.fmrib.ox.ac.uk/fsl/). The B_0 fieldmap was first calculated as the difference in phase between the two gradient echo images divided by the echo time difference (4.5 ms). The resulting complex fieldmap was phase-unwrapped using the Phase Region Expanding Labeller for Unwrapping Discrete Estimates (PRELUDE)[**8**] and then registered to the EPI data (first b=0 image) via a rigid body registration. The fieldmap-based distortion correction was then applied to the EPI images in the phase-encoding direction using FMRIB's Utility for Geometrically Unwarping EPIs (FUGUE). In the rest of the article, we will refer to this approach as the B_0M method.

Prior to tensor computation, DWIs were processed with a pipeline consisting of the following steps: 1) the T2WFSE image was aligned to the anterior commissure-posterior commissure (AC-PC) plane [**9**] and used as the target image (structural template) for all 4 DWI data; 2) both the structural template and the distorted EPI image (the first b=0 image in the DWI dataset) were noise padded to eliminate spurious boundaries; 3) All DWIs were corrected for motion and eddy current distortion [**10**]; 4) the structural template image was registered to the first b=0 image in the DWI dataset with an MI based rigid body registration to create a structural target for EPI distortion correction; 5) The deformation field for EPI correction was calculated in the native DWI space using BSP and B_0M respectively; 6) For each method, the computed deformation field was applied to all DWIs in their native space; 7) DWIs were then reoriented to the structural template space, with proper rotation of the b-matrix [**10**]. Following these correction steps the diffusion tensor was computed using non-linear fitting [**11**] and its derived quantities including FA and Trace (TR) were calculated.

2.4 Evaluation of results and statistical analysis

The effects of EPI distortion on the SD maps were first evaluated by visual inspection. For a quantitative assessment, the Wilcoxon signed-rank test was used on each subject for the comparison of the SD maps from different methods. The median of the SD map is computed as a global measurement of the performance of the corresponding EPI distortion correction method for each subject. The EPI correction method with the lowest median SD has the best overall performance. Population statistics were performed by paired t-test analysis of the median SD values across 5 subjects.

In order to inspect the spatial distribution of the effects in the population of five subjects, a hierarchical coarse-to-fine image registration pipeline [**12**] was used to transform each subject's structural image to Montreal Neurological Institute (MNI) template colin27 [**13**]. The computed transformation was then used to spatially normalize the corresponding SD maps from DWI datasets with BSP, B_0M correction, and without EPI correction (NoC) into the template colin27 space. An average SD map for FA and TR across 5 subjects was generated for each method (represented as $SD_{Avg,FA,BSP}$, SD_{Avg,FA,B_0M} and $SD_{Avg,FA,NoC}$ respectively).

3 Results

Fig. 1 shows the distorted EPI images (b=0) from 4 DWI datasets with different phase-encoding directions as well as the undistorted target image. The distortions are more pronounced in regions close to tissue-air interfaces such as the frontal poles and the temporal lobes near the petrous bone.

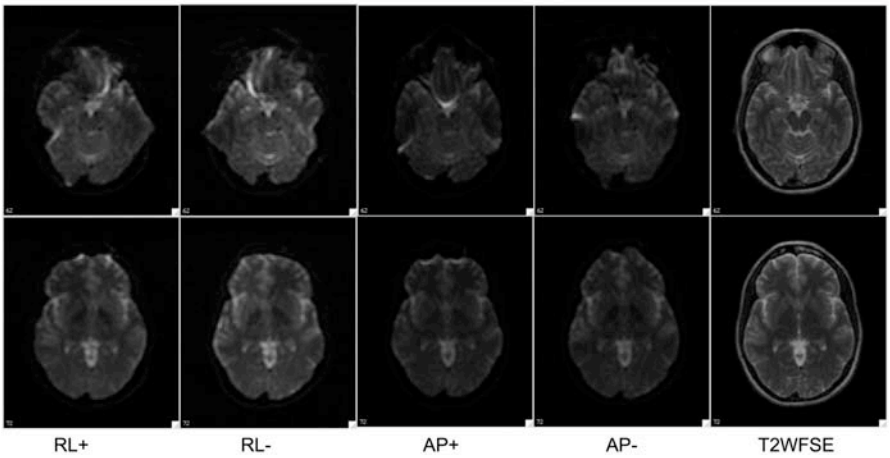

Fig. 1. The EPI distorted image slices with different phase encoding directions and the anatomically correct T2-FSE image slices of the same subject are shown here.

Fig. 2 shows a magnified view of an axial slice in a region of the brain relatively remote from sources of susceptibility variation. Arrows are marked at the same locations in all images to facilitate appreciating the degree of local distortion. Even at this location the uncorrected EPI image shows an appreciable amount of distortion, and both correction methods (BSP and B_0M) have successfully reduced the distortion.

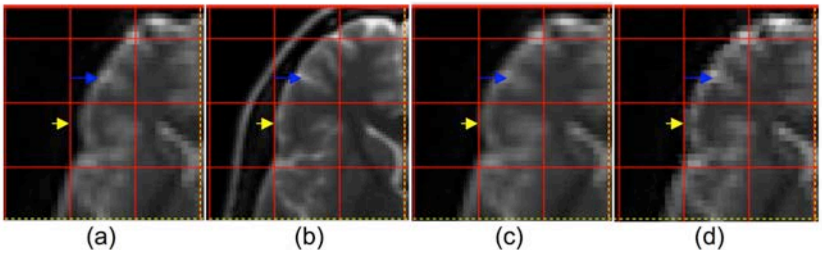

Fig. 2. An example of the distortion correction: (a) the original distorted RL- b=0 EPI image, (b) undistorted T2WFSE image, (c) the corrected image with BSP and (d) the corrected image with B_0M.

Mean and SD images from a representative subject were computed and displayed for FA (Fig. 3) and TR (Fig. 4). As expected for both FA and TR, higher SD values are visible in regions most affected by magnetic susceptibility variations such as tempral and frontal regions including the corpus callosum. SD decreases after EPI distortion correction with both methods. TR SD images demonstrate high variability at the top of the brain, and in periventricular regions.

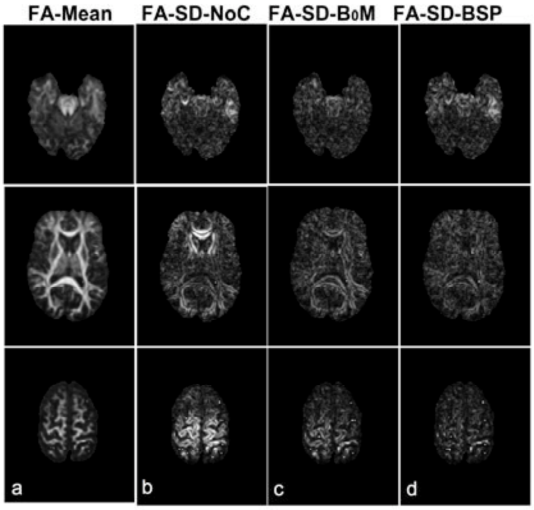

Fig. 3. Results from a representative subject. (a) mean FA image with BSP correction (display range [0 0.95]), (b, c, and d) SD maps (display range [0 0.3]) of FA images from DTI datasets with no EPI correction (NoC), B_0M correction, and BSP correction respectively.

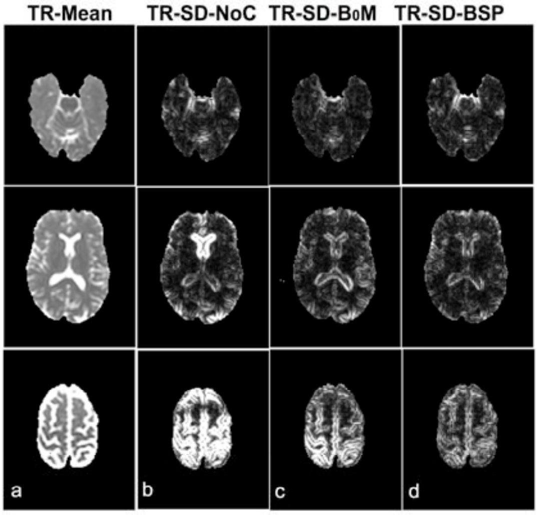

Fig. 4. Results on a representative subject: (a) mean TR image with BSP correction with display range [0 5000 μm^2/s], (b, c, and d) SD maps (display range [0 1000 μm^2/s]) of TR images from DTI datasets with no EPI correction (NoC), B_0M correction, and BSP correction respectively.

In Fig. 5, the average performance of BSP across the population is compared to that of B_0M by computing the variability difference map $STD_{Avg,B_0M} - STD_{Avg,BSP}$. The dark regions in Fig. 5(b)&(c) indicate that, for EPI distortion correction, the B_0M method performs better than the BSP method, and the bright regions are where BSP performs better than B_0M. BSP consistently provides better correction in rostral regions (e.g. corpus callosum, top of the brain), while B_0M performs better at the base of the brain, including temporal lobes, brainstem, and cerebellum.

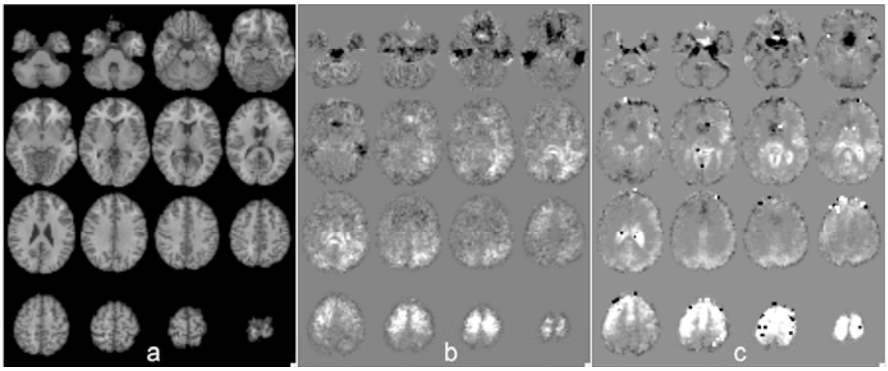

Fig. 5. Performance comparison of BSP and B_0M across population. (a) MNI colin27; difference in the variability of (b) FA ($SD_{Avg,FA,B_0M} - SD_{Avg,FA,BSP}$) with the display range of [-0.03 0.03], and (c) TR ($SD_{Avg,TR,B_0M} - SD_{Avg,TR,BSP}$) with range [-200 200 $\mu m^2/s$].

The median SD value of FA and TR from all brain voxels in each of the 5 subjects with or without EPI correction (BSP, B_0M, and NoC) is shown in Table 1. The percent change in median SD with different EPI distortion correction strategies is also calculated (e.g. B_0M vs. NoC = 100*(B_0M-NoC)/NoC). Compared to the SD values with no EPI correction, on average, B_0M reduced the median SD for FA by 12.8% and the median SD for TR by 16.2%. BSP lowered the average median SDs of FA by 16.3% and TR by 23.2%. For all 5 subjects, BSP consistently provided lower median SD than B_0M for both FA (range [2.0% 6.9%]) and TR (range [5.3% 14.2%]). These results were confirmed by the voxel-wise Wilcoxon signed-rank tests, which showed that for all 5 subjects, B_0M and BSP resulted in significantly lower SD values (FA or TR) than NoC and SD values from BSP were significantly lower than that of B_0M.

Paired two-tailed t-tests show that, across the population, median SD from BSP or B_0M are significantly lower than NoC at $p < 0.0005$ (FA) and $p < 0.006$ (TR), and the median SD from BSP is significantly lower than B_0M at $p < 0.012$ (FA and TR).

Table 1. Comparison of median values of SD maps (FA/TR) with or without EPI distortion correction.

Subject		Median SD			Percent Change %		
		NoC	B_0M	BSP	B_0M vs. NoC	BSP vs. NoC	BSP vs. B_0M
FA	1	0.0402	0.0347	0.0334	-13.7	-17.1	-4.0
	2	0.0413	0.0373	0.0365	-9.5	-11.7	-2.5
	3	0.0431	0.0373	0.0365	-13.6	-15.4	-2.1
	4	0.0435	0.0366	0.0347	-15.9	-20.3	-5.5
	5	0.0445	0.0397	0.0368	-11.4	-17.2	-7.0
TR	1	186.9	153.4	141.3	-17.9	-24.4	-8.5
	2	136.2	122.0	115.8	-10.4	-15.0	-5.4
	3	139.4	117.1	110.8	-16.0	-20.5	-5.7
	4	206.5	163.9	143.5	-20.6	-30.5	-14.2
	5	172.5	144.7	128.2	-16.2	-25.7	-12.8

4 Discussion

One goal of this work was to propose a framework that would enable evaluating the performance of different EPI distortion correction methods in the context of DTI. We found that our relatively simple approach of calculating SD maps of the DTI quantities of interest for datasets with different phase-encoding directions can be effectively used for this purpose. The best EPI distortion correction strategy would produce an SD map with the lowest overall magnitude. Moreover, by analyzing SD maps, one can assess potential regional effects of the different correction algorithms. The SD maps of both FA and TR were computed and evaluated, since different DTI quantities may show different local sensitivity to the same EPI distortion. In fact, the spatial pattern of increased variability is not identical for FA and TR. For example, TR shows a clear pattern of increased variability in periventricular regions that is not present in FA.

For uncorrected data, the effects of misalignment were very noticeable in the genu of the corpus callosum for both FA and TR, ventral portions of the frontal lobe in proximity of the frontal sinuses mostly for TR, and ventral portions of the temporal lobe near the petrous bone for FA. These results are consistent with the fact that the largest distortions are to be expected in regions where B_0 inhomogeneities are most pronounced.

We found high SD values in regions at the top of the brain, a region that is not normally associated with EPI distortions because it is distant from sinuses and other air-filled cavities. The effects of misalignment on the SD of both FA and TR could be magnified in apical brain regions because of the presence of sharp boundaries between CSF, gray matter, and white matter.

Both EPI distortion correction methods, BSP and B_0M, were effective in reducing the EPI geometric distortions and significantly improved the reproducibility of DT-derived quantities. Interestingly, BSP showed an overall better performance than

B_0M, although the two methods showed different performance in different regions. B_0M was clearly superior in infratentorial regions including brainstem and cerebellum, as well as in the ventral areas of the temporal lobes. BSP was better than B_0M in all rostral brain regions. While it is easy to understand why B_0M performs better than BSP at the base of the brain where the susceptibility gradients are steep, it is more difficult to explain why B_0M does not do as well as BSP in the rostral areas of the brain. One could hypothesize that the distortions at the top of the brain are not completely caused by B_0 inhomogeneities but we have been unable to identify a definitive cause.

The most important practical conclusion of our work is that in the absence of B_0 field data, successful EPI distortion correction of DTI data can be performed with a B-spline image registration approach using an undistorted T2-weighted image as the registration target.

In future work, one may combine these two methods to reach a more accurate deformation field for the whole brain in EPI distortion correction, such as using the deformation field from B_0M as an initialization to correct regions at the base of brain with severe signal loss, and the BSP method as a finer step to improve the distortion correction in supratentorial brain regions.

Reference

1. P. Jezzard and R. S. Balaban: Correction for geometrical distortion in echo planar images from Bo field variations, *Magn Reson Med*, vol. 34, pp. 65–73, 1995.
2. N. K. Chen and A. M. Wyrwicz: Optimized distortion correction technique for echo planar imaging, *Magn Reson Med*, vol. 45, pp. 525-8, 2001.
3. N. K. Chen and A. M. Wyrwicz: Correction for EPI distortions using multi-echo gradient-echo imaging, *Magn Reson Med*, vol. 41, pp. 1206-13, 1999.
4. R. M. Weisskoff and T. L. Davis: Correcting gross distortion on echo planar images, *Proceedings of the SMRM 11th Annual Meeting*, pp. 4515, 1992.
5. J. Kybic, P. Thevenaz, A. Nirkko, and M. Unser: Unwarping of unidirectionally distorted EPI images," *IEEE Trans Med Imaging*, vol. 19, pp. 80-93, 2000.
6. C. Studholme, R. T. Constable, and J. S. Duncan: Accurate alignment of functional EPI data to anatomical MRI using a physics-based distortion model, *IEEE Trans Med Imaging*, vol. 19, pp. 1115-27, 2000.
7. T. S. Yoo, *Insight into Images: Principles and Practice for Segmentation, Registration, and Image Analysis*. Wellesey, MA: AK Peters Ltd., 2004.
8. M. Jenkinson: Fast, automated, N-dimensional phase-unwrapping algorithm, *Magn Reson Med*, vol. 49, pp. 193-7, 2003.
9. P. L. Bazin, J. L. Cuzzocreo, M. A. Yassa, W. Gandler, M. J. McAuliffe, S. S. Bassett, and D. L. Pham: Volumetric neuroimage analysis extensions for the MIPAV software package, *J Neurosci Methods*, vol. 165, pp. 111-21, 2007.
10. G. K. Rohde, A. S. Barnett, P. J. Basser, S. Marenco, and C. Pierpaoli: Comprehensive approach for correction of motion and distortion in diffusion-weighted MRI, *Magn Reson Med*, vol. 51, pp. 103-14, 2004.
11. P. J. Basser, J. Mattiello, and D. LeBihan: Estimation of the effective self-diffusion tensor from the NMR spin echo, *J Magn Reson B*, vol. 103, pp. 247-54, 1994.

12. M. Wu, O. Carmichael, P. Lopez-Garcia, C. S. Carter, and H. J. Aizenstein: Quantitative comparison of AIR, SPM, and the fully deformable model for atlas-based segmentation of functional and structural MR images, *Hum Brain Mapp*, vol. 27, pp. 747-54, 2006.
13. C. J. Holmes, R. Hoge, L. Collins, R. Woods, A. W. Toga, and A. C. Evans: Enhancement of MR images using registration for signal averaging, *Journal of Computer Assisted Tomography*, vol. 22, pp. 324-333, 1998.

A Subdivision Approach to Tensor Field Interpolation

Inas A. Yassine and Tim McGraw

West Virginia University, Morgantown WV 26506, USA,
`iyassine@mix.wvu.edu, Tim.McGraw@mail.wvu.edu`

Abstract. We propose a scheme for tensor field interpolation which is inspired by subdivision surfaces in computer graphics. The method applies to Cartesian tensors of all ranks and imposes smoothness on the interpolated field by constraining the divergence and curl of the tensor field. Applying the method involves only a sparse matrix-vector multiplication at each iteration. Results are presented for rank 1, 2 and 4 tensors. These examples demonstrate that the subdivision scheme can better preserve FA and interpolate rotations than some other interpolation methods.

1 Introduction

Many alternatives to componentwise linear interpolation of tensors have been proposed. Geodesic [1–3], log-Euclidean [4], tensor spline [5], and geodesic-loxodrome [6] approaches formulate interpolation in terms of intrinsic distances on some manifold. Some methods have the desirable property of monotonically interpolating some scalar measure, such as determinant [1–4] or other orthogonal invariants [6]. In this work we propose a subdivision scheme based on minimizing the divergence and curl of the continuous tensor field which interpolates a given set of tensors. Divergence constraints are commonly used in simulations [7, 8] of incompressible fluid flows.

The term "subdivision" refers to a computer graphics technique for recursively refining meshes. A subdivision scheme defines a mechanism for adding new vertices to a mesh and updating the mesh connectivity. The limit surface obtained after an infinite number of iterations can be shown to be a smooth surface in some cases - a bicubic B-spline for the scheme of Catmull-Clark [9] and a biquadratic B-spline in the case of Doo-Sabin [10]. The subdivision process is often analyzed as a linear equation $p^{n+1} = Sp^n$ where p is the set of vertices in the mesh and the superscripts denote iteration number. The subdivision matrix S characterizes the subdivision process of generating new vertices as linear combinations of the old vertices.

Weimer and Warren [11] extended the concept of subdivision to fluid flows. Starting with a coarse vector field representing fluid velocity, their technique generated a dense vector field corresponding to the solution of the Navier-Stokes equation. Similarly, our method can be seen as the solution of a system of partial differential equations.

2 Vector Field Subdivision

We will first formulate the subdivision scheme for vector field interpolation which will help explain the tensor field subdivision scheme in the next section of this paper. Our formulation is much simpler than that of Warren and Weimer [11]. Given velocity vectors at the corners of a cube (or square in 2D) we construct a velocity field which is simultaneously as incompressible and irrotational as possible. This can be seen as a physical constraint on the flow, or alternatively since we may wish to interpolate vector fields other than fluid velocity fields, this can also be seen merely as a smoothness constraint since spurious sources/sinks and vortices can introduce regions of rapidly changing vector direction and length.

The strength of sources or sinks in a fluid flow can be quantified by the divergence of the velocity field, and the strength of vortices can be quantified by the curl

$$div\, v = \frac{\partial v_x}{\partial x} + \frac{\partial v_y}{\partial y} + \frac{\partial v_z}{\partial z},\ curl\, v = \begin{bmatrix} \frac{\partial v_z}{\partial y} - \frac{\partial v_y}{\partial z} \\ \frac{\partial v_x}{\partial z} - \frac{\partial v_z}{\partial x} \\ \frac{\partial v_y}{\partial x} - \frac{\partial v_x}{\partial y} \end{bmatrix} \tag{1}$$

where $v = [v_x, v_y, v_z]^T$ is the vector field. These are usually denoted by the shorthand $\nabla \cdot v$ and $\nabla \times v$ respectively. We will approximate these operators discretely by using finite differences

$$\Delta_x = \frac{1}{2}(v(x+1,y,z) - v(x-1,y,z)), \tag{2}$$

$$\begin{aligned} \Delta_x^+ &= v(x+1,y,z) - v(x,y,z), \\ \Delta_x^- &= v(x,y,z) - v(x-1,y,z) \end{aligned} \tag{3}$$

which are the central, forward and backward differences respectively. The subdivision operation takes as input a coarse grid of vectors (2×2 in 2D, or $2 \times 2 \times 2$

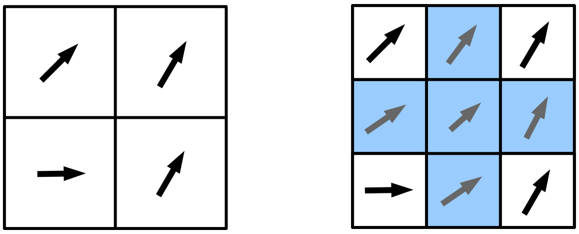

Fig. 1. Illustration of the subdivision process in 2D. The first subdivision iteration replaces the 2×2 grid of vectors (v^0) with a 3×3 grid of vectors (v^1). The vectors in the corners of the domain (white background) are interpolated. The remaining 5 vectors are computed by minimizing the divergence and curl of the field. The next subdivision step would interpolate all 9 vectors. The process can be repeated to obtain v^n, a grid of size $2^n + 1 \times 2^n + 1$.

in 3D) we will call v^0 and produces a refined grid (3×3 in 2D, or $3 \times 3 \times 3$ in 3D) we will call v^1 as shown in Figure (1). The process will proceed iteratively and each step will interpolate the results of the previous step. The system of equations which determine v^{n+1} given v^n specify 3 types of requirements:

1. Interpolation. The vectors at iteration n should be interpolated in step $n+1$. In the first step we have

$$\begin{aligned} v^n(1,1) &= v^{n+1}(1,1) \\ v^n(1,3) &= v^{n+1}(1,3) \\ v^n(3,1) &= v^{n+1}(3,1) \\ v^n(3,3) &= v^{n+1}(3,3). \end{aligned} \tag{4}$$

   where the array v^n has been padded to be the same size as v^{n+1} so that indices at corresponding corners are equal.
2. Divergence minimization. The divergence at each point in v^{n+1} is set to zero, and written in terms of v^n when a corner point is involved. If the central difference equation involves a point outside the domain, forward or backward differences are used instead. There will be one equation for each vector in v^{n+1}. Each equation will be of the form

$$0 = \Delta_x v_x + \Delta_y v_y + \Delta_z v_z. \tag{5}$$

   The superscript on v is $n+1$ for the new voxels being computed, and n for the voxels being interpolated.
3. Curl minimization. The curl is handled analogously to the divergence. For the 2D example there is only one nonzero component of the curl for each vector. In the 3D case there will be 3 components per voxel of the form

$$0 = \Delta_y v_z - \Delta_z v_y \tag{6}$$

$$0 = \Delta_z v_x - \Delta_x v_z \tag{7}$$

$$0 = \Delta_x v_y - \Delta_y v_x \tag{8}$$

   for a total of 81 equations in the first step.

By reshaping v into column vector the equations can be rearranged in the form

$$0 = Av^n + Bv^{n+1} \tag{9}$$

Both matrices A and B are sparse and contain only elements with values $(-1, -\frac{1}{2}, 0, \frac{1}{2}, 1)$ Overall, in the 2D case we have to solve for 18 vector components in v^{n+1} given 22 equations. In 3D we solve for 81 vector components given 112 equations. The equations are solved in the least squares sense by

$$v^{n+1} = -B^+ Av^n \tag{10}$$

where the pseudoinverse $B^+ = (B^T B)^{-1} B^T$. This is a subdivision scheme in which the subdivision matrix is $S = -B^+ A$. The result is a vector field where the magnitudes of the divergence and curl are minimized while interpolating the coarse vector field. The influence of the divergence and curl minimization can be separately controlled by using a weighted least squares approach. We implement this by scaling the divergence equations in Eq. (9) by $\sigma_{div} = 0.9$ and the curl equations by $\sigma_{curl} = 0.1$. Results of vector field interpolation are shown in Figure 2. Note that even though curl and divergence are minimized in the least squares sense they are not guaranteed to equal zero. The subdivision process can generate rotational and nonsolenoidal flows.

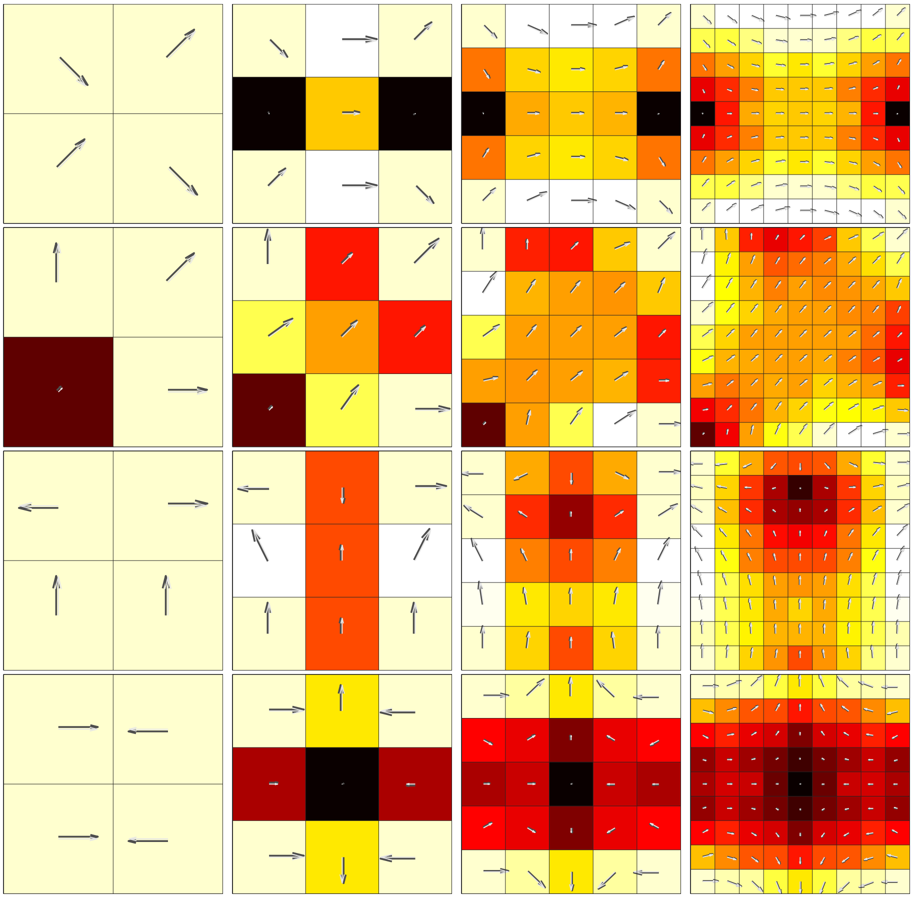

Fig. 2. Vector Field Subdivision. Four examples (top to bottom) of the vector field subdivision process. The field to be interpolated (left) is subdivided 3 times (results shown left to right). The background image is vector magnitude.

3 Tensor Field Subdivision

We will now extend the vector field interpolation results of the previous section to tensor fields. We use the same constraints (interpolation, divergence minimization and curl minimization) by simply substituting the definitions of the divergence and curl of tensors of arbitrary rank.

3.1 Tensor Field Divergence

The divergence of a rank 2 tensor field is a vector field of the same dimension. For a symmetric tensor we have

$$div \begin{bmatrix} D_{xx} & D_{xy} \\ D_{xy} & D_{yy} \end{bmatrix} = \begin{bmatrix} \frac{\partial D_{xx}}{\partial x} + \frac{\partial D_{xy}}{\partial y} \\ \frac{\partial D_{xy}}{\partial x} + \frac{\partial D_{yy}}{\partial y} \end{bmatrix} \tag{11}$$

$$div \begin{bmatrix} D_{xx} & D_{xy} & D_{xz} \\ D_{xy} & D_{yy} & D_{yz} \\ D_{xz} & D_{yz} & D_{zz} \end{bmatrix} = \begin{bmatrix} \frac{\partial D_{xx}}{\partial x} + \frac{\partial D_{xy}}{\partial y} + \frac{\partial D_{xz}}{\partial z} \\ \frac{\partial D_{xy}}{\partial x} + \frac{\partial D_{yy}}{\partial y} + \frac{\partial D_{yz}}{\partial z} \\ \frac{\partial D_{xy}}{\partial x} + \frac{\partial D_{yy}}{\partial y} + \frac{\partial D_{zz}}{\partial z} \end{bmatrix}. \tag{12}$$

To perform interpolation we form an equation for each of the vector components in Equation (11) or (12). For each such equation the corresponding row of matrices A, B has the appropriate elements assigned.

A good intuition can be gained about the nature of vector divergence by observing that near sources the vector field has positive divergence and locally the vectors appear to point away from the source. Conversely, near a sink the vector appear to converge toward the sink. The meaning of tensor field divergence can be appreciated by considering the diffusion equation when the concentration gradient is constant, but not necessarily zero

$$\frac{\partial C}{\partial t} = div(D\nabla C) = div(D) \cdot \nabla C. \tag{13}$$

Then at steady state $\frac{\partial C}{\partial t} = 0$ is achieved for $div(D) = 0$. Under the given conditions, this is equivalent to saying that the inhomogeneous tensor field D does not transform any constant vector field into a vector field with nonzero divergence.

In general, the divergence of a rank n tensor field is a rank $(n-1)$ tensor field given in Einstein notation as $\partial_i D_i$. This notation indicates that for all possible values of index i, the tensor components are differentiated with respect to that index and summed over. Note that when the field consists of totally symmetric tensors the divergence tensor is also totally symmetric.

3.2 Tensor Field Curl

The curl of a rank 2 tensor field is a vector in 2D and a rank 2 tensor in 3D,

$$curl \begin{bmatrix} D_{xx} & D_{xy} \\ D_{xy} & D_{yy} \end{bmatrix} = \begin{bmatrix} \frac{\partial D_{xy}}{\partial x} - \frac{\partial D_{xx}}{\partial y} \\ \frac{\partial D_{yy}}{\partial x} - \frac{\partial D_{xy}}{\partial y} \end{bmatrix} \tag{14}$$

$$curl \begin{bmatrix} D_{xx} & D_{xy} & D_{xz} \\ D_{xy} & D_{yy} & D_{yz} \\ D_{xz} & D_{yz} & D_{zz} \end{bmatrix} = \begin{bmatrix} \frac{\partial D_{xz}}{\partial y} - \frac{\partial D_{xy}}{\partial z} & \frac{\partial D_{yz}}{\partial y} - \frac{\partial D_{yy}}{\partial z} & \frac{\partial D_{zz}}{\partial y} - \frac{\partial D_{yz}}{\partial z} \\ \frac{\partial D_{xx}}{\partial z} - \frac{\partial D_{xz}}{\partial x} & \frac{\partial D_{xy}}{\partial z} - \frac{\partial D_{yz}}{\partial x} & \frac{\partial D_{xz}}{\partial z} - \frac{\partial D_{zz}}{\partial x} \\ \frac{\partial D_{xy}}{\partial x} - \frac{\partial D_{xx}}{\partial y} & \frac{\partial D_{yy}}{\partial x} - \frac{\partial D_{xy}}{\partial y} & \frac{\partial D_{yz}}{\partial x} - \frac{\partial D_{xz}}{\partial y} \end{bmatrix}. \tag{15}$$

The curl of a rank n tensor field is a rank $(n+d-3)$ tensor field in d dimensions defined as $\varepsilon_{ijk}(\partial_j D_k)$ where ε_{ijk} is the Levi-Civita symbol (permutation tensor)

$$\varepsilon_{ijk} = \begin{cases} +1 & (i,j,k) \text{ is an even permutation of indices} \\ -1 & (i,j,k) \text{ is an odd permutation of indices} \\ 0 & \text{otherwise.} \end{cases} \tag{16}$$

4 Results

The results of rank 2 tensor field subdivision are shown in Figure 3, along with linear and log-Euclidean interpolation for comparison. Note that in the bottom row of voxels in both examples (top and bottom of Figure 3) FA is better preserved for the subdivision scheme than in the linear and log-Euclidean interpolation cases. The subdivision scheme results in a smooth rotation of the diffusion tensor.

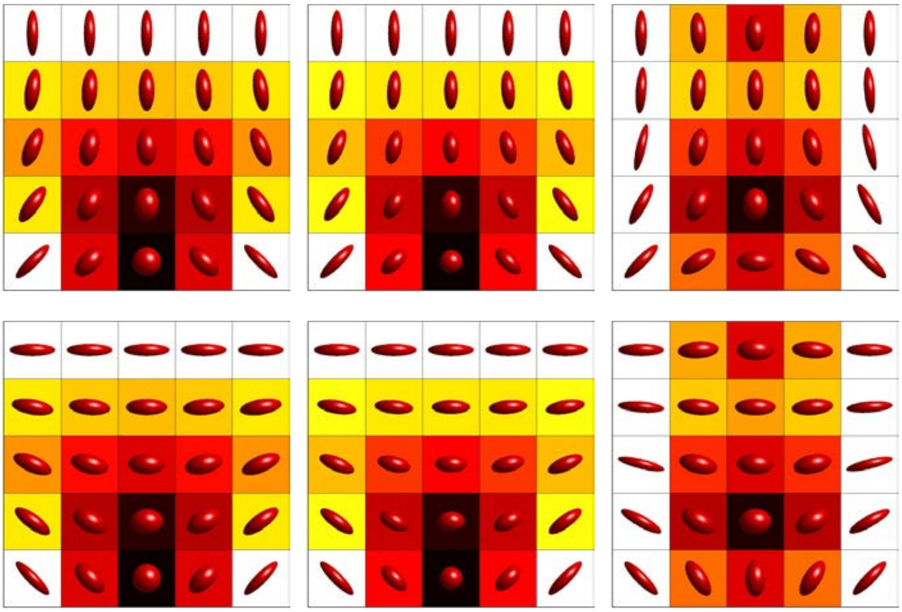

Fig. 3. Rank 2 tensor field interpolation. Linear interpolation (left), Log-Euclidean interpolation (center), 2 subdivision steps (right). The background image is FA.

High angular resolution diffusion imaging can overcome some limitations or rank 2 diffusion tensor imaging. Models for the diffusivity function have been formulated in terms of tensors of various ranks [12], rank 4 tensors in particular [13] and sequences of tensors of increasing rank [14]. To demonstrate the generality of the subdivision scheme, we present the results of subdivision applied to rank 4 tensor fields in Figure 4, along with linear interpolation results. In these examples it is apparent that the subdivision scheme encourages rotation in the peaks of the diffusivity profiles during interpolation. Note that these do not necessarily correspond to fiber directions. In the case of linear interpolation, the peaks in diffusivity merely grow and shrink while maintaining their orientation.

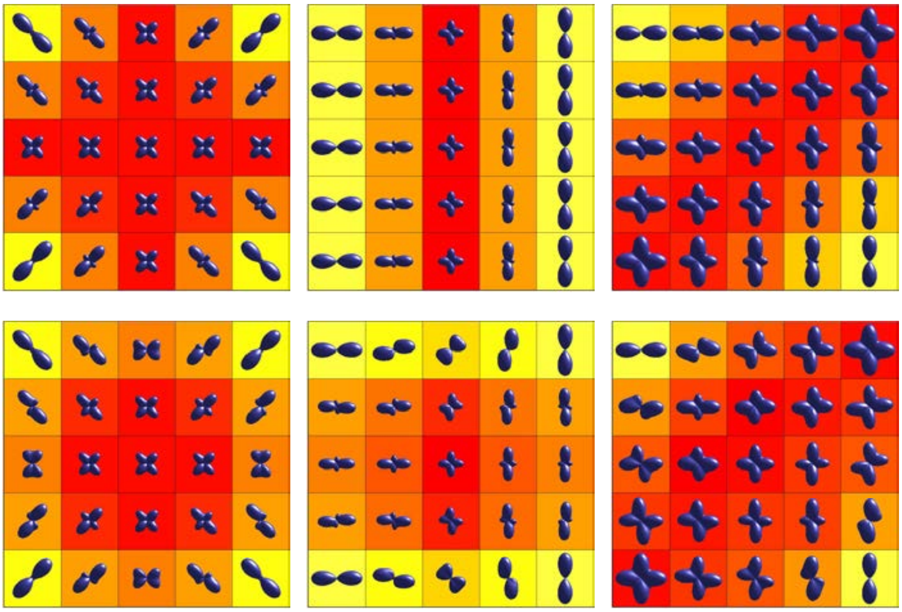

Fig. 4. Rank 4 tensor field interpolation. Linear (top), subdivision (bottom).

5 Conclusions

We have presented a scheme for tensor field interpolation which can be extended to tensors of arbitrary rank. The method is computationally efficient - It requires only a sparse matrix-vector multiplication at each step, and the matrix can be precomputed since it is independent of the data. Results show that the technique better preserves FA during interpolation in some cases than linear and log-Euclidean interpolation.

Future work will investigate the tensor basis functions underlying this subdivision scheme. Stam [15] analyzed the subdivision surface in terms of the eigensystem of the subdivision matrix. This is apt since the limit surface (if it exists) is given by $p^\infty = S^\infty p^0$ where p^∞ can be shown to be an eigenvector of S with corresponding eigenvalue $= 1$. This analysis permits exact evaluation of the limit surface without recursion.

References

1. Fletcher, P., Joshi, S.: Riemannian geometry for the statistical analysis of diffusion tensor data. Signal Processing **87**(2) (2007) 250–262
2. Pennec, X., Fillard, P., Ayache, N.: A Riemannian Framework for Tensor Computing. International Journal of Computer Vision **66**(1) (2006) 41–66
3. Batchelor, P., Moakher, M., Atkinson, D., Calamante, F., Connelly, A.: A rigorous framework for diffusion tensor calculus. Magn Reson Med **53**(1) (2005) 221–5
4. Arsigny, V., Fillard, P., Pennec, X., Ayache, N.: Fast and simple calculus on tensors in the Log-Euclidean framework. Proceedings of MICCAI (2005) 259–267
5. Barmpoutis, A., Vemuri, B., Shepherd, T., Forder, J.: Tensor Splines for Interpolation and Approximation of DT-MRI With Applications to Segmentation of Isolated Rat Hippocampi. Medical Imaging, IEEE Transactions on **26**(11) (2007) 1537–1546
6. Kindlmann, G., Estepar, R.S.J., Niethammer, M., Haker, S., Westin, C.F.: Geodesic-loxodromes for diffusion tensor interpolation and difference measurement. In: Tenth International Conference on Medical Image Computing and Computer-Assisted Intervention (MICCAI'07). Lecture Notes in Computer Science 4791, Brisbane, Australia (October 2007) 1–9
7. Feldman, B.E., O'Brien, J.F., Arikan, O.: Animating suspended particle explosions. In: Proceedings of ACM SIGGRAPH 2003. (August 2003) 708–715
8. Jeong-Mo Hong, Jong-Chul Yoon, C.H.K.: Divergence-constrained moving least squares for fluid simulation. In: Computer Animation and Virtual Worlds. (September 2008) to appear
9. Catmull, E., Clark, J.: Recursively generated B-spline surfaces on arbitrary topological meshes. Computer Aided Design **10** (1978) 350–355
10. Doo, D., Sabin, M.: Behaviour of recursive subdivision surfaces near extraordinary points. Computer Aided Design **10**(6) (1978) 356–360
11. Weimer, H., Warren, J.: Subdivision schemes for fluid flow. Proceedings of the 26th annual conference on Computer graphics and interactive techniques (1999) 111–120
12. Özarslan, E., Mareci, T.: Generalized diffusion tensor imaging and analytical relationships between diffusion tensor imaging and high angular resolution diffusion imaging. Magnetic Resonance in Medicine **50**(5) (2003) 955–965
13. A. Barmpoutis, B. Jian, B.C.V., Shepherd, T.M.: Symmetric positive 4th order tensors and their estimation from diffusion weighted mri. In LNCS 4584 (Springer) Proceedings of IPMI07: Information Processing in Medical Imaging (2-6 July 2007) 308–319
14. Liu, C., Bammer, R., Acar, B., Moseley, M.: Characterizing non-gaussian diffusion by using generalized diffusion tensors. Magnetic Resonance in Medicine **51**(5) (2004) 924–937
15. Stam, J.: Exact evaluation of Catmull-Clark subdivision surfaces at arbitrary parameter values. Proceedings of the 25th annual conference on Computer graphics and interactive techniques (1998) 395–404

A Unified Parametric Model of White Matter Fiber Tracts

Moo K. Chung[1,2], Jee Eun Lee[2], Gary Park[1,2],Mariana Lazar[3],
Nicholas T. Lange[5,6], Janet E. Lainhart[4], Andrew L. Alexander[2]

[1]Department of Biostatistics and Medical Informatics
[2]Waisman Laboratory for Brain Imaging and Behavior
University of Wisconsin, Madison
[3]Center for Biomedical Imaging, Department of Radiology
New York University School of Medicine, New York
[4] Department of Psychiatry
University of Utah, Salt Lake City
[5] Departments of Psychiatry and Biostatistics
Harvard University Schools of Medicine and Public Health
[6] Neurostatistics Laboratory, McLean Hospital. Boston
mkchung@wisc.edu

Abstract. We present a novel unified framework for explicitly parameterizing white fiber tracts. The coordinates of tracts are parameterized using a Fourier series expansion. For an arbitrary tract, a 19 degree cosine expansion is found to be sufficient to reconstruct the tract with an error of about 0.26 mm. By adding specific periodic constraints to open tracts, we can avoid using the sine basis. Then each tract is fully parameterized with 60 parameters, which results in a substantial data reduction. Unlike available spline models, the proposed method does not have internal knots and explicitly represents the tract as a linear combination of basis functions. This simplicity in the representation enables us to design statistical models, register tracts and segment tracts in a unified Hilbert space formulation.

1 Introduction

Diffusion tensor imaging (DTI) may be used to characterize the microstructure of biological tissues using measures of the magnitude, anisotropy and aniotropic orientation [2]. In general, it is assumed that the direction of greatest diffusivity (the major eigenvector of the diffusion tensor) is most likely aligned to the local orientation of the white matter fibers. White matter tractography offers the unique opportunity to map out, segment and characterize the trajectories of white matter fiber bundles noninvasively in the brain. Most deterministic tractography algorithms use the local diffusion tensor orientation (primarily the major eigenvector) to estimate the local direction of propagation along the reconstructed pathway or fiber tract [3] [10] [17] [19]. Tractography has been used to visualize and map out major white matter pathways in individuals and brain atlases [7] [20] [29] [30], segment specific white matter areas for region of interest analyses [15], quantify white matter morphometry and connections [23] [27], and visualize the relationships between brain pathology (e.g., brain tumors, vascular malformations, other lesions) and white matter anatomy for clinical applications like neurosurgical planning [1] [21] [22]. However, tractography data can be challenging to interpret and quantify. Whole brain tractography studies often generate many thousand tracts and require tedious manual selection of tract groups for subsequent analyses. Recent efforts have attempted to cluster [24] and automatically segment white matter tracts [25] as well as characterize tract shape parameters [4]. Many of these techniques can be quite computationally demanding given the sizes of the data sets. Clearly efficient methods for characterizing tract shape, regional tract segmentation and clustering, tract registration, averaging and quantitation would be of tremendous value to the clinical and diffusion imaging research communities. In this study, we present a novel approach for parameterizing tract features both shape and spatial location - using Fourier descriptors.

Fourier descriptors has been previously used to classify tracts [4]. The Fourier coefficients are computed by the Fourier transform that involves the both sine and cosine series expansion. Then the sum of the squared coefficients are obtained up to degree 30 for each tract and the k-means clustering is used to classify the fibers globally. The authors conclude that a downside of using Fourier descriptors is that they are not local and it is not possible to make statement about a specific portion of the curve. Although the Fourier coefficients are global and mainly used for globally classifying shapes [28], it is still possible to obtain local shape information and make a statement about local shape characteristics [8]. In this study, we propose to use the Fourier descriptor as a parameterization for local shape representation.

3D curve matching using splines has previously been described mainly in the computer vision literature [9] [11] [16]. Unfortunately, splines are not easy to model and to manipulate explicitly as compared to Fourier descriptors due to the introduction of knots. In Clayden et al. [9], the cubic-B spline is used to parameterize the median of a set of tracts for tract dispersion modeling. Matching two splines with different numbers of knots is not computationally trivial and has been solved using a sequence of ad-hoc approaches. In Gruen et al. [11], the optimal displacement of two cubic spline curves are obtained by minimizing the sum of squared Euclidean distances. The minimization is nonlinear so an iterative updating scheme is used. On the other hand, there is no need for any numerical optimization in obtaining the displacement vectors in our method due to the very nature of the Hilbert space framework. The optimal solution is embedded in the representation itself.

Instead of using the squared distance of coordinates, others have used the curvature and torsion to find the similarity between two curves [13] [16] [18]. In [18], curvature and torsion were estimated using a finite difference scheme and the sum of the squared distance of curvature and torsion differences were minimized in an iterative fashion. Due to the space limitation, we will not consider this alternate approach.

This paper describes how to obtain local shape information employing cosine series, a special case of Fourier expansion. To our knowledge, this is the first paper that describes white fiber bundles using an *explicit* functional representation. Then using this representation, we demonstrate how to register two tracts and average multiple tracts. The ability to register tracts of varying shape and length enables us to develop a shape similarity based tract segmentation. We will further demonstrate the feasibility of this idea.

2 Methods

2.1 Image Acquisition and Processing

DTI data were acquired on a Siemens Trio 3.0 Tesla Scanner with an 8-channel, receive-only head coil. DTI was performed using a single-shot, spin-echo, EPI pulse sequence and SENSE parallel imaging (undersampling factor of 2). Diffusion-weighted images were acquired in 12 non-collinear diffusion encoding directions with diffusion weighting factor (b=0) 1000 s/mm^2 in addition to a single reference image. Data acquisition parameters included the following: contiguous (no-gap) fifty 2.5mm thick axial slices with an acquisition matrix of 128x128 over a FOV of 256mm, 4 averages, repetition time (TR) = 7000 ms, and echo time (TE) = 84 ms. Two-dimensional gradient echo images with two different echo times of 7 ms and 10 ms were obtained prior to the DTI acquisition for correcting distortions related to magnetic field inhomogenieties.

Eddy current related distortion and head motion of each data set were corrected using AIR and distortions from field inhomogeneities were corrected using custom software algorithms based on [14]. Distortion-corrected DW images were interpolated to $2 \times 2 \times 2$mm voxels and the six tensor elements were calculated using a multivariate log-linear regression method [2].

The images were isotropically resampled at 1mm^3 resolution before applying the white matter tractography algorithm. The second order Runge-Kutta streamline algorithm with tensor deflection [17] was used. The trajectories were initiated at the center of the seed voxels and were terminated if they either reached regions with the factional anisotropy (FA) value smaller then 0.15 or if the angle between two consecutive steps along the trajectory was larger than $\pi/4$. At this sampling rate, the algorithm usually produces more than 300000 tracts per brain. As an illustration, subsampled 500 tracts are shown in Figure 3. Each tract consists of 105 ± 54 control points. The distance between control points is approximately 1mm. Whole brain tracts are stored as a file of size approximately 600MB. This is a somewhat inefficient way of storing the tract data. We present an efficient scalable data representation technique that can reduce the amount of data by a factor of 500% with a minimum loss of information. Our scalable representation can be retrieved later to give more detailed representation iteratively.

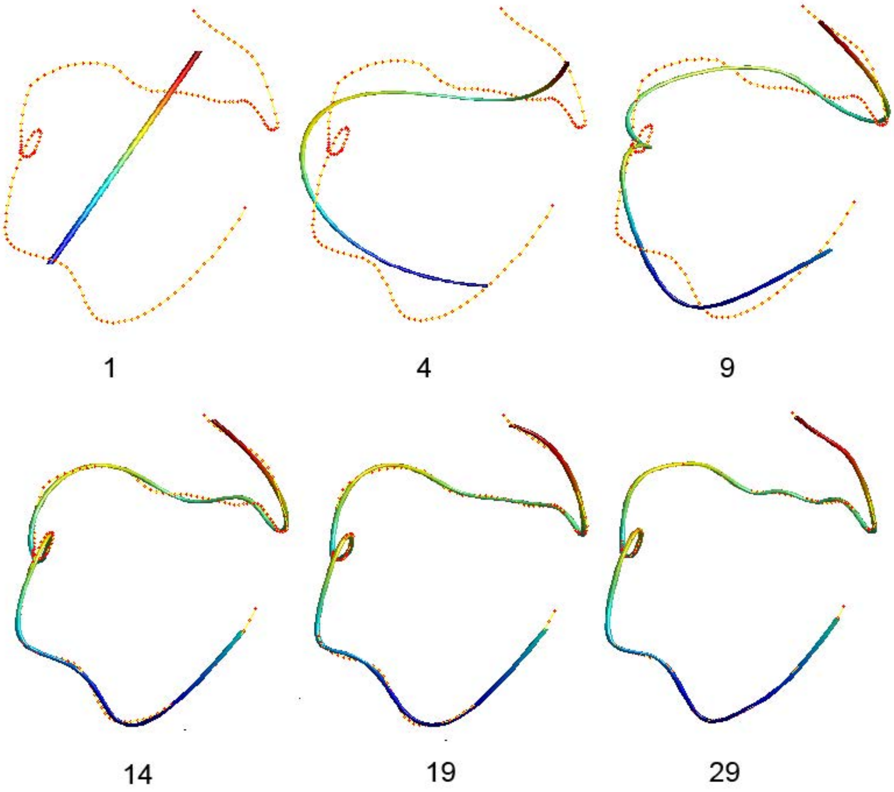

Fig. 1. Cosine series representation of a tract at various degrees. Red dots are control points. The degree 1 representation is a straight line that fits all the control points in a least squares fashion. The degree 19 representation (60 parameters) is used through out the study.

2.2 Parameterizing tracts

Consider a tract $\mathcal{M}$ consisting of n control points $p_1, \cdots, p_n$ along the tract. The second order Runge-Kutta streamline algorithm constructs tracts such that the Euclidian distance between the control points, i.e. $\|p_i - p_{i-1}\|$ is 1mm. Then we are interested in estimating a function that best represents the tract consisting of the noisy control points. This problem can be solved using piecewise continuous polynomials such as splines [26]. However, we will avoid using splines because they reintroduce control points that connect each piece of polynomials. Further, it is not straightforward to build an explicit statistical model using splines. Therefore, we have developed a novel representation technique that avoids all the drawbacks of splines.

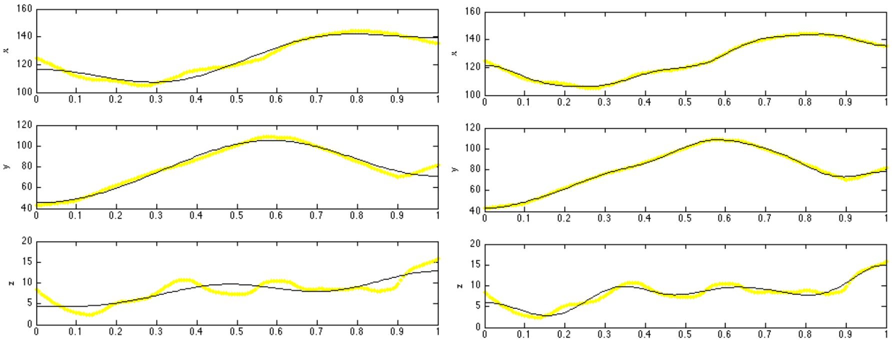

degree 4 representation

degree 9 representation

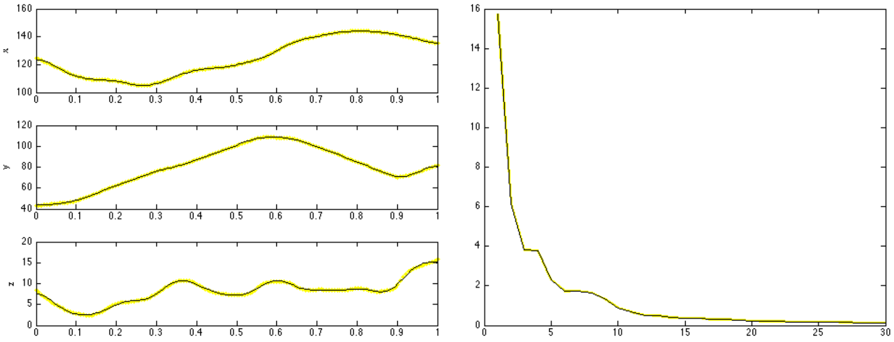

degree 19 representation

average reconstruction error

Fig. 2. The plot of x-,y- and z-coordinates over parameter space $[0, 1]$. The yellow line is the tractography result and the black line is the reconstruction at degree 9 (left) and 19 (middle). The figure in the right is the average reconstruction error over the degree of representation. The error decreases exponentially as the degree increases.

Consider a mapping ζ that maps the control point p_j onto the unit interval $[0, 1]$ as

$$\zeta : p_j \rightarrow \frac{\sum_{i=1}^{j} \|p_i - p_{i-1}\|}{\sum_{i=1}^{n} \|p_i - p_{i-1}\|} = t_j. \tag{1}$$

This is the ratio of the arc-length from the point p_1 to p$_j$, to p_1 to p_n. We let this ratio to be t_j. We assume $\zeta(p_1) = 0$. Then we estimate a smooth map $\zeta^{-1} : [0, 1] \rightarrow \mathcal{M}$ that passes through $\zeta^{-1}(t_j) = p_j$ in a least squares fashion.

Consider the space of square integrable functions in $[0, 1]$ denoted by $\mathcal{L}^2[0, 1]$. Let us solve the eigenequation

$$\Delta f + \lambda f = 0. \tag{2}$$

in $[0, 1]$. The eigenfunctions will naturally form an orthonormal basis in $\mathcal{L}^2[0, 1]$. Instead of solving (2) in the interval $[0, 1]$ directly, let us solve it in $\mathbb{R}$ with the periodic constrain

$$f(t+2) = f(t).$$

Putting the periodic constrain guarantees the eigenfunctions to be the usual Fourier sine and cosine functions making numerical implementation straightforward. The reason we did not give the period 1 constraint is that it forces the function defined in $[0,1]$ to be periodic. Then from the period 2 constraint, the tract coordinates are defined only in the intervals $\cdots, [-2,-1], [0,1], [2,3]\cdots$, there is a gap in the intervals $\cdots, (-1,0), (1,2), (3,4)\cdots$. We can fill the gap by padding with zeros or some constant values but this will result in the Gibbs phenomenon (ringing artifacts) [8] at the point of discontinuity $\cdots -2,-1,0,1,2,\cdots$. One way of filling the gap while making the function continuous across the whole intervals is by putting the constraint of evenness, i.e. $f(t) = f(-t)$ in the interval $[-1,0]$. The only eigenfunctions satisfying these two constraints are the cosine functions of the form

$$\psi_0(t) = 1, \psi_l(t) = \sqrt{2}\cos(l\pi t)$$

with the corresponding eigenvalues $\lambda_l = l^2\pi^2$ for integers $l > 0$. The constant $\sqrt{2}$ is introduced to make the eigenfunctions orthonormal in $[0,1]$ so that

$$\int_0^1 \psi_l(t)\psi_m(t)\, dt = \delta_{lm}. \tag{3}$$

Let $\mathcal{H}_k$ be the subspace spanned by up to the k-th degree eigenfunctions:

$$\mathcal{H}_k = \{\sum_{l=0}^{k} c_l\psi_l(t) : c_l \in \mathbb{R}\}.$$

Then we estimate a smooth function $\zeta^{-1} \in \mathcal{L}^2[0,1]$ in the subspace $\mathcal{H}_k$.

If we denote the coordinates of $\zeta^{-1}(t)$ as $(\zeta_1^{-1}, \zeta_2^{-1}, \zeta_3^{-1})$, the k-th degree *cosine series representation* of ζ^{-1} is given by

$$(\zeta_1^{-1}, \zeta_2^{-1}, \zeta_3^{-1})(t) = \sum_{l=0}^{k} (c_{l1}, c_{l2}, c_{l3})\psi_l(t). \tag{4}$$

The Fourier coefficient vectors $c_l = (c_{l1}, c_{l2}, c_{l3})$ are estimated by solving the system of equations

$$\underbrace{\begin{pmatrix} \zeta_1^{-1}(t_1) & \zeta_2^{-1}(t_1) & \zeta_3^{-1}(t_1) \\ \zeta_1^{-1}(t_2) & \zeta_2^{-1}(t_2) & \zeta_3^{-1}(t_2) \\ \vdots & \vdots & \vdots \\ \zeta_1^{-1}(t_n) & \zeta_2^{-1}(t_n) & \zeta_3^{-1}(t_n) \end{pmatrix}}_{Y} = \underbrace{\begin{pmatrix} \psi_0(t_1) & \psi_1(t_1) & \cdots & \psi_k(t_1) \\ \psi_0(t_2) & \psi_1(t_2) & \cdots & \psi_k(t_2) \\ \vdots & \vdots & \ddots & \vdots \\ \psi_0(t_n) & \psi_1(t_n) & \cdots & \psi_k(t_n) \end{pmatrix}}_{\Psi} \underbrace{\begin{pmatrix} c_{01} & c_{02} & c_{03} \\ c_{11} & c_{12} & c_{13} \\ \vdots & \vdots & \vdots \\ c_{k1} & c_{k2} & c_{k3} \end{pmatrix}}_{C}.$$

The least squares estimation is given by

$$C = (\Psi'\Psi)^{-1}\Psi' Y.$$

Fig. 3. Left: control points (red) obtained from the second order Runge-Kutta streamline algorithm. For visualization purpose, only 500 tracts with length larger than 50mm are shown. Yellow lines are line segments connecting consequent control points. Right: 19 degree cosine series representation of control points.

The proposed least squares estimation technique avoids using the Fourier transform [4] [6] [12]. The drawback of the FFT is the need for a predefined regular grid system so some sort of interpolation is needed. After various experiments, we decided to use $k = 19$ through out the paper (Figure 1). This gives the average error of 0.26mm along the tract. The plot of the average reconstruction error for other degrees is given in Figure 2 (lower right plot).

The advantage of the cosine series representation is that, instead of recording the coordinates of all control points, we only need to record $3 \cdot (k + 1)$ number of parameters for all possible tract shape. This is a substantial data reduction considering that the average number of control points is 105 (315 parameters).

2.3 Averaging White Matter Fiber Bundles

The ability to register one tract to another tract is crucial for any sort of population study, possibly via the use of the tract-based template construction. Since tracts are now represented as functions, the registration will be formulated as a minimization problem in a function space $\mathcal{H}_k$, thus avoiding numerical optimization [11] [13] [16] [18].

Suppose the Fourier representation of η^{-1} is given by

$$(\eta_1^{-1}, \eta_2^{-1}, \eta_3^{-1})(t) = \sum_{l=0}^{k} (d_{l1}, d_{l2}, d_{l3}) \psi_l(t). \tag{5}$$

Let us examine how to register tract (4) to tract (5). Consider the displacement vector field $u = (u_1, u_2, u_3)$ between ζ^{-1} and η^{-1}. We will search an appro-

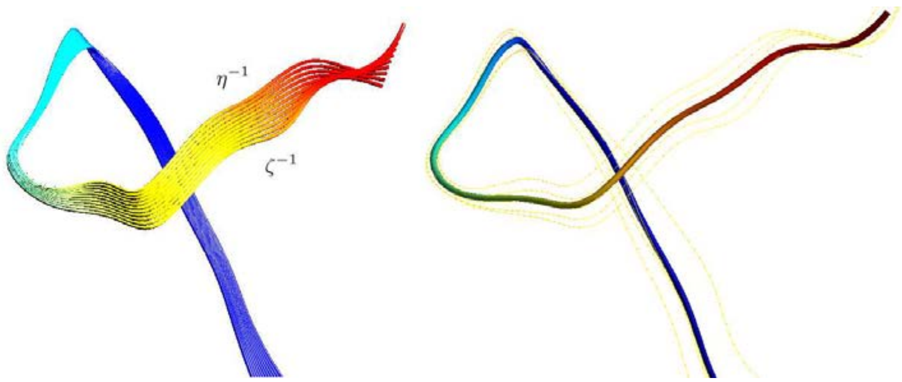

Fig. 4. Left: the trajectory of registration from ζ^{-1} to η^{-1} is represented as other intermediate tracts. The intermediate tracts are artificially generated using the optimal displacement u^*: $\zeta^{-1} + \alpha u^*$, where $\alpha \in [0, 1]$. Right: average of a bundle consisting of 5 tracts.

priate displacement u in the subspace $\mathcal{H}_k$ such that the discrepancy between $\zeta^{-1}(t) + u(t)$ and $\eta^{-1}(t)$ is minimized. The discrepancy ρ between two surfaces is measured as the integral of the sum of squared distance:

$$\rho(\zeta^{-1} + u, \eta^{-1}) = \int_0^1 \|\zeta^{-1}(t) + u(t) - \eta^{-1}(t)\|^2 \, dt. \tag{6}$$

Let u^* be the optimal displacement satisfying

$$u^*(t) = \arg \min_{u \in \mathcal{H}_k} \rho(\zeta^{-1} + u, \eta^{-1}). \tag{7}$$

Then we claim that the optimal displacement is given by

$$u^*(t) = \sum_{l=0}^{k} (d_{l1} - c_{l1}, d_{l2} - c_{l2}, d_{l3} - c_{l3}) \psi_l(t). \tag{8}$$

The proof requires substituting ζ^{-1} and η^{-1} with the cosine series expansion and letting

$$u(t) = \sum_{l=0}^{k} (\beta_{l1}, \beta_{l2}, \beta_{l3}) \psi_l(t)$$

in the expression (6). Then the expression becomes the unconstrained positive definite quadratic program with respect to β_{lj}. So the global minimum always exists and obtained by differentiating with respect to β_{lj}. Note that $\rho(\zeta^{-1} + u^*, \eta^{-1}) = 0$. Figure 4 shows how the tract ζ^{-1} is registered to the other tract η^{-1}.

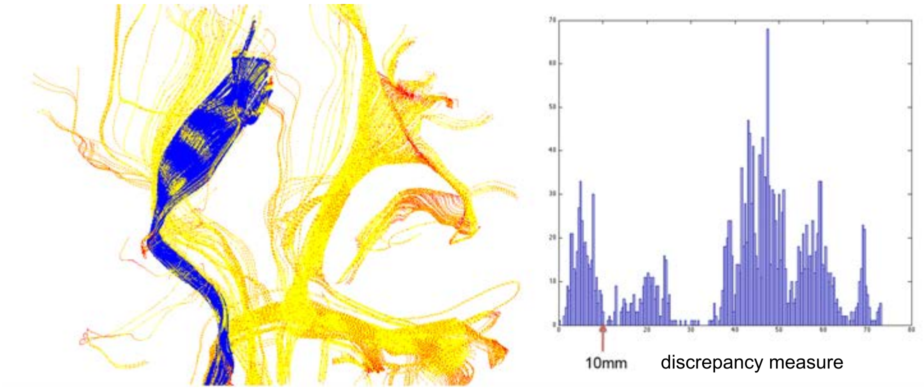

Fig. 5. Left: Right: histogram of discrepancy measure from a reference tract. Thresholding at 10mm gives the blue colored tracts.

Based on the idea of registering tracts by matching Fourier coefficients, we have constructed the average of a white fiber bundle consisting of m tracts as

$$\overline{\zeta^{-1}}(t) = \sum_{l=0}^{k} (\overline{c_{l1}}, \overline{c_{l2}}, \overline{c_{l3}})\psi_l(t), \tag{9}$$

where $\overline{c_{li}}$ is the sample mean of the coefficients corresponding to the i-th coordinate for m tracts. As an illustration, we show how to average five tract in Figure 4.

2.4 White Matter Fiber Segmentation

Based on the discrepancy measure ρ, we have investigated the feasibility of shape-based fiber bundle segmentation. Given two cosine series representation of tracts ζ^{-1} and η^{-1}, the discrepancy measure is simplified as

$$\begin{aligned}\rho(\zeta^{-1}, \eta^{-1}) &= \int_0^1 \left\|\zeta^{-1}(t) - \eta^{-1}(t)\right\|^2 \, dt \\ &= \int_0^1 \sum_{j=1}^{3} \left[\sum_{l=0}^{k} (c_{lj} - d_{lj})\psi_l(t)\right]^2 \, dt \\ &= \sum_{j=1}^{3} \sum_{l=0}^{k} (c_{lj} - d_{lj})^2.\end{aligned}$$

We have used the orthonormality condition (3) in removing the integral in the expression. The advantage of our discrepancy measure is that it is automatically obtained once the cosine series representations are computed. Among 2172 tracts visualized in Figure 5, one tract in the middle of the blue fiber bundle was selected as a reference tract ζ^{-1} then we computed the total discrepancy between the reference tract and the rest of tracts. By normalizing the discrepancy by the total arc-length of ζ^{-1}, we obtain the mean discrepancy measure along the tract. The histogram of the mean discrepancy is given in Figure 5. The histogram shows significant clustering in about 5 clusters. Since the histogram is visibly so well clustered, we did not use any automatic clustering algorithm. 357 tracts within the 10mm discrepancy error are selected and colored blue.

We have proposed a reference tract based segmentation using the discrepancy measure ρ. We can extend the proposed framework to segmenting multiple bundles. Given a collection of tracts $\zeta^{(1)}, \cdots, \zeta^{(n)}$, we measure cross discrepancy

$$\rho_{ij} = \rho(\zeta^{(i)}, \zeta^{(j)}).$$

We may need to normalize ρ_{ij} with the total arc-lengths. Then we can construct the discrepancy matrix (ρ_{ij}) and apply various classification techniques used in clustering correlation matrices [5] [31] for automatic clustering of tracts.

3 Conclusion

We have presented a unified parametric representation of white matter fiber tracts. The method explicitly models tracts using the orthonormal cosine basis. The model parameter estimation is done in the least squares fashion in a computationally efficient manner. The 19 degree representation is found to be sufficient within the 0.26mm reconstruction error. The representation will parameterize tracts of varying length and shape with 60 parameters achieving significant data reduction. The representation is used to register, average and segment tracts in a unified Hilbert space framework. Future work will attempt to use these parametric tract shape measures to perform automatic tract extraction, characterization of tract morphologic shape in different population groups, and multiple subject spatial normalization and tract segmentation.

Acknowledgement

This work was supported by NIH Mental Retardation/Developmental Disabilities Research Center (MRDDRC Waisman Center), NIMH 62015 (ALA), NIMH MH080826 (JEL) and NICHD HD35476 (University of Utah CPEA).

References

1. K. Arfanakis, M. Gui, and Lazar M. Optimization of white matter tractography for pre-surgical planning and image-guided surgery. *Oncology Report*, 15:1061–1064, 2006.
2. P.J. Basser, J. Mattiello, and D. LeBihan. MR diffusion tensor spectroscopy and imaging. *Biophys J.*, 66:259–267, 1994.

3. P.J. Basser, S. Pajevic, C. Pierpaoli, J. Duda, and A. Aldroubi. In vivo tractography using dt-mri data. *Magnetic Resonance in Medicine*, 44:625–632, 2000.
4. P.G. Batchelor, F. Calamante, J.D. Tournier, D. Atkinson, D.L. Hill, and A. Connelly. Quantification of the shape of fiber tracts. *Magnetic Resonance in Medicine*, 55:894–903, 2006.
5. P. Blinder, I. Baruchi, V. Volman, H. Levine, D. Baranes, and Jacob. E.B. Functional topology classification of biological computing networks. *Natural Computing*, 4:339–361, 2005.
6. T. Bulow. Spherical diffusion for 3d surface smoothing. *IEEE Transactions on Pattern Analysis and Machine Intelligence*, 26:1650–1654, 2004.
7. M. Catani, R.J. Howard, S. Pajevic, and D.K. Jones. Virtual in vivo interactive dissection of white matter fasciculi in the human brain. neuroimage. *NeuroImage*, 17:77–94, 2002.
8. M.K. Chung, L. Shen Dalton, K.M., A.C. Evans, and R.J. Davidson. Weighted fourier representation and its application to quantifying the amount of gray matter. *IEEE transactions on medical imaging*, 26:566–581, 2007.
9. J.D. Clayden, A.J. Storkey, and M.E. Bastin. A probabilistic model-based approach to consistent white matter tract segmentation. *IEEE Transactions on Medical Imaging*, 11:1555–1561, 2007.
10. T.E. Conturo, N.F. Lori, T.S. Cull, E. Akbudak, A.Z. Snyder, J.S. Shimony, R.C. McKinstry, H. Burton, and M.E. Raichle. Tracking neuronal fiber pathways in the living human brain. In *Natl Acad Sci USA*, volume 96, 1999.
11. A. Gruen and A. Devrim. Least squares 3d surface and curve matching. *ISPRS Journal of Photogrammetry Remote Sensing*, 59:151–174, 2005.
12. X. Gu, Y.L. Wang, T.F. Chan, T.M. Thompson, and S.T. Yau. Genus zero surface conformal mapping and its application to brain surface mapping. *IEEE Transactions on Medical Imaging*, 23:1–10, 2004.
13. A. Gueziec, X. Pennec, and N. Ayache. Medical image registration using geometeric hashing. *IEEE Computational Science and Engineering*, 4:29–41, 1997.
14. P. Jezzard and R.S. Balaban. Correction for geometric distortion in echo planar images from b0 field variations. *Magn. Reson. Med.*, 34:65–73, 2007.
15. D.K. Jones, M. Catani, C. Pierpaoli, S.J. Reeves, S.S. Shergill, M. O'Sullivan, P. Golesworthy, P. McGuire, M.A. Horsfield, A. Simmons, S.C. Williams, and R.J. Howard. Age effects on diffusion tensor magnetic resonance imaging tractography measures of frontal cortex connections in schizophrenia. *Human Brain Mapping*, 27:230–238, 2006.
16. E. Kishon, T. Hastie, and H. Wolfson. 3d curve matching using splines. In *Proceedings of the European Conference on Computer Vision*, pages 589–591, 1990.
17. M. Lazar and A.L. Alexander. Lazar, m. and weinstein, d.m. and tsuruda, j.s. and hasan, k.m. and arfanakis, k. and meyerand, m.e. and badie, b. and rowley, h. and haughton, v. and field, a. and witwer, b. and alexander, a.l. *White Matter Tractography Using Tensor Deflection*, 18:306–321, 2003.
18. A. Leemans, J. Sijbers, S. De Backer, E. Vandervliet, and P. Parizel. Multiscale white matter fiber tract coregistration: A new feature-based approach to align diffusion tensor data. *Magnetic Resonance in Medicine*, 55:1414–1423, 2006.
19. S Mori, B.J. Crain, V.P. Chacko, and P.C. van Zijl. Three-dimensional tracking of axonal projections in the brain by magnetic resonance imaging. *Annals of Neurology*, 45:256–269, 1999.
20. S. Mori, W.E. Kaufmann, C. Davatzikos, Stieljes, L. Amodei, K. Fredericksen, G.D. Pearlson, E.R. Melhem, M. Solaiyappan, G.V. Raymond, H.W. Moser, and P.C.

van Zijl. Imaging cortical association tracts in the human brain using diffusion-tensor-based axonal tracking. *Magnetic Resonance in Medicine*, 47:215–223, 2002.

21. M. Mller, J. Frandsen, G. Andersen, A. Gjedde, P. Vestergaard-Poulsen, and L. stergaard. Dynamic changes in corticospinal tracts after stroke detected by fibretracking. *Journal of Neurol. Neurosurg. Psychiatry*, 78:587–592, 2007.
22. C. Nimsky, O. Ganslandt, P. Hastreiter, R. Wang, T. Benner, A.G. Sorensen, and R. Fahlbusch. Preoperative and intraoperative diffusion tensor imaging-based fiber tracking in glioma surgery. *Neurosurgery*, 56:130–137, 2005.
23. P.G. Nucifora, R. Verma, E.R. Melhem, R.E. Gur, and R.C. Gur. Leftward asymmetry in relative fiber density of the arcuate fasciculus. *Neuroreport.*, 16:791–794, 2005.
24. L.J. O'Donnell, M. Kubicki, M.E. Shenton, M.H. Dreusicke, W.E. Grimson, and C.F. Westin. A method for clustering white matter fiber tracts. *American Journal of Neuroradiology*, 27:1032–1036, 2006.
25. L.J. O'Donnell and C.F. Westin. Automatic tractography segmentation using a high-dimensional white matter atlas. *IEEE Transactions on Medical Imaging*, 26:1562–1575, 2007.
26. S. Pajevic, A. Aldroubi, and P.J. Basser. A continuous tensor field approximation of discrete dt-mri data for extracting micro-structural and architectural features of tissues. *Journal of Magnetic Resonance*, 154:85–100, 2002.
27. T.P. Roberts, F. Liu, A. Kassner, S. Mori, and A. Guha. Fiber density index correlates with reduced fractional anisotropy in white matter of patients with glioblastoma. *American Journal of Neuroradiology*, 26:2183–2186, 2005.
28. L. Shen, J. Ford, F. Makedon, and A. Saykin. surface-based approach for classification of 3d neuroanatomical structures. *Intelligent Data Analysis*, 8:519–542, 2004.
29. P. Thottakara, M. Lazar, S.C. Johnson, and A.L. Alexander. Probabilistic connectivity and segmentation of white matter using tractography and cortical templates. *Neuroimage*, 29, 2006.
30. P.A. Yushkevich, H. Zhang, T.J. Simon, and J.C. Gee. Structure-specific statistical mapping of white matter tracts. *Neuroimage*, in press, 2008.
31. A. Zizzari, U. Sniffert, B. Michaelis, G. Gademann, and S. Swiderski. Detection of tumor in digital images of the brain. 2001.

Poster Session

Accelerated Persistent Angular Structure

Ken Sakaie

The Cleveland Clinic, Imaging Institute, 9500 Euclid Avenue,
Mailcode U-15, Cleveland, OH 44195
`sakaiek@ccf.org`

Abstract. Diffusion tensor analysis of even high angular resolution diffusion weighted imaging can yield inaccurate results at points of crossing fibers. Persistent angular structure (PAS) is able to resolve crossing fibers at signal to noise ratios and diffusion weightings that are low but typical of clinical scans, but current implementations require prohibitively long computation times. By reimplementing the PAS calculation, we find that computation times can be dramatically reduced without significant changes in accuracy. Whole-brain mapping of white-matter fiber pathways, which to date is largely hindered by the fiber-crossing problem, may therefore become a more accessible reality.

Key words: Diffusion tensor, Tractography, Partial volume, Crossing fibers

1 Introduction

Diffusion-Weighted Magnetic Resonance Imaging (DW-MRI), together with the diffusion tensor model, can be used to infer the microstructure of tissue noninvasively and *in vivo* [1]. In highly aligned white matter in the brain, the principal eigenvector of the diffusion tensor indicates, on a voxel-by-voxel basis, the local orientation of nerve fibers. Fiber tractography interpolates the local orientation information to map fiber pathways throughout the brain [2],[3]. However, the diffusion tensor model assumes local homogeneity of fiber direction and, in regions of crossing fibers, will provide misleading information [4]. This so called crossing fiber problem limits reliable tensor-based tractography to large pathways with highly aligned fibers.

Numerous solutions to the crossing fiber problem have been proposed. Most use a High Angular Resolution Diffusion Imaging (HARDI) [5] acquisition as the basis of a higher-order analysis scheme that can indicate the orientation of multiple fibers. A conceptually straightforward extension of the diffusion tensor model is to fit HARDI data to two or more discrete tensors [5],[6],[7] or multiple diffusion components [8]. Spherical deconvolution [9],[10] describes the HARDI signal as a continuous distribution of single-fiber signals. Higher order tensors [11],[12],[13], other extensions of the tensor [14],[15], and model-free approaches such as q-space [16], q-ball [17], and the diffusion orientation transform [18] can also characterize complex diffusion geometries. Given the large number of analysis methods, it can be difficult to choose an optimal one for a given experiment.

In one of the few quantitative comparisons of analysis methods, Persistent Angular Structure (PAS) was found to be more accurate than Q-ball in clinically accessible ranges of signal-to-noise ratio, diffusion-weighting, and number of diffusion gradient directions [19]. PAS has been shown to be a form of spherical deconvolution, but gains its high degree of noise immunity from a maximum entropy prior implemented by nonlinear optimization [20]. A publicly available implementation of the PAS calculation is incorporated in a powerful, portable, and open-source package, Camino [21]. Unfortunately, the computation time is prohibitively long, requiring *weeks* to analyze a whole-brain dataset on a single processor [22]. However, is the long computation time inherent to the PAS calculation or an artifact of the implementation? In this paper, we examine the impact on accuracy and timing of the following aspects of the PAS calculation:

- The nonlinear optimization uses a numerical integral to calculate an objective function. Camino iterates the numerical integral at ever-finer resolutions as long as the objective function exceeds a threshold. The trade off between accuracy and computation time of the *iteration process* is examined.
- Camino uses a Levenberg-Marquardt algorithm from Numerical Recipes [23] to perform the optimization, which has known inefficiencies [24]. A robust algorithm from the freely available PORT 3 library [25], [26] is implemented to determine the role of the *optimization algorithm.*
- Camino uses Java, which is not considered optimal for numerical computations. The PAS calculation was coded in C++ to determine the role of *programming language.*

2 Theory

DW-MRI measures the relative ease of movement of water with respect to a diffusion sensitizing magnetic field gradient [27]. The gradient is characterized by a wavenumber, $\boldsymbol{q}$, which reflects the strength, duration, and orientation of the diffusion sensitizing gradients [28]. We follow the derivation in Jansons and Alexander [29].

The signal in a given voxel is then given by:

$$A(\boldsymbol{q}) = A^*(0) \int_{\mathrm{I\!R}^3} p(\boldsymbol{x}) \exp(i\boldsymbol{q} \cdot \boldsymbol{x}) d\boldsymbol{x} \tag{1}$$

where $A^*(0)$ is the signal in the absence of the diffusion sensitizing gradient and $p(\boldsymbol{x})$ is the probability of water displacement along $\boldsymbol{x}$.

The PAS is a projection of features of $p(\boldsymbol{x})$ on the sphere. Peaks of the PAS reflect underlying fiber orientations. When first introduced, noise immunity was built into the PAS through the principle of maximum entropy [29], yielding the following functional form:

$$pas(\hat{\boldsymbol{x}}) = \exp\left(\sum_{j=0}^{N} \lambda_j \cos(\hat{\boldsymbol{q}} \cdot r\hat{\boldsymbol{x}})\right) \tag{2}$$

where λ are lagrange multipliers introducing constraints from the data. Unit vectors $\hat{\boldsymbol{q}}$ and $\hat{\boldsymbol{x}}$ specify the orientation of the diffusion-sensitizing magnetic field gradients and the orientational coordinates of the PAS, respectively. The constant scalar r is the radius on which features of $p(\boldsymbol{x})$ are projected and effectively controls the sharpness of features of the PAS. Antipodal symmetry of diffusion in assumed. The PAS has been shown to be equivalent to the fiber orientation distribution introduced by Tournier in his development of spherical deconvolution [20].

3 Code Implementation

Calculation of the PAS involves minimization, with respect to the lagrange multipliers, of the root-mean-square difference between the calculated (equation 1) and measured signal. The Camino implementation of the calculation uses a Levenberg-Marquardt algorithm based on that given in Numerical Recipes [23]. Each step of the minimization requires a numerical integration of equation 1 over the unit sphere. The numerical integral is performed by summing over a set of points on the sphere [30], P, containing 1082 points. The error is calculated by comparison with a large set of points, Q, containing 122500 points. While the error is larger than a preset threshold, the calculation is repeated with successively larger sets, P, containing 1922, 4322, 8672, 15872, and 32672 points. The computational cost largely resides in the numerical integration step and rises rapidly as the size of the set of points increases. This iterative error-checking methodology is therefore a likely source of computational inefficiency.

A practical approach was taken to weigh different contributions to accuracy and computation time. The same simulated and in-vivo diffusion-weighted data were evaluated by four different sets of code:

1. **Camino**: The original Camino implementation of the PAS calculation was used as a baseline for accuracy and computation time.
2. **FastCamino**: Camino was re-compiled so that only the smallest set of points was used in the calculation. This configuration is used to evaluate the role of the iterative error-checking methodology.
3. **NR-C**: The PAS calculation was performed in C using the Levenberg-Marquardt algorithm, mrqmin.c, from Numerical Recipes and the smallest set of points for the numerical integration. When compared with the Fast-Camino, this configuration compares the performance of Java and C.
4. **PORT**: The Levenberg-Marquardt algorithm was replaced by a trust-region algorithm, N2G, from the PORT 3 library using the smallest set of points for the numerical integration. This algorithm is reputed to perform better than standard Levenberg-Marquardt algorithms, particularly when residuals are large [31]. When compared with NR-C, this configuration provides an assessment of the role of fit algorithm in the PAS calculation.

Camino version 2, revision 490 and Java version 1.5.0_07 were used. The Numerical Recipes library [23] was compiled with the gnu C compiler, gcc version 4.1.2.

The PORT library was compiled by the gnu fortran compiler, g77 version 3.4.6. The libraries were linked to a homebuilt C++ program using g++, version 4.1.2. Calculations were performed on Linux cluster with five 2.33 GHz quad-core Intel Xeon processors.

4 Test Data

Simulated signal mimicking isotropic diffusion, a single fiber, and two crossing fibers with crossing angles of 30°, 60°, and 90° were generated. Diffusivity of $0.7 \times 10^{-3} mm^2/sec$ was used for the isotropic signal. Single fiber signals were generated using the diffusion tensor model [1] with eigenvalues of $(1.4, 0.35, 0.35) \times 10^{-3} mm^2/sec$. Individual fibers in the crossing fiber configurations had equal partial volume fractions. The acquisition profile had 8 signals without diffusion weighting and 71 diffusion-weighted signals with orientations chosen by an electrostatic repulsion algorithm [32] and b-value of $1000 sec/mm^2$. 1000 Rician noise realizations were generated for each configuration with signal to noise ratio (SNR) of 20, selected to match the observed SNR *in vivo*.

In vivo data were acquired in a single subject with a protocol that received local internal review board approval. Images were acquired on a 3 tesla Siemens Trio (Siemens Medical Systems, Erlangen Germany) with a 12 channel head coil. Acquisition parameters were: 128 x 128 matrix, 256 x 256 mm FOV, 48 slices 2mm thick, partial fourier fraction 5/8, TE/TR=102/7700 msec, 4 repeats, b-value = $1000 sec/mm^2$, 71 diffusion-weighted image volumes with orientations chosen by an electrostatic repulsion algorithm [32], and 8 b=0 image volumes acquired at equal intervals among the diffusion-weighted volumes. Diffusion weighting was achieved with a twice-refocused spin echo to minimize eddy current artifacts [33]. Motion correction was implemented using FSL [34] by coregistering b=0 image volumes to one another and then coregistering individual diffusion-weighted images to the mean b=0 volume using an affine transformation. SNR in white matter is approximately 20.

5 Evaluation

For simulated data, mean and standard deviation surfaces, among noise realizations, of the PAS for each fiber configuration [9] were generated for qualitative evaluation.

Quantitative comparisons were performed by calculating the correlation function, as proposed by Anderson [35], between equivalent PAS generated by each new code implementation and the PAS generated by the original Camino implementation. The correlation function ranges from 0 to 1, with 0 indicating no correlation and 1 indicating perfect correlation. An advantage of the correlation function is that it compares functions as a whole.

Accuracy of peak positions, for simulated data, was also assessed. Peak positions were calculated using the *sfpeaks* function from Camino [21]. Peaks were grouped into sets that were nearest one of the true peaks, and the mean direction and sample spherical variance [36] were calculated for each set. The sample spherical variance ranges from ∼0, corresponding to highly aligned peaks, to ∼1, corresponding to highly dispersed peaks. Computation time was also recorded and is reported as that required by a single cpu.

6 Results and Discussion

A qualitative assessment of accuracy is given by visualizing glyphs representing the PAS amplitude in space. Figure 1 depicts the mean and (mean + standard deviation) surfaces [9] of the PAS for each fiber configuration and code implementation. Differences among the code implementations are slight, indicating that all methods have consistent performance in terms of accuracy. Note that, for the low-angle crossing of 30°, separate peaks are not resolved, consistent with the performance of other fiber resolution methods [37],[38].

A quantitative assessment of consistency is determined by calculation of correlation functions. For each noise realization of simulated data and for each voxel of in vivo data, the correlation function was calculated between each of the new code implementations and standard Camino implementation. The results are summarized in table 1. The mean and standard deviation among all noise realizations for all fiber configurations and for in vivo data are reported. Note that FastCamino, in which iterative error-checking is disabled, results in PAS that are nearly identical to those generated with the standard implementation.

Table 1. Correlation function(mean±sd) [10] between standard Camino and other code implementations

Code Implementation	Simulated Data	*In Vivo* Data
Fast Camino	0.998±0.018	0.999±0.012
NR-C	0.958±0.037	0.91±0.019
PORT	0.925±0.086	0.81±0.017

Peak position accuracy is reported for simulated data in table 2. Reported values are for one of the peaks from the 60° crossing fiber configuration. Zenith and azimuth angles and spherical variance are comparable among all code implementations. For comparison, the true zenith and azimuth angles are 60° and 0°, respectively, and the ideal value of spherical variance is zero.

Computation times are reported in table 3, and are reported as equivalent single-cpu times. The mean computation time among all fiber configurations is reported for each code implementation, equivalent to computation time for 1000 voxels of data. The in vivo dataset contains 130995 voxels in tissue, typical for a whole-brain acquisition. By comparing the computation time of FastCamino

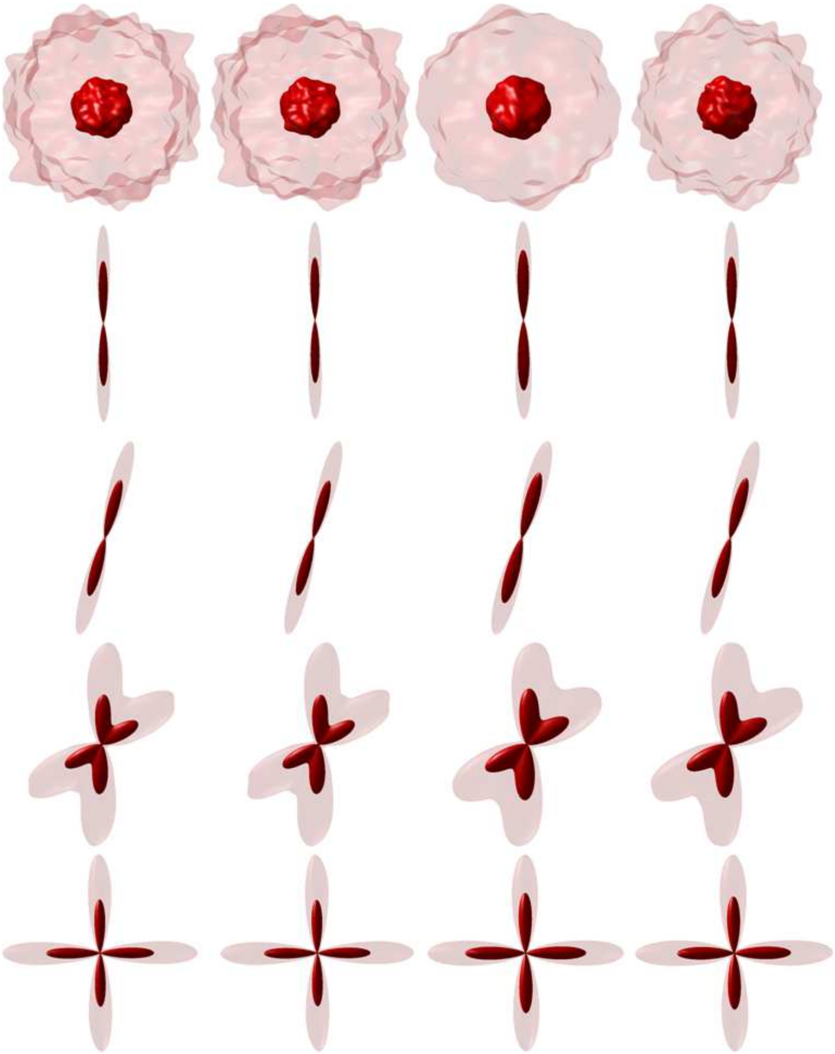

Fig. 1. PAS calculated using (*left to right*) Camino, FastCamino, NR-C, and PORT from simulated data (SNR=20) for (*top to bottom*) isotropic diffusion, a single fiber, and fibers crossing at 30°, 60°, and 90°.

Table 2. Zenith and azimuth angles (*degrees*) of mean direction and sample spherical variance for one peak from simulated data, 60° crossing fiber configuration

Code Implementation	Zenith Angle	Azimuth Angle	Sample Spherical Variance
Camino	67.03	1.39	0.142
Fast Camino	66.95	1.45	0.146
NR-C	67.74	1.78	0.145
PORT	67.00	1.80	0.150

with standard Camino, it can be seen that a huge portion of the computation time is consumed by the iterative error-checking. Combined with the results from the correlation function analysis above, these results suggest that vast improvements in efficiency can be achieved through modification of the error-checking scheme without incurring significant changes in accuracy. Comparison of Fast-Camino and NR-C yields the surprising result that Java actually performs the calculation faster than C. Finally, implementation of a trust-region fit algorithm from the PORT library suggests that computation time can be reduced substantially to a level that is competitive with Markov Chain Monte Carlo Methods [6],[39],[34]. Although the correlation of PORT with Camino is the lowest among the comparisons, visualization of the PAS from simulations (figure 1) and in vivo (figure 2) suggest consistency in orientation information.

Table 3. Single-cpu computation times for simulated (1000 voxels) and *in vivo* (130995 voxels) data

Code Implementation	Simulated Data (*minutes*)	*In Vivo* Data (*hours*)
Camino	1574	806
Fast Camino	41	52
NR-C	118	136
PORT	10	24

7 Conclusion

This study indicates that dramatic improvements in the performance of the PAS calculation can be achieved by changes to certain aspects of the implementation. Of particular interest is the high accuracy of the PORT algorithm even with a small set of points for numerical integration. The PAS calculation is still rather long for clinical use or for studies of large numbers of subjects. However, the substantial improvement in computation time without large penalty in accuracy suggests that PAS may become a more widely useful method. PAS has been

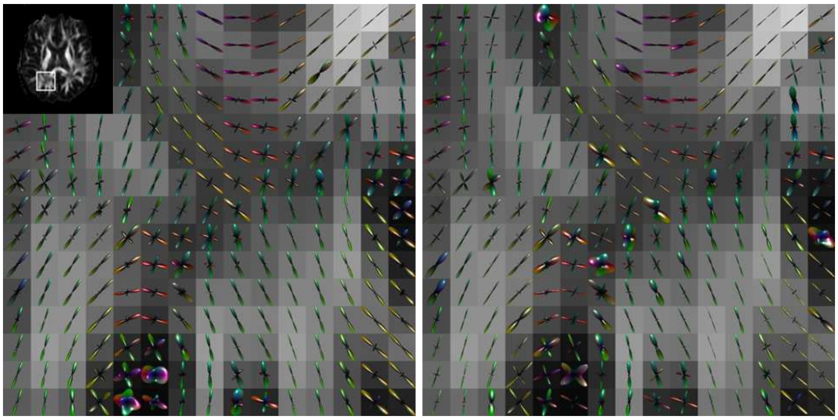

Fig. 2. PAS calculated from in vivo data by Camino (*left*) and PORT (*right*) in a region depicted by a white box on a fractional anisotropy map (*inset*).

shown to accurately resolve crossing fibers even at relatively low SNR and low b-values [19] that are typical of clinical scans. As whole-brain fiber tractography is largely hindered by the crossing fiber problem, a practical implementation of PAS may facilitate more routine mapping of white matter fiber pathways over larger regions of the brain.

Acknowledgments. The author acknowledges support from the National Multiple Sclerosis Society (grant RG 3751-B-2). Thanks to Mark Lowe for valuable comments and to Derrek Tew, Devjani Bedakar, and Jian Lin for data acquisition and processing.

References

1. Basser, P.J., Mattiello, J., LeBihan, D.: MR diffusion tensor spectroscopy and imaging. Biophys J 66, 259-267 (1994)
2. Mori, S., Crain, B.J., Chacko, V.P., van Zijl, P.C.: Three-dimensional tracking of axonal projections in the brain by magnetic resonance imaging. Ann Neurol 45, 265-269 (1999)
3. Conturo, T.E., Lori, N.F., Cull, T.S., Akbudak, E., Snyder, A.Z., Shimony, J.S., McKinstry, R.C., Burton, H., Raichle, M.E.: Tracking neuronal fiber pathways in the living human brain. Proc Natl Acad Sci U S A 96, 10422-10427 (1999)
4. Alexander, A.L., Hasan, K.M., Lazar, M., Tsuruda, J.S., Parker, D.L.: Analysis of partial volume effects in diffusion-tensor MRI. Magn Reson Med 45, 770-780 (2001)
5. Tuch, D.S., Reese, T.G., Wiegell, M.R., Makris, N., Belliveau, J.W., Wedeen, V.J.: High angular resolution diffusion imaging reveals intravoxel white matter fiber heterogeneity. Magn Reson Med 48, 577-582 (2002)
6. Behrens, T.E., Berg, H.J., Jbabdi, S., Rushworth, M.F., Woolrich, M.W.: Probabilistic diffusion tractography with multiple fibre orientations: What can we gain? Neuroimage 34, 144-155 (2007)

7. Kreher, B.W., Schneider, J.F., Mader, I., Martin, E., Hennig, J., Il'yasov, K.A.: Multitensor approach for analysis and tracking of complex fiber configurations. Magn Reson Med 54, 1216-1225 (2005)
8. Assaf, Y., Basser, P.J.: Composite hindered and restricted model of diffusion (CHARMED) MR imaging of the human brain. Neuroimage 27, 48-58 (2005)
9. Tournier, J.D., Calamante, F., Gadian, D.G., Connelly, A.: Direct estimation of the fiber orientation density function from diffusion-weighted MRI data using spherical deconvolution. Neuroimage 23, 1176-1185 (2004)
10. Anderson, A.W.: Measurement of fiber orientation distributions using high angular resolution diffusion imaging. Magn Reson Med 54, 1194-1206 (2005)
11. Liu, C., Bammer, R., Acar, B., Moseley, M.E.: Characterizing non-Gaussian diffusion by using generalized diffusion tensors. Magn Reson Med 51, 924-937 (2004)
12. Ozarslan, E., Mareci, T.H.: Generalized diffusion tensor imaging and analytical relationships between diffusion tensor imaging and high angular resolution diffusion imaging. Magn Reson Med 50, 955-965 (2003)
13. Descoteaux, M., Angelino, E., Fitzgibbons, S., Deriche, R.: Apparent diffusion coefficients from high angular resolution diffusion imaging: estimation and applications. Magn Reson Med 56, 395-410 (2006)
14. Zhan, W., Gu, H., Xu, S., Silbersweig, D.A., Stern, E., Yang, Y.: Circular spectrum mapping for intravoxel fiber structures based on high angular resolution apparent diffusion coefficients. Magn Reson Med 49, 1077-1088 (2003)
15. Jensen, J.H., Helpern, J.A., Ramani, A., Lu, H., Kaczynski, K.: Diffusional kurtosis imaging: the quantification of non-gaussian water diffusion by means of magnetic resonance imaging. Magn Reson Med 53, 1432-1440 (2005)
16. Wedeen, V.J., Hagmann, P., Tseng, W.Y., Reese, T.G., Weisskoff, R.M.: Mapping complex tissue architecture with diffusion spectrum magnetic resonance imaging. Magn Reson Med 54, 1377-1386 (2005)
17. Tuch, D.S.: Q-ball imaging. Magn Reson Med 52, 1358-1372 (2004)
18. Ozarslan, E., Shepherd, T.M., Vemuri, B.C., Blackband, S.J., Mareci, T.H.: Resolution of complex tissue microarchitecture using the diffusion orientation transform (DOT). Neuroimage 31, 1086-1103 (2006)
19. Alexander, D.C.: Multiple-fiber reconstruction algorithms for diffusion MRI. Ann N Y Acad Sci 1064, 113-133 (2005)
20. Alexander, D.C.: Maximum entropy spherical deconvolution for diffusion MRI. Inf Process Med Imaging 19, 76-87 (2005)
21. Cook, P.A., Bai, Y., Nedjati-Gilani, S., Seunarine, K.K., Hall, M.G., Parker, G.J., Alexander, D.C.: Camino: Open-Source Diffusion-MRI Reconstruction and Processing. In: 14th Scientific Meeting of the ISMRM, p. 2759. Seattle (2006)
22. Sakaie, K.E.: How Fast Can PAS Go? In: 16th Scientific Meeting of the ISMRM, p. 3323. Toronto (2008)
23. Press, W.H., Teukolsky, S.A., Vetterling, W.T., Flannery, B.P.: Numerical Recipes in C. Cambridge University Press, Cambridge (1992)
24. Hanson, R.J.: Cooking with 'Numerical Recipes' on a PC. SIAM News 28, 18 (1990)
25. Blue, J., Fox, P., Fullerton, W., Gay, D., Grosse, E., Hall, A., Kaufman, L., Petersen, W., Schryer, N.: PORT Mathematical Subroutine Library. 1997.
26. Netlib Repository at UTK and ORNL. `http://www.netlib.org/port`
27. Stejskal, E.O., Tanner, J.E.: Spin Diffusion Measurements: Spin Echoes in the Presence of a Time-Dependent Field Gradient. J Chem Phys 42, 288-292 (1964)
28. Callaghan, P.T.: Principles of Magnetic Resonance Microscopy. Oxford University Press, Oxford (1991)

29. Jansons, K.M., Alexander, D.C.: Persistent angular structure: new insights from diffusion magnetic resonance imaging data. Inverse Problems 19, 1031-1046 (2003)
30. Hardin, R.H., Sloane, N.J.A., Smith, W.D.: Tables of spherical codes with icosahedral symmetry. 2000.
31. Nocedal, J., Wright, S.J.: Numerical Optimization, ed. Glynn, P.,Robinson, S.M. Springer-Verlag, New York (1999)
32. Jones, D.K., Horsfield, M.A., Simmons, A.: Optimal strategies for measuring diffusion in anisotropic systems by magnetic resonance imaging. Magn Reson Med 42, 515-525 (1999)
33. Reese, T.G., Heid, O., Weisskoff, R.M., Wedeen, V.J.: Reduction of eddy-current-induced distortion in diffusion MRI using a twice-refocused spin echo. Magn Reson Med 49, 177-182 (2003)
34. Smith, S.M., Jenkinson, M., Woolrich, M.W., Beckmann, C.F., Behrens, T.E., Johansen-Berg, H., Bannister, P.R., De Luca, M., Drobnjak, I., Flitney, D.E., Niazy, R.K., Saunders, J., Vickers, J., Zhang, Y., De Stefano, N., Brady, J.M., Matthews, P.M.: Advances in functional and structural MR image analysis and implementation as FSL. Neuroimage 23 Suppl 1, S208-219 (2004)
35. Anderson, A.W.: Theoretical analysis of the effects of noise on diffusion tensor imaging. Magn Reson Med 46, 1174-1188 (2001)
36. Mardia, K.V., Jupp, P.E.: Directional Statistics. Wiley Series in Probability and Statistics. John Wiley & Sons, Ltd, Chichester, England (2000)
37. Tournier, J.D., Calamante, F., Connelly, A.: Robust determination of the fibre orientation distribution in diffusion MRI: Non-negativity constrained super-resolved spherical deconvolution. Neuroimage 35, 1459-1472 (2007)
38. Zhan, W., Yang, Y.: How accurately can the diffusion profiles indicate multiple fiber orientations? A study on general fiber crossings in diffusion MRI. J Magn Reson 183, 193-202 (2006)
39. Behrens, T.E., Woolrich, M.W., Jenkinson, M., Johansen-Berg, H., Nunes, R.G., Clare, S., Matthews, P.M., Brady, J.M., Smith, S.M.: Characterization and propagation of uncertainty in diffusion-weighted MR imaging. Magn Reson Med 50, 1077-1088 (2003)

Adaptive Distance Learning Scheme for Diffusion Tensor Imaging using Kernel Target Alignment

P.R. Rodrigues[1], A. Vilanova[1], T.Twellmann[2], and B.M. ter Haar Romeny[1]

[1] Department of Biomedical Engineering, Eindhoven University of Technology,
WH 2.103, 5600 MB Eindhoven, The Netherlands
`P.R.Rodrigues@tue.nl`
[2] MeVis Medical Solutions AG, Universitätsallee 29, 28359 Bremen, Germany

Abstract. In segmentation techniques for Diffusion Tensor Imaging (DTI) data, the similarity of diffusion tensors must be assessed for partitioning data into regions which are homogeneous in terms of tensor characteristics. Various distance measures have been proposed in literature for analysing the similarity of diffusion tensors (DTs), but selecting a measure suitable for the task at hand is difficult and often done by *trial-and-error*.

We propose a novel approach to semiautomatically define the similarity measure or combination of measures that better suit the data. We use a linear combination of known distance measures, jointly capturing multiple aspects of tensor characteristics, for comparing DTs with the purpose of image segmentation. The parameters of our adaptive distance measure are tuned for each individual segmentation task on the basis of user-selected ROIs using the concept of Kernel Target Alignment. Experimental results support the validity of the proposed method.

1 Introduction

Diffusion Weighted MRI [1] constitutes a valuable tool that allows a non-invasive look at fibrous structures. Among the most important applications of Diffusion Tensor Imaging (DTI) is the study of brain connectivity or of the fibrous structure of muscle tissue such as the heart [2,3]. DTI has also been used to identify subtle abnormalities in several diseases such as stroke schizophrenia and multiple sclerosis [4].

In DTI more than six gradient directions are scanned, enough to compute the *diffusion tensor* (DT) per voxel, representing the local pattern of directional tissue diffusivity. The diffusion tensor is represented by a 3×3 positive definite symmetric matrix $\mathbf{D}$. The diffusion coefficients in each direction $\boldsymbol{r}$ are given by $\boldsymbol{r}^T\mathbf{D}\boldsymbol{r}$.

A common way to visualise the tensor data (Vilanova et al. [2]) is by fiber tracking. Given the DT field, fiber tracking techniques try to reconstruct the fibrous structures (i.e., fiber tracts).

In several applications, such as comparison between subjects, it is interesting to segment structures at a higher semantic level, e.g. coherent white matter bundles such as the *corpus callosum*, [5–7]. It is also necessary to derive statistical properties of diffusion tensors (DTs) to identify differences in tissue morphology, e.g., between healthy and pathological areas [4]. For these reasons, clustering techniques have been used to group individual fiber tracts into coherent structures [8]. However these methods deal with derived structures from the tensor field (i.e., do not use directly the original full tensor information). Therefore they are very sensitive to the used fiber tracking method and the parameter setting of those. An alternative to clustering fibers is the direct segmentation of the tensor field in volumetric regions. These methods assume that tensors will belong to the same bundle if they are similar to each other. Several segmentation techniques have been presented in the last years [5–7, 9–11]. These techniques require the notion of (dis)similarity of two DTs, i.e., a measure which indicates when a tensor is considered to be similar enough to belong to the same region. Clearly, the segmentation results are highly dependent on the choice of measure. So here again the problem of how to define distance (or other dissimilarity measures) in the DTI codomain imposes itself. Different similarity measures for DTs have been introduced in the past. Alexander et al. [12] and Peeters and Rodrigues et al [13] extensively analysed the different (dis)similarity measures, which are of different nature and sometimes lack physiological significance. Therefore, it is difficult to predict which measure will give better, or similar results. The choice of measure depends on the application at hand. Usually an ad-hoc definition of parameter values and choice of similarity measures is used.

The contribution presented in this paper lies in the assessment of tensor field homogeneity characteristics by automatically determining a suitable parameterised similarity measure simultaneously capturing multiple aspects of tensor characteristics. The results of the presented method can then be used in any segmentation algorithm as, for example, region growing.

This problem of *metric learning* and parameter estimation has been addressed before in the machine learning and pattern recognition literature [14,15]. We extended these methods for the particular problem of diffusion tensor segmentation. With the proposed pre-processing distance learning algorithm, the parameters for a segmentation algorithm, Region Growing, are inferred from the data. A seeding region is selected (by the user) and the algorithm will segment the spatially connected 3D section with the diffusion tensors that are similar to the initial chosen region and dissimilar to the rest. The initially flexible learning scheme adapts itself to the task at hand. This technique can be used for different segmentation algorithms and for illustration we present the results using region growing.

2 Methods

The main goal of this work is to assess what distance or combination of distances better express the homogeneity characteristics of a structure defined in a tensor field, e.g., the brain. The results of the distance/parameter learning are then used to drive a Region Growing segmentation algorithm (see Figure 1). The distance learning algorithm infers the distance(s) that best discriminates a selected Region of Interest (ROI) from the entire image volume represented by a random sample of DTs. The optimal combination of distances will then be used in the segmentation algorithm and a spatially connected volume of tensors is obtained. Then the user will be able to further improve the process by adding additional negative ROIs, i.e., examples of tensors that are different from the target region and provide complementary information.

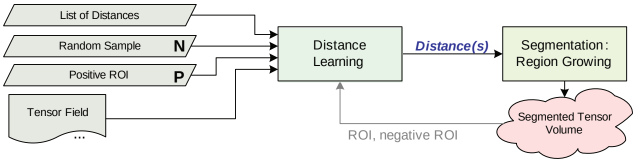

Fig. 1. Global gist of the distance/parameter learning and segmentation

Figure 2 shows the details of the distance learning algorithm. From the tensor field volume data we define a labeled set $\mathbf{S} = (\mathbf{D_i}, l_i)$ of n DTs $\mathbf{D}$ with a label l. The set S is defined as the union of two subsets of DTs: $\mathbf{P}$, a set of representative DTs from a user defined ROI (positive ROI), where $l = +1$; and $\mathbf{N}$, a set of representative DTs for the whole volume (negative ROI), where $l = -1$.

Distance matrices are constructed by calculating the distance between all pairs of tensors in the set $\mathbf{S}$. Each row is considered as a feature vector with the distance from a tensor to all others in the training set. From these feature vectors, symmetric matrices, referred to as kernel matrices (i.e., Gram Matrices), are calculated by computing all possible inner products between each vector. For a uniform behavior of the algorithm, without minding the scale, a normalisation of the individual kernel matrices is performed. Then, with a linear combination of the different kernel matrices, one per considered distance, we define a new kernel matrix $\mathbf{K}$ with a set of unknown parameters (the weights).

Using a grid search based method, the weights are estimated in order to maximize the Kernel Target Alignment measure described in Section 2.3. This maximum gives the best alignment between the kernel matrix $\mathbf{K}$ and an equally sized label matrix, i.e., which combination of distances provides the best discrimination for the considered data.

In the following, we describe the optimization of the kernel target alignment for the distance learning. In Section 2 several elements of the algorithm are introduced and in Section 3 experiments of the distance learning algorithm are presented.

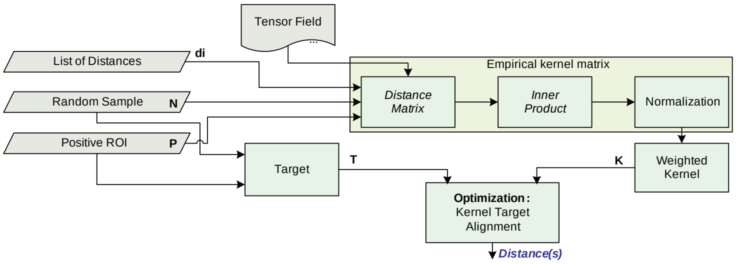

Fig. 2. Detailed scheme of the distance learning algorithm

2.1 Distances

A distance measure d has to be such that $d(\mathbf{A}, \mathbf{B})$ is small if tensors **A** and **B** are similar [13]. The distance learning algorithm does not require the distance to be a metric, the triangle inequality is not a requisite.

Distance measures convey different aspects of a diffusion tensor. While some capture changes in individual degrees of freedom (e.g., difference in anisotropy), others use the full tensor information. Thus their use is sometimes redundant, i.e., different measures describe common tensor attributes. There are measures that use the full tensor, like *Riemannian* based measures, that have a mathematical nature which does not have a direct intuition of the physiological meaning. Thus, the results are not that predictable. Other measures like the ones presented by Kindlmann et al [10] decompose tensor variations into changes in shape and orientation, covered by three invariant gradients and three rotation tangents. In this work, a tunable difference measure between two DTs is introduced. This measure uses a weighted sum of the individual measures. However, the definition of the weights depends on the task. Furthermore, this is only good for very small differences, since the invariant gradient and rotation tangent coordinate frame is not accurately defined for a large difference between tensors. Therefore, we do not use these measures.

In order to show the flexibility of our framework, we evaluate the following set of different distances [13]: difference of FA (ds_{FA}), difference of MD ds_{MD}, angular difference d_{ang1}, Frobenius distance d_{L2}, geometric distance d_g, Log-Euclidean distance d_{LE} and the symmetrized Kullback-Leibler d_{KL}. These measures are chosen because they are distances, $d(\mathbf{D_1}, \mathbf{D_1}) = 0$, symmetric and positive. Other similarity measures could be used, however they must be converted into a distance measure, see Haasdonk et al [16].

2.2 Empirical Kernel Matrices

The main idea of kernel methods is to map the input data (i.e. here distance between tensors) to a feature space provided with a dot product. The mapped data is then dichotomized. A kernel matrix for a measure m, can be regarded as a pairwise similarity (i.e., an element is similar to itself, $m(A, A) = 1$) between all elements of a set, represented in a feature space.

A kernel matrix $\mathbf{K}$ for a set of L feature vectors can be regarded as a matrix of pairwise similarity, measured by their pairwise innerproduct. Each feature vector represents a single object, in our case a DTI voxel. For a set $\mathbf{S} = \mathbf{P} \cup \mathbf{N}$ of L objects o_j, the feature vector $\boldsymbol{f_i} = [d(o_i, o_1), ..., d(o_i, o_L)]$ representing o_i is computed by evaluating a distance measure between o_i and all other objects in $\mathbf{S}$.

As presented in Pekalska et al [17], a kernel $\mathbf{K}$ can be defined as a mapping of the feature vectors $\boldsymbol{f_i}$. The kernel matrix is then the inner-product between the feature vectors

$$K_{ij} \ \equiv < \boldsymbol{f}_i, \boldsymbol{f}_j > = \ \sum_k d(\mathbf{D_i}, \mathbf{D_k}) d(\mathbf{D_j}, \mathbf{D_k}) \tag{1}$$

where K_{ij} is the element in row i and column j of the kernel $\mathbf{K}$.

Each element in the kernel matrix effectively depends on all tensors in the training data. The kernel has high values for similar classes, but close to 0 for inter-class tensors. For geometric interpretation, consider that the inner product depicts the angle between two vectors. Now we have a kernel matrix, i.e., the set of all possible inner products, and it is symmetric and positive definite.

For a uniform behavior of the algorithm, without minding the scale of the used measures, a normalisation must be performed. We can normalise kernel matrices in such a way that the features lie on the surface of a unit hypersphere. This normalisation [18] can be done directly in the kernel as follows:

$$\widetilde{K}(f_i, f_j) = \frac{K(f_i, f_j)}{\sqrt{K(f_i, f_i) K(f_j, f_j)}} \tag{2}$$

A normalised kernel $\mathbf{K}$ from a distance measure m will be referred as $\mathbf{K^m}$.

2.3 Alignment

Christiani et al [19] proposed a method to assess the quality of a binary clustering. This measure, referred to as Kernel Target Alignment (KTA), depicts how good a kernel is with respect to a given set of labeled objects (the target) with the notion of good clustering, i.e., high similarity within clusters and low similarity between clusters. This notion is captured using the Frobenius inner product between these matrices. The Frobenius product between two matrices $\mathbf{V}$, $\mathbf{P}$ is defined as $< \mathbf{V}, \mathbf{P} >_F = \sum_{ij} v_{ij} p_{ij}$.

The *alignment* between two arbitrary kernels $\mathbf{K_1}$ and $\mathbf{K_2}$ is

$$A(\mathbf{K_1}, \mathbf{K_2}) = \frac{< \mathbf{K_1}, \mathbf{K_2} >_F}{\sqrt{< \mathbf{K_1}, \mathbf{K_1} >_F < \mathbf{K_2}, \mathbf{K_2} >_F}} \tag{3}$$

A target matrix is constructed from the set of n tensors $\mathbf{S}$. We define a vector of labels $\mathbf{y} \in \{-1, +1\}^n$ where 1 is the label for the positive set $\mathbf{P}$, and -1 for the negative set **N**. The target is then calculated using the matrix product $\mathbf{T} = \mathbf{y}^T\mathbf{y}$ and the alignment can now be expressed as

$$A(\mathbf{K}, \mathbf{T}) = \frac{<\mathbf{K}, \mathbf{T}>_F}{n\sqrt{<\mathbf{K}, \mathbf{K}>_F}}, \text{ since } <\mathbf{T}, \mathbf{T}>_F = n^2 \tag{4}$$

Linear combination of kernels: In machine learning, the problem of learning an adequate distance metric for the input space of data from a set of similar/dissimilar objects has been addressed in many studies in the recent years like Igel et al [14].

So far, we have a set of normalized kernels $\mathbf{K^m}$, one for each m measure. However, some kernels, i.e. some measures, may be more discriminative than others. Therefore, we introduce new parameters $w_m, m = 1, .., l$, with l as the number of distances to evaluate, and a new kernel will be constructed from the linear combination of the individual kernels:

$$\mathbf{K}(\overline{\mathbf{w}}) = \sum_{m=1}^{l} w_m \mathbf{K^m}, \text{ and } \sum_{m=1}^{l} w_m = 1, \ \overline{\mathbf{w}} = (w_1, ..., w_l), \ \forall_m w_m \geq 0 \tag{5}$$

Now, using the KTA measure, equation 4, with this kernel, and analysing the result of the alignment for different weights will result in assessing which linear combination of measures gives best discrimination for the analysed data. KTA is then a function of the weights w_m and its maximum will give the most appropriate measure, i.e., combination of measures. If the measures are not orthogonal to each other and do not represent specific characteristics of the tensor, a clear interpretation of the resulting weights cannot be given. Furthermore, an unique solution is not, necessarily, achieved. However, we still expect that the method will give a good balance of the measures and they will give good results although we cannot associate to the measures a clear interpretation.

2.4 Parameter Tuning using a Grid-Search based Method

The selection of weights is achieved by maximizing the alignment between the linear combination of kernels **K** and the target matrix **T**

$$argmax_{\overline{w}}(A(\mathbf{K}(\overline{\mathbf{w}}), \mathbf{T})) = argmax_{\overline{w}}\left(\frac{<\mathbf{K}, \mathbf{T}>_F}{n\sqrt{<\mathbf{K}, \mathbf{K}>_F}}\right) \tag{6}$$

To determine the KTA's maximum, a grid-search in the parameter space spanned by the weights w_m is performed. The KTA is calculated at each point on the grid of parameter values, i.e., for each combination of w_m, with the above mentioned constraint, equation 5.

2.5 Region Growing

We apply our method for region growing segmentation as a proof of concept of the presented distance learning method. The weights, $\overline{w}$, that result from the previous distance learning method are used to drive the Region Growing segmentation algorithm. The algorithm starts growing from the initially selected ROI. During the growing process the assignment of voxels is controlled by a voxel-to-neighborhood homogeneity predicate. A voxel is added to the region if its average weighted distance to the neighborhood, i.e., voxels already segmented and directly adjacent, is smaller than the average and standard deviation of the weighted distance between all pair of tensors in the seeding ROI.

3 Results

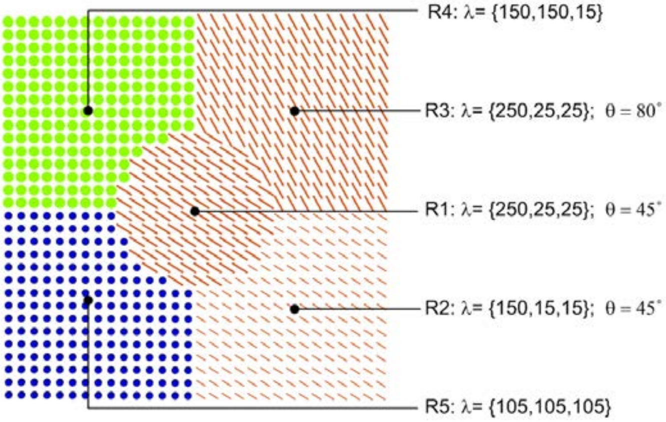

Fig. 3. Superquadric glyphs [20] showing the five distinct regions in a 30 × 30 tensor synthetic image. DTs have λ as eigenvalues.

The synthetic image shown in Figure 3 was designed so that the regions, despite having distinct DTs, share some properties with other region but are different to others., e.g., R1 has the same anisotropy as R2 and R3. With this synthetic data we intend to illustrate the behavior of the presented algorithm.

Considering this, to segment R1 an adequate distance must be chosen, for example d_{FA} would segment R1, R2 and R3. In these tests, the grid search method is done with $step = 0.1$. Choosing a ROI in R1, and randomly sampling 45 DTs, our algorithm estimates $w_{d_{L2}} = 1.0$ as the best discriminating distance. With these parameters, the region growing algorithm successfully segments only R1. Choosing a ROI between R1 and R2, the algorithm estimates a combination of two distances, $w_{d_{FA}} = 0.3$ and $w_{d_{ang1}} = 0.7$. As we can reason, what discriminates these two regions from the rest is their coherent orientation (45 degrees), distinct to R3, and FA, distinct to R4 and R5. The results were computed in a AMD Athlon 64 X2 Dual Core Processor 4800+ 2.41 GHz, with 3GB of RAM. The distance learning algorithm took about 8 seconds, per example.

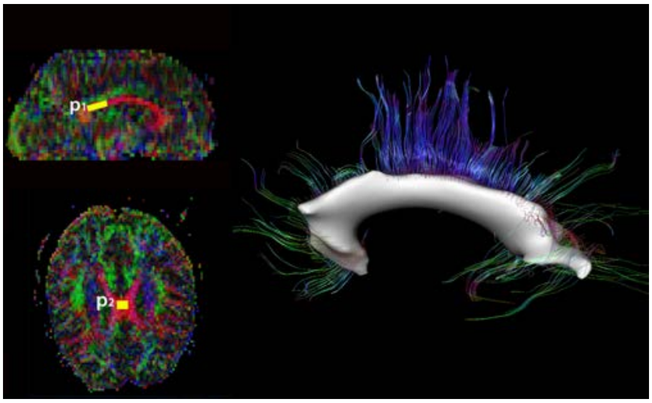

Fig. 4. Right: Fusion of the segmented *corpus callosum*, in a 128 × 128 × 30 DT volume, and the commissural fibers, colored using the typical RGB mapping of the main eigenvector. The estimated combination of distances is $d_{FA} = 0.5$ and $d_{ang1} = 0.5$. **Left:** P_1 and P_2 were used as positive ROIs.

Figure 4 shows the algorithm applied in a DTI brain dataset. Two positive ROIs were selected within the corpus callosum. Because the random sampling of the brain selected several DTs in the gray matter, the algorithm infers d_{FA} as the most suitable measure. This results in the segmentation of the white matter. In order to improve this, a white matter masking is done by sampling of DTs with a FA threshold, i.e., 50 DTs are used as negative examples if $FA > 0.70$. Then, the algorithm estimates $w_{d_{FA}} = 0.5$ and $d_{ang1} = 0.5$ as the best discriminating combination of measures. The obtained result does not capture entirely the corpus callosum, as can be seen by the commissural fibers manually clustered by physicians. The result is not surprising since the defined region of interest does not represent the span of DTs orientations. The distance learning algorithm took 10 seconds to compute.

In Figure 5 a positive ROI was selected within the right cingulum. With 30 random DTs taken with anisotropy $FA > 0.65$, the algorithm took 9 seconds to estimate $w_{d_{ang1}} = 1.0$ as the best measure, since the cingulum is a cylinder-like bundle with DTs coherently aligned.

4 Conclusions and Future Work

We proposed a distance learning method, based on kernel target alignment, for the optimization of Diffusion Tensor Imaging segmentation algorithms. As demonstrated, the method infers the most suitable distance(s) and parameters for the selected segmentation problem from the homogeneity/inhomogeneity characteristics of the data.

The used measures are of different nature and capture different aspects of the tensor data. Some measures isolate changes in individual degrees of freedom

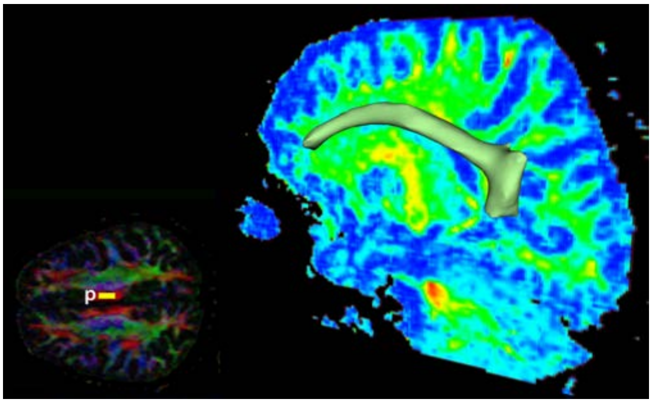

Fig. 5. Right: Right cingulum segmented with estimated $w_{d_{ang1}} = 1.0$, in a 231 × 172 × 131 DT volume, with **p** (yellow) as positive ROI, as seen in the **Left**. The sagittal plane, on the right, shows the FA map while the plane on the left shows the RGB color coding of the main eigenvector (red: sagittal plane; green: transverse plane; blue: coronal plane).

in the tensor data (e.g., difference in anisotropy). However, other measures, e.g., Log-Euclidean distance, d_{LE}, have no physiological significance and yield no clear intuition of distance between tensors. We present an initially flexible learning scheme that infers the combination of measures that give good results. Although, the resulting similarity measure will not be necessarily intuitive.

Furthermore the developed methods can be applied in other segmentation problems. For instance, Schultz [11] extended the use of structure tensors to diffusion tensor fields by combining Kindlmann's invariant gradients and rotation tangents [10,21]. The invariant's weights used to define the distance measure are set in an ad-hoc way. Our framework could help in the definition of the weights needed to tune the segmentation, based on the specific problem at hand.

In this paper, we presented a proof of concept with synthetic data and real data. This shows the potential of the presented method. However, doing a good evaluation is a challenging problem, starting in the definition of a good ground truth.

The grid search method used to find the optimal weights can be improved. As future work, we will investigate other, more computationally efficient, methods to solve the KTA optimization.

The present algorithm can be extended to HARDI (High Angular Resolution Diffusion Imaging) approaches to diffusion. It is still unknown what are the useful distances between two spherical functions such as DOT and Q-ball for applications like segmentation [22,23].

Acknowledgements

This work was supported by: Fundação para a Ciência e a Tecnologia (FCT, Portugal) under grant SFRH/BD/24467/2005, and the Netherlands Organization for Scientific Research (NWO-VENI grant 639.021.407).

References

1. Basser, P.J., Mattiello, J., Lebihan, D.: MR diffusion tensor spectroscopy and imaging. Biophysical Journal **66** (1994) 259–267
2. Vilanova, A., Zhang, S., Kindlmann, G., Laidlaw, D.: An introduction to visualization of diffusion tensor imaging and its applications. In Weickert, J., Hagen, H., eds.: Visualization and Processing of Tensor Fields. Mathematics and Visualization. Springer (2005) 121–153
3. Zhukov, L., Barr, A.H.: Heart-muscle fiber reconstruction from diffusion tensor MRI. In: Proceedings of IEEE Visualization 2003, IEEE Computer Society (2003) 597–602
4. Melhem, E.R., Mori, S., Mukundan, G., Kraut, M.A., Pomper, M.G., van Zijl, P.C.: Diffusion tensor MR imaging of the brain and white matter tractography. American Journal of Roentgenology **178**(1) (2002) 3–16
5. Wang, Z., Vemuri, B.C.: DTI segmentation using an information theoretic tensor dissimilarity measure. IEEE Trans. Med. Imaging **24**(10) (2005) 1267–1277
6. Zhukov, L., Museth, K., Breen, D., Whitaker, R., Barr, A.: Level set modeling and segmentation of DT-MRI brain data. Journal of Electronic Imaging **12**(1) (2003) 125–133
7. Rousson, M., Lenglet, C., Deriche, R.: Level set and region based surface propagation for diffusion tensor mri segmentation. In Sonka, M., Kakadiaris, I.A., Kybic, J., eds.: ECCV Workshops CVAMIA and MMBIA. Volume 3117 of Lecture Notes in Computer Science., Springer (2004) 123–134
8. Moberts, B., Vilanova, A., van Wijk, J.J.: Evaluation of fiber clustering methods for diffusion tensor imaging. In: IEEE Visualization, IEEE Computer Society (2005) 9
9. Lenglet, C., Rousson, M., Deriche, R.: DTI segmentation by statistical surface evolution. IEEE Trans. Med. Imaging **25**(6) (2006) 685–700
10. Kindlmann, G., Ennis, D.B., Whitaker, R.T., Westin, C.F.: Diffusion tensor analysis with invariant gradients and rotation tangents. IEEE Trans. Med. Imaging **26**(11) (November 2007) 1483–1499
11. Schultz, T., Burgeth, B., Weickert, J.: Flexible segmentation and smoothing of DT-MRI fields through a customizable structure tensor. In: Advances in Visual Computing. Lecture Notes in Computer Science, Springer (2006) 455–464
12. Similarity Measures for Matching Diffusion Tensor Images. In: Proc. British Machine Vision Conference BMVC99. (1999)
13. Peeters, T., Rodrigues, P., Vilanova, A., ter Haar Romeny, B.: Analysis of distance/similarity measures for diffusion tensor imaging. In Laidlaw, D.H., Weickert, J., eds.: Visualization and Processing of Tensor Fields: Advances and Perspectives. Springer, Berlin (2008) in Press.
14. Igel, C., Glasmachers, T., Mersch, B., Pfeifer, N., Meinicke, P.: Gradient-based optimization of kernel-target alignment for sequence kernels applied to bacterial gene start detection. IEEE/ACM Trans. Comput. Biol. Bioinformatics **4**(2) (2007) 216–226

15. Schölkopf, S., Mika, B., Burges, S., Knirsch, C., Müller, P., Rätsch, K., Smola, G.: Input space vs. feature space in kernel-based methods. IEEE Transactions on Neural Networks **10**(5) (1999) 1000–1017
16. Haasdonk, B., Bahlmann, C.: Learning with distance substitution kernels. In Rasmussen, C.E., Bülthoff, H.H., Schölkopf, B., Giese, M.A., eds.: Pattern Recognition, 26th DAGM Symposium, August 30 - September 1, 2004, Tübingen, Germany, Proceedings. Volume 3175 of Lecture Notes in Computer Science., Springer (2004) 220–227
17. Pekalska, E., Paclik, P., Duin, R.: A Generalized Kernel Approach to Dissimilarity Based Classification. Journal of Machine Learning Research **2** (2001) 175–211
18. Graf, A.B.A., Borer, S.: Normalization in support vector machines. In: Proceedings of the 23rd DAGM-Symposium on Pattern Recognition, London, UK, Springer-Verlag (2001) 277–282
19. Cristianini, N., Shawe-Taylor, J., Kandola, J.: On kernel target alignment. Proceedings of the Neural Information Processing Systems, NIPS'01 (2002) 367–373
20. Kindlmann, G.: Superquadric tensor glyphs. In: Proceeding of The Joint Eurographics - IEEE TCVG Symposium on Visualization. (May 2004) 147–154
21. Kindlmann, G.L., Estépar, R.S.J., Niethammer, M., Haker, S., Westin, C.F.: Geodesic-loxodromes for diffusion tensor interpolation and difference measurement. In Ayache, N., Ourselin, S., Maeder, A.J., eds.: MICCAI (1). Volume 4791 of Lecture Notes in Computer Science., Springer (2007) 1–9
22. Descoteaux, M., Deriche, R.: Segmentation of q-ball images using statistical surface evolution. In Ayache, N., Ourselin, S., Maeder, A.J., eds.: MICCAI (2). Volume 4792 of Lecture Notes in Computer Science., Springer (2007) 769–776
23. Wassermann, D., Descoteaux, M., Deriche, R.: Diffusion maps clustering for magnetic resonance Q-Ball imaging segmentation. International Journal in Biomedical Imaging (2007) In press.

Brain activation detection using diffusion-weighted and BOLD fMRI: a comparative study

Laurent Risser[1,2], Philippe Ciuciu[1,2], Toshihiko Aso[1,2], and Denis Le Bihan[1,2]

[1] CEA, I^{2}BM, NeuroSpin, F-91191 Gif-sur-Yvette, France,
`firstname.lastname@cea.fr`,
[2] IFR 49, Functional neuroimaging institute, Paris, France *

Abstract. Recent studies have shown that diffusion-weighted functional Magnetic Resonance Imaging (dw-fMRI) could detect brain activity earlier than conventional Blood Oxygen Level-Dependent (BOLD) fMRI. The goal of this paper is to quantitatively and robustly compare these two imaging techniques in terms of ability to detect brain activity and quickness of activations detection. An image sequence analysis algorithm allowing the detection of significant activation has been developed. It also evaluates Hemodynamic Response Functions (HRF) for BOLD sequences and Diffusion Response Functions (DRF) for dw-sequences with a very few hypothesis on their shape. This algorithm is voxel-based and accounts for several sessions simultaneously. It has been applied to different imaging sequences acquired on five subjects using the same experimental design at two different spatial resolutions. For ease of comparison, dw- and BOLD sequences were acquired at each resolution. Compared to dw-sequences, the BOLD sequences have a much higher Signal to Noise Ratio (SNR) and a larger extent of activation. Significant activity was however detected earlier using dw-sequences in certain subjects but not the others. Results in this direction are shown and discussed.

1 Introduction

Functional neuroimaging has enabled major advances in the understanding of the brain. Approach such as BOLD fMRI allows to observe the three dimensional brain activity. Neuronal activity is however indirectly imaged because of delayed neurovascular effects. Alternative functional imaging methods have then been explored [1]. In particular, recent studies [2, 3] have shown that dw-fMRI with strong diffusion weighting could constitute a more direct measure of brain activity than BOLD fMRI. This could bring new insights in the chronometry of neuronal processes underlying brain activation and make easier the comparison with electrical imagery modalities such as EEG/MEG. fMRI sequences acquired using dw-signal are however poorly understood until now. As shown in [4], neuronal activation observed using dw-fMRI could be directly linked to a vascular

---

* The autors thank the Région île de France for funding.

contribution and then be similar to what is already observed on the BOLD signal. Hence, in this work we resort to a reliable approach for comparing both acquisition techniques in terms of detection power and quickness of activations. To this end, we estimate the HRF and DRF time courses in a non-parametric manner.

2 Data description

This study focuses on the analysis of two datasets that differ in terms of spatial resolution. They were both obtained at 3 Tesla in the same neuroimaging centre. For all sequences, an experimental block design consisting of an alternation of four rest and stimulation periods was implemented. Ten seconds stimuli were delivered to the subject every thirty seconds. Visual stimulation was based on contrast-reversing checkerboard. The use of a block design maximizes the contrast to noise ratio between rest and stimulation periods and then makes the detection of activation easier. However it is not optimal for characterizing the DRF or HRF time course since it systematically samples the same time points of these curves. See [5] for details. The first dataset was obtained on two subjects at a relatively low resolution in order to permit an efficient detectability. Slice thickness is 3.8 mm with 50 % gap and in-plane resolution is 3.75×3.75 mm^2. For each session, 140 volumes were scanned at a rate of one volume every second. For each subject, ten sessions have been acquired using spin echo sequences with b=1800 s/mm^2 (high diffusion sensitization), four using b=0 s/mm^2 (without diffusion sensitization) and two using gradient-echo sequences (BOLD signal). For our comparison purpose, BOLD and b=1800 s/mm^2 sequences are of main interest. In this paper, dataset 1 refers to these sequences. The second dataset, referenced dataset 2 in the following, was obtained on three subjects at higher spatial resolution ($2 \times 2 \times 3$ mm^3) to permit more localized analyses at the expense of the SNR. Its main interest is that it permits to study the influence of the diffusion sensitization b. For each subject, ten runs were indeed acquired with b=1200 s/mm^2, with b=1800 s/mm^2 and with b=2400 s/mm^2. Six BOLD sequences were also acquired for each subject. All analyzed images have only undergone slice timing correction and realignment on high resolution anatomical scans. They have however neither been spatially nor temporally filtered.

3 Method

3.1 Presentation

Our study aims at localizing significant activations and evaluating the canonical HRF or DRF to the same stimulus. As far as possible, little assumptions about the response function shapes have to be introduced. Therefore, we have implemented an extension of the voxel-based algorithm described in [6] to a multisession context with heteroscedastic noise (different noise variances across sessions) and variable drift parameters. This extension however assumes constant

HRF and DRF across trials. As presented in [6], HRF and DRF coefficients are estimated in the maximum a posteriori sense. Since, their posterior distribution is Gaussian, their estimates coincide with the posterior mean. The standard deviations derive from the main diagonal of the corresponding covariance matrices.

3.2 HRF and DRF estimation algorithm

For session $i = 1 : I$, model $(\mathcal{M}_i)$ described in [6] reads: $y_i = X_i h + P_i l_i + b_i$ where $y_i \in \mathbb{R}^{N_i}$ is the time series acquired in session i in a given voxel, $h \in \mathbb{R}^{K+1}$ the impulse response, $X_i \in \mathbb{R}^{N_i} \times \mathbb{R}^{K+1}$ the binary onset matrix, $P_i \in \mathbb{R}^{N_i} \times \mathbb{R}^{Q_i}$ the low frequency orthogonal basis, $l_i \in \mathbb{R}^{Q_i}$ the nuisance parameters and $b_i \in \mathbb{R}^{N_i}$ the Gaussian white noise. Impulse response h is the HRF for BOLD sequences and the DRF for dw-sequences.

Binary onset matrices have been built accounting for sustained stimulations, which last about ten seconds. HRF and DRF are then assumed constant across stimulus occurence. It is worth noticing that this assumption could not be tenable in all brain regions.

In [6], the mean of b_i is assumed to vary across sessions but its variance is assumed constant. Here, we consider session-dependent baselines and variances r_i. Noise means are modelled through l_i since P_i contains a constant column. Let $\mathbf{y} = [y_1^t, \ldots, y_I^t]^t$, $\mathbf{l} = [l_1^t | \ldots | l_I^t]^t$ and $\theta = [r_1, \ldots, r_I]$. Assuming that the sessions are independent of each other, the multi-session likelihood reads:

$$\begin{aligned} p(\mathbf{y}|h, \mathcal{M}; \theta, \mathbf{l}) &= \prod_{i=1}^{I} p(y_i|h, \mathcal{M}; r_i, l_i) \\ &= \prod_{i=1}^{I} (2\pi r_i)^{\frac{-N_i}{2}} \exp\left(-||y_i - X_i h - P_i l_i||^2 / 2r_i\right). \end{aligned} \tag{1}$$

Due to the large number of unknown parameters, maximum likelihood estimation may provide unstable results. Hense akin to [6], prior information on the sought DRF or DRF is introduced. Following [6], their amplitude is close to zero at their first and end time points and their variations are supposed to be smooth. The first condition is introduced by setting the first and last parameters of h to zero while the second one is achieved by setting an a priori Gaussian probability function $\mathcal{N}(0, \boldsymbol{R}_H)$ on h. The prior covariance matrix $\sigma_h^2 \boldsymbol{R}$ is built up from $\boldsymbol{R} = (\boldsymbol{D}_2^t \boldsymbol{D}_2)^{-1}$, where $\boldsymbol{D}_2$ approximates the second order derivative and σ_h^2 stands for the prior variance. The Maximum a posteriori (MAP) estimate is then derived from the combination of the likelihood (eq. 1) with the prior density using Bayes' rule:

$$p(h|\mathbf{y}, \mathcal{M}; \theta, \mathbf{l}) \sim \mathcal{N}(\hat{h}^{\mathrm{MAP}}, V) \tag{2}$$

with: $V^{-1} = \sum_{i=1}^{I} \frac{1}{r_i} X_i^t X_i + \sigma_h^{-2} \boldsymbol{R}^{-1}$ and $\hat{h}^{\mathrm{MAP}} = V \sum_{i=1}^{I} \frac{1}{r_i} X_i^t (y_i - P_i \hat{l}_i)$. An Expectation-Conditional-Maximization (ECM) algorithm is used for the simultaneous estimates of h, the underlying hyperparameters (r_i, σ_h^2) and the nuisance variables l_i. This iterative strategy is slightly different from the one described in [6]. After initialization, each iteration follows these steps: (1) Computation of V. (2) Estimation of $\hat{h}^{\mathrm{MAP}}$. (3) $\forall i$: $\hat{l}_i = P_i^t(y_i - X_i\hat{h}^{\mathrm{MAP}})$. (4) $\forall i$: $\varepsilon_i(\hat{l}_i) = ||y_i - P_i\hat{l}_i - X_i\hat{h}^{\mathrm{MAP}}||^2 + tr(X_iVX_i^t)$. (5) $\forall i$: $\hat{r}_i = \varepsilon_i(\hat{l}_i)/N_i$. (6) $\sigma_h^2 = \mathrm{tr}\{(\hat{h}^{\mathrm{MAP}}(\hat{h}^{\mathrm{MAP}})^{+}V_{m,m})\boldsymbol{R}^{-1}\}/(K-1)$. Local convergence is achieved whenever the relative error becomes lower than 10^{-3}.

3.3 Detection of significant activation

The algorithm described above allows voxel-based and multisession estimation of the HRF and DRF coefficients in a Bayesian framework. Activation detection then relies on the comparison of the pointwise estimation of $\hat{h}$ with a zero-valued vector h_0. For doing so, we introduce the null hypothesis H_0: $h = h_0$. When this hypothesis is rejected, the voxel under study is considered as activating. Considering $p(h|\dots) \sim \mathcal{N}(\hat{h}, V)$, one can write that $h - h_0 \sim \mathcal{N}(\hat{h} - h_0, V)$. Let X be the random variable such that $X = [h - h_0] \sim V^{-1/2}(\hat{h} - h_0)$, then X follows a χ^2 distribution with $K-1$ degrees of freedom, where $K-1$ is the number of estimated HRF or DRF coefficients. H_0 is thus rejected whenever the P-value of the χ^2 statistical test satisfies: $P(X \geq X_0) \leq 0.05$, with $X_0 = V^{-1/2}\hat{h}$.

4 Results

4.1 Activation detectability

A subject and sequence type dependent analysis has been applied to the data presented in Section 2. We used the definition presented in subsection 3.3 to study activation detectability and localization of brain activations. P-values for the three imaging sequence types are presented in Fig. 1 for the most interesting slice of Subject 1. Voxels concomitently activating for the three imaging sequence types are also displayed. Activity is detected in the primary visual cortex using BOLD sequences of dataset 1 and 2. Using dw-sequences, activating voxels are also detected in this cortical area at low spatial resolution (Dataset 1). Their number is smaller than using BOLD sequences and seems to decrease for increasing b values. False positives are also observed in other brain regions. This occurs because we do not account for the multiple comparison problem, ie we do not control the presence of at least one false positive in the search volume (FWER). Note that false positives are more numerous in BOLD because of higher SNR.

At high spatial resolution, due to lower SNR, no activation cluster voxels was found for any b-value. In order to measure the influence of b, the signal was averaged over Regions Of Interests (ROIs) located in the primary visual cortex. For each of the three subjects, these ROIs, of about 1000 voxels (2.6×2.6×2.6 cm^3), were manually designed by an expert. Our algorithm was then applied to the mean signal in these ROIs using single-session analyses. Significant activations were found in all 18 BOLD sessions, in (24,21,4) sessions out of 30 for $b = (1200, 1800, 2400)\mathrm{s/mm}^2$, respectively. Such fluctuations are probably due

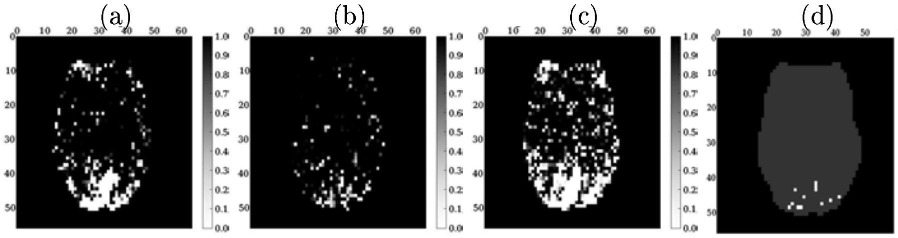

Fig. 1. (a-c) Axial view of the P-values obtained from Slice 2 of Subject 1 when analysing the three imaging sequence types. Radiological conventions are used (left is right). **(a)** P-values for $b = 0$ s/mm^2. **(b)** P-values for $b = 1800$ s/mm^2. **(c)** P-values for the BOLD dataset. **(d)** Voxels considered as activating for the three imaging sequence types in the same slice (in white).

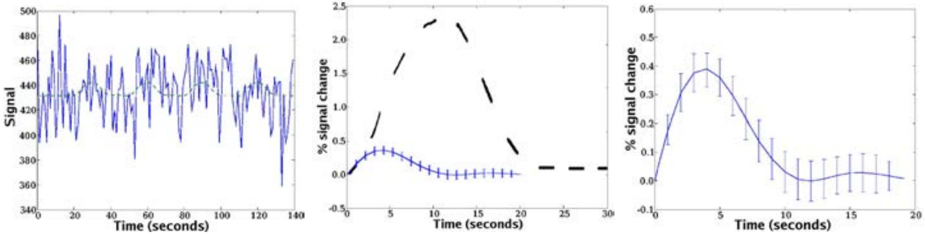

Fig. 2. (left) Fit of the adjusted signal ($b = 1800$ s/mm^2) for session 1 and subject 1 at the voxel $\tilde{v}$ of highest activity. Blue solid line represents the dw-fMRI time serie. Green dashed line depicts the fit $\hat{y}_1$. **(center)** Dashed line represents total % signal changes at $\tilde{v}$. Solid line is the corresponding DRF $\hat{h}$. **(right)** DRF $\hat{h}$ at $\tilde{v}$.

to a decreasing SNR for increasing b values. Mean total percent signal change in significantly activating sessions was about 2.18 % for BOLD sequences and around 0.50 % for dw-sequences. This is maybe due a smaller spatial extent of the region-based activity that can be detected at high diffusion sensitization. Activations detectability in a large averaged ROI is then robust for reasonably high diffusion sensitization but clearly decrease when b>1800s/mm^2.

4.2 HRF and DRF comparison

We aim here at statistically finding whether the voxels eliciting significant activations in the sense already defined present faster activation using dw-fMRI than using classical BOLD fMRI. We also want to characterize the influence of the diffusion sensitization level. In Fig. 2, we show for Subject 1 the DRF estimate $\hat{h}$ and the fit of the adjusted b=1800 s/mm^2 signal $\hat{y}_1$ given by $\hat{y}_1 = X_1\hat{h} + P_1\hat{l}_1$ over the first session ($i = 1$) at the voxel $\tilde{v}$ where the strongest activation occurs. Standard deviations derived from the diagonals of posterior covariance matrix, are reported at each time point of $\hat{h}$.

In dataset 1, in order to only compare significant activations, we extracted the HRF and DRF associated to the voxels which are concomitantly activating for the three imaging sequences. There are 29 and 15 voxels for Subjects 1 and

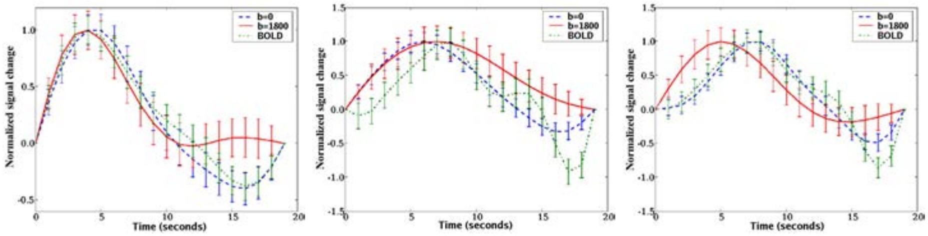

Fig. 3. Normalized HRF and DRF at three voxels. Time-to-peak and time to half-peak are given in seconds in the following order: [$b = 0$ s/mm^2, $b = 1800$ s/mm^2, BOLD]. **(left)** TTP=[4.5, **3.8**, 4.0]. TTHP=[1.3, **1.1**, 1.2]. **(center)** TTP=[**5.8**, 6.9, 7.8]. TTHP=[2.1, **2.1**, 4.2]. **(right)** TTP=[7.6, **4.9**, 7.2]. TTHP=[4.3, **1.6**, 3.9].

2, respectively. Notice that very few additional voxels would have been taken into account with pairwise sequences comparison including $b = 1800$ s/mm^2 sequences. At higher spatial resolution, in dataset 2, no voxel was concomitantly activating for all sequence types. We then studied the averaged signal in the ROI presented in subsection 4.1. HRF and DRF extracted from sessions corresponding to significant activations were taken into consideration. All DRF and HRF estimates were normalized to make their comparison easier. Hence, their peak intensity is set to 1. Fig. 3 depicts the corresponding normalized HRF and DRF estimates at three voxels in subject 1. In dataset 1, for about the third of the 44 voxels, brain activity is detected faster using dw-sequences than using BOLD sequences (see Fig. 3(right)). For about another third of these voxels, the DRF and HRF look similar except in their undershoot part as illustrated in Fig. 3(left). This is probably due to the local high vascular influence at these time points. For the last third of voxels the DRF ($b = 1800$ s/mm^2) are very smooth (see Fig. 3(center)). That might have been the signature of a strong influence of the a priori on the DRF shape. These curves have then been reestimated without prior constraint. It turns out that the non-smoothed DRF have a similar shape. Therefore, the prior constraint reasonably regularizes the DRF estimates. In the second dataset, the shapes of the DRF and HRF curves assessed within the ROI are similar to the shapes presented Fig. 3. They are also highly reproducible along sessions for each imaging sequence type and each subject.

Time-to-peak (TTP) and time to half-peak (TTHP) of the DRF and HRF time courses were extracted and put altogether for each sequence type and subject. Tables 1(a-b) summarize their means and standard deviations. Non-parametric Kruskal-Wallis test was applied to each subject in order to discriminate the sequence types in terms of TTP and TTHP. Differences were considered as significant for P-value lower than 5 %; see Tables 1(c-d) for detail.

No significant difference between $b = 0$ s/mm^2 and $b = 1800$ s/mm^2 sequences was observed in dataset 1. Regarding the comparison between $b = 0$ s/mm^2 and BOLD sequences, we find faster TTP and TTHP using $b = 0$ s/mm^2 sequences but only for Subject 1. Similarly, the TTHP is significantly faster using $b =$

Table 1. (a)-(b) Mean TTP and TTHP in seconds for dataset 1 and dataset 1, respectively. Errors are within parenthesis. **(c)-(d)** P-values of the Kruskal-Wallis tests applied to the TTPs and TTHPs of dataset 1 and dataset 2, respectively.

(a)	Time-to-peak			Time to half-peak		
	b=0	b=1800	BOLD	b=0	b=1800	BOLD
Subject 1	**5.86** (1.30)	6.00 (1.64)	6.72 (1.37)	2.22 (0.96)	**1.91** (0.54)	3.52 (1.55)
Subject 2	**4.85** (1.24)	5.28 (1.35)	5.07 (1.24)	1.83 (0.69)	**1.67** (0.43)	2.03 (0.81)

(b)	Time-to-peak				Time to half-peak			
	b=1200	b=1800	b=2400	BOLD	b=1200	b=1800	b=2400	BOLD
Subject 3	5.41 (0.62)	5.30 (0.57)	**4.60** **(0.14)**	6.03 (0.92)	1.80 (0.41)	**1.70** **(0.31)**	**1.70** **(0.14)**	2.18 (0.95)
Subject 4	4.85 (1.42)	**4.51)** **(0.71)**	NR (NR)	6.20 (1.29)	1.88 (0.29)	**1.41** **(0.18)**	NR (NR)	2.41 (0.97)
Subject 5	4.63 (0.54)	4.48 (0.72)	5.50 (0.70)	**4.23** **(0.79)**	1.42 (0.19)	**1.41** **(0.24)**	1.60 (0.28)	1.53 (0.37)

(c)	Time-to-peak			Time to half-peak		
	b=1800 vs. b=0	b=1800 vs. BOLD	b=0 vs. BOLD	b=1800 vs. b=0	b=1800 vs. BOLD	b=0 vs. BOLD
Subject 1	0.65	0.10	**0.021**	0.50	$\mathbf{10^{-4}}$	$\mathbf{10^{-3}}$
Subject 2	0.37	0.77	0.57	0.76	0.29	0.52

(d)	Time-to-peak			Time to half-peak		
	b=1200 vs. b=1800	b=1200 vs. BOLD	b=1800 vs. BOLD	b=1200 vs. b=1800	b=1200 vs. BOLD	b=1800 vs. BOLD
Subject 3	0.63	0.19	0.15	0.63	0.42	0.51
Subject 4	0.07	0.13	**0.028**	$\mathbf{10^{-3}}$	0.33	**0.016**
Subject 5	0.78	0.76	0.91	0.96	0.67	0.82

1800 s/mm^2 than using BOLD sequences but this only holds for Subject 1. For Subject 2, the mean TTHP is faster using $b = 1800$ s/mm^2 but at a non-significant level. This might be due to an important vascular contribution on the diffusion signal for Subject 2, where the two thirds of the DRF and HRF estimates present numerous similarities. Similarly to what has been observed in the ROI we find significantly faster TTP and TTHP using dw-sequences for only one subject out of three. Interestingly the TTHP is also significantly earlier using $b = 1200$ s/mm^2 than using $b = 1800$ s/mm^2 for this subject. Note that no comparison between b=2400 s/mm^2 and BOLD sequences has been possible because of the poor SNR at $b = 2400$ s/mm^2. These spatially averaged time series have also been studied using subject and sequence type dependent multisession leading to similar conclusions.

5 Discussion

BOLD and dw-sequences performed on five subjects were compared using a non-parametric estimation of their impulse response. Detection power was found much smaller in dw-sequences than in BOLD sequences. This ability to detect brain activations from high resolution diffusion sensitized data (dataset 2) was not sufficient to perform voxel-dependent analyses because of poor SNR. However, significant activity were found in dataset 1 containing two subjects. We have shown that activation detection was found significantly earlier using $b = 1800$ s/mm^2 than using BOLD signal for one subject out of two. In the second dataset, the study of the averaged signal in manually designed ROIs located in the primary visual cortex led to the same result for one subject out of three. One can however note that the activation detection seems slightly earlier using dw-sequences. To conclude, future work should investigate the reasons that might explain this lack of reproductibility across subjects. Complementary analyses (not shown here) seem to indicate that the dw-signal seems to be a mixture of two contributions, one from neuronal origin and the other expressing a vascular component. Hence, ongoing work is devoted to model the DRF as a sum of a canonical HRF weighted by a voxel-dependent non-parametric neuronal component.

References

1. Jasanoff, A.: Bloodless fMRI. Trends in Neurosciences **30**(11) (2007)
2. Le Bihan, D., Aso, T., Urayama, S., Hamakawa, T., Fukuyama, H.: Direct and fast detection of neuronal activation in the human brain with diffusion MRI. Proc. Natl. Acad. Sci. USA **103**(21) (May 2006) 8263–8268
3. Le Bihan, D.: The 'wet mind': water and functional neuroimaging. Phys Med Biol **52**(7) (Mar. 2007) 57–90
4. Miller, K.L., Devlin, D.P.B.H., Robson, M.D., Wise, R.G., Woolrich, M.W., Jezzard, P., Behrens, T.E.: Evidence for a vascular contribution to diffusion FMRI at high b-value. Proc. Natl. Acad. Sci. USA **104**(52) (Dec. 2007) 20967–20972
5. Birn, R., Cox, R., Bandettini, P.A.: Detection versus estimation in event-related fMRI: choosing the optimal stimulus timing. Neuroimage **15**(1) (Jan. 2002) 252–264 Rapid communication.
6. Ciuciu, P., Poline, J.B., Marrelec, G., Idier, J., Pallier, C., Benali, H.: Unsupervised robust non-parametric estimation of the hemodynamic response function for any fMRI experiment. IEEE Trans. Med. Imag. **22**(10) (Oct. 2003) 1235–1251

Brain Fiber Architecture, Genetics, and Intelligence: A High Angular Resolution Diffusion Imaging (HARDI) Study

Ming-Chang Chiang[1], Marina Barysheva[1], Agatha D. Lee[1], Sarah Madsen[1], Andrea D. Klunder[1], Arthur W. Toga[1], Katie L. McMahon[2], Greig I. de Zubicaray[2], Matthew Meredith[2], Margaret J. Wright[3], Anuj Srivastava[4], Nikolay Balov[4], Paul M. Thompson[1]

[1]Laboratory of Neuro Imaging, Dept. of Neurology, UCLA School of Medicine, Los Angeles, CA
[2]Functional MRI Lab., Centre for Magnetic Resonance, Univ. Queensland, Brisbane, Australia
[3]Queensland Institute of Medical Research, Brisbane, Australia
[4]Dept. of Statistics, Florida State University, Tallahassee, FL

Abstract. We developed an analysis pipeline enabling population studies of HARDI data, and applied it to map genetic influences on fiber architecture in 90 twin subjects. We applied tensor-driven 3D fluid registration to HARDI, resampling the spherical fiber orientation distribution functions (ODFs) in appropriate Riemannian manifolds, after ODF regularization and sharpening. Fitting structural equation models (SEM) from quantitative genetics, we evaluated genetic influences on the Jensen-Shannon divergence (JSD), a novel measure of fiber spatial coherence, and on the generalized fiber anisotropy (GFA; [1]) a measure of fiber integrity. With random-effects regression, we mapped regions where diffusion profiles were highly correlated with subjects' intelligence quotient (IQ). Fiber complexity was predominantly under genetic control, and higher in more highly anisotropic regions; the proportion of genetic versus environmental control varied spatially. Our methods show promise for discovering genes affecting fiber connectivity in the brain.

1 Introduction

Diffusion profiles of brain white-matter fibers are intermediate phenotypes that can be causally related to more basic biological measures, such as genetic variations across subjects, and to more high-order cognitive processes, such as intellectual performance. They serve as a valuable link in the quest to find genes that influence cognition and disease, as fiber integrity may be associated with genetic variation using quantitative genetic modeling, and with cognitive scores (such as intelligence quotient or IQ).

In this paper we analyzed the high angular resolution diffusion imaging (HARDI) data of 90 twin subjects. Studies of identical and fraternal twins – who share all or half of their genes respectively - are informative for understanding the genetic control of brain structure and function. We measured the regional complexity of diffusion orientation distribution functions (ODF) by applying statistics to high-dimensional HARDI data in appropriate Riemannian manifolds. We visualized associations between diffusion profiles and genetic and environmental factors, and with IQ, by fitting structural equation (SEM) and random-effects regression (RRM) models at each voxel. To our knowledge, these are

---

This work was funded in part by NIH grant R01 HD050735.

the first 3D maps of genetic influences on HARDI, and reveal that HARDI signals that are genetically controlled, to some extent, are also correlated with intelligence.

2 Methods

2.1 Subject Description and Image Acquisition

HARDI data were acquired from 22 pairs of monozygotic (MZ; 20 males/24 females; age = 25.1±1.5 years) and 23 pairs of dizygotic twins (DZ; all same-sex pairs; 20 males/26 females; age = 23.5±2.2 years) on a 4T Bruker Medspec MRI scanner using an optimized diffusion tensor sequence [2]. Imaging parameters were: 21 axial slices (5 mm thick), FOV = 23 cm, TR/TE 6090/91.7 ms, 0.5 mm gap, with a 128×100 acquisition matrix. 30 images were acquired: 3 with no diffusion sensitization (i.e., T2-weighted images) and 27 diffusion-weighted images in which the gradient directions were evenly distributed on the hemisphere [2]. The reconstruction matrix was 128×128, yielding a 1.8×1.8 mm^2 in-plane resolution. Total scan time was 3.05 minutes.

2.2 DTI Registration

For each subject, diffusion tensor (DT) images (denoted by D_{ij}, $1 \leq i, j \leq 3$) were computed from the HARDI signals using MedINRIA software (http://www-sop.inria.fr/asclepios/software/MedINRIA). One diagonal component image (D_{11}) was manually stripped of nonbrain tissues, yielding a binary brain extraction mask (cerebellum included). The masked image was then registered to the ICBM53 average brain template with a 12-parameter linear transformation using the software FLIRT [3], and resampled to isotropic voxel resolution (dimension: 128×128×93 voxels, resolution: 1.7×1.7×1.7 mm^3). The resulting transformation parameters were used to rotationally reorient the tensor at each voxel [4], and then affine align the tensor-valued images based on trilinear interpolation of the log-transformed tensors [5]. All affine-registered DT images were then registered to a randomly selected subject's image (a MZ subject), using an inverse-consistent fluid registration algorithm that minimizes the symmetrized Kullback-Leibler divergence (sKL-divergence) of the two tensor-valued images [6].

2.3 HARDI Processing and Registration

Orientation distribution functions (ODF) for water diffusion were computed voxelwise from the HARDI signals using the Funk-Radon Transform (FRT) [1]. We used Descoteaux’s method [7], which expands the HARDI signals as a spherical harmonic (SH) series, simplifying the FRT to a linear matrix operation on the coefficients. To estimate the SH coefficients, we set the order of the SH series to 4, and added a Laplacian smoothing regularizer to reduce the noise level, and also a Laplacian sharpening regularizer to help detect the peaks of the ODF, as in [7]. The estimated ODF was normalized to unit mass, creating a diffusion probability density function (PDF) parameterized by spherical angle.

Images of the diffusion ODFs were registered to the target subject by applying the corresponding DTI mapping (both affine and fluid mappings) in the previous section. To keep the direction of the diffusion ODFs oriented with the direction of the underlying fibers, ODFs were reoriented using the Preservation of Principal Direction (PPD) method [4], where the principal direction of the ODF was determined by principal component analysis [8]. A generalized fractional anisotropy (GFA) map was constructed from the registered ODF ψ [1]:

$$GFA = \sqrt{n\sum_{i=1}^{n}\left(\psi(\mathbf{u}_i) - \langle\psi\rangle\right)^2 \Big/ \left[(n-1)\sum_{i=1}^{n}\psi(\mathbf{u}_i)^2\right]}. \quad \textbf{(1)}$$

Here $\mathbf{u}_i$, $1 \le i \le n$, are n gradient directions, and $\langle\psi\rangle$ is the mean of the ODF with respect to spherical angle.

Spatial interpolation of HARDI ODFs is a new issue, and is required when the registration mapping falls on non-lattice points. We addressed this by taking the square root of the ODF: the Riemannian manifold for the square root of a PDF is isomorphic to a unit sphere and there are closed form expressions defining the geodesic distance, exponential and inverse exponential mappings [9]. The interpolated square-rooted ODF (sqrt-ODF) ϕ at point (x, y, z) was then constructed by finding the weighted Karcher mean of its 8 diagonal neighbors ϕ_i in 3D at lattice points (x_i, y_i, z_i), which minimizes the square sum of the geodesic distance d:

$$\phi = \arg\min \textstyle\sum_{i=1}^{8} w_i d(\phi, \phi_i)^2. \quad \textbf{(2)}$$

Here w_i is the trilinear interpolation weight defined as $w_i = \left(1-|x-x_i|\right)\left(1-|y-y_i|\right)\left(1-|z-z_i|\right)$. The weighted Karcher mean ϕ was computed using a gradient descent approach as in [9].

2.4 Measuring Regional Complexity of Diffusion

We defined the regional complexity of diffusion using the generalized Jensen-Shannon divergence (JSD) [10]. JSD measures the dissimilarity of n probability distributions, given by:

$$JSD_w(\mathbf{p}_1, \ldots, \mathbf{p}_n) = H\left(\textstyle\sum_{i=1}^{n} w_i \mathbf{p}_i\right) - \textstyle\sum_{i=1}^{n} w_i H(\mathbf{p}_i). \quad \textbf{(3)}$$

Here $\mathbf{p}_i = \left\{p_{ij}, 1 \le j \le k \middle| \sum_{j=1}^{k} p_{ij} = 1\right\}$, and $w = \left\{w_i, 1 \le i \le n \middle| \sum_{i=1}^{n} w_i = 1\right\}$. $H(\bullet)$ is the Shannon entropy, defined as $H(\mathbf{p}) = -\sum_{j=1}^{k} p_j \log p_j$. $JSD_w(\mathbf{p}_1, \ldots, \mathbf{p}_n) = 0$ if and only if all $\mathbf{p}_1, \ldots, \mathbf{p}_n$ are equal. The complexity of diffusion at voxel $\mathbf{x}$ was defined as the JSD for the ODF at $\mathbf{x}$ and its contiguous 26 ODFs. We adopted an equal weight of $1/n$ for simplicity.

2.5 Statistical Analysis of Structural Models for Twins

To analyze genetic and environmental correlations in twins, structural equation models (SEM; [11, 12]) can evaluate contributions of additive genetic (A), shared environmental (C) and random environmental (E) components to the covariances of the observed variables (y) for MZ and DZ twins, according to the following model:

$$y_j = aA_j + cC_j + eE_j, \tag{4}$$

where $j = 1$ or 2 for the first or second twin in the same pair. Since A, C, and E are unobservable variables, their weights $\theta = (a, c, e)$ were estimated by comparing the covariance matrix implied by the model, $\Sigma(\theta)$, and the sample covariance matrix of the observed variables, $\mathbf{S}$, using maximum-likelihood fitting:

$$F_{ML,\theta} = \log|\Sigma(\theta)| + trace(\Sigma^{-1}(\theta)\mathbf{S}) - \log|\mathbf{S}| - p, \tag{5}$$

where $p = 2$ is the number of observed variables. Under the null hypothesis that the population covariance matrix of the observed variables equals $\Sigma(\theta)$, and the n-sample data y are multivariate normal, $T_{ML,\theta} = (n-1)F_{ML,\theta}$ follows a χ^2 distribution with $p(p+1)-t$ degrees of freedom, where t is the number of free model parameters. Acceptance of the null hypothesis ($p > 0.05$) indicates a good fit for the model.

Parameter fitting based on the above χ^2 distribution may be biased if the sample data are non-normal. To free SEM from distributional assumptions, we used permutation methods to determine goodness of fit [13]. At each voxel, the GFA or JSD of the diffusion ODFs served as the observed variable, with the subject's age regressed out. We computed $T_{ML,\theta}$ using the Broyden-Fletcher-Goldfarb-Shanno (BFGS) method [14] to minimize F_{ML} in (5) in the original sample, as well as in 2000 permuted samples in which the twin pairs' MZ or DZ labels were randomly shuffled. In each permutation relabeling, four null hypotheses with different θ were evaluated, for fitting the E: $\theta = (e)$, CE: $\theta = (c, e)$, AE: $\theta = (a, e)$, and ACE: $\theta = (a, c, e)$ models, and the p-values, p_E, p_{CE}, p_{AE}, and p_{ACE}, were determined separately by comparing $T_{ML,\theta}$ in the true labeling to the permutation distribution. Since the permutation distribution of the χ^2 statistic $T_{ML,\theta}$ may differ from its original distribution, we rescaled the sample data using the Bollen-Stine transformation for each null hypothesis [13]:

$$\mathbf{Z} = \mathbf{Y}\mathbf{S}^{-1/2}\Sigma^{1/2}(\theta). \tag{6}$$

Here $\mathbf{Y}$ is an $n\times 2$ matrix of the observed variables for the n twin pairs. Matrix square roots were computed by Cholesky factorization. The rows of $\mathbf{Z}$ instead of $\mathbf{Y}$ were permuted.

The four permutation p-values, p_E, p_{CE}, p_{AE}, and p_{ACE}, were compared at each voxel and the voxel was assigned to one of E, CE, AE, and ACE models if the p-value for that model was greater than the other three and also greater than 0.05. Color-coded maps visualized the optimal model fitted at each voxel, with E coded as blue, CE as green, AE as red, and ACE as yellow. For better visualization, we defined “model clusters”, i.e. sets of connected (26-neighborhood) voxels where the same model fitted, for each of the four models, and displayed only clusters of more than 10,000 voxels.

2.6 Linkage of Diffusion Anisotropy or Complexity with Cognitive Function

We used random-effects regression models (RRM) [15] to measure correlations between the full-scale intelligence quotient (FSIQ) and GFA or JSD. Ordinary regression methods are inappropriate because observations are clustered within twin pairs, violating the assumption that observations must be statistically independent. In RRM, the lack of independence is addressed by adding a random variable α_i, to incorporate the clustering of the observed variables within the *i*th pair, into the ordinary regression equations:

$$\mathbf{y}_i = \mathbf{X}_i\beta + \mathbf{1}_i\alpha_i + \varepsilon_i. \tag{7}$$

Here $\mathbf{y}_i$ = the 2×1 vector of observed variables (GFA or JSD) within the *i*th pair, β = a $(q+1)\times 1$ vector of unknown regression coefficients, $\mathbf{X}_i$ = a known $2\times(q+1)$ covariate matrix, $\mathbf{1}_i$ = a 2×1 vector of ones, and ε_i represents the 2×1 error vector. q was set to 1 for subjects’ FSIQ score as the covariate. We assumed that α_i and ε_i, and thus $\mathbf{y}_i$, were normally distributed, with $\alpha_i \sim \mathrm{N}(0, \sigma_\alpha^2)$, $\varepsilon_i \sim \mathrm{N}(0, \sigma^2\mathbf{I}_2)$, and $\mathbf{y}_i \sim \mathrm{N}(\mathbf{X}_i\beta, \sigma_\alpha^2\mathbf{1}_i\mathbf{1}_i^{\mathrm{T}}+\sigma^2\mathbf{I}_2)$, where $\mathbf{I}_m$ represents an $m\times m$ identity matrix. Estimation of these unknown parameters (β, σ_α^2, σ^2) was based on maximum marginal likelihood (MML) methods detailed in [15].

We applied RRM to each voxel and tested the significance of the correlations by comparing the full ($\beta = [\beta_0, \beta_{\mathrm{IQ}}]^{\mathrm{T}}$; β_0 is a constant) and the reduced ($\beta = \beta_0$) models, which gave a significance *P*-value based on Wilks' lambda distribution [16]: $\Lambda = \left|\Sigma_{full}\right| / \left|\Sigma_{reduced}\right| \sim \Lambda(p, \nu H, \nu E)$, where Σ is the estimated covariance matrix of $\mathbf{y}_i$. $p = 2$ is the number of subjects in each pair, $\nu H = 1$ is the difference in the number of parameters between full and reduced models, and $\nu E = n-q-1$, where n is the number of twin pairs. Overall significance was assessed using the positive false discovery rate (pFDR) method [17]. A pFDR value < 0.05 was considered to be significant.

3 Results

Fig. 1 displays the spatial distribution of the average JSD (averaged across all 90 subjects). The average JSD increases with GFA, suggesting that JSD is sensitive to the complexity of ODFs in major white matter fibers with high diffusion anisotropy, especially in regions where anisotropy values vary over a small spatial neighborhood.

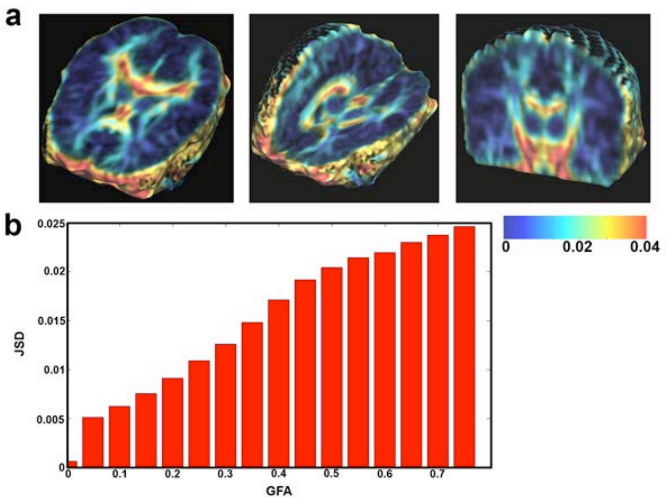

Fig. 1. (**a**) The color-coded map shows that the JSD, a measure of fiber complexity, is greater in regions of high diffusion anisotropy (e.g., the corpus callosum), especially at interfaces between high and low anisotropy. This trend is clear when plotting JSD against the GFA (**b**). This property of JSD is useful because in DTI/HARDI studies, diffusion properties are more informative in highly anisotropic regions, where fiber structures are highly resolved.

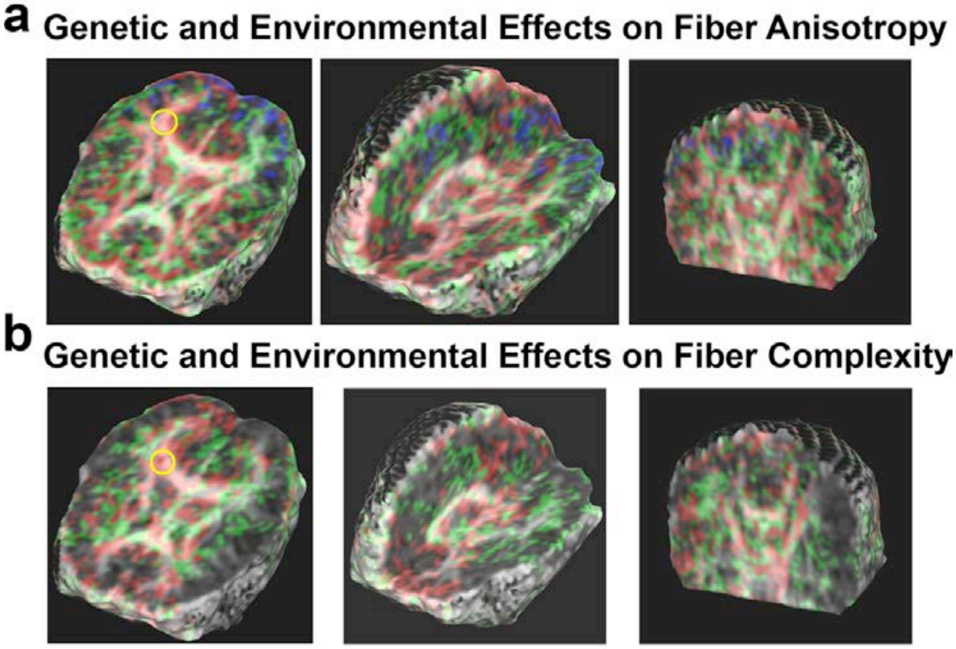

Fig. 2. The color-coded map shows which model fits best for the covariance matrices of (**a**) GFA, a measure of fiber integrity, and (**b**) JSD for fiber complexity, at each voxel. Voxels where the E model fits best are coded as blue, CE as green, and AE as red. For GFA and JSD, major fiber structures, such as the corpus callosum, cingulum, and internal capsules, are optimally fitted using the AE and the CE models. Model fitting is visibly asymmetrical in the cingulum fibers: the AE model fits in the right cingulum (yellow circles in (a) and (b)), while the CE model fits better in the left cingulum.

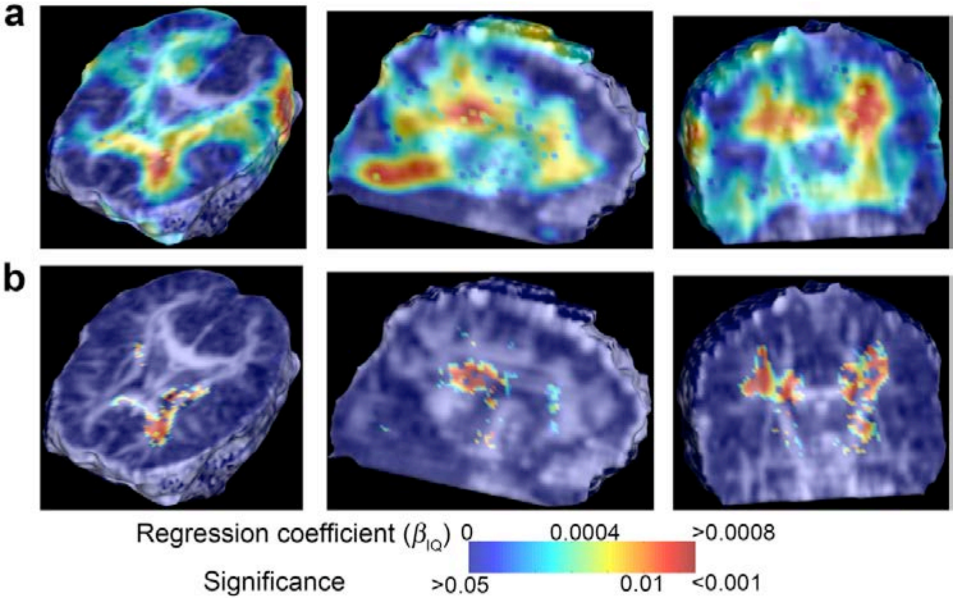

Fig. 3. Correlations of GFA with the FSIQ score based on random-effects regression, visualized as maps of (**a**) regression coefficients (β_{IQ}) and (**b**) *P*-values. Higher diffusion anisotropy is associated with higher IQ in the left anterior region of the *corona radiata*, *cingulum*, and internal capsule.

Fig. 2 shows the covariance structure fitting for GFA and JSD maps in the 90 twins. When the AE model fits best, variation in GFA or JSD values is more attributable to genetic influences, i.e., the covariance structures are best accounted for by additive genetic (added effect of genes) and random environmental effects (random experimental error is also lumped into the E term). When the CE model fits best, the variation in the observed measures is more due to environmental influences shared by twins reared in the same family [11]. The full ACE model, where all terms fit at once, could not be fitted for either GFA or JSD. For both GFA and JSD measures, more voxels had AE as the best-fitting model than CE or any other model, indicating that diffusion properties are more genetically influenced than environmentally influenced, in most brain regions.

Fig. 3 shows that GFA is positively correlated with FSIQ scores in the *corona radiata*, corpus callosum and internal capsule (pFDR = 0.04). The correlations of JSD with FSIQ scores were not significant (pFDR = 0.21; figures not shown). Fiber measures were highly genetically controlled, especially in regions of high diffusion anisotropy. We also found that higher diffusion anisotropy is correlated with better intellectual performance in specific WM regions. Based on these measures and algorithms, future studies may be able to detect individual genes contributing to fiber architecture, and relate white matter integrity to cognition.

References

1. Tuch, D.S., *Q-ball imaging.* Magn Reson Med, 2004. **52**(6): 1358-72.
2. Jones, D.K., Horsfield, M.A., and Simmons, A., *Optimal strategies for measuring diffusion in anisotropic systems by magnetic resonance imaging.* Magn Reson Med, 1999. **42**(3): 515-25.
3. Jenkinson, M. and Smith, S., *A global optimisation method for robust affine registration of brain images.* Med Image Anal, 2001. **5**(2): 143-56.
4. Alexander, D.C., et al., *Spatial transformations of diffusion tensor magnetic resonance.* IEEE Transactions on Medical Imaging, 2001. **20**: 1131-1139.
5. Arsigny, V., et al., *Fast and simple calculus on tensors in the log-Euclidean framework*, in *Int Conf Med Image Comput Comput Assist Interv (MICCAI).* 2005. p. 115-22.
6. Chiang, M.C., et al., *Fluid Registration of Diffusion Tensor Images Using Information Theory.* IEEE Transactions on Medical Imaging, 2008. **27**: 442-456.
7. Descoteaux, M., et al., *Regularized, fast, and robust analytical Q-ball imaging.* Magn Reson Med, 2007. **58**(3): 497-510.
8. Chiang, M.-C., et al. *Information-theoretic analysis of brain white matter fiber orientation distribution functions.* in *IPMI* 2007. Kerkrade, The Netherlands.
9. Srivastava, A., Jermyn, I., and Joshi, S.H. *Riemannian Analysis of Probability Density Functions with applications in Vision.* in *CVPR* 2007. Minneapolis, Minnesota, USA.
10. Lin, J., *Divergence measures based on the Shannon entropy.* IEEE Trans. Information Theory, 1991. **37**(1): 145-151.
11. Neale, M.C., Cardon, L.R., and the NATO Scientific Affairs Division, *Methodology for genetic studies of twins and families.* 1992, Dordrecht; Boston: Kluwer Academic Publishers. xxv, 496 p.
12. Schmitt, J.E., et al., *A multivariate analysis of neuroanatomic relationships in a genetically informative pediatric sample.* Neuroimage, 2007. **35**(1): 70-82.
13. Bollen, K.A. and Stine, R.A., *Bootstrapping goodness-of-fit measures in structural equation models.* Sociological Methods Research, 1992. **21**(2): 205-229.
14. Press, W.H., et al., *Numerical recipes in C++.* 2nd ed. 2002: Cambridge Univ. Press. viii, 318 p.
15. Hedeker, D., Gibbons, R.D., and Flay, B.R., *Random-effects regression models for clustered data with an example from smoking prevention research.* J Consult Clin Psych, 1994. **62**(4): 757-65.
16. Rencher, A.C., *Methods of multivariate analysis.* 2nd ed. 2002, New York: J. Wiley.
17. Storey, J.D., *A direct approach to false discovery rates.* J Roy Stat Soc B, 2002. **64**(3): 479-498.

Compressed Sensing of Multiple Intra-Voxel Orientations with Traditional DTI

Bennett A. Landman[1], Pierre-Louis Bazin[2], and Jerry L. Prince[1,3]

Biomedical Engineering[1]; Radiology[2]; Electrical and Computer Engineering[3],
Johns Hopkins University, Baltimore, MD, USA, `landman@jhu.edu`. ⋆

Abstract. Diffusion tensor imaging (DTI) is widely used to characterize tissue microarchitecture and brain connectivity. However, traditional tensor techniques cannot represent multiple, independent intra-voxel orientations, so DTI suffers serious limitations in regions of crossing fibers. We present a new application of compressed sensing, Crossing Fiber Angular Resolution of Intra-voxel structure (CFARI), to resolve multiple tissue orientations. CFARI identifies a parsimonious tissue model on a strictly voxelwise basis using traditional DTI data. Reliable estimates of multiple intra-voxel orientations are demonstrated in simulations, and intra-voxel fiber orientations consistent with crossing fiber anatomy are revealed with typical *in vivo* DTI data.

1 Introduction

Diffusion weighted MRI provides unique, non-invasive contrasts that are sensitive to *in vivo* cytoarchitecture [1]. One widespread application, diffusion tensor imaging (DTI), is a clinically practical approach enabling the study of three-dimensional tissue structure through a tensor model [2]. With DTI, the tensor eigenstructure of each voxel provides local measures of diffusivity, anisotropy, and tissue orientation, which can establish global connectivity through fiber tracking [3]. Tensors represent only one independent, dominant direction per voxel, so DTI suffers from serious limitations in regions where distinct fiber populations with differing orientations occupy the same voxel. This is known as the "crossing fiber problem," and in these regions the dominant tensor orientation may be ambiguous or misleading [4]. Substantial effort has been devoted to overcoming the crossing fiber problem through resolution of intra-voxel structure.

Acquisition of many diffusion weighted directions and use of large diffusion sensitizations enable the study of the diffusion process in more detail than is possible with typical DTI protocols. Multiple intra-voxel tissue orientations have been visualized with three-dimensional, non-parametric diffusion propagators [5] and their two-dimensional projections (e.g., [6, 7]). Parametric modeling approaches based on deconvolution have also been suggested [8, 9]. Applications of these methods to clinical research is severely hindered by their requirements for elaborate and time-consuming data acquisition protocols.

⋆ This project was supported by NIH/NINDS 1R01NS056307.

There has been increasing interest in identifying multiple intra-voxel orientations from data that are available with typical clinical DTI sequences. Kim et al. used independent component analysis to fit a prolate tensor mixture [10], while Peled et al. employed cylindrically constrained two-tensor models to identify two independent directions within a voxel [11]. These approaches are highly sensitive to noise, and Peled et al. suggested limiting application to areas of known fiber crossing to avoid erroneous detections. Recently, Ramirez-Manzanares et al. proposed an approach similar to deconvolution in which diffusion basis functions represent tissue diffusivities [12]. A major obstacle confronting these approaches is the complexity of representing heterogeneous intra-voxel structure. Using restricted two-component models [10, 11] greatly reduces variability, but risks over- or under-fitting. Alternatively, substantial spatial regularization and probability models have been suggested to stabilize a more general approach [12].

To address the crossing fiber problem, we suggest that one is interested in a parsimonious (and reproducible) explanation of the observed signals in terms of orientated intra-voxel components. Although initially developed as an alternative to Nyquist sampling, compressed sensing (CS) offers a simple and elegant solution to precisely this problem (cf. [13]). In CS, data are represented in two uncorrelated basis sets, one during sensing and another during reconstruction. When the signals under consideration can be sparsely represented in the reconstruction basis, there are efficient and robust algorithms to recover the information from noisy observations taken with the sensing basis. In practice, it is efficient to use a random sensing basis for CS, but randomization is not required.

In this manuscript, we demonstrate a new method of resolving crossing fibers through CS which we call Crossing Fiber Angular Resolution of Intra-voxel structure (CFARI). Our method is presented in the spirit of prior deconvolution methods, in which one assumes that a only small number of tissues architectures are relevant for any given voxel. Prior approaches have restricted the model order or employed extensive spatial regularization. With CFARI, we explicitly identify a parsimonious tissue model on a voxelwise basis and achieve reliable estimates of multiple intra-voxel orientations on both simulated and in vivo DTI data.

2 Methods

CFARI is based on the classical non-exchanging, multi-compartment tissue model [2]. Each voxel consists of a finite mixture of discrete and independent compartments, and the diffusivity within each compartment is defined by the Stejskal-Tanner tensor formulation. The observed signal, S_k, along the k^{th} diffusion weighting direction ($\boldsymbol{g}_k$) is determined by the exponential mixture model,

$$S_k = S_0 \sum_{i=1}^{N} f_i e^{-b\boldsymbol{g}_k^T \mathbf{D}_i \boldsymbol{g}_k} + \eta \,. \tag{1}$$

S_0 is a noise-free reference signal in the absence of diffusion weighting, N is the number of possible compartments (tensors) within each voxel, f_i is the (unknown) mixture component for each compartment, b is the diffusion sensitization parameter, $\mathbf{D}_i$ is the tensor associated with the i^{th} compartment, and η is a noise term that follows a Rician distribution. It is assumed that the *reconstruction basis* $\{\mathbf{D}_i\}$–i.e., the set of possible diffusion tensors that may comprise a voxel–is fixed and known. Given this framework, the vector, $\boldsymbol{y}$, of K observed attenuations, where each attenuation is defined as $y_k = S_k/S_0$, can be rewritten in matrix form as,

$$\boldsymbol{y}_{\mathrm{K}\times 1} = \mathbf{S}_{\mathrm{K}\times\mathrm{N}} \boldsymbol{f}_{\mathrm{N}\times 1} + \tilde{\boldsymbol{\eta}}_{\mathrm{K}\times 1}, \tag{2}$$

where the matrix $\mathbf{S}$ comprises a set of exponential terms derived from Eq. 1 and $\tilde{\eta}$ is a scaled noise term. At an SNR of greater than 5:1, Rician noise is well approximated by a Gaussian distribution [14], so a least squares estimator is appropriate. With Eq. 2, we may immediately write the CS criteria for selecting the mixture components,

$$\boldsymbol{f} = \underset{f}{\operatorname{argmin}} ||\mathbf{S}\boldsymbol{f} - \boldsymbol{y}||_{\mathrm{L2}} + \beta ||\boldsymbol{f}||_{\mathrm{L1}}, \tag{3}$$

where β is a strictly positive *sparsity regularization parameter.* Low β's lead to least squares fitting of the observed signal with the specified basis, while high β's force greater emphasis on a sparse model. There are efficient numerical methods to address optimization problems of the form of Eq. 2; in this work, we use the interior point method of Koh et al.[15].

Since CFARI is designed to work with existing, traditional DTI data, the sensing basis—i.e., the choices of b-values and diffusion encoding directions—is considered to be determined by external requirements (such as reliability of clinical contrasts). There are two remaining design choices that must be addressed: the reconstruction basis and the sparsity regularization parameter. Here, we choose a simple mixture model: the $\mathbf{D}_i$'s are chosen to be cylindrically symmetric, of equal diffusivities, and regularly distributed on a sphere. The lateral columns of the spinal cord provide a good model of homogeneous white matter tracts; accordingly, we model all $\mathbf{D}_i$'s as cylindrically symmetric tensors with FA=0.71 and $\lambda_1 = 2 \times 10^{-3}$ mm^2/s. To provide regularly spaced orientations on the sphere, we choose a fifth order tessellation of a dodecahedron (having 241 symmetric orientations) as the orientations, yielding $N = 241$ distinct possible mixture components. The regularization parameter β was selected empirically through simulations to produce a trade off between minimal error and robustness against model mismatch.

Data were motion corrected with FSL FLIRT (FMRIB, Oxford, UK). CFARI was performed using custom Matlab software and the l1_ls toolbox [15]. Fiber tracking was performed with custom software, INtravoxel Fiber Assignment by Continuous Assignment (INFACT), which is loosely based on FACT [3] and visualized with DTIStudio (Johns Hopkins University, Baltimore, MD). Briefly, INFACT initializes fiber tracking at every voxel with the dominant direction with the highest weighting f_i. Tracking proceeded in both directions by continuous piecewise linear assignment. At each step, the orientation was selected as the dominant direction with the nearest neighbor voxel that minimized the following importance weighting, $w_i = f_i|\boldsymbol{v}_i \cdot \boldsymbol{v}_{\text{last}}|^\gamma$, where $\boldsymbol{v}_i$ is the principle eigenvector of tensor $\mathbf{D}_i$, $\boldsymbol{v}_{\text{last}}$ is the unit vector representing the last step in tracking, and γ is a regularization parameter that emphasizes continuity. *Ad hoc* experiments showed that $\gamma = 4$ was a reasonable choice. Investigations into tracking in complex, *in vivo* 3-D environments and probabilistic fiber tracking strategies are ongoing.

3 Experiments

3.1 Simulations

Monte Carlo simulations of a typical clinical DTI sequence were performed using two repetitions of 30 diffusion weighting directions [16], five averaged unweighted reference acquisitions, and Rician distributed noise. The SNR of the simulations was defined as the ratio of the noise standard deviation on the complex coefficients and the (noise-free) unweighted signal intensity.

Simulations explored the reliability of orientation estimation from a bi-tensor model to explore the joint influence of β and model mismatch at an SNR of 25:1. For each of 50 linearly spaced axial diffusivities from 0.5×10^{-3} (FA=0) to 3.0×10^{-3} mm^2/s (FA=0.81), 50 logarithmic steps in β were explored from 10^{-2} to 10^2. For each pair, the expected error was assessed with 50 Monte Carlo iterations where two, distinct, random tensors were selected and the error was evaluated using CFARI with a reconstruction basis consisting of 241 tensors. The process was repeated for reconstruction bases with FAs of 0.55 ($\lambda_1 = 1.3 \times 10^{-3}$), 0.71 ($\lambda_1 = 2.0 \times 10^{-3}$), and 0.81 ($\lambda_1 = 3.0 \times 10^{-3}$). Error was assessed as the mean angular difference between each estimated orientation and the closest orientation in the truth model, weighted by the estimated fraction: $E = \sum_i f_i \min_{j \in \text{model}} \angle(\boldsymbol{v}_i, \boldsymbol{v}_j)$.

The following three simulations were performed with $\beta = 5$ and the truth model and the reconstruction basis set with FA=0.71. (1) To investigate the choice of angular orientations, the expected error was compared when 136 orientations (fourth order tessellated dodecahedron) and 376 orientations (sixth order tessellated dodecahedron) were used as the reconstruction basis at an SNR of 15:1. (2) To explore the SNR dependence of CFARI, 100 Monte Carlo iterations were performed at 19 linearly spaced SNR levels between 5:1 and 50:1 with a mixture of 1, 2, or 3 random tensors. (3) The angular resolution of CFARI was explored at an SNR of 15:1 with 1,000 Monte Carlo random combinations of two tensors. The estimated error was mapped against the angular separation of the tensors and smoothed with a Parzen kernel (Gaussian, $\sigma = 10°$). The maximum attenuation of the basis set was matched to the average maximum image attenuation in the corpus callosum by setting $\lambda_1 = 1.5 \times 10^{-3}$ mm^2/s.

Intra-voxel crossing fibers were studied with a simulated phantom in which two fiber tracts of FA=0.71 run from opposite corners (SNR=15:1 and $\beta = 5$). Each tract's partial fraction falls off with a Gaussian curve (FWHM=8 voxels). The two tracts were augmented with an isotropic component ($\lambda_1 = \lambda_2 = \lambda_3 = 3 \times 10^{-3}$ mm^2/s) such that the total fraction of each voxel summed to 1.

Results. β influences the error rate, but error rates were stable over two orders of magnitude (Fig. 1A-C). To avoid possible null solutions, we selected and recommend using $\beta = 1$ to 15. Once several hundred tensors were used to span the space of orientations, little influence on the specific choice of basis set was observed. Simulated errors were not significantly different (two-tailed t-test, $p \geq 0.5$) when using 136 orientations ($11.82° \pm 0.75$) and 376 orientations ($11.62° \pm 0.69$). Errors increased at low SNR (Fig. 1D), and showed some angular variability (Fig. 1E). In the crossing fibers simulation, the CFARI intra-voxel structure visually corresponded to truth model, and fiber tracking was successful passed through the intersection with CFARI while resulting in non-sensible results for traditional FACT tracking (Fig. 2).

3.2 In Vivo Study

For an empirical comparison, two DTI studies on a 3T system (Intera, Philips Medical Systems, The Netherlands) of a healthy 33 year old female were selected from ongoing clinical research protocol. Written informed consent was obtained prior to investigation. Each study used a multi-slice, spin echo, single-shot EPI sequence (SENSE = 2.0) to acquire 60 slices (parallel to AC-PC) with 2.2 mm nominal resolution, reconstructed in plane to 0.9375 mm, covering the brain, brainstem, and cerebellum. Diffusion weighting was applied with the Jones30 (b = 700 s/mm^2, TR/TE = 6768/69 ms). Five unweighted reference images were acquired and averaged in k-space.

CFARI identified intra-voxel orientations that are visually consistent with the well-known locations and orientations of major fiber crossings (Fig. 3). Fibers running lateral through the corpus callosum and superior through the internal capsule are visible (Fig. 4). This region typically manifests as an "FA black hole" on DTI and prevents tracking of corpus callosal fibers to the lateral hemispheres. CFARI identifies sufficient crossing information such that fiber tracts may pass from the corpus callosum to the lateral hemispheres, which is physiologically indicated.

4 Discussion

CFARI provides a robust framework for identifying intra-voxel structure with traditional DTI and show great promise in helping to resolve the crossing fiber problem. Although similar in spirit to existing deconvolution approaches, CFARI uses sparsity to stabilize estimation with limited data (rather than spatial consistency or limited model order). The estimated intra-voxel structure is driven only by information from individual voxels, so we can exploit incorporate spatial regularization through fiber tracking "momentum."

When the truth model is of higher FA ("more sharp") than the reconstruction basis, CFARI is robust to model mismatch (Fig. 1A-C). Lowering the FA of the basis set to improve robustness increases overall error. When the truth

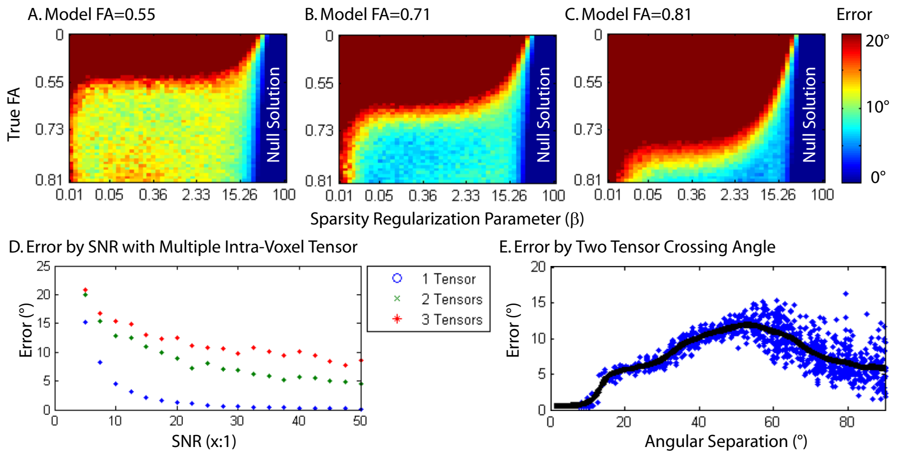

Fig. 1. *First Row:* Increasing β improved the accuracy, yet null solutions are found with high β. Higher FA basis sets leads to more reliable orientation estimates when the truth model matches the basis (compare A,B,C: 12°, 8°, and 6° error, respectively). When the truth model had an FA less than the basis set, error rapidly increased ($\geq 20°$). However, the error did not substantially increase when the truth model was of higher FA than the basis set. *Second Row:* CFARI errors improve with increasing SNR (D), but do not rapidly converge for multi-tensor mixtures. The error are greatest for fibers crossing near 55° (E).

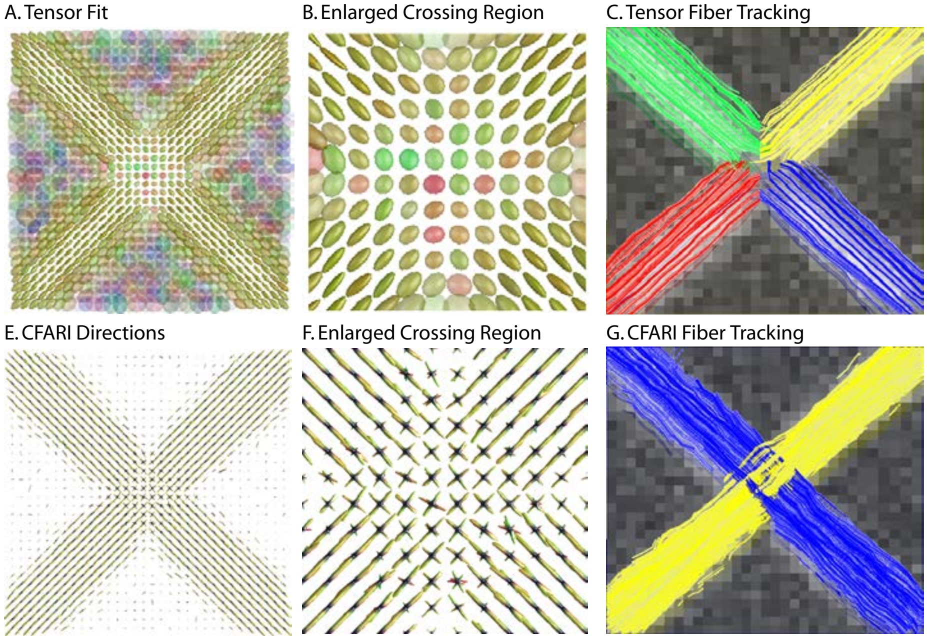

Fig. 2. Simulated crossing fibers with tensors and CFARI at an SNR of 15:1. For each voxel, the five CFARI directions with the highest partial fraction are shown weighted by partial fraction and FA.

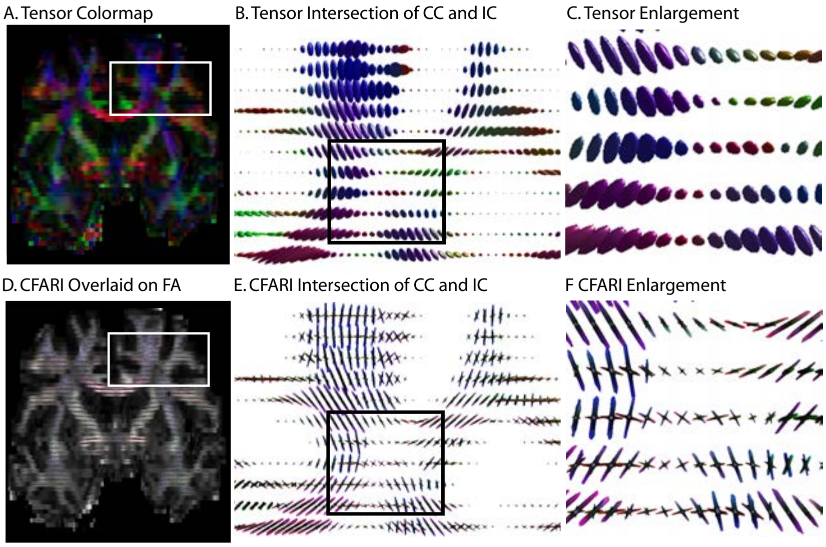

Fig. 3. CFARI identified consistent intra-voxel structure in the crossing fibers between the corpus callosum (CC, lower left, red) and internal capsule (IC, blue, lower right). Conventional tensor modeling does not preserve the connectivity of the corpus callosum to the lateral hemispheres.

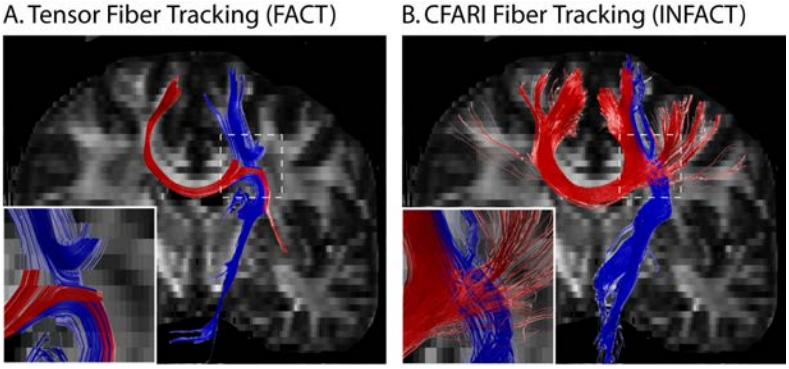

Fig. 4. CFARI enables tracking (B) of fibers from the corpus callosum (red) to the lateral hemispheres through the cortiospinal tract (blue). Traditional DTI (A) does not reliably track through this crossing region.

model is precisely sparse, very high regularization parameters dramatically reduce erroneously detected orientations, however, this substantially reduces the power of CFARI to detect multiple orientations. Thus, we recommend a high, yet conservative value of β. Metrics to classify missed detections are warranted and under study. CFARI identifies single tensors at low SNR with very little error, but several degrees of error persist for multi-tensor mixtures even at high

SNR (Fig 1D). This is expected because we use a constant β, but CS fitting does not converge to a least squares estimate at high SNR when β is constant. The proposed approach works well with clinical data, but it would be appropriate to adjust β based on the the data to further generalize CFARI for a wider range of SNR. In simulation, CFARI enabled tracking through a region of substantial tract overlap and with partial volume effects with from isotropic contamination (Fig. 2). In vivo, CFARI identified intra-voxel structures which visually agree with the expected anatomy. Neither are possible with traditional DTI analysis.

References

1. Le Bihan, D., van Zijl, P.C.: From the diffusion coefficient to the diffusion tensor. NMR in Biomedicine **15**(7-8) (2002) 431–4
2. Basser, P.J., Jones, D.K.: Diffusion-tensor MRI: theory, experimental design and data analysis - a technical review. NMR Biomed **15**(7-8) (2002) 456–67
3. Mori, S., van Zijl, P.C.: Fiber tracking: principles and strategies - a technical review. NMR Biomed **15**(7-8) (2002) 468–80
4. Wiegell, M.R., Larsson, H.B., Wedeen, V.J.: Fiber crossing in human brain depicted with diffusion tensor MR imaging. Radiology **217**(3) (2000) 897–903
5. Wedeen, V.J., Reese, T.G., Tuch, D.S., Weigel, M.R., Dou, J.G., Weiskoff, R.M., Chessler, D.: Mapping fiber orientation spectra in cerebral white matter with fourier-transform diffusion MRI. In: ISMRM, Denver, Colorado (2000)
6. Frank, L.R.: Characterization of anisotropy in high angular resolution diffusion-weighted MRI. Magnetic Resonance in Medicine **47**(6) (2002) 1083–99
7. Tuch, D.S.: Q-ball imaging. Magn Reson Med **52**(6) (2004) 1358–72
8. Tournier, J.D., Calamante, F., Gadian, D.G., Connelly, A.: Direct estimation of the fiber orientation density function from diffusion-weighted MRI data using spherical deconvolution. Neuroimage **23**(3) (2004) 1176–85
9. Anderson, A.W.: Measurement of fiber orientation distributions using high angular resolution diffusion imaging. Magn Reson Med **54**(5) (2005) 1194–206
10. Sungheon, K., Jeong-Won, J., Singh, M.: Estimation of multiple fiber orientations from diffusion tensor MRI using independent component analysis. IEEE Trans Nuc Sci **52**(1) (2005) 266–73
11. Peled, S., Friman, O., Jolesz, F., Westin, C.F.: Geometrically constrained two-tensor model for crossing tracts in DWI. Magn reson imaging **24**(9) (2006) 1263–70
12. Ramirez-Manzanares, A., Rivera, M., Vemuri, B.C., Carney, P., Mareci, T.: Diffusion basis functions decomposition for estimating white matter intravoxel fiber geometry. IEEE Trans Med Imaging **26**(8) (2007) 1091–102
13. Williams, D.: Special section - compressive sampling. IEEE Sig. Proc. **25**(2) (2008)
14. Wood, J.C., Johnson, K.M.: Wavelet packet denoising of magnetic resonance images: importance of rician noise at low SNR. Magn Reson Med **41**(3) (1999) 631–5
15. Koh, K., Kim, S.J., Boyd, S.: An efficient method for large-scale l1-regularized convex loss minimization. In: IEEE ITA Workshop. (2007) 223–30
16. Skare, S., Hedehus, M., Moseley, M.E., Li, T.Q.: Condition number as a measure of noise performance of diffusion tensor data acquisition schemes with MRI. J Magn Reson **147**(2) (2000) 340–52

Early Detection of Treatment Response for GBM Brain Tumor using ADC Map of DW-MRI

Jing Huo[1], Whitney Pope[1], Kazunori Okada[2], Jeffery Alger[3], Hyun Jung Kim[1], Yang Wang[1], Jonathan Goldin[1], and Matthew Brown[1]

[1] Department of Radiological Sciences, David Geffen School of Medicine, University of California in Los Angeles, {`jhuo,wpope,gracekim,yangwang, jgoldin,mbrown`}`@mednet.ucla.edu`
[2] Computer Science Department, San Francisco State University, `kazokada@sfsu.edu`
[3] Department of Neurology and Department of Radiological Sciences, David Geffen School of Medicine, University of California in Los Angeles, `jralger@ucla.edu`

Abstract. This preliminary study explores novel methods using diffusion weighted(DW) MR images as a biomarker to detect early GBM brain tumor response to treatment. Apparent diffusion coefficient(ADC) map, calculated from DW-MR images, can provide unique information of tumor response at cellular level. In this study, we investigate whether changes in ADC histograms between two scans, taken 5-7 weeks apart before and after treatment, could predict treatment effectiveness before lesion size changes are observed on later scans. The contribution of our work is to exploit quantitative pattern classification techniques for the prediction. For both pre- and post-treatment scans, we first compute the histogram from the ADC values covered within the tumor. Then we apply supervised learning on features extracted from the histogram for classification. We evaluated our approach with pool data of 86 patients with GBM under chemotherapy while 40 responded and 46 did not respond based on tumor size reduction. We compared Fisher's linear discriminant analysis, AdaBoost and random forests classifier using leave one out cross validation(LOOCV), resulting in the best accuracy of 67.44%.

1 Introduction

Glioblastoma multiforme(GBM) is the most common and aggressive type of primary brain tumor. There are many clinical trials underway to assess the ability of new drugs and strategies to treat glioblastoma and extend the duration of patient survival. The traditional way of assessing treatment response is to measure the size of the tumors after the treatment. However, efficacy can only be evaluated weeks or months after treatment.

Diffusion weighted MRI has tremendous potential for monitoring early changes in tumor cellularity that are thought to be reflective of treatment response [1]. It provides image contrast determined by microscopic motion of water molecules in the tissue. The mobility of water molecules is highly related to cell density within tumors.

Apparent diffusion coefficient(ADC) is the parameter to measure water molecule motions. In general, water movement inside cells is more restricted than outside. Thus, increasing cell density tends to lower ADC, whereas increased edema(more interstitial water) results in higher ADC values. Therefore, ADC values in treated brain tumors could not only theoretically increase due to cell kill(and thus reduced cell density), but also decrease due to inhibition of edema.

A number of related studies have investigated methods to overcome the overall complicated situation and separate the competing effects. In [2], they observe the shift of ADC histogram and conclude that the mean ADC value increases when tumor cells are killed. In [3], they calculate pixelwise the ADC value changes along with time and display it as a functional diffusion map for correlation with clinical response.

In this paper, we investigate statistical techniques and pattern classification methods to predict tumor responses using ADC map. We extract statistical features from the histogram of tumor ADC values, compare the feature differences between pre- and post-treatment scans, and compare three machine learning-based classification methods. By doing this, we explore the effectiveness of the machine learning approaches in this clinical context.

This paper is organized as follows. The next section describes the image analysis of the ADC map, histogram features and the three classifiers that we compared. In the following result section, we report the results of our comparative study for the different classifiers. The final section offers our discussion on the experimental results as well as our future work.

2 Method

2.1 Image Protocols and Image Analysis

ADC map is calculated from diffusion weighted(DW) images. DW images can be acquired with echo-planar pulse sequences plus DW gradients. The signal intensity of DW images is equal to the signal intensity on a T2-weighted(T2w) image decreased by an amount dependent on the rate of diffusion. [4]

$$SI = SI_0 * e^{-b*ADC} \tag{1}$$

with b being the diffusion sensitivity factor, ADC being the apparent diffusion coefficient, and SI_0 being the signal intensity when b=0 sec/mm^2. With b known, ADC maps are calculated from DW images by equation 1.

Three steps are as follows to get the tumor contour on ADC maps. First of all, radiologists contoured tumors on post-contrast T1-weighted(T1w) images using a semi-automated segmentation tool [5]. Next, tumor contours were mapped from T1w to ADC using rigid body transformation. The mapping was performed using DICOM header information, i.e. image position and image orientation, to compute transformation parameters. Finally, radiologists visually evaluated the contours on ADC images and manually corrected the tumor contours on ADC. An example of the mapping from T1w to ADC is shown in figure 1.

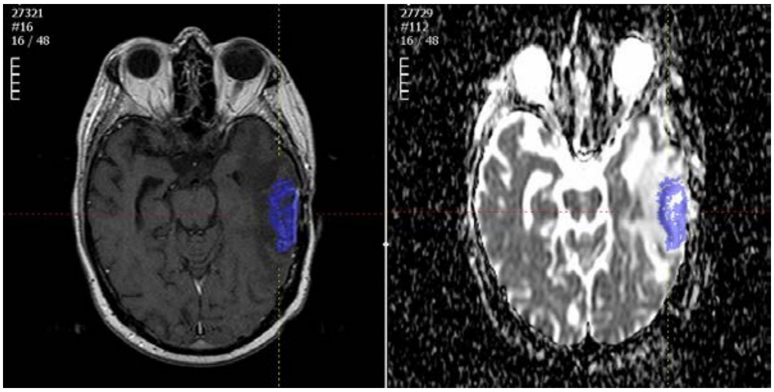

Fig. 1. Examples of the tumor region mapping from post-contrast T1w to ADC map: on the left is the post contrast T1w image with manually contoured tumor; on the right is the ADC map with mapped tumor.

Afterwards, the histogram of the ADC value within the tumor region was obtained. Figure 2 shows two examples of tumor ADC histograms for both pre- and post-treatment. The upper histogram shows the ADC value distribution before the drug treatment, while the lower one shows the ADC value distribution after the drug treatment. On the left is an example of non-responding tumors, while on the right is an example of responding tumors.

2.2 Feature Extraction and Classification

The difference of the features extracted from pre- and post-treatment histograms are used as the input to a tumor response classifier.

According to the clinical studies [2, 6, 1, 7, 3], the ADC value should change after treatment. In our data set, we observe the histograms for both responding and non-responding tumors. We find out that histograms change not only in mean, but also in shapes. Therefore, we bring in the idea of finding the patterns in ADC histogram changes by use of statistical classification methods.

The features we get from histograms are statistical features of the distribution of the ADC values within the tumor: mean, standard deviation, skewness, kurtosis, median, IQR(interquartile range), 25% percentile, and 75% percentile.

We obtain 8-dimensional feature vectors for both pre- and post-treatment tumor histograms. Afterwards, we calculate the difference between pre- and post-treatment tumor histogram by calculating both the absolute change and the change rate of the features. Therefore, we have 16-dimensional vector as the difference feature vector. Besides, we apply the earth mover's distance(EMD) [8, 9] as a metric to directly evaluate the distance between the histograms. The calculated EMD value is appended as the 17th element in the difference feature vector.

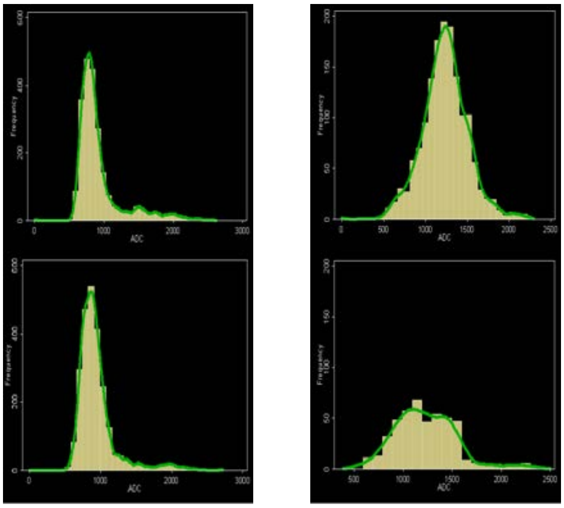

(a) (b)

Fig. 2. Examples of histograms from two tumors and two time points of pre-(top row) and post-treatment(bottom row). (a):example of non-responding tumors. (b):example of responding tumors.

The 17-dimensional difference feature vector will be the input to the classifier. For classification, we investigate three classification techniques with different characteristics: fisher linear discriminant analysis, AdaBoost and random forests classifier. We will discuss the reasons why we choose these three classifiers in the results section.

Fisher's linear discriminant analysis(FLDA)[10] is a classification method that projects high-dimensional data onto a line, and perform classification in one dimensional space. The criterion for classification is to maximize the distance between the projected mean between classes and minimize the projected variance of each class. For our two-class case, the cost function and the solution are:

$$\max J(w) = \frac{|m_1 - m_2|^2}{s_1^2 + s_2^2} \quad with \quad solution: \quad w = S_w^{-1}(m_2 - m_1) \tag{2}$$

where S_w stands for the within-class scatter matrix, m represents a mean, s^2 represents a variance, and the subscripts denote the two classes. As for classification criteria, assuming we have the projected class means well separated, we can choose the average of the two projected means as a threshold for classification.

$$y(x) = w^T x - 0.5 * w^T(m_1 + m_2) \tag{3}$$

The AdaBoost algorithm, introduced by Freund and Schapire [11], is a boosting algorithm that can combine simple and moderately accurate classifiers into a final strong classifier to improve the final accuracy. It is iterative algorithm. In each iteration, a weak classifier is selected to minimize the average training error. Afterwards, the weights on training samples are redistributed in such a way that the weight of accurately classified samples will be reduced while the weight of ill classified samples is raised. Therefore, AdaBoost "focuses in" on the informative or "difficult" ones [10]. The final classifier aggregates the selected weak classifier from each iteration, and the vote for each weak classifier is a function of its accuracy.

Random forests(RF) [12] is a classifier that combines many decision trees. Each tree depends on values of a random vector sampled independently and with equal distribution. Each tree casts a unit vote for the most popular case at input, and random forests outputs the class that is the mode of the classes output by individual trees. Breiman [13] suggests the generalization error for forests converges to a limit as the number of trees in the forest becomes large. The error of a forest of tree classifiers depends on the strength of the individual trees in the forest and the correlation between them. Using a random selection of features to split each node yields error rates that compare favorably to Adaboost but are more robust with respect to noise.

3 Results

3.1 Experimental Design

We included a total of 86 patients with GBM in our preliminary study. Tumors were diagnosed by board-certified radiologists as responding or non-responding to drugs based on the size change according to later scans. All the ones that present over 50% increase in volume is defined as non-responders, whereas the rest are defined as responders. The baseline scans and follow-up scans were 5-7 weeks apart. The DWI was performed in three or six orthogonal directions and diffusion weighting is b=1000 sec/mm^2. The axial plane resolution for DWI has 0.9375mm by 0.9375mm or 1.797mm by 1.797mm pixel size. The slice thickness for DWI is 3,5, or 7mm.

The statistical features were extracted from histograms of ADC values within the tumor region for both pre- and post-treatment scans. The difference between pre- and post-treatment features was calculated as the input to the classifiers. FLDA, AdaBoost, and RF tree classifiers were applied to the data, and results from the three classifiers were compared. We implemented FLDA in Matlab, while we used AdaBoost and RF classifier implemented in the open source data mining software Weka [14]. We validated the performance by LOOCV method.

3.2 Classification Performance

FLDA was evaluated with all permutations of 2-feature pairs for our 17-dimensional feature space. Among all the 136 combinations of feature pairs, the best classifier was with EMD and 75 percentile difference, resulting in a correctly classified rate of 67.44%. Figure 3 shows the scatter plot of the data samples with the two features.

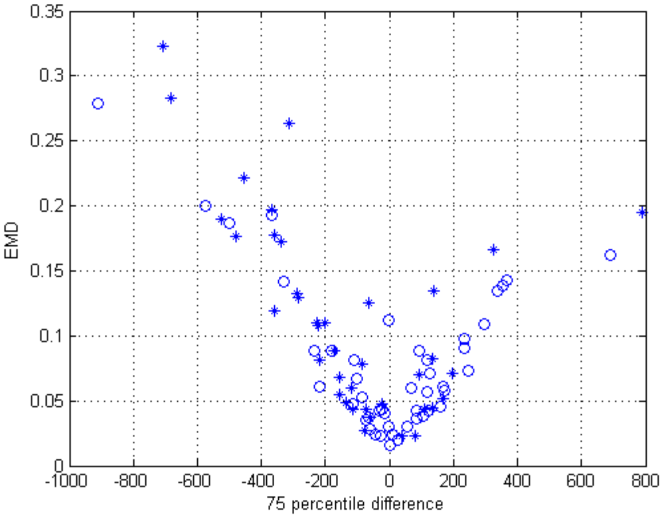

Fig. 3. The feature pair with the highest accuracy: $*$ denotes responding samples, while o denotes non-responding samples.

Table 1. Comparison between AdaBoost and random forests classifier

Classifier	*Sensitivity*	*Specificity*	*Accuracy*
AdaBoost	67.5%	63%	65.12%
Random forests	67.5%	63%	65.12%

Visual inspection on Figure 3 promptly reveals that our data is not linearly separable even in the feature space with the best classification rate. This indicates that non-linear classifiers may be more effective in solving our problem. For this reason, we also considered AdaBoost and RF classifiers. Our LOOCV experiments with the Weka implementation of AdaBoost resulted in 65.12% correct classification rate with 10 learning iterations in average. Not only the resulting accuracy is worse than the one for FLDA, but AdaBoost also selected the median difference, kurtosis ratio, 25 percentile difference, STD difference, skewness ratio, and kurtosis difference, which are different from the ones selected by the FLDA.

Next we evaluated the RF classifier as another non-linear classification approach. The report [15] suggests that RF classifier performs quite well, even in the presence of noise in training data, while AdaBoost is susceptible to the noise in training data in comparison with the bagging algorithm [16]. The results of

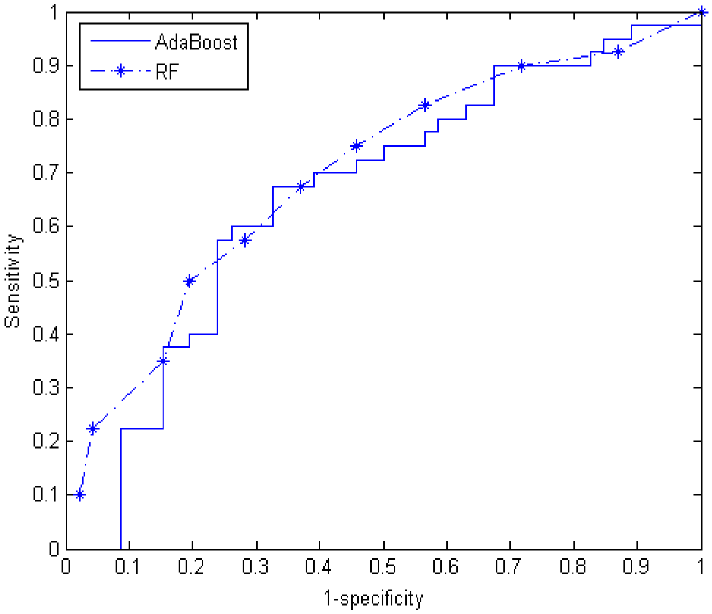

Fig. 4. The ROC curve drawn from Weka on leave-one-out cross validation, with green line for random forests classifier and red line for AdaBoost classifier.

our experiment with the Weka implementation show that the final random forest is composed of 10 trees, each of which is constructed considering five random features. The LOOCV accuracy of the resulting system was 65.12%, the same as AdaBoost classifier.

In table 1, the sensitivity, specificity, and accuracy drawn from Weka report for AdaBoost and RF classifier are compared. With the current dataset, AdaBoost and RF classifier report the same results, yet worse than FLDA.

4 Discussion

In our preliminary study, we exploited statistical pattern classification approaches towards early detection of treatment response using an ADC map.

Cell density and edema may be reflected in ADC values before size changes are apparent on standard MRI sequences. Therefore ADC holds promise as a biomarker, both in determining which tumors are more likely to respond to treatment, and to determine which tumors are actually responding. This will have major implications for clinical trials.

With our current dataset, we obtain comparable performance between all three classifiers tested. More future work will be to use mixture models to quantitize the tumor part and edema part since they show different patterns in histogram changes.

References

1. Ross, B.D., Moffat, B.A., Gebarski, S.S., Quint, D.J., Johnson, T.D., Junck, L., Robertson, P.L., Muraszko, K.M., Dong, Q., Meyer, C.R., Bland, P.H., McConville, P., Geng, H., Rehemtulla, A., Chenevert, T.L.: Evaluation of cancer therapy using diffusion magnetic resonance imaging. Molecular Cancer Therapeutics **2** (2003) 581–587
2. Chenevert, T.L., Stegman, L.D., Taylor, J.M.G., Robertson, P.L., Greenberg, H.S., Rehemtulla, A., etc., B.D.R.: Diffusion magnetic resonance imaging: an early surrogate marker of therapeutic efficacy in brain tumors. Journal of the National Cancer Institute **92**(24) (2000)
3. Moffat, B.A., Chenevert, T.L., Lawrence, T.S., Meyer, C.R., Johnson, T.D., Dong, Q., Tsien, C., Mukherji, S., Quint, D.J., Gebarski, S.S., Robertson, P.L., Junck, L.R., Rehemtulla, A., Ross, B.D.: The functional diffusion map: an imaging biomarker for the early prediction of cancer treatment outcome. Neoplasia **8(4)** (2006) 259–267
4. Pamela W. Schaefer, M.: Diffusion-weighted mr imaging of the brain. Radiology **217** (2000) 331–345
5. Otsu, N.: A threshold selection method from gray level histograms. IEEE Trans. Systems, Man and Cybernetics **9** (1979) 62–66
6. Barker, F.G., Prados, M.D., Chang, S.M., Gutin, P.H., Lamborn, K.R., Larson, D.A., Malec, M.K., McDermott, M.W., Sneed, P.K., Wara, W.M., Wilson, C.B.: Radiation response and survival time in patients with glioblastoma multiforme. J Neurosurg **84(3)** (1996) 442–448
7. Hamstra, D.A., Chenevert, T.L., Moffat, B.A., Johnson, T.D., Meyer, C.R., Mukherji, S., Quint, D.J., Gebarski, S.S., Fan, X., Tsien, C., Lawrence, T.S., Junck, L.R., Rehemtulla, A., Ross, B.D.: Evaluation of the functional diffusion map as an early biomarker of time-to-progression and overall survival in high-grade glioma. PNAS **102** (2005) 16759–16764
8. Y. Rubner, C.T., Guibas., L.J.: A metric for distributions with applications to image databases. Proceedings of the 1998 IEEE International Conference on Computer Vision (1998) 59–66
9. Ling, H., Okada, K.: An efficient earth mover's distance algorithm for robust histogram comparison. IEEE Trans. on Pattern Analysis and Machine Intelligence **29(5)** (2007) 840–863
10. Duda, R.O., Hart, P.E., Stork, D.H.: Pattern Classification. Wiley Interscience (2000)
11. Freund, Y., Schapire, R.E.: A short introduction to boosting. Journal of Japanese Society for Artificial Intelligence **14** (1999) 771–780
12. Ho, T.K.: Random decision forest. In: Proceedings of the 3rd Internation Conference on Document Analysis and Recognition. (1995) 278–282
13. Breiman, L.: Random decision forest. Machine Learning **45** (2001) 5–32
14. Witten, I.H., Frank, E.: Data Mining: Practical machine learning tools and techniques. Morgan Kaufmann, San Francisco (2005)
15. Pal, M.: Random forests for land cover classification. In: Geoscience and Remote Sensing Symposium, Proceedings of IEEE International. (2003) 3510– 3512
16. Breiman, L.: Bagging predictors. Machine Learning **24**(2) (1996) 123–140

A Fiber Tractography Based Examination of Neurodegeneration on Language-Network Neuroanatomy

Jeffrey T. Duda[1], Brian Avants[2], Jane Asmuth[1], Hui Zhang[2], Murray Grossman[3], and James C. Gee[2]

[1] Department of Bioengineering, University of Pennsylvania, USA,
`jtduda@seas.upenn.edu`,
[2] Department of Radiology, University of Pennsylvania, USA.
[3] Department of Neurology, University of Pennsylvania, USA.

Abstract. Diffusion tensor (DT) images provide information regarding the micro-architecture of the underlying soft tissue. This directional information may be used to track white matter pathways as well as to quantify connectivity patterns in the brain. Our objective is to build a model of expected neuroanatomical fiber connections from a set of control data and to use this model to to detect *in vivo* evidence of disruption in the human language network. This connectivity model provides the basis for a new DT-based measure, fiber-directed diffusion, which is related to the Gaussian model of directional diffusion probability and enables assessment of disconnection in cortical networks. We apply this technique to study a specific form of fronto-temporal dementia (FTD), semantic dementia (SD), which compromises semantic memory. Models of language network connections are created in an atlas and warped to a subject specific template to examine connectivity properties along the language pathways. Differences between an elderly control population and an SD population are detected in the left arcuate fasciculus and left inferior longitudinal fasciculus, suggesting that SD neurodegeneration induces loss of both connectivity and computational structure.

1 Introduction

Neurodegenerative disease affects millions of individuals each year while treatment and understanding of these diseases, and their relationship to behavior, remains generally elusive [1]. Post-Mort-em studies have revealed protein aggregations that are focal in nature [2, 3], but increasing evidence suggests potential involvement of entire systems of the brain [4, 5]. A unique window onto the disease process can be gained through DT magnetic resonance imaging, which quantifies subtle *in vivo* changes in brain connectivity [6, 7] which can be correlated with changes in cognition [8] or other clinical measurements [9, 10]. In addition, white matter focused diffusion tensor MRI show promise for increasing clinical diagnosis and detection of dementia phenotypes [8, 5].

FTD is an early-onset neurodegenerative condition with an average age of onset in the sixth decade of life [11–13]. The condition is almost as common as AD in individuals less than 65 years of age [12, 14, 15] with survival typically eight years from onset [11, 15]. The disease is due to a disorder of tau metabolism or the accumulation of a ubiquinated protein known as TDP-43 [16]. The major clinical features of FTD include primary progressive aphasia (PPA) or a disorder of social comportment and personality together with limited executive resources [17–19], although there is substantial empirical evidence that all patients with FTD have impairments in language [20]. Recent studies have begun to demonstrate longitudinal decline on language measures in clinical [21, 20] and pathologically-defined [22] populations. Semantic dementia (SD) is a form of PPA characterized by fluent and circumlocutory spontaneous speech, which may be empty in content, and is associated over time with difficulty understanding single words and objects. Recent evidence suggests the primary involvement of the left hemisphere language network in the evolution of SD [4, 20]. In SD, the anterior temporal lobe is indicated and associated with decline in semantic fluency [23]

The use of DTI in tract based studies is a topic that has received much attention recently [24–27] and the TBSS method [28] has proven to be particularly useful in whole-brain analysis of FA. Specifically, performing tractography in tensor atlases has been shown to be a reliable method for extracting fiber tracts of interest [29]. Here the focus is limited to the the language network and we incorporate a metric that is sensitive to variation in tensor shape as well as orientation in relation to a model of expected fiber direction. The key aspect of this contribution is a new tool to quantify prior-based connective likelihood that increases power for detecting population differences and aids in direct interpretation of DT data in terms of a meaningful neuroanatomical context.

2 Methods

Our current approach extends previous DT based studies by building an explicit model of the language network white matter pathways within a multi-variate atlas in order to identify particular local regions that may be associated with reduced connectivity. Image normalization is used to transform the model pathways into the space of a subject-specific atlas created from an elderly control population. These expected fiber pathways are used to examine the underlying tensor values in the control population as well as in SD patients.

2.1 Model fiber pathways in the language network

In order to identify fiber tracts of interest, a multi-variate atlas consisting of both T1 and DT data is used. Regions of interest are identified in the T1 component while the DT component is used for fiber tracking. The Camino Toolkit [30] is used to perform whole-brain deterministic tractography where all voxels with an fractional anisotropy (FA) greater than 0.15 are used as seed points. A constant step size of 0.3 mm is used along with linear interpolation of the principal direction of diffusion vector field. Fibers are terminated when they enter a voxel with FA less than 0.15 or when local curvature of a fiber exceeds 45 degrees. In a manner similar to previous work [31, 29], ROI's are carefully identified in order to extract the fibers associated with the fiber bundles of interest: arcuate fasciculus (AF), inferior longitudinal fasciculus (ILF) and uncinate fasciculus (UF). The extracted fiber bundles are illustrated in figure 1.

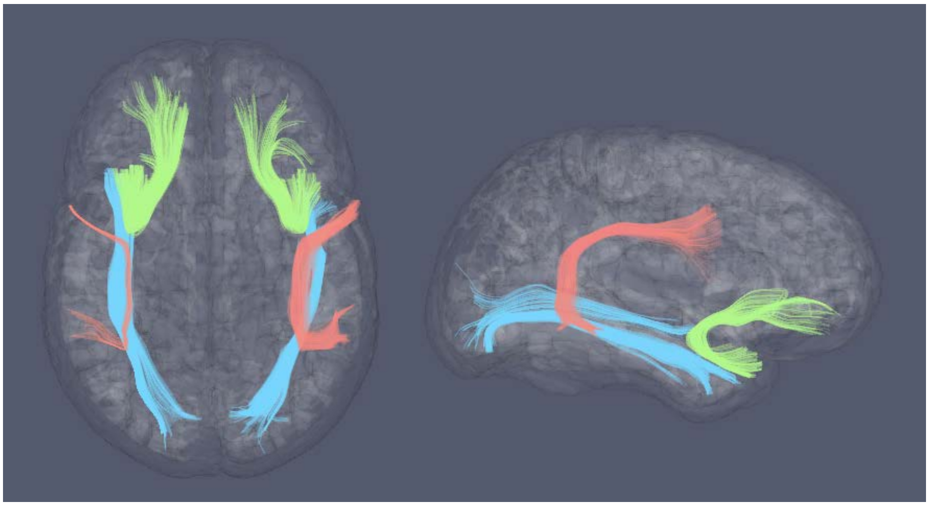

Fig. 1. Language network models are created using deterministic tracking in a multivariate atlas. These model fiber bundles are transformed to a population specific atlas. Axial and sagittal views are presented with the arcuate fasciculus (orange), uncinate fasciculus (green) and inferior longitudinal fasciculus (blue).

A subject-specific atlas is created from the DT images for an elderly control population (N=11) and SD patients (N=7) [32]. Images of FA are calculated from the DT component of the multi-variate atlas and from the elderly control population. Symmetric normalization (SyN) [33] is used on the FA images to determine a mapping between the templates. This mapping is then used to transform the model fiber bundles into the elderly control template.

2.2 Examining connectivity along fibers

In order to identify potential alterations to tissue micro-architecture, we require a metric that uses the fiber direction information provided by the model pathways to interrogate the underlying tensor data in each individual. One such measure is the fiber directed diffusion (FDD) [34] and here we use a normalized version of this metric (nFDD). FDD is the diffusion coefficient for diffusion along v, the tangent to a fiber passing through diffusion tensor D.

$$FDD = v^T D v \tag{1}$$

Here, for additional insight, we show how this metric relates to the eigenvalues $(\lambda_1, \lambda_2, \lambda_3)$ and eigenvectors (e_1, e_2, e_3) of D. By diagonalizing D, we obtain the matrices R and Λ where R contains the eigenvectors of D, and Λ is a diagonal matrix of the eigenvalues. This provides us with $D = R^T \Lambda R$ which leads to:

$$FDD = v^T R^T \Lambda R v \tag{2}$$

$$FDD = v^T \left[e_1, e_2, e_3\right] \Lambda \left[e_1^T, e_2^T, e_3^T\right]^T v \tag{3}$$

$$FDD = \left[v \cdot e_1, v \cdot e_2, v \cdot e_3\right] \Lambda \left[v \cdot e_1, v \cdot e_2, v \cdot e_3\right]^T \tag{4}$$

$$FDD = \lambda_1 \left(v \cdot e_1\right)^2 + \lambda_2 \left(v \cdot e_2\right)^2 + \lambda_3 \left(v \cdot e_3\right)^2 \tag{5}$$

Our primary interest lies in examining the proportion of diffusion that occurs in a direction coincident with the direction the fiber passing through the tensor so we normalize by the trace of D:

$$nFDD = \frac{v^T D v}{tr(D)} = \frac{\lambda_1 \left(v \cdot e_1\right)^2 + \lambda_2 \left(v \cdot e_2\right)^2 + \lambda_3 \left(v \cdot e_3\right)^2}{\lambda_1 + \lambda_2 + \lambda_3} \tag{6}$$

While this metric has not been studied extensively, it has a number of features that make it suitable for use in this study. The normalization insures that it's values lie between 0 and 1.0 which facilitates statistical analysis. The value will be high in areas that exhibit both high FA and a high degree of similarity between the direction of the model fiber and the primary direction of diffusion. Conversely, the value will be low in regions of decreased FA, such as that resulting from demyelination and in regions of increased fiber tortuosity which may also be an indicator of neurodegeneration. Finally, we indicate that this measure is related to the Gaussian model of directional diffusion which states that the probability of diffusion along a particular direction, v, is given by $\sum_i \lambda_i \left(v \cdot e_i\right) / \sum_i \lambda_i$. Thus, this measurement provides a direct interpretation of the underlying DT data in terms of a specific connective model alleviating, to a degree, the difficulty associated with traditional, tract-blind scalar reductions of the diffusion tensor. We now show that this measure increases detection sensitivity in a small population study of SD versus controls.

3 Results

For the UF and ILF, the corresponding model fibers in each hemisphere appear very similar. However, the AF in the left hemisphere is much larger than that in the right hemisphere, a property reported in previous work [35]. Each individual's template-aligned DT data is used to calculate the nFDD at every point along the model pathways. A Student's t-test is performed at each point and we only consider results with an FDR-corrected p-value < 0.2. Compared to elderly controls, SD subjects show multiple areas of reduced nFDD in the left AF. Regions of reduced nFDD are also detected in the left ILF as is one region of increased nFDD. These results are illustrated in figure 2.

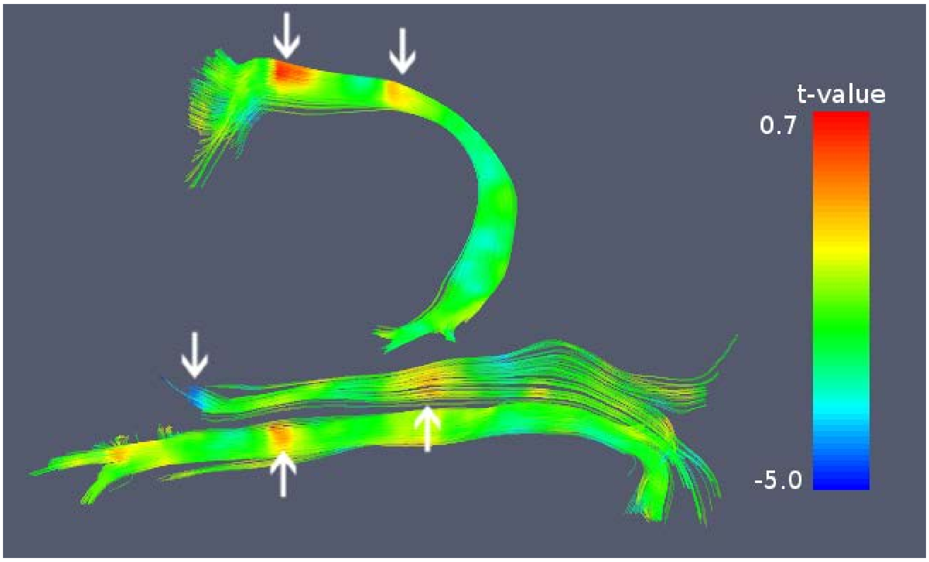

Fig. 2. Regions of reduced nFDD were detected in both the left ILF (bottom) and the left AF (top) as well as a small region of increased nFDD in the ILF. Both are shown here in a sagittal view. The AF is translated along the z-axis to allow full visualization of the ILF. Arrows indicate clusters where FDR corrected p-values were less than 0.2

To gain additional insight into the properties of the nFDD, alternative metrics typically found in DT studies were examined in a similar manner. These additional metrics include FDD, FA, axial diffusion (AD), radial diffusion (RD) and mean diffusion (MD). In the case of FDD, MD, and AD no significant differences are detected. RD analysis provides one small cluster near near the anterior of the left AF with a peak t-value of 3.19. Analysis with FA provides similar results to nFDD in the left AF, but the clusters sizes are smaller and the peak t-value is 6.1. Both FA and RD fail to identify any significant differences in the left ILF.

4 Discussion

This study demonstrates that diffusion tensor tractography may be combined with image registration techniques to create a system-based model for delineating white matter connectivity differences in SD. Additionally, we utilize a metric, nFDD, that leverages both the shape and orientation information provided by the tensor to identify localized white matter differences between control and patient populations. An examination of typical metrics used in DT-based studies illustrates the ability of nFDD to detect subtle white matter differences that may not be identified by more standard measures.

The study of an SD population provides a particularly relevant population for examining connectivity. The semantic fluency impairments exhibited by SD patients is a type of conduction aphasia. In this case, symptoms result primarily from a reduction in communication between cortical regions [36]. The left AF is believed to play an integral role as it provides communication between Wernicke's area and Broca's area. This clinical background supports the evidence of reduced connectivity in the left AF provided by our fiber tract-based study.

The use of a model of expected fiber orientation provides the framework that allows nFDD to be used. Here we focused on attempting to identify localized regions of alteration in white matter structure. However, the model pathways provide a framework for examining connectivity on a larger scale. Future work will focus on examining potential methods for using this wide spread connectivity information to look for more subtle white matter changes such as those that may result from diffuse axonal injury. By integrating the nFDD along the expected pathways it may be possible to elucidate information regarding more wide-spread losses in connectivity than is possible with the current localized methods.

References

1. Kipps, C.M., Davies, R.R., Mitchell, J., Kril, J.J., Halliday, G.M., Hodges, J.R.: Clinical significance of lobar atrophy in frontotemporal dementia: application of an mri visual rating scale. Dement Geriatr Cogn Disord **23**(5) (2007) 334–342
2. Harasty, J.A., Halliday, G.M., Kril, J.J., Code, C.: Specific temporoparietal gyral atrophy reflects the pattern of language dissolution in alzheimer's disease. Brain **122 (Pt 4)** (1999) 675–686
3. Davies, R.R., Hodges, J.R., Kril, J.J., Patterson, K., Halliday, G.M., Xuereb, J.H.: The pathological basis of semantic dementia. Brain **128**(Pt 9) (2005) 1984–1995
4. Pobric, G., Jefferies, E., Ralph, M.A.L.: Anterior temporal lobes mediate semantic representation: mimicking semantic dementia by using rtms in normal participants. Proc Natl Acad Sci U S A **104**(50) (2007) 20137–20141
5. Kril, J.J., Halliday, G.M.: Clinicopathological staging of frontotemporal dementia severity: correlation with regional atrophy. Dement Geriatr Cogn Disord **17**(4) (2004) 311–315
6. Rose, S.E., Chen, F., Chalk, J.B., Zelaya, F.O., Strugnell, W.E., Benson, M., Semple, J., Doddrell, D.M.: Loss of connectivity in alzheimer's disease: an evaluation of white matter tract integrity with colour coded mr diffusion tensor imaging. J Neurol Neurosurg Psychiatry **69**(4) (2000) 528–530

7. Yoshiura, T., Mihara, F., Koga, H., Noguchi, T., Togao, O., Ohyagi, Y., Ogomori, K., Ichimiya, A., Kanba, S., Honda, H.: Cerebral white matter degeneration in frontotemporal dementia detected by diffusion-weighted magnetic resonance imaging. Acad Radiol **13**(11) (2006) 1373–1378
8. Borroni, B., Brambati, S.M., Agosti, C., Gipponi, S., Bellelli, G., Gasparotti, R., Garibotto, V., Luca, M.D., Scifo, P., Perani, D., Padovani, A.: Evidence of white matter changes on diffusion tensor imaging in frontotemporal dementia. Arch Neurol **64**(2) (2007) 246–251
9. Grossman, M., Libon, D.J., Forman, M.S., Massimo, L., Wood, E., Moore, P., Anderson, C., Farmer, J., Chatterjee, A., Clark, C.M., Coslett, H.B., Hurtig, H.I., Lee, V.M.Y., Trojanowski, J.Q.: Distinct antemortem profiles in patients with pathologically defined frontotemporal dementia. Arch Neurol **64**(11) (2007) 1601–1609
10. Grossman, M., Wood, E.M., Moore, P., Neumann, M., Kwong, L., Forman, M.S., Clark, C.M., McCluskey, L.F., Miller, B.L., Lee, V.M.Y., Trojanowski, J.Q.: Tdp-43 pathologic lesions and clinical phenotype in frontotemporal lobar degeneration with ubiquitin-positive inclusions. Arch Neurol **64**(10) (2007) 1449–1454
11. Hodges, J.R., Davies, R., Xuereb, J., Kril, J., Halliday, G.: Survival in frontotemporal dementia. Neurology **61**(3) (2003) 349–354
12. Rossoand, S.M., Kaatand, L.D., Baksand, T., Joosseand, M., de Koningand, L., Pijnenburgand, Y., de Jongand, D., Dooijesand, D., Kamphorstand, W., Ravidand, R., Niermeijerand, M.F., Verheijand, F., Kremerand, H.P., Scheltensand, P., van Duijnand, C.M., van Heutinkand, P., Swietenand, J.C.: Frontotemporal dementia in the netherlands: patient characteristics and prevalence estimates from a population-based study. Brain **126** (2003) 2016–2022
13. Grossman, M.: Imaging in frontotemporal dementia. In: The human frontal lobes: Functions and Disorders. Guilford (2006) 408–421
14. Knopman, D.S., Petersen, R.C., Edland, S.D., Cha, R.H., Rocca, W.A.: The incidence of frontotemporal lobar degeneration in Rochester, Minnesota, 1990 through 1994. Neurology **62**(3) (2004) 506–508
15. Cairns, N., Lee, V., Trojanowski, J.Q.: Frontotemporal dementia. In: The human frontal lobes: Functions and Disorders. Guilford (2006) 408–421
16. Lee, V.M., Goedert, M., Trojanowski, J.Q.: Neurodegenerative tauopathies. Annu Rev Neurosci **24** (2001) 11211159
17. Davis, K.L., Price, C., Moore, P., Campea, S., Grossman, M.: Evaluating the clinical diagnosis of Frontotemporal degeneration: A re-examination of Neary et al. Neurology **56** (1998) A144–A145
18. McKhann, G., Trojanowski, J.Q., Grossman, M., Miller, B.L., Dickson, D., Albert, M.: Clinical and pathological diagnosis of frontotemporal dementia: Report of a work group on frontotemporal dementia and Pick's disease. Arch Neurol **58** (2001) 1803–1809
19. Fellows, L.K., Farah, M.J.: Different underlying impairments in decision-making following ventromedial and dorsolateral frontal lobe damage in humans. Cereb Cortex **15** (2005) 58–63
20. Libon, D.J., Xie, S.X., Moore, P., Farmer, J., Antani, S., McCawley, G., Cross, K., Grossman, M.: Patterns of neuropsychological impairment in frontotemporal dementia. Neurology **78** (2007) 369–375
21. Blair, M., Marczinski, C.A., Davis-Faroque, N., Kertesz, A.: A longitudinal study of language decline in alzheimers disease and frontotemporal dementia. J Int Neuropsychol Soc **13** (2007) 237–245

22. Grossman, M., Libon, D.J., Forman, M.S., et al: Distinct antemortem profiles in pathologically defined patients with frontotemporal dementia. Arch Neurol (2007)
23. Grossman, M., McMillan, C., Moore, P., Ding, L., Glosser, G., Work, M., Gee, J.C.: Whats in a name: voxel-based morphometric analyses of mri and naming difficulty in alzheimers disease, frontotemporal dementia and corticobasal degeneration. Brain **127** (2004) 628–649
24. Corouge, I., Fletcher, P.T., Joshi, S., Gouttard, S., Gerig, G.: Fiber tract-oriented statistics for quantitative diffusion tensor mri analysis. Medical Image Analysis (2006)
25. Ding, Z., Gore, J.C., Anderson, A.W.: Classification and quantification of neuronal fiber pathways using diffusion tensor mri. Magnetic Resonance in Medicine (2003)
26. Jones, D.K., Catani, M., Pierpaoli, C., Reeves, S.J.C., Shergill, S.S., O'Sullivan, M., Golesworthy, P., McGuire, P., Horsfield, M.A., Simmons, A., Williams, S.C.R., Howard, R.J.: Age effects on diffusion tensor magnetic resonance imaging tractography measures of frontal cortex connections in schizophrenia. Human Brain Mapping (2005)
27. Fillard, P., Gilmore, J., Lin, W., Piven, J., Gerig, G.: Quantitative analysis of white matter fiber properties along geodesic paths. In: Medical Image Computing and Computer-Assisted Intervention. Volume 2879 of Lecture Notes in Computer Science. (2003)
28. Smith, S.M., Jenkinson, M., Johansen-Berg, H., Rueckert, D., Nichols, T.E., Mackay, C.E., Watkins, K.E., Ciccarelli, O., Cader, M.Z., Matthews, P.M., Behrens, T.E.J.: Tract-based spatial statistics: Voxelwise analysis of multi-subject diffusion data. NeuroImage (2006)
29. Yushkevich, P.: Structure-specific statistical mapping of white matter tracts. NeuroImage **In Press**(Available online) (2008)
30. Cook, P.A., Bai, Y., Hall, M.G., Nedjati-Gilani, S., Seunarine, K.K., Parker, G.J.M., Alexander, D.C.: Camino: Open-source diffusion-MRI reconstruction and processing. In: Proceedings of the 14th Scientific Meeting of the International Society for Magnetic Resonance in Medicine. (2006) 2759
31. Wakana, S., Jiang, H., Nagae-Poetscher, L.M., van Zijl, P.C.M., Mori, S.: Fiber tract-based atlas of human white matter anatomy. Radiology (2004)
32. Zhang, H., Avants, B.B., Yushkevich, P.A., Woo, J.H., Wang, S., McCluskey, L.F., Elman, L.B., Melhem, E.R., Gee, J.C.: High-dimensional spatial normalization of diffusion tensor images improves the detection of white matter differences in amyotrophic lateral sclerosis. IEEE Transactions on Medical Imaging — Special Issue on Computational Diffusion MRI **26**(11) (2007) 1585–1597 PMID: 18041273.
33. Avants, B.B., Epstein, C.L., Grossman, M., Gee, J.C.: Symmetric diffeomorphic image registration with cross-correlation: Evaluating automated labeling of elderly and neurodegenerative brain. Med Image Anal **12**(1) (2008) 26–41
34. Duda, J.T., Simon, T., Gee, J.C.: Examining tissue micro-architecture via interrogation of diffusion tensor fiber tractography. In: International Conference on Human Brain Mapping. (2006)
35. Nucifora, P.G., Verma, R., Melhem, E., Gur, R.E., Gur, R.C.: Leftward asymmetry in relative fiber density of the arcuate fasciculus. NeuroReport **16**(8) (2005) 791–794
36. Catani, M., ffytche, D.H.: The rises and falls of disconnection syndromes. Brain (2005)

A Framework for Joint Analysis of Structural and Diffusion MRI

Ran Tao [1,2] , P.Thomas Fletcher[1,2], Ross T. Whitaker[1,2]

[1] Scientific Computing and Imaging Institute, University of Utah
[2] School of Computing, University of Utah

Abstract. Diffusion tensor MRI (DTI) is a promising brain imaging technology with applications in clinical diagnosis, brain development and pathology, and basic neuroscience. There is a strong interest in the clinical community for using DTI in concert with conventional MRI and combining white matter connectivity with morphological and functional analyses. This paper presents a processing pipeline for the joint analysis of structural and diffusion tensor MRI. This pipeline addresses the simultaneous alignment and filtering of diffusion weighted images to correct eddy current artifacts and the alignment of those images to structural T1 MRI to correct for susceptibility artifacts, and this paper demonstrates the importance of performing these corrections. It also shows how a T1-based, group specific atlas can be used to generate grey matter regions of interest that can drive subsequent connectivity analyses. The result is a system that can be combined with a variety of tools for MRI analysis for tissue classification, morphometry, and cortical parcellation.

1 Introduction

Diffusion tensor imaging (DTI) is a promising brain imaging technology with a variety of clinical and scientific applications. Recent research results suggest that DTI could be useful for diagnosing ischemia and brain injuries, studying brain development and aging, and characterizing neurological disorders [1], as well as mapping white-matter pathways [2]. While qualitative evaluations of tractography are still interesting and quite common, the neuroscience community is moving quite strongly toward using DTI for quantitative evaluations of white-matter characteristics either directly on the image of tensors [3] or in conjunction with a method for specifying regions of interest. DTI is proving to effective for quantifying properties of white-matter regions, but perhaps the most promising use of this technology is in the analysis of brain *connectivity*. Connectivity, however, is not a strictly local property, and there is a strong interest in the clinical community for using DTI in concert with conventional MRI, and combine the analysis of connectivity with morphological and functional analyses. Yet the literature shows very little research that has achieved a joint, quantitative analysis of DTI and structural MRI at the level of specific white-matter tracts or paths.

The combination DTI with structural or functional MRI raises some challenging technical problems. One of the main issues is the problem of geometric alignment. The diffusion-weighted images (DWIs), typically acquired with an echo-planar imaging sequence (EPI), taken at different gradient directions, are subject to several types of geometric distortion. First is the problem of eddy currents, which result from the fast switching of magnetic fields of the gradients, necessary for time-effective acquisitions. These residual currents result in a scaling, shift, and shear (affine) warp along the gradient direction. The EPI sequences are quite fast, and thus there is typically little head motion during the acquisition of a single gradient. However, the overall sequence can take minutes, causing a further misalignment (3D rigid transformation) between gradient directions. These gradient-dependent affine warps and rigid motions can cause artifacts when the DWI images are combined to produce tensors.

A second source of distortion are inhomogeneities in the magnetic field caused by differences in the magnetic susceptibility within field of view of the scanner. EPI requires a homogeneous magnetic field, and magnetic interfaces within the human head (e.g. sinuses and bone) result in local image distortion or signal dropout. The result is that all of the DWI images undergo a nonlinear warp (relative to a typical T1 structural image) along the phase-encoded direction of the sequence.

The combination of these affects not only undermines the quality of the tensor estimates, but significantly impacts one's ability to either use structural and functional MRI to either drive the DTI analysis (e.g. seed regions for tracts) or jointly analyze connectivity with other quantities such as functional response, cortical thickness, and morphology. This paper presents a set of algorithms for the joint analysis of structural and diffusion-weighted MRI. This pipeline addresses the simultaneous alignment and filtering of DWI images to correct eddy current artifacts and the subsequent alignment of those images to structural, T1 MRI to correct for susceptibility artifacts, and this paper demonstrates the importance of performing these corrections. It also shows how a T1-based, group specific atlas can be used to generate grey-matter regions of interest that can drive subsequent connectivity analyses. The result is a system that can be combined with a variety of tools for MRI analysis for tissue classification, morphometry, and cortical parcellation.

2 Related Work

There are two areas of related research. These are previous methods for preventing or correcting EPI distortions and earlier work that explicity combines DTI and structural/functional images.

In general, eddy current distortion is addressed either through the pulse sequence [4], or by applying a data-driven, post-processing step to register the DW images to a baseline image [5, 6]. Here we consider the post-processing approach because of the ability to deal with a large body of retrospective data and data from large, ongoing studies, for which acquisition parameters are already in place.

The other major source of geometric distortion is susceptibility artifacts, which are modeled as a nonlinear, patient specific warp along the phase-encoding direction of the EPI sequence. This can be done by either acquiring associated field maps and explicity modeling the distortion [7] or using a data-driven, post-processing algorithm that coregisters, via a nonlinear warp, the EPI and structural (e.g., T1) images of the same patient [8]. The most promising approach, is, in principle to use the field maps to explicitly account for the susceptibility. In practice, however, there are some challenges. First, field maps themselves, when they are available, are noisy and must undergo some preprocessing. Second, effective use of field for distortion correction requires knowledge of a set of acquisition parameters, which are not always readily available and can have somewhat distinct interpretations between different sequences and scanners. Finally, even with field maps there remain errors in the system, in both the accuracy of the field maps and (somewhat smaller) distortions in the structural or functional data. Thus, if the goal is alignment to anatomical (T1) data, field maps will get the data close, but there is, in many cases, still a need to correct for residual, nonlinear distortions. Therefore, we propose a data driven approach that explicitly aligns the baseline image to a T1 image using a diffeomorphic flow along the phase direction. A framework to combine diffusion and structural images has been proposed in [9, 10]. A general nonlinear 3D registration was used to map the diffusion imagery to the T1 MRI. For group analysis, a DTI atlas was built from individual DWIs and the ROIs were manunally chosen on the atlas. Then the ROIs were mapped back to each subject's DWIs to perform tractography analysis. Our registration approach differs in that our transformations explicitly model head motion, eddy currents, and susceptibility artifacts to combine DTI and structural imaging. Furthermore, we build a structural atlas from the individual T1 images in which we define grey matter ROIs. These ROIs are then mapped back to each individual DTI for white matter pathway analysis.

The second body of relevant work is the scientific research in combining analysis of structural or functional MRI with DTI. There are several studies that explore statistical relationships between fMRI and DTI-derived quantities. For instance, Baird et. al [11] describe a combined analysis of DTI and fMRI and correlations between BOLD responses (object recognition task) and FA levels in the corpus callosum. FA correlations are computed per subject with values in active regions, avoiding the need for direct, per-subject correspondence between DTI and fMRI images. Upadhyay et al. [12] use activation regions (auditory stimuli) to seed a probabilistic tractography analysis, and rely on registration to an atlas of both anatomical and DTI images. Olesen et. al [13] show a correlation between FA and BOLD responses in a developmental (pediatric) study, and rely on linear warps of DTI and structural data to a common atlas. Quantitative results for BOLD response and FA are computed on a regional basis. There is some work outside of functional MRI on combining DTI with anatomical scans. For instance, Gilmore et. al [14] analyze postnatal development of white matter by combining T1, T2, and DTI analysis. They use a 3D spline deformation to align anatomical scans to the DTI. Studholme [15] describes a joint anatomical/DTI registration strategy and demonstrates improved localization.

3 Combined DTI and Structural Analysis Pipeline

In this section we detail the steps involved in the proposed pipeline for combining DTI and structural image analysis. The process is demonstrated using images from five healthy individuals from the control group of an ongoing autism study. We used high-resolution T1 and T2 weighted MR images and a DT-MRI for each individual. The output of the pipeline is a diffusion tensor image, expressed in the coordinates in which it is acquired, but which has undergone a nonlinear, geometric correction so that it aligns it to an associated anatomical image by a rigid transformation. A general outline of our pipeline, illustrated in Figure 1, is as follows:

1. Preprocess structural images to remove skull, correct bias field, normalize intensities, and segment tissue classes (to provide a white matter mask).
2. Correct diffusion tensor images for eddy currents, head motion, and EPI distortions, resulting in coregistered T1, T2, and DTI for each subject.
3. Build a structural atlas from all subjects' T1 images. Seed regions for tract endpoints are manually delineated in the structural atlas and then mapped from the atlas to each individual.
4. Automatically segment white matter tracts and quantify diffusion properties using volumetric pathway analysis.

These steps are described in detail below.

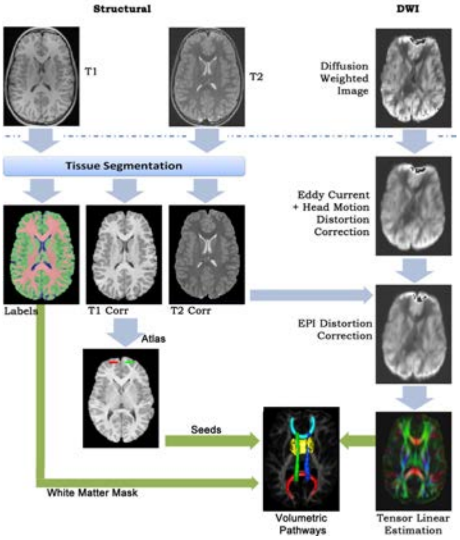

Fig. 1. Joint structural and diffusion image analysis pipeline.

3.1 Structural Image Preprocessing

We coregister and segment the T1 and T2 MR images into gray matter, white matter and cerebrospinal fluid (CSF) tissue classes using a modified version of the Expectation Maximization method described in [16]. This process includes bias field correction of the images as well as an intensity normalization based on the tissue classes. We then rigidly align the T1, T2, and segmentation label images to the B0 image using a normalized correlation image match between B0 and T2 .

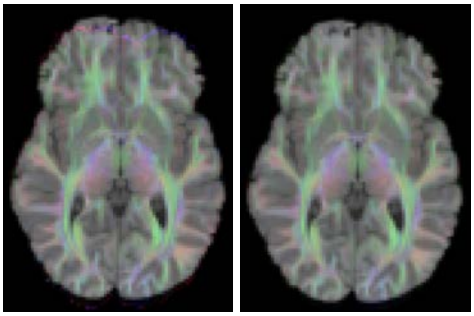

Fig. 2. Eigenvector color image overlayed on T1 using uncorrected DTI (left) and DTI corrected for head motion, eddy current, and EPI distortion (right).

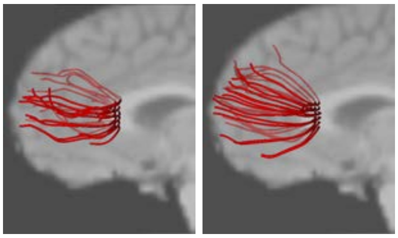

Fig. 3. Comparison of fiber tracking in the uncorrected (left) and corrected (right) DTI.

3.2 Diffusion Image Preprocessing

We first correct diffusion weighted images for head motion and eddy current distortions using the method described in [6]. Each diffusion weighted image is registered to the B0 image using mutual information and a transformation model of the linear effects of eddy current distortions combined with a rigid transformation to model head motion.Each gradient direction is rotated through the rotation matrix derived from the corresponding head motion correction. The updated gradient directions are used to address the issue of tensor reorientation.

Next, we correct for EPI distortions by warping the B0 image to the T2 weighted MRI. Let $I_{\mathrm{B0}}, I_{\mathrm{T2}}$ be the B0 and T2 images, respectively, defined on the image domain $\Omega \subset \mathbb{R}^3$. We model EPI distortions by a displacement field, $h : \Omega \rightarrow \Omega$, restricted to lie in the phase-encoding direction, in our case, along the y-axis. To ensure that the resulting image transformation is smooth and preserves topology, we use a diffeomorphic image registration [17] .

The results of the DTI alignment to the T1 image for one case are shown in Figure 2. Both DTIs are displayed as a colormap of the major eigenvector direction overlayed onto the T1 image. Notice that the original image has artifacts at the posterior edge due to misalignment of the DWI from eddy current and head motion. Also, the EPI distortion can be seen in the frontal lobe. The corrected image alleviates these problems and matches well with the T1.

To demonstrate the effects the distortion correction steps can have on DTI analysis, we performed a fiber tracking from the genu of the corpus callosum in both the uncorrected and corrected DTIs. Figure 3 shows the resulting fibers overlayed on a midsagittal slice from the T1 image. Because tractography combines tensor orientation with *relative tensor positions*, we expect tracts in the corrected data will differ from those in the original DTI acquisition. In Figure 3 we see that the corrected DTI produces more fibers, and that these fibers extend farther to the gray matter than in the uncorrected image.

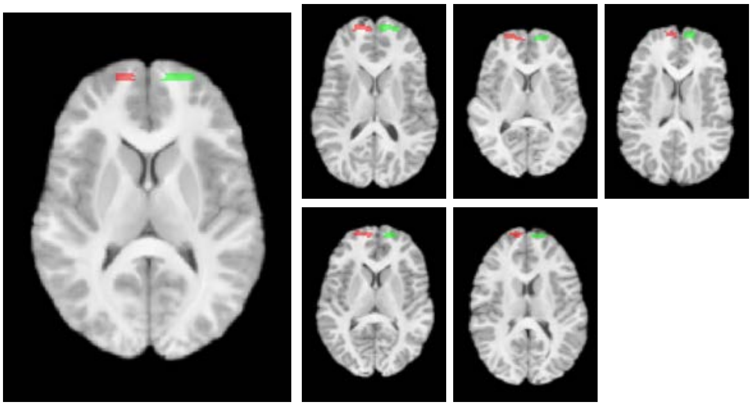

Fig. 4. The structural atlas built from the five T1 images with manually outlined frontal forceps seeds (left). The seeds mapped to each of the individual cases (right).

3.3 Group Atlas

We wish to delineate white-matter tracts as connecting specific grey-matter regions, which form the endpoints. Manual delineation of these endpoint regions for a large number of cases is tedious and prone to inconsistencies. To address these issues, we propose to manually delineate the seed regions in a structural atlas. The seeds can then be mapped back to the individual images. A structural group atlas is built from the T1 images of each individual using an unbiased diffeomorphic atlas building method [18]. This procedure results in an atlas image $\hat{I}$ and diffeomorphic transformations h_i that match each T1 image I_i to the atlas. This atlas is then used to manually delineate the endpoints of the white matter tracts of interest, producing binary seed images, $\hat{S}_j$. These seed images are then mapped back to the individual images, I_i, via $S_ij = \hat{S}_j \circ h_i^{-1}$.

Figure 4 shows the atlas built from the five subjects' T1 images. Endpoints of the forceps major, forceps minor, and left and right cingulum were manually

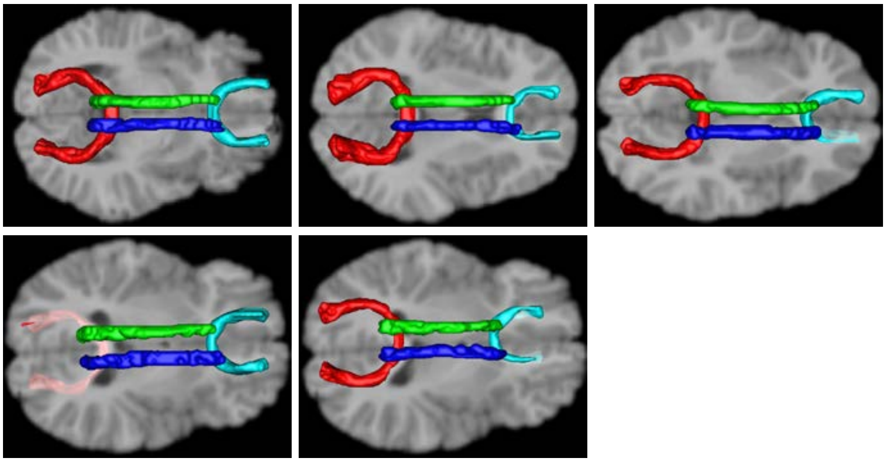

Fig. 5. Automatically extracted volumetric pathways [20] of the major and minor forceps and the cingulum bundles in each of the five cases.

delineated in the atlas. The forceps minor seeds are shown with the atlas in Figure 4. Finally, the forceps minor seeds mapped from the atlas to each individual are shown on the right side of Figure 4.

3.4 DTI Analysis

Because we are interested in white-matter paths that connect specific grey-matter regions, we opt for the *optimal path* strategy for DTI tractography [19]. In this paper we use the seeds mapped from the atlas to each individual as input for the automatic segmentation of the white matter tracts using the region-to-region volumetric method of described [20]. In that method, a voxel in an image is identified as belonging to a pathway if there is a path between the two input regions, passing through that voxel, with a cost that is within a specified tolerance of the of overall optimum.

We ran the volumetric connectivity analysis for each of the five cases in our study using the seeds mapped from the atlas as input. The resulting volumetric pathways for the major and minor forceps and the left and right cingulum bundles are shown in Figure 5.

4 Conclusion and Discussion

We have presented a comprehensive framework for combining structural and diffusion tensor MRI. This includes correction of the diffusion weighted images for head motion, eddy current artifacts, and EPI distortions caused by magnetic field inhomogeneity. We also demonstrated how an anatomical atlas built from the T1 images can be used to define seeds for all of the diffusion tensor images simultaneously. Finally, volumetric pathway analysis was used to automatically segment white matter tracts.

The pipeline presented in this paper provides the necessary foundations for performing a joint analysis of anatomical information derived from T1, functional data from fMRI, and white matter properties derived from DTI. We expect this will be important in studying correlations between white matter connectivity and functional activity, as well as structural gray matter properties, such as cortical thickness or volume. Also, the combination of structural and diffusion imaging allows us to construct detailed anatomical atlases, which could serve as a coordinate system for group analysis, and could be combined with cortical parcellation techniques to produce whole-brain connectivity maps. This T1/DTI alignment also provides an opportunity to include the DTI images in the atlas building procedure, for instance, using the T1/DTI registration method in [15].

References

1. Sundgren, P., Dong, Q., Gomez-Hassan, D., Mukherji, S., Maly, P., Welsh, R.: Diffusion tensor imaging of the brain: review of clinical applications. Neuroradiology **46** (2004) 339–350
2. Jellisona, B., Fielda, A., Medowb, J., Lazarc, M., Salamatd, M.S., Alexanderc, A.: Diffusion tensor imaging of cerebral white matter: A pictorial review of physics, fiber tract anatomy, and tumor imaging patterns. American Journal of Neuroradiology **25** (2004) 356–369
3. Snook, L., Plewes, C., Beaulieu, C.: Voxel based versus region of interest analysis in diffusion tensor imaging of neurodevelopment. NeuroImage **34** (2007) 243–252
4. Alexander, A., J. Tsuruda, D.P.: Elimination of eddy current artifacts in diffusion-weighted echo-planar images: The use of bipolar gradients. Magnetic Resonance in Medicine **38** (1997) 1016–1021
5. Mangin, J., Poupon, C., Clark, C., Bihan, D.L., Bloch, I.: Eddy-current distortion correction and robust tensor estimation for mr diffusion imaging. In: MICCAI. (2001) 186–194
6. Rohde, G., Barnett, A., Basser, P., Marenco, S., C, C.P.: Comprehensive approach for correction of motion and distortion in diffusion-weighted mri. Magnetic Resonance in Medicine **51** (2004) 103–114
7. Weisskoff, R., Davis, T.: Correcting gross distortion on echo planar image. In: Proc. of the 11th SMRM meeting. (1992)
8. Studholme, C., Constable, R., Duncan, J.: Accurate alignment of functional epi data to anatomical mri using a physics based distortion model. In: IEEE Trans. Med. Imaging. (2000) 1115–1127
9. Cook, P., Zhang, H., Avants, B., Yushkevich, P., Alexander, D., Gee, J., Ciccarelli, O., Thompson, A.: An automated approach to connectivity-based partitioning of brain structures. In: MICCAI. (2005) 164–171
10. Gee, J., Zhang, H., Dubb, A., Avants, B., Yushkevich, P., Duda, J.: Anatomy-based visualizations of diffusion tensor images of brain white matter. In: Visualization and Processing of Tensor Fields. (2006) 155–163
11. Baird, A., Colvin, M., VanHorn, J., Inati, S., Gazzaniga, M.: Functional connectivity: Integrating behavioral, diffusion tensor imaging, and functional magnetic resonance imaging data sets. J. of Cognitive Neuroscience 687–693
12. Upadhyay, J., Ducros, M., Knaus, T., Lindgren, K., Silver, A., Tager-Flusberg, H., Kim, D.: Function and connectivity in human primary auditory cortex: a combined fmri and dti study at 3 tesla. Cereb Cortex (2007)

13. Olesen, P., Nagy, Z., Westerberg, H., Klingberg, T.: Combined analysis of DTI and fMRI data reveals a joint maturation of white and grey matter in a fronto-parietal network. Brain Res Cogn Brain Res **18** (2003) 48–57
14. Gilmore, J., Lin, W., Corouge, I., Vetsa, Y., Smith, J., Kang, C., Gu, H., Hamer, P., Lieberman, J., Gerig, G.: Early postnatal development of corpus callosum and corticospinal white matter assessed with quantitative tractography. AJNR (2007)
15. Studholme, C.: Incorporating dti data as a constraint in deformation tensor morphometry between t1 mr images. In: IPMI. (2007) 223–232
16. Leemput, K.V., Maes, F., Vandermeulen, D., Suetens, P.: Automated model-based tissue classification of MR images of the brain. IEEE Trans. on Medical Imaging **18**(10) (1999) 897–908
17. Christensen, G.E., Joshi, S.C., Miller, M.I.: Volumetric transformation of brain anatomy. IEEE Trans. Med. Imaging **16**(6) (1997) 864–877
18. Joshi, S., Davis, B., Jomier, M., Gerig, G.: Unbiased diffeomorphic atlas construction for computational anatomy. NeuroImage **23** (2004) S151–S160
19. O'Donnell, L., Haker, S., Westin, C.F.: New approaches to estimation of white matter connectivity in diffusion tensor MRI: elliptic PDEs and geodesics in a tensor-warped space. In: MICCAI. (2002) 459–466
20. Fletcher, P., Tao, R., Jeong, W., Whitaker, R.: A volumetric approach to quantifying region-to-region white matter connectivity in diffusion tensor mri. In: IPMI. (2007) 346–358

GTRACT: An Open Source Diffusion Tensor and Fiber Tracking Toolkit

Vincent A. Magnotta[1,2,3], Greg Harris[1], Madhura Ingalhalikar[1,3], and Xiaodong Tao[4]

[1] Department of Radiology, University of Iowa, Iowa City, IA, USA,
vincent-magnotta@uiowa.edu, madhura-ingalhalikar@uiowa.edu,
[2] Department of Psychiatry, University of Iowa, Iowa City, IA, USA,
gregory-harris@uiowa.edu,
[3] Department of Biomedical Engineering, University of Iowa, Iowa City, IA, USA
[4] GE Research, Niskayuna, New York, USA, taox@research.ge.com ⋆

Abstract. GTRACT is an open source toolkit for the analysis of magnetic resonance diffusion weighted images. The toolkit provides algorithms for the analysis of diffusion weighted images using a Tensor framework. This includes tools for motion and eddy current correction, noise filtering, Tensor estimation, anisotropy mapping, and rigid and non-rigid registration with anatomical image data. Fiber tracking algorithms have also been included allowing users to extract specific fiber tracts from the within the Tensor field. The tools have been designed to support a pipeline processing of the data. A graphical user interface to the tools is provided using the Slicer3 execution model. The tools support the NRRD image format and output tracts in VTK format which is supported by the NA-MIC toolkit and can be visualized in Slicer3.

1 Introduction

Knowledge of brain connectivity plays a role in better understanding the normal brain, abnormal development, and neurodegeneration. Diffusion tensor (DT) imaging has been utilized to study a large number of neurological and psychiatric disorders including: cerebral ischemia, diffuse axonal injury, multiple sclerosis, epilepsy, alzheimers disease, brain tumors, schizophrenia, and metabolic disorders. The use of diffusion tensor imaging for these applications has developed into a quantitative measure of brain connectivity similar to quantification of the brain tissue compartments (grey matter, white matter, and CSF) using tissue classification. Analysis of DT data has included region-of-interest (ROI) based analysis of anisotropy maps, voxel based morphometry, and tractography.

One of the main interests in DT imaging is its ability to potentially describe fiber tracts between two locations in the brain. Diffusion tensor measurements are defined for each voxel and post processing algorithms are required to extend these to form fiber tracts. The main assumption in DT tractography is that the

---

⋆ Funding for this work was provided by grants NIH NS050568.

direction of the fibers is collinear with the direction of the largest eigenvector. These methods are based on connectivity between regions being estimated from the long-range continuity in the diffusion tensor field. This technique has the potential to be invaluable for visualization and quantification of connectivity between brain regions. Much of the initial work in fiber tracking began using streamline approaches. This approach was formalized by Basser et al. [1]. The problem is similar to flow propagation in fluid dynamics.

This paper describes and open source toolkit, GTRACT, that provides a complete diffusion tensor analysis pipeline. The tools included in this software suite are described in the next section.

2 Methods

2.1 Preprocessing

The first task in diffusion tensor imaging is the conversion of image data from DICOM format into a standard image format. GTRACT has chosen to conform with the developing standard of using the NRRD (Nearly Raw Raster Data) format that has explicit support for handling of the diffusion tensor gradient information. A conversion program has been developed that supports the direct conversion of DICOM formatted images into the NRDD format. Support for both GE and Siemens image data has been tested including both mosaic and single slice DICOM files from Siemens. The program reads the applied gradients direction, b-value, and direction cosines from the appropriate DICOM fields.

The next step in the analysis pipeline is the removal of motion and eddy current artifacts from the data. Diffusion weighted images, similar to fMRI data, are collected over several minutes using a single shot EPI based sequence. The resulting motion does not blur the images, but is instead modeled as rigid body motion between the three dimensional volumes acquired. However, unlike fMRI analysis, the signal intensity varies significantly between the acquired images. The b=0 image is collected with no or limited diffusion weighting. Its signal intensity is similar to a T2 weighted scan. The images with large diffusion weighting have substantially reduced signal intensity and the signal between applied directions is modulated based on the orientation of the underlying white matter. Therefore, a mutual information metric is used to align the images. In addition to subject motion, the scans are also susceptible to eddy current artifacts that result from the application of the large diffusion encoding gradients. Since the gradient orientations are changing throughout the experiment, the distortion in the resulting images is dependent on the gradient direction. The distortion in the images can be accounted for using an affine model for the image registration process. GTRACT includes options for both rigid body and affine based transformation models allowing the user to specify if they would like to model the eddy current artifacts.

The fixed image for the image registration is typically the b=0 image and each of the diffusion weighted images are fit to this baseline image. Since, the rotation of images changes the orientation of the diffusion gradient relative to image orientation, the estimated rotation component from the transforms are used to adjust the orientation of the diffusion gradient relative to the image volume.

2.2 Tensor Analysis

Once images are co-registered, the diffusion weighted images are then ready to be used for tensor estimation. The signal-to-noise ratio (SNR) is low in diffusion tensor imaging especially in the images with applied diffusion gradients. Noise filtering is one potential way to increase the SNR. For diffusion tensor imaging, it is also relatively important to maintain the spatial resolution and minimize blurring in the images especially if fiber tracking is desired downstream. Therefore, the GTRACT software provides the user with the ability to perform low pass edge preserving filtering in the form of a median filter. The radius of the median filter can be specified in all three directions providing the ability to filter only in the plane of the acquired images for images with highly anisotropic voxels or in all three dimensions if the images acquired with isotropic spacing. After filtering, a tensor representation of the data based on the signal intensity decay, b-values applied, and the diffusion directions is estimated.

From the diffusion tensor various anisotropy indices can be computed. The scalar metrics support by GTRACT include: Fractional Anisotropy (FA), Relative Anisotropy (RA), Volume Ratio (VR), Lattice Index (LI), Coherence Index (CI), Mean Diffusivity (ADC), Axial Diffusivity (AD), Radial Diffusivity (RD). These scalars provide different information about the underlying white matter and are all rotationally invariant metrics of the diffusion process.

2.3 Anatomical Alignment

One final step in the analysis of diffusion tensor scalar maps is the co-registration of this data with a high resolution anatomical image. Often the high resolution anatomical image is a 3D T1 weighted volume. Two registration methods are supported for alignment with the anatomical image, rigid and B-spline. The rigid registration performs a nine parameter fit with the anatomical images. This registration can be used as the only registration method in the case that other tools have been used to correct susceptibility artifacts such as field mapping based approaches. The rigid registration can also be used to initialize the B-Spline transform.

The B-Spline transform is a deformable transform, where the user can control the amount of deformation based on the number of control points as well as the maximum distance that these points can move. This allows the susceptibility related distortions to be minimized in the diffusion weighted images without the acquisition of the a field mapping dataset. It is recommended that for image registration with the B-Spline transform that the anatomical image be skull stripped (i.e. image containing only brain with skull removed). This requirement exists because of the fat saturation that is applied to the EPI images eliminates

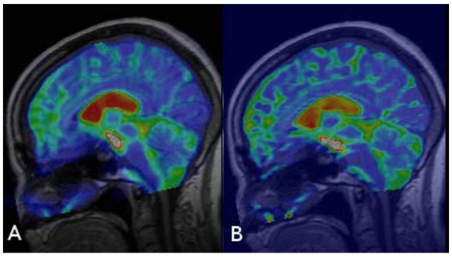

Fig. 1. Alignment of the b=0 image with the anatomical T1 weighted image. The anatomical images is the background image and the diffusion tensor b=0 image is overlaid in color. (A) Shows the result after rigid registration, and (B) Shows the result after B-spline registration. The improvements in the B-Spline registyration can be seen back to the ventricular region. This is particularly evident in the boundary of the genu of the corpus callosum and the ventricles.

most of the signal from the skull in the diffusion tensor images. An example of the quality improvement in registration of the diffusion tensor images with the anatomical image using a B-Spline registration is shown in Fig 1.

The registration with the anatomical dataset allows the user to map regions of interest from the anatomical images into the space of the acquired diffusion tensor imaging data where they can be used to seed fiber tracking algorithms as described below. The registration also allows the user to map the scalar images into the space of the anatomical images where they can be analyzed using ROI or voxel based approaches.

2.4 Fiber Tracking

One of the great appeals of diffusion tensor imaging is the ability to generate estimates of fiber tracts *in vivo*. While the GTRACT suite was originally developed around the GTRACT (Guided Tensor Restore Anatomical Connectivity Tractography) algorithm [2], several modes of fiber tracking are now supported. Free tracking is a basic streamlines algorithm as proposed by Basser et al. [1] This algorithm starts fiber tracking from a single region of interest and continues tracking until it hits a termination criteria. Termination criteria include high curvature, low anisotropy, and fiber length. The streamlines algorithm is similar to the free tracking method except that only fibers terminating in an ending region defined by the user are retained. This allows the user to readily extract only the fiber tracts of interest while ignoring all other tracts. The streamlines algorithm includes the option for utilizing the Tensor deflection (TEND) algorithm proposed by Lazar et al. [3]. The TEND algorithm is specified by the following equation

$$v_{out} = f_{e1} + (1 - f) * ((1 - g)v_{in} + gD \cdot v_{in}) \tag{1}$$

where v_{out} is the outgoing vector direction, v_{in} is the incoming vector direction defined in the previous step, e_{in} is the primary eigenvector direction, where D is the diffusion tensor. The parameters f and g define the relative weight of the three directional terms. In the case that the $f = 0$ and $g = 0$, this equation simplifies to the standard streamline equation

$$v_{out} = f_{e1} + v_{in} \qquad (2)$$

Graph search tracking is the first step in the full GTRACT algorithm developed by Cheng et al. [2]. This method was developed to generate fibers in a tensor representation where crossing fibers occur. The graph search algorithm follows the primary eigenvector in non-ambiguous regions and utilizes branching and a graph search algorithm in ambiguous regions. Ambiguous tracking regions are defined based on two criteria: branching anisotropy threshold, and branching curvature. When the anisotropy values are below the branching anisotropy value or the curvature is above the branching angle, several tracking paths are considered. The first is the standard primary eigenvector direction. The second is the secondary eigenvector direction. This is based on the assumption that these regions may be oblate regions. If the user enables the random walk option, then a third direction is also considered. This direction is defined by a cone pointing from the current position to the centroid of the ending region. The interior angle of the cone is specified by the user with the branch angle parameter. A vector contained inside of the cone is selected at random and used as the third direction. This method can also utilize the TEND option where the current tracking direction replaces the the primary eigenvector in the TEND algorithm.

The second phase of the GTRACT algorithm is guided tracking. This method incorporates anatomical information about the track orientation using an initial guess of the fiber track. In the original proposed GTRACT method, this would be created from the fibers resulting from the graph search tracking. However, in practice this can be created using any method or could be defined manually. The graph search tracking may generate fairly rough tracks especially in regions of low FA, therefore a center line fiber is estimated for the resulting tracts. This tends to be a smooth estimate of the mean fiber position. In guided tracking, the primary eigenvector direction is compared to the direction specified by the guide fiber. If the angle deviates more than a user specified value (typically 20-30 degrees) then the direction specified by the guide fiber is utilized instead of the primary eigenvector direction.

A second class of algorithms utilized for fiber tracking is based on energy minimization. One such method is the fast marching fiber tracking algorithm. This algorithm is based on the work by Parker et al. [4] In the fast marching algorithm in the GTRACT suite of tools, anisotropy has been added to the cost function calculation. The user has the ability to weight the contribution of anisotropy to the cost function. This algorithm is broken into two parts. The first phase of the algorithm generates a cost image. This starts with a seed region specified by the user. The cost of the path tracking from the seed region to every voxel in the brain is computed. The cost is based on the direction of

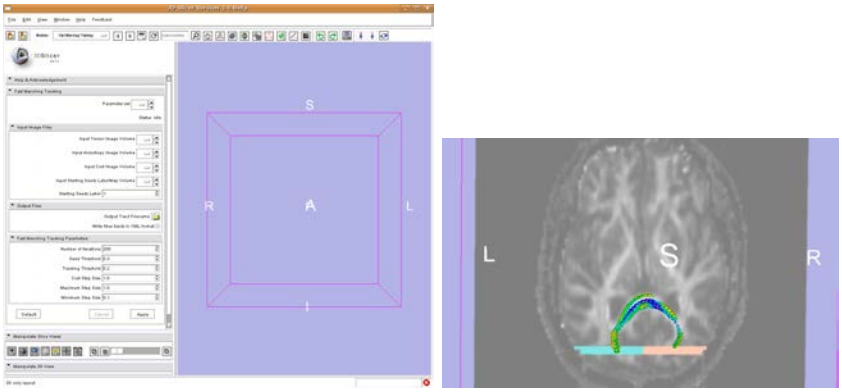

Fig. 2. The GTRACT fast marching graphical user interface is shown in Slicer3 on the left. On the right, tracts of the forceps major produced using the GTRACT tracking algorithm and visualized in Slicer3 are shown.

the front, the primary eigenvector direction, and the anisotropy value. Once the cost image is generated, the user can then generate tracts between any region of the brain and the seed region specified in the previous step. Fiber tracks are generated using a gradient descent solution from the defined regions back to the seed points specified in the creation of the cost image.

2.5 Slicer3 Integration

The GTRACT software is built upon the National Alliance for Medical Image Computing (NA-MIC) libraries including ITK, VTK, and Slicer3 [5]. The tool is available from the Neuroimaging Informatics Tools and Resources Clearinghouse (NITRC), http://www.nitrc.org.

The programs contained within the GTRACT have been built using the Slicer3 execution model. This provides a convenient way to define command line parameters for the program using an XML file description. The XML file also serves as a way to create a graphical user interface within Slicer3 (Fig 2). The resulting fiber tracts are saved in VTK format and contain the diffusion at each point along the fiber tract. The resulting fiber tracts and tensor representation can be readily visualized within the Slicer3 environment (Fig 2).

2.6 Fiber Tracking in Schizophrenia

Twelve male patients with a DSM-IV diagnosis of schizophrenia with (mean age 32±9.5 years) and ten normal controls (five males and five females, age 43.5±9.0 years) were recruited into this study. After informed consent was obtained from the Institutional Review Boards at the University of Iowa and University of New Mexico. Subjects were imaged twice on a 1.5T Siemens scanner within a twenty four hour period. A multi-modal imaging protocol was used to collect T1, T2 and diffusion weighted images. Diffusion tensor images were obtained with the following protocol: TE=80ms, TR=9500ms, flip angle=90°, FOV=256x256mm, Matrix=128x128, slice thickness=2.0mm, slice gap = 0.2mm, number of slices=65, NEX=4, b-value=1000s/mm^2, bandwidth=1346Hz/pixel, number of diffusion directions=6.

The structural MR scans were analyzed using the BRAINS software [6]. A standard image analysis pipeline was utilized that included the following steps: 1) spatial alignment of the T1 weighted scan along the AC-PC line and the interhemispheric fissure; 2) co-registration of the T2 images to the spatially aligned T1; 3) tissue classification; 4) brain extraction; and 5) neural network regional brain labeling. The neural network defined regions of interest for the thalamus and the cerebellar white matter (corpus medullary) were verified by an expert anatomical rater and manually edited if required.

The diffusion tensor images were processed using a standard image analysis pipeline using the GTRACT tools. The diffusion weighted images were co-registered to the b=0 image using a mutual information affine registration to eliminate the effects of motion. Next, a 3x3x3 voxel neighborhood median filter was applied to the diffusion weighted images, and then the tensor field was calculated using a background suppression threshold of 100 on the b=0 image. A fractional anisotropy (FA) image was then calculated. The b=0 image from the DTI series was co-registered to the AC-PC aligned T1 image using the same mutual information registration algorithm used for motion correction of the diffusion tensor images. This registration was then inverted to map regions of interest into the acquisition space of the diffusion weighted images. For the tract tracing, we focused on one major pathway, which represents the connection between the cerebellum and the thalamus. The artificial neural network defined regions of interest were used as starting and ending regions for fiber tracking with the GTRACT software.

The reliability of the fiber tracts were compared between the two time points by correlating the FA along the fiber tracts. The resulting fiber tracts were compared between patients with schizophrenia and normal controls.

3 Results

While the reliability of the GTRACT was previously addressed [2], correlations for this sample were determined between the scanning sessions. Correlation coefficients of the FA values along the fiber tracts in the control subjects were 0.94 and 0.95 for the left cerebellum to right thalamus and right cerebellum to left thalamus respectively. The patients with schizophrenia had slightly lower correlation coefficients of 0.87 and 0.88.

For the fiber tracts connecting the left cerebellum to the right thalamus, the patients with schizophrenia had a significant reduction ($p<0.05$) in FA values along the fiber tracts. Most of this region was between the cerebellar peduncles projecting towards the red nucleus. This difference in FA values between the patients and controls was similar in both the test and retest measurements. For the tracts between the right cerebellum and the left thalamus a significant reduction ($p<0.05$) in the FA values for the patients was found in the same region.

4 Discussion

The GTRACT software suite is an open source toolkit for the analysis of diffusion tensor data that includes tools for image format standardization, motion and eddy current correction, alignment with anatomical images, tensor decomposition, rotationally invariant scalar mapping, and fiber tracking. The reliability of the estimated fiber tracts generated from this tool has been previously established using digital phantoms and scan/rescan evaluation of fiber tracts running between the cerebellum and thalamus. The reliability of the fiber tracts should be accessed on a tract by tract basis. In addition, comparison between the various fiber tracking algorithms is warranted.

These tools have been use to evaluate changes in the tracts running between the cerebellum and thalamus. The tracts in the region of the cerebellar peduncles projecting towards the red nucleus. Similar findings were found in the tracts running from the left cerebellum to right thalamus and between the left cerebellum and right thalamus. This suggests that deficits in the connectivity between the cerebellum and thalamus is not a reduced over the entire tract, but may reflect discrete regions where deficits exist between these regions. Further exploration to needed to fully understand how these changes are related to cognitive changes and symptoms seen in schizophrenia.

References

1. Basser, P., Pajevic, S., Pierpaoli, C., Duda, J., Aldroubi, A.: In vivo fiber tractography using dt-mri data. Magn Reson Med **44**(4) (2000) 625–32
2. Cheng, P., Magnotta, V., Wu, D., Nopoulos, P., Moser, D., Paulsen, J., Jorge, R., Andreasen, N.: Evaluation of the gtract diffusion tensor tractography algorithm: a validation and reliability study. Neuroimage **31**(3) (2006) 1075–1085
3. Lazar, M., Weinstein, D., Tsuruda, J., Hasan, K., Arfanakis, K., Meyerand, M., Badie, B., Rowley, H., Haughton, V., Field, A., Alexander, A.: White matter tractography using diffusion tensor deflection. Hum Brain Mapp **18**(4) (2003) 306–21
4. Parker, G., Wheeler-Kingshott, C., Barker, C.: Estimating distributed anatomical connectivity using fast marching methods and diffusion tensor imaging. IEEE Trans Med Imaging **21**(5) (2002) 505–12
5. Pieper, S., Lorensen, B., Schroeder, W., Kikinis, R.: The na-mic kit: Itk, vtk, pipelines, grids and 3d slicer as an open platform for the medical image computing community. Proceedings of IEEE International Symposium on BioMedical Imaging: From Nano to Macro (2006) 698–701
6. Magnotta, V., Harris, G., Andreasen, N., O'Leary, D., Yuh, W., Heckel, D.: Structural mr image processing using the brains2 toolbox. Comput. Med. Imaging Graph. **26**(4) (2002) 251–264

How Many Gradients are Sufficient in High-Angular Resolution Diffusion Imaging (HARDI)?

Liang Zhan[1], Ming-Chang Chiang[1], Alex D. Leow[1], Siwei Zhu[2],
Marina Barysheva[1], Arthur W. Toga[1], Katie L. McMahon[3], Greig I. de Zubicaray[3],
Matthew Meredith[3], Margaret J. Wright[4], Paul M. Thompson[1]

[1] Laboratory of Neuro Imaging, Department of Neurology,
UCLA School of Medicine, Los Angeles, CA, USA
[2] Dept. of Mathematics, UCLA, Los Angeles, CA, USA
[3] Functional MRI Laboratory, Centre for Magnetic Resonance,
University of Queensland, Brisbane, Australia
[4] Queensland Institute of Medical Research, Brisbane, Australia

Abstract. We scanned 61 healthy adults with 105-gradient HARDI at 4 Tesla, and examined how the number of diffusion gradients affects the signal-to-noise ratio (SNR) for several common DTI-derived scalar measures: the fractional and relative anisotropy (FA, RA) mean diffusivity (MD), and volume ratio (VR). HARDI applies diffusion-sensitive magnetic field gradients to the brain at a range of spherical angles (typically >100) to analyze white matter microstructure and integrity. We optimized the angular distribution energy on gradient image subsets of size $1 \leq N \leq 94$, to artificially reduce the angular sampling. 7 gradients are mathematically sufficient to determine FA/RA/MD/VR, but by increasing the number of diffusion-sensitized gradients from 20 to 94, SNR improved by 69.23% and 19.93% for VR and RA, and by 12.24% and 8.77% for FA and MD. Measures involving products of 3 eigenvalues (e.g., VR) were noisier, requiring more gradients to determine. FA SNR rose rapidly with more gradients than are routinely collected, suggesting advantages of HARDI even for standard neuroscientific studies.

Keywords: High-Angular Resonance Diffusion Imaging, fractional anisotropy, relative anisotropy, mean diffusivity, volume ratio, Signal-to-Noise ratio**.**

1 Introduction

High-angular resolution diffusion imaging (HARDI) is a powerful extension of MRI, based on applying diffusion-sensitized gradients to the brain in 100 or more different directions. This can quantify anisotropic water diffusion in brain tissue, providing exquisite insight into local fiber orientation and integrity. Many early diffusion imaging studies used the *diffusion tensor* model [1], which describes the anisotropy of water diffusion in tissues by estimating, from a set of *K* diffusion-sensitized images, the 3x3 covariance matrix of a Gaussian distribution. Each voxel's signal intensity in the *k*-th image is decreased, by water diffusion, according to the Stejskal-Tanner equation [2]: $S_k = S_0 \, exp \, [-b \mathrm{g}_k^T \mathrm{D} \, \mathrm{g}_k]$, where S_0 is the non-diffusion weighted signal intensity, D is the 3x3 diffusion tensor, g_k is the direction of the diffusion gradient and *b* is Le Bihan's factor containing information on the pulse sequence, gradient strength, and physical constants. Although only 7 gradients are mathematically sufficient to determine the diffusion tensor, MRI protocols with higher angular and radial resolution (e.g., HARDI) have been proposed to resolve more complex diffusion geometries that a single tensor fails to model, e.g. fiber crossings and intermixing of tracts.

Recent technical advances have made HARDI more practical. A 14 minute scan can typically sample over 100 angles (with 2 mm voxels at 4 Tesla). HARDI's improved signal-to-noise ratio can be used to reconstruct fiber pathways in the brain with extraordinary angular detail, identifying anatomical features, connections and disease biomarkers not seen with conventional MRI. If more angular detail is available, fiber orientation distribution functions (ODFs) can be reconstructed from the raw HARDI signal using deconvolution methods [3,4], yielding mathematically rich models of fiber geometries using probabilistic mixtures of tensors [5, 6], fields of von Mises-Fisher mixtures [7], or higher-order tensors (i.e., 3x3x…x3 tensors) [8,9]**.** Recent work on stochastic tractography [10, 11] has also exploited the increased angular detail in HARDI, and fluid registration methods have also aligned HARDI ODFs using specialized Riemannian metrics [12].

Ironically, most clinical studies with diffusion imaging still rely on simple scalar measures, such as fractional anisotropy (FA) or mean diffusivity (MD), which can be computed from the diffusion tensor approximation. FA poorly reflects the multidimensional complexity of the ODF, but it is sensitive to white matter deterioration in aging and neurodegenerative diseases, so many clinical studies have concluded that it is unnecessary to collect many more than the 7 gradient images that suffice to determine the diffusion tensor uniquely. Given the trade-off between the available signal-to-noise (SNR) and the time required to collect more gradient images, some studies argue that 20 gradient directions are sufficient to accurately compute FA [13,14], and such acquisition protocols are now typical. Here we aimed to determine whether this is optimal, by examining the signal-to-noise gains, for different standard diffusion-tensor derived indices (FA/MD/RA/VR), with the increased gradient numbers in HARDI. Although simulations suggest that SNR will increase with increasing gradient numbers in DTI [15-17], simulations may not represent the achievable SNR, as many sources of noise (e.g., subject motion, physiological sources of noise, susceptibility of real brain tissue) can only be modeled by empirically studying a population. As such, we scanned 61 subjects with 105-gradient HARDI, providing practical information on real human data that has not previously been available.

2 Materials and Methods

2.1 Subjects and image acquisition

105-gradient HARDI data were acquired from 61 healthy adult subjects (age: 24.5±1.4SD years; 29 men/32 women) on a 4 Tesla Bruker Medspec MRI scanner using an optimized diffusion tensor sequence [16, 18]. 105 images were acquired: 11 baseline (b_0) images with no diffusion sensitization (i.e., T2-weighted images) and 94 diffusion-weighted images (b-value 1159 s/mm^2) in which gradient directions were evenly distributed on the hemisphere [2]. Imaging parameters were: TE/TR 92.3/8250 ms, 55 x 2mm contiguous slices, FOV = 23 cm. The reconstruction matrix was 128 x 128, yielding a 1.8x1.8 mm^2 in-plane resolution. The total scan time was 14.5 minutes.

2.2 Data processing

HARDI data for all 61 subjects were loaded into MedINRIA, a DTI analysis program developed by the INRIA research project *Asclepios* [19]. MedINRIA provides state-of-the-art algorithms for tensor reconstruction and denoising, with a simple user interface and triaxial/3D viewer (http://www-sop.inria.fr/asclepios/software/MedINRIA; **Figure 1**). To eliminate extracerebral tissues, a subject-specific binary mask of the brain was created based on a Partial Volume Classification (PVC) of the corresponding registered 3D T1-weighted structural images [20] and aligned by 9-parameter transformation to the corresponding diffusion tensor images.

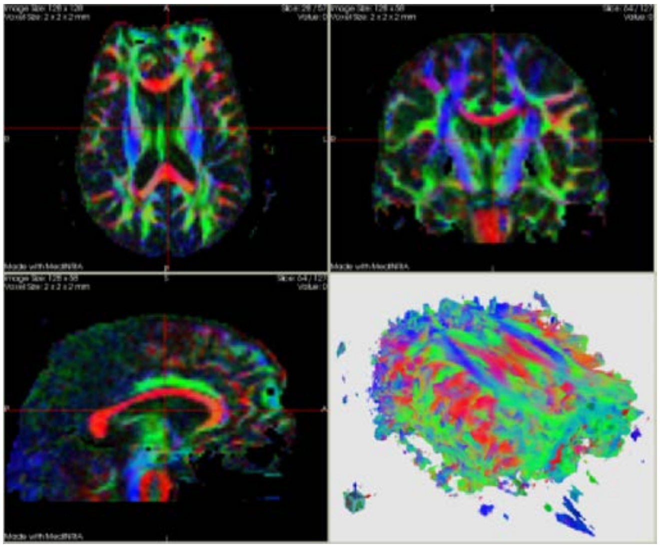

Figure 1. Tensor Reconstruction and Eigenstructure Visualization from HARDI. The 105 gradient images per subject were reconstructed using a tensor approximation at each voxel. The diffusion tensor eigenvalues were retained to compute the scalar diffusion parameters FA/MD/RA/VR. Here the RGB color code indicates the normalized principal eigenvector

direction (x,y,z) of the local diffusion tensor, showing that the HARDI sequence resolves fiber geometry and orientation in detail (red colors show the *corpus callosum*; *bottom left*).

In the Diffusion Tensor (DT) model, a tensor is fitted at each voxel to the set of diffusion images, and maps of indices sensitive to fiber integrity such as fractional or relative anisotropy (FA, RA), mean diffusivity (MD) or volume ratio (VR), may be computed from the tensors' eigenvalues (λ_1, λ_2, λ_3). [18] pointed out that the performance of FA and MD estimation depends on the tensor estimation method. In MedINRIA, a Log-Euclidean (LE) metric is used for tensor estimation, in which matrices with null or negative eigenvalues are at an infinite distance from any positive definite matrix. For each subject, DT images (denoted by $D_{ij,}$ $1 \leq i, j \leq 3$) and FA, RA MD, and VR maps were computed from the HARDI signals standard formulae (**Equation 1**).

$$\begin{aligned}
FA &= \sqrt{\frac{3}{2}\left(\frac{(\lambda_1-\hat{\lambda})^2+(\lambda_2-\hat{\lambda})^2+(\lambda_3-\hat{\lambda})^2}{\lambda_1^2+\lambda_2^2+\lambda_3^2}\right)}\\
MD &= \frac{\lambda_1+\lambda_2+\lambda_3}{3}\\
RA &= \sqrt{\frac{(\lambda_1-\lambda_2)^2+(\lambda_1-\lambda_3)^2+(\lambda_2-\lambda_3)^2}{2(\lambda_1+\lambda_2+\lambda_3)^2}}\\
VR &= \frac{\lambda_1\lambda_2\lambda_3}{\bar{\lambda}^3}\\
\bar{\lambda} &= \frac{\lambda_1+\lambda_2+\lambda_3}{3}
\end{aligned} \qquad \textbf{(1)}$$

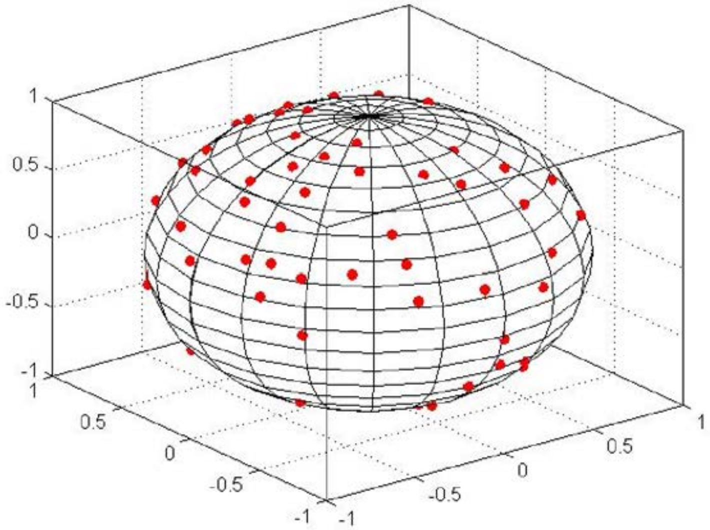

Figure. 2. Spherical distribution of angles at which diffusion-sensitized gradient images were collected, for the 105-gradient HARDI sequence. Each red dot represents one gradient image.

We artificially reduced the angular sampling of the 105-gradient sequence by optimizing the angular distribution energy [2] on subsets of size 1≤*N*≤94 of the diffusion-sensitized gradient images. Since each gradient image is applied in a direction that may be represented as one point (a_i, 1≤i≤105) on the surface of the unit sphere (**Figure 2**), the optimality of a gradient vector set is typically defined using PDEs based on electrostatic repulsion, or based on summed spherical distance metrics that attempt to maximize the distance between points on the sphere. Although other approaches are possible (see [22]), in our formulation, we optimized the angular distribution energy by maximizing the summation of the least distances between all points in the Riemannian manifold (**Equation 2**). In Equation 2, a_i and a_j represent two different points on the unit spherical surface.

$$\mathrm{E} = argmax\left(\sum_{i=1}^{105}\sum_{j=1}^{105} argmin\left(distance_R\left(a_i, a_j\right)\right)\right) \quad (i \neq j) \qquad (2)$$

For each subject and angular resolution (1≤*N*≤94), we computed SNR for the FA, MD, RA and VR maps by using all optimized gradient subsets and all 11 baseline (b_0) images, to measure SNR effects with a constant number of b_0 images (this conservative approach slightly favors sequences with fewer gradients, for which fewer than 11 baseline images would typically be collected). Each map's SNR was defined as the ratio of the mean voxel value to the standard deviation of the voxel values. Although this definition does subtract the biological variation in DTI-derived signal across the brain, that component of variation may be assumed constant for all gradient subsets (1≤*N*≤94), and is therefore not a confound when comparing SNR across gradient numbers. We preferred this approach over selecting a relatively homogeneous region or subset of voxels for our computations; we acknowledge that alternative SNR definitions may be reasonable when specific anatomical tissue classes are the target of study.

3 Results and Discussion

A traditional DTI sequence with a total of 30 gradients might be computed from 27 diffusion-sensitized gradient imaging and 3 baseline images. As we had collected 11 baseline images, to avoid confounding effects we kept the number of b_0 images constant while varying the number of diffusion-sensitized images. Figure 3 shows some representative maps of FA, MD, RA and VR based on HARDI17, HARDI38 and HARDI105 (where the numbers refer to the total number of gradient images).

We found that SNR rose sharply for FA, MD, RA and VR and reached 90% of the available SNR with 22, 19, 31 and 64 of the available 94 diffusion-sensitized gradients. By increasing the number of diffusion-sensitized gradients from 20 to 94, SNR improved by 69.23% and 19.93% for VR and RA, and by 12.24% and 8.77% for FA and MD (**Figure 4**). Measures involving products of 3 eigenvalues (e.g., VR) were noisier, requiring more gradients to determine, but even FA SNR rose rapidly with more gradients than are routinely collected.

HARDI offers increased SNR even for routine brain mapping studies using tensor-derived measures, such as FA, which requires only 7 gradients to determine analytically. Our findings are consistent with studies by Hasan et al. [23], who used bootstrap methods, Monte Carlo simulations and phantom data to show that SNR(RA)/SNR(FA) rises with moderate increases in angular sampling, from 6 to 21. FA and RA are also analytically derivable from each other using closed form formulae, so that the standard deviation of FA, $\sigma(FA)=(1/3)(FA/RA)^3\sigma(FA)$, giving $SNR(FA)/SNR(RA)=3/(3-2FA^2)=1+2RA^2$, if $SNR(FA)=FA/\sigma(FA)$. This means that the maximum SNR advantage SNR(FA)/SNR(RA) is 3 at the highest theoretical anisotropy value (FA=RA=1). Paradoxically, researchers have largely followed the advice that 7-20 gradients suffice to determine F. This reduces acquisition times, but longer acquisitions may provide better SNR not just for tractography but also for routine scalar maps of fiber integrity. Whether or not this increased SNR translates into smaller minimal sample sizes to detect clinically relevant effects depends on the biological variation in these measures across subjects, which deserves further study. Landman et al. [21] also noted that the diffusion tensor orientation (principal eigenvector) depends not just on the angular sampling, but also on patient motion, field inhomogeneity, and EPI-related distortions), and at low SNR, FA measures may not just be noisy, but also biased. Further studies of scanner field strength, spatial resolution, tolerability, motion artifacts, and clinical effect sizes will clarify the added benefit of HARDI's SNR for neuroscientific studies.

4 Conclusions

Based on our current results, more than 20 DWIs should be enough to achieve a satisfactory SNR results for FA, ADC and 30 DWIs for RA, but for VR, more DWIs are needed to improve the SNR.

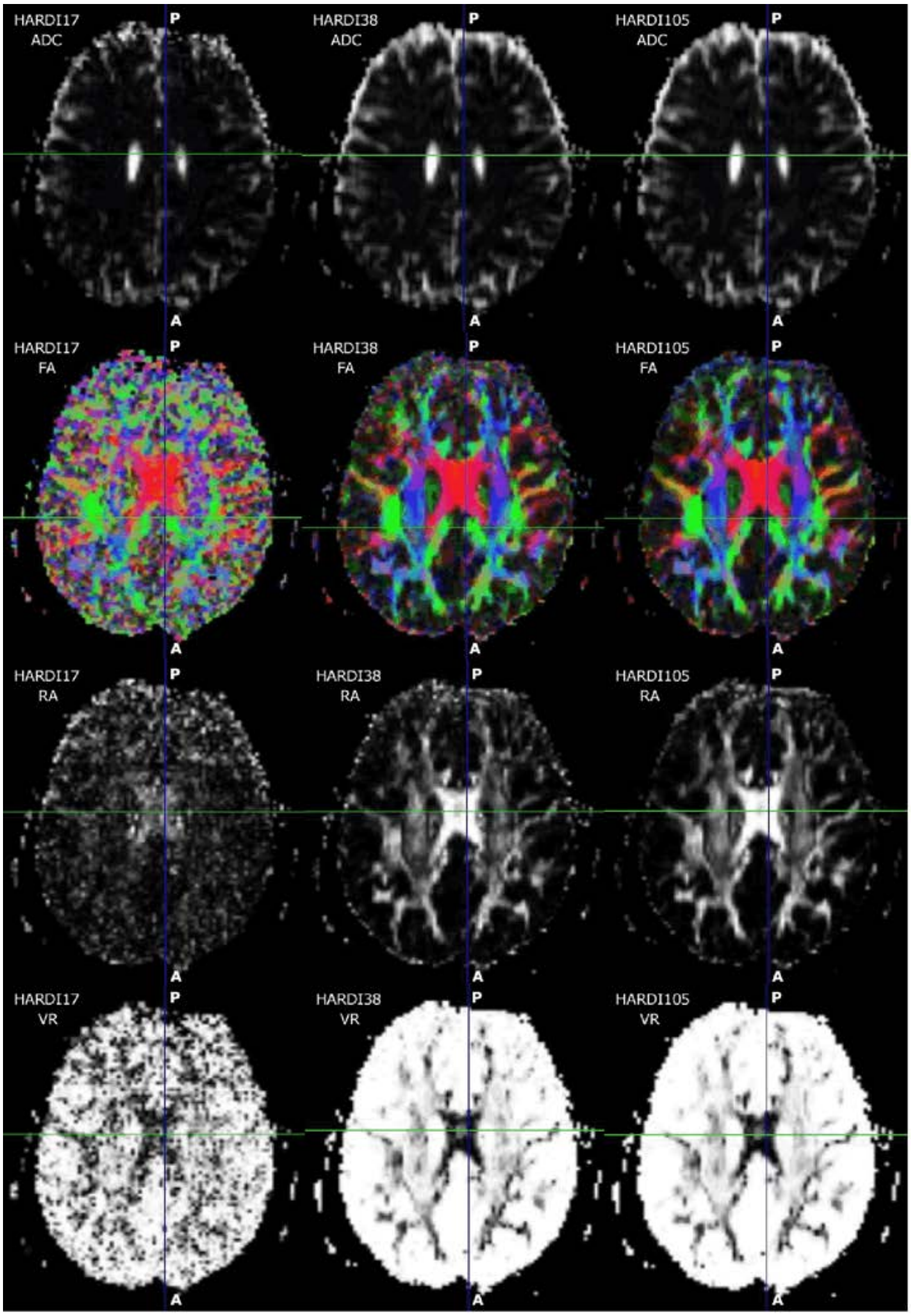

Figure 3. SNR increases for all 4 DTI-derived scalar measures as the number of HARDI gradients is steadily increased. Rows 1-4 show axial slices through the MD map (also known as ADC or average diffusion coefficient), FA map, RA map and VR map. Column 1 is computed from HARDI17 (i.e., the 11 b_0 and 6 non-b_0 images), Column 2 is from HARDI38 (i.e., 27 non-b_0 images), and Column 3 is from HARDI105 (the full protocol of 94 non-b_0 images).

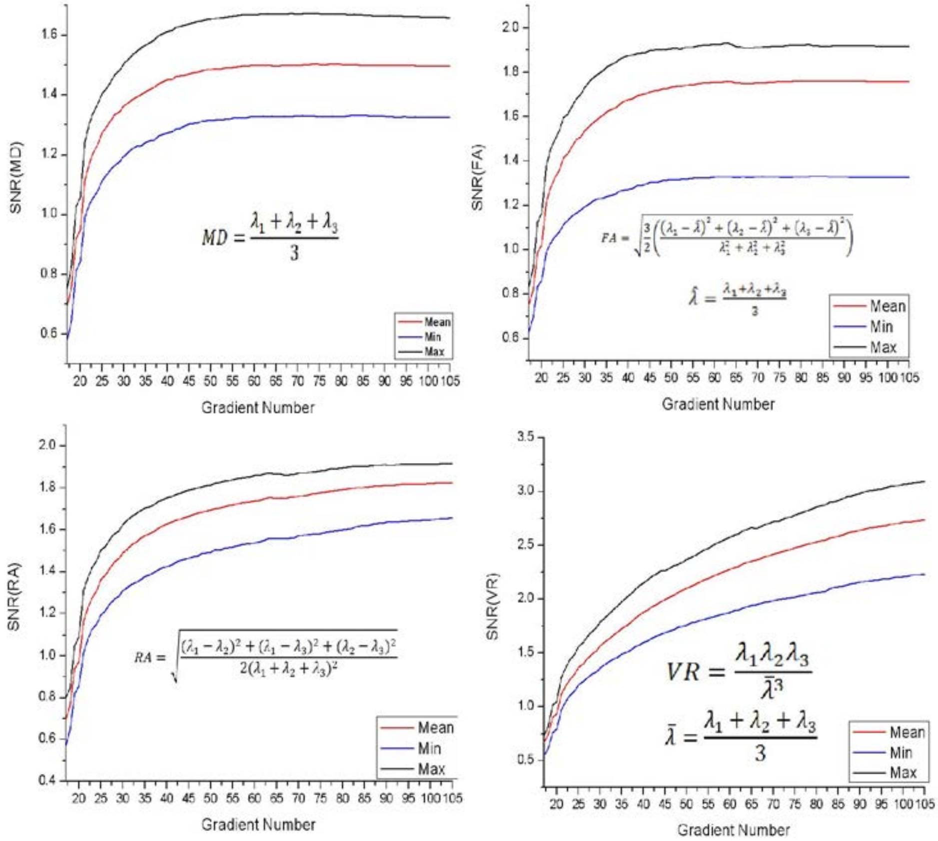

Figure 4. SNR trends with increasing numbers of HARDI gradients. For MD (*top left*), FA (*top right*), RA (*bottom left*), and VR (*bottom right*), the red curves show the average SNR from all 61 subjects, while the top and bottom curves represent the subjects with best and worst SNR. Similar trends appear for the individuals and for the group average SNR. Parameters that involve products of eigenvalues tend to be noisier (e.g., VR), and benefit more from greater angular sampling. The average and individual plots are all monotonically increasing, and FA does not plateau until well beyond the number of gradients typically collected (~20).

References

1. Basser PJ, Pierpaoli C. Microstructural and physiological features of tissues elucidated by quantitative diffusion tensor MRI. J. Magn. Reson., vol. B 111, no. 3, pp.209-219 (1996).
2. Stejskal, EO, Tanner JE. Spin diffusion measurements: spin echoes in the presence of a time-dependent field gradient. J. Chem. Phys. 42:288-292 (1965).
3. Descoteaux M, Angelino E, Fitzgibbons S, Deriche R. A fast and robust ODF estimation algorithm in q-ball imaging. In Third IEEE International Symposium on Biomedical Imaging: from Nano to Macro, pages 81–84, Arlington, Virginia, USA (2006).

4. Tournier JD, Calamante F, Gadian D, Connelly A. Direct estimation of the fiber orientation density function from diffusion-weighted MRI data using spherical deconvolution. NeuroImage, 23:1176–1185, (2004)
5. Jian B, Vemuri BC, Özarslan V, Carney PR, Mareci TH. A novel tensor distribution model for diffusion-weighted MR signal. NeuroImage 37: 164-176. (2007)
6. Leow AD, Zhu S, de Zubicaray GI, Meredith M, Wright M, Thompson PM. The Tensor Distribution Function, ISBI (2008).
7. McGraw T, Vemuri BC, Yezierski B, Mareci T. Von Mises-Fisher mixture model of the diffusion ODF. Biomedical Imaging: Nano to Macro, 3rd IEEE International Symposium on Biomedical Imaging: 65-68. (2006)
8. Ozarslan E, Vemuri BC, Mareci TH. Higher rank tensors in diffusion MRI, Visualization and Image Processing of Tensor Fields, (2005).
9. Barmpoutis A, Vemuri BC. Exponential Tensors: A framework for efficient higher-order DT-MRI computations. In Proceedings of ISBI07: IEEE International Symposium on Biomedical Imaging: Page(s): 792-795. (2007)
10. Perrin M, Poupon C, Rieul B. Validation of q-ball imaging with a diffusion fibre-crossing phantom on a clinical scanner. Phil Trans R Soc Lond B Biol Sci 360:881–891 (2005)
11. Jbabdi S, Woolrich MW, Andersson JLR et al. A Bayesian framework for global tractography. NeuroImage 37:116-129. (2007)
12. Chiang MC, Barysheva M, Lee AD, Madsen SK, Klunder AD, Toga AW, McMahon KL, de Zubicaray GI, Meredith M, Wright MJ, Srivastava A, Balov N, Thompson PM. Mapping Genetic Influences on Brain Fiber Architecture with High Angular Resolution Diffusion Imaging (HARDI), ISBI (2008).
13. Ni H, Kavcic V, Zhu T, Ekholm S, Zhong J. Effects of Number of Diffusion Gradient Directions on Derived Diffusion Tensor Imaging Indices in Human Brain. American Journal of Neuroradiology 27:1776-1781. (2006)
14. Hasan KM., Narayana PA. Retrospective Measurement of the Diffusion Tensor Eigenvalues from Diffusion Anisotropy and Mean Diffusivity in DTI. Magnetic Resonance in Medicine, 56:(1):130-137. (2006)
15. Jones DK. Determining and Visualizing Uncertainty in Estimates of Fiber Orientation from Diffusion Tensor MRI. MRM;49:7-12 (2003)
16. Jones DK, Horsfield MA, Simmons A. Optimal strategies for measuring diffusion in anisotropic systems by magnetic resonance imaging. Magnetic Resonance in Medicine. 42(3): 515-525. (1999)
17. Alexander DC, Barker GJ. Optimal imaging parameters for fiber-orientation estimation in diffusion MRI. Neuroimage 27:357–67 (2005)
18. Pend H, Arfanakis K. Diffusion tensor encoding schemes optimized for white matter fibers with selected orientations. Magnetic Resonance Imaging 25: 147-153. (2007)
19. Pennec X, Fillard P, Ayache N. A Riemannian Framework for Tensor Computing. International Journal of Computer Vision, 66(1):41-66, January 2006. Note: A preliminary version appeared as INRIA Research Report 5255, (2004).
20. Shattuck, D.W. and R.M. Leahy, BrainSuite: an automated cortical surface identification tool. Med Image Anal, 6(2): p. 129-42 (2002)
21. Landman BA, Farrell J.A.D., Smith SA, Mori S, Prince JL. Tradeoffs between tensor orientation and anisotropy in DTI: Impact of Diffusion Weighting Scheme. International Society for Magnetic Resonance in Medicine, 15th Scientific Meeting, Berlin. (2007)
22. Hasan KM, Narayana PA. DTI parameter optimization at 3.0 T: potential application in entire normal human brain mapping and multiple sclerosis research. MedicaMundi 49(1):30-45 (2005).
23. Hasan KM, Alexander AL, Narayana PA. Does fractional anisotropy have better noise immunity characteristics than relative anisotropy in diffusion tensor MRI? An analytical approach. Magn Reson Med;51(2):413–417.(2004)

Multiresolution decomposition of HARDI and ODF profiles using spherical wavelets

Irina Kezele[1,2*], Maxime Descoteaux[1,2], Cyril Poupon[1,2], Pierrick Abrial[3], Fabrice Poupon[1,2], and Jean-François Mangin[1,2]

[1]NeuroSpin, CEA, France, [2]IFR49, France, [3]DAPNIA, CEA, France
`irina.kezele@cea.fr` [⋆]

Abstract. High Angular Resolution Diffusion Imaging (HARDI) is deemed to capture worthy information about the structure in which the diffusion process takes place. HARDI allows us to examine relatively wide angular frequency range of diffusion signal that, due to the complexity of both the diffusion process and its milieu, may spread over multiple frequency bands. Therefore, we opt for multiscale analysis ensuring that all frequencies are adequately probed, but also we favor those frequencies that are trusted more important for our specific aims. Inherent sphericity of the HARDI signal motivated us to take on the concepts of multiscale spherical wavelet decomposition and its derivatives. This permits a sparse and denoised representation of both the HARDI signal and its Funk-Radon transform (the diffusion orientation distribution function (ODF)), presumably associated to the angular distribution of brain fibre bundles via structural link with diffusion. We apply the method to real physical phantoms showing fibre bundles crossing, as well as to a real brain data set. The results reveal the potential of the method to infer interesting structural information captured only by a small number of spherical wavelet coefficients.

1 Introduction

High Angular Resolution Diffusion Imaging [1, 2] has been introduced with the aim of exploring the non-Gaussianity of the diffusion process, and in an attempt to resolve complex fibre constellations, typically indiscernible by diffusion tensor imaging (DTI) [3]. HARDI offers much richer descriptions of diffusion process (at a resolution accessible by conventional MR scanners), however it sets heavy computational burden for data processing. Since the directions of maximal diffusion (that are implied by average principal fibre orientations inside a voxel) are unknown a priori, HARDI explores the space in a uniform manner, and thus despite its obvious gain over DTI, it still suffers from a certain amount of information redundancy. A number of approaches for “simplification” and regularization of Apparent Diffusion Coefficient profiles (ADCp) resulting from

---

[⋆] Authors would like to thank Bertrand Thirion, Philippe Ciuciu, and Jean-Luc Starck for helpful discussions. This work is supported by Marie Curie Actions individual postdoctoral fellowship, EU.

HARDI by projection onto predefined bases were demonstrated [1, 4, 5]. The preliminary work was oriented towards spherical harmonics (SHs) [1, 4], that offered a suitable spherical basis for high ADCp compression as well as some fast algorithms for diffusion orientation function (ODF) reconstruction [6, 7]. However, the SH decomposition is not localized and is therefore not fully adapted to the problem at hand (e.g., ODF sparsity). Nonetheless, SHs have been successfully applied to recently introduced deconvolution methods for fibre orientation density (FOD) estimation [8–10], followed by a number of other, possibly more signal-adapted bases [10]. It is interesting to note that deconvolution methods for FOD estimation probe the signal locally, thanks to the finite spacial support of the convolution kernel, which allows for sparse representations. However, the low-pass nature of this kernel makes the deconvolution methods extremely susceptible to noise. Posing additional constraints, such as positivity and regularity [9, 10], is thus imperative for reliable FOD reconstruction. A good side of these deconvolution techniques is that they can yield accurate FOD estimates even at relatively low b-values, as well as they do not necessitate multiple b-value acquisition schemes. Recently, Michailovich et al. [11], derived an elegant framework for multiscale ridgelet analysis of HARDI signal. Using matching pursuit technique, the authors managed to reduce the representation of the signal to as little as 10 basis functions in the defined ridgelet frame.

In our study, designed in parallel and conducted independently of [11] (as well as postulated on different starting points, and somewhat different final goals), we propose to denoise and sharpen ODF directly, employing multiscale spherical wavelet analysis. Nonetheless, despite its different spirit, a part of our approach appears to be directly linked to a segment of the study of Michailovich et al. Herein, we show this association and adopt a part of the method (the ridgelet construction) from [11], to avoid signal integration over perpendicular planes.

We explicitly search for the relevant and localized diffusion information on multiple scales. The algorithm we employ is an extension of the well known "à trous" algorithm from 2D to the sphere [12]. It is an undecimated (hence, redundant) wavelet transform, with cubic B-spline scaling function, defined on the sphere. The transformation redundancy actually helps us to avoid Gibbs aliasing inherent to orthogonal or bi-orthogonal basis [13]. Also, although the explicit data reconstruction may not be mandatory for a number of applications (e.g., the FOD estimation), the positive side of the algorithm is that it is fully invertible (unlike some other spherical wavelet algorithms [12]), and that it allows us to introduce data conditioned constraints for the reconstruction. By linking the wavelet analysis in ODF "space" with a similar analysis in the signal space via Funk-Radon transform, we define a framework to probe the HARDI data in such a way that our study of the signal results directly in a sparse representation of angular content of diffusion. Since our preliminary study on spherical wavelets included experiments on HARDI signal, we start out by reviewing them, to subsequently pass on to the main subject of this report.

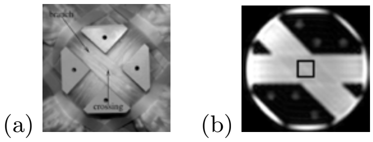

Fig. 1. Physical phantom at: (a) 90°, and (b) 45° (fast spin-echo map and ROI)).

2 Methods

2.1 Data acquisition: We demonstrate the method on two real physical phantoms [14], emulating two fibre bundles crossing at 45° and 90°, respectively [14]. The phantom data were acquired on a 1.5T Signa MR system (GE Healthcare, Milwaukee), TE/TR =130ms/4.5s,12.0s (45° and 90° phantom, respectively), BW=200KHz. To enhance the SNR (keeping $\mathrm{SNR}_{min} > 4$), large voxel dimensions were used (FOV = 32cm, matrix size of 32x32). We analyze the data acquired at two b-values of $b = 2000/8000$ smm^{-2}, along 4000 uniformly distributed orientations (see Fig. 1). The method is also applied to a real data set, acquired on a 1.5T Signa MR system (GE Healthcare, Milwaukee), TE/TR=100.2 ms/19s, BW=200KHz, FOV=24cm on a 128x128 matrix, TH=2mm, 60 axial slices, $b = 0/3000$ smm^{-2} (SNR ≈ 2), 200 uniformly distributed orientations. This dataset is part of the publicly available HARDI database [15].

2.2 Spherical wavelet transform of HARDI: For preliminary tests of HARDI signal decomposition of diffusion phantoms, we used an undecimated, spherical wavelet transform. For the herein described application, we employed an isotropic transform, with cubic B-spline scaling function. This function is shown to be very close to Gaussian, converges to zero rapidly, and in addition, it fulfills the dilation equation [12]. The algorithm is derived directly from the Fast Fourier Transform (FFT)-based wavelet transform [13], and being defined on the sphere, it relies on SH transform. The scaling function, $\Phi_{l_c}(\theta, \phi)$, where l_c is the cutoff frequency, and where (θ, ϕ) follow the physics convention (i.e., θ is longitude and ϕ is azimuth) exhibits azimuthal symmetry, and thus, its spherical harmonics transform does not depend on the phase m:

$$\Phi_{l_c}(\theta, \phi) = \Phi_{l_c}(\theta) = \sum_{l=0}^{l_c} \hat{\Phi}_{l_c}(l, 0) Y_{l,0}(\theta, \phi), \tag{1}$$

where $Y_{l,m}$ are the SH basis functions, and $\hat{\Phi}_{l_c}$ is the SH transform of Φ_{l_c}.

This greatly simplifies the convolution with HARDI signal $h(\theta, \phi)$, which reduces to:

$$\hat{c_0}(l, m) = (\widehat{\Phi_{l_c} * h})(l, m) = \sqrt{\frac{4\pi}{2l+1}} \hat{\Phi}_{l_c}(l, 0) \hat{h}(l, m), \tag{2}$$

where operator $*$ stands for the convolution, $\hat{c_0}(l,m)$ are the SH coefficients of the resulting convolution corresponding to order l, and phase number m, and $\hat{h}(l,m)$ are the SH coefficients of HARDI signal h.

The multiresolution decomposition of h is performed on a dyadic scale, by convolving h with the rescaled versions of the scaling function Φ_{l_c} (dyadically dividing the cutoff frequency l_c): $c_j = \Phi_{2^{-j}l_c} * h$, where j ($j = 1 \ldots J$) is the scale, and $\Phi_{2^{-j}l_c}$ is a rescaled Φ_{l_c} with 2^j times lower cutoff frequency. The decomposition can be done recursively as $c_{j+1} = c_j * f_j$ (setting $c_0 = h$), where f_j represents a low pass filter associated to each scale j, is a function of the scaling function Φ_{l_c}, and whose SH transform $\hat{F}_j$ is defined as follows:

$$\hat{F}_j(l,m) = \begin{cases} \frac{\hat{\Phi}_{2^{-(j+1)}l_c}(l,m)}{\hat{\Phi}_{2^{-j}l_c}(l,m)} & \text{if} \quad l < 2^{-(j+1)}l_c \quad \text{and} \quad m = 0 \\ 0 & \text{else} \end{cases} \tag{3}$$

Following the approach of the "à trous" algorithm, the wavelet coefficients are defined as the difference between two consecutive low-pass filtered versions of h:

$$w_{j+1} = c_j - c_{j+1}, \tag{4}$$

This relation implies that the high-pass filter g to obtain the wavelet coefficients directly, is given in SH base by: $\hat{G}_j(l,m) = 1 - \hat{F}_j(l,m)$, where f_j is defined in SH, as in (5) above, at each scale j. The scaling function itself is defined in SH space: $\hat{\Phi}_{l_c} = \frac{3}{2}B_3(\frac{2l}{l_c})$, and $B_3(x) = \frac{1}{12}(|x-2|^3 - 4|x-1|^3 + 6|x|^3 - 4|x+1|^3 + |x+2|^3)$. The eq. 4 above implies a straightforward reconstruction scheme:

$$c_0(\theta,\phi) = c_J(\theta,\phi) + \sum_{j=1}^{J} w_j(\theta,\phi), \tag{5}$$

However, the basis redundancy necessitates the usage of additional constraints for synthesis. For this preliminary application to HARDI, we followed the same algorithm as in [12]. We impose a least squares constraint to the solution at each scale and obtain the following, recursive relation: $\hat{c}_j = \hat{c}_{j+1}\bar{\hat{F}} + \hat{w}_{j+1}\bar{\hat{G}}$, where $\bar{\hat{F}}$ and $\bar{\hat{G}}$ are filters conjugate to $\hat{F}$ and $\hat{G}$ (defined above).

Wavelet coefficients filtering To meet the request on data sparsity (which directly leads to their compression), we introduce an additional step that follows after the signal decomposition. This step concerns wavelet coefficients shrinkage (or filtering), which is, further, shown to be extremely effective in data denoising and contrast sharpening [16]. Wavelet filtering is, in general, a non-linear transformation of the wavelet coefficients, at each analyzed scale. It is well known that with the aim of sparse signal representation, the filtering should be done by minimizing the L0 norm of these coefficients. It is also known that the L0 minimization leads to a NP-hard problem, and that the minimization of L1 norm results in the sparsest solution, closest to the one obtained by L0 minimization. It is worthwhile noting that if the wavelet basis were orthogonal, filtering based on hard thresholding would provide us with the exact solution to the L0 minimization [13]. Since the noise of diffusion weighted MR in each direction follows Rician distribution, it is difficult to estimate the exact distribution of noise on wavelet coefficients that is, at each scale, given as a convolution of noise over different directions with the wavelet band-pass filter. Hence, to define a 95% threshold for wavelet coefficient shrinkage, we perform permutations of signal coefficients along different directions, calculate the wavelet coefficients of thus synthesized signals, order them increasingly by their magnitude, and locate the value at 95%. The average of this value from all permutations defines the 95% threshold. At each wavelet scale we preserve only those coefficients whose magnitude is larger than the threshold. This way, the signal is denoised, and the number of coefficients for its final representation is highly reduced.

2.3 Spherical wavelet transform of ODF: The cubic B-spline based wavelet transform of HARDI signal is proven useful for data compression, but as aforementioned, that is not our final goal. We are rather interested in obtaining a sparse representation of ODF (or similarly, a sparse representation of FOD). This may show quite beneficial for fibre tracking applications. If we assume that ODF is given as a finite sum of probability distribution functions on the sphere, where each of these functions describes the angular probability of finding a WM fibre bundle along a predefined set of directions (centered at a prescribed direction) [7], then a natural decomposition of ODF would be onto a basis of such functions. Typically, for a fibre bundle oriented along a certain direction d, its contribution to ODF in the observed voxel is thought to be a Gaussian function on the sphere, centered at d (under the assumption of gaussianity of the diffusion process [7]). However, due to complex WM architecture, including different types of fibre-crossings and similar non-trivial fibre configurations, as well as due to limited capacity of imaging tools to resolve such configurations, the bandwidth of the elementary ODF-building function cannot be assumed uniform across the imaged WM. For that reason, we favor multiscale approach for ODF analysis. Consequently, we employ spherical wavelet transform to ODF, similarly to what has been described for HARDI signal. Despite our aspiration to decompose ODFs, we would like to work directly on HARDI signal by incorporating the link between the signal and its ODF over Funk-Radon transform, and thus avoid noise propagation. Since both the HARDI signal and its ODF are symmetric and real functions on the sphere, they can be represented by modified SH basis,$Y_n(l, m)$, that is symmetric and real, taking into account only pair orders l, as defined in [7].

Further, this signal symmetry also allows us to symmetrize cubic B-spline scaling function Φ, and its associated wavelet function W. As the latter two are also real, they can be likewise represented by the same symmetric and real SH basis. Letting $\boldsymbol{u}$ represent a unit direction on the sphere and N the maximal order of modified SH basis corresponding to the chosen cutoff frequency l_c, we first express the convolution on the sphere between the ODF, Ψ, and scaling function $\varPhi$ as

$$(\varPsi * \varPhi)(\boldsymbol{u}) = \sum_{n=1}^{N} \hat{\varPsi}_n \hat{\varPhi}_n Y_n(\boldsymbol{u}). \tag{6}$$

Then, the Funk-Radon transform (FRT) [2] of the signal, expressed as great circle integrals over perpendicular directions to $\boldsymbol{u}$, is solved analytically [7] yielding:

$$\varPsi(\boldsymbol{u}) = \underbrace{\int_{\boldsymbol{v}\perp\boldsymbol{u}} \delta(\boldsymbol{u},\boldsymbol{v})h(\boldsymbol{v})d\boldsymbol{v}}_{\text{FRT}} \quad \Longrightarrow \quad \hat{\varPsi}_n = 2\pi P_{l_n}(0)\hat{H}_n, \tag{7}$$

where δ is spherical Dirac delta function, h the HARDI signal defined on the sphere, P_{l_n} the Legendre polynomial of order l_n corresponding to order n of the modified SH basis, and $\hat{\varPsi}_n$, $\hat{\varPhi}_n$, and $\hat{H}_n$ stand for the nth component of the spherical harmonic transform of $\varPsi$, $\varPhi$, and h respectively. Eqs. 6 and 7 imply the following identity:

$$(\varPsi * \varPhi)(\boldsymbol{u}) = \sum_{n=1}^{N} 2\pi P_{l_n}(0)\hat{H}_n \hat{\varPhi}_n Y_n(\boldsymbol{u}), \tag{8}$$

On the other hand, if we observe the integral of the convolution of the signal h and scaling function $\varPhi$ over the great circle in the plane perpendicular to $\boldsymbol{u}$, we can derive the following identity :

$$\begin{aligned} \int_{\boldsymbol{v}\perp\boldsymbol{u}} \delta(\boldsymbol{u},\boldsymbol{v})(\varPhi * h)(\boldsymbol{v})d\boldsymbol{v} &= \int_{\boldsymbol{v}\perp\boldsymbol{u}} \delta(\boldsymbol{u},\boldsymbol{v}) \sum_{n=1}^{N} \hat{\varPhi}_n \hat{H}_n Y_n(\boldsymbol{v})d\boldsymbol{v} \\ &= \quad \sum_{n=1}^{N} \hat{\varPhi}_n \hat{H}_n 2\pi P_{l_n}(0) Y_n(\boldsymbol{u}), \end{aligned} \tag{9}$$

It follows from Eqs. 6-9 that $(\varPsi * \varPhi)(\boldsymbol{u}) = \int_{\varOmega} \delta(\boldsymbol{u},\boldsymbol{v})(\varPhi * h)(\boldsymbol{v})d\varOmega$.

Since spherical wavelets were defined as a difference of two scaling functions at successive scales (Eq. 4), the identity in Eq. 8 is equally applicable to wavelet functions W. This means that projecting ODF onto the spherical wavelet basis (defined in Sec. 2.2) equals to projecting the HARDI signal onto the same basis and integrating those HARDI signal projections along the great circles perpendicular to given ODF directions.

Michailovich et al [11], elegantly derived a ridgelet frame in the signal space, with the ridgelet-generating function based on Gauss-Weierstrass kernel. They decompose the signal onto the ridgelet frame, and use the obtained ridgelet coefficients to decompose the ODF onto the Funk-Radon duals of the ridgelet frame. We now show that the integration over great circles of HARDI signal convoluted by cubic B-spline scaling function equates to HARDI signal convolution by the ridgelet generated from cubic B-spline scaling function. Following the outline for ridgelet generation described in [11], and using the identity from eq. 1, the ridgelet generating function $\varPhi_B$ based on the cubic B-spline scaling function is defined as:

$$\Phi_B(\boldsymbol{u}) = \int_{\Omega} \delta(\boldsymbol{u}, \boldsymbol{v}) \Phi(\boldsymbol{v}) d\boldsymbol{v} = \sum_{n=1}^{N} \underbrace{\hat{\Phi}_n 2\pi P_{l_n}(0)}_{\hat{\Phi_{Bn}}} Y_n(\boldsymbol{u}) \tag{10}$$

and thus the Eqs. 6 and 10 result in:

$$(\Psi * \Phi)(\boldsymbol{u}) = \sum_{n=1}^{N} \hat{\Phi_{Bn}} \hat{H}_n Y_n(\boldsymbol{u}), \tag{11}$$

Similar to wavelet definition, we define the ridgelets as the difference of ridgelet generating functions Φ_B at two successive resolution scales j, $W_{Rj+1} = \Phi_{Bj} - \Phi_{Bj+1}$. Then, directly from equation 11:

$$(\Psi * W)(\boldsymbol{u}) = \sum_{n=1}^{N} \hat{W_{Rn}} \hat{H}_n Y_n(\boldsymbol{u}), \tag{12}$$

In words, to find the projections of ODF onto the wavelet basis, we directly project HARDI signal onto the ridgelet basis:

$$\begin{aligned} \Psi(\boldsymbol{u}) &= (\Psi * \Phi_J)(\boldsymbol{u}) \Phi_J + \sum_{j=1}^{J} (\Psi * W_j)(\boldsymbol{u}) W_j \\ &= (h * \Phi_{BJ})(\boldsymbol{u}) \Phi_J + \sum_{j=1}^{J} (h * W_{Rj})(\boldsymbol{u}) W_j \\ &= \Psi(\boldsymbol{u})_L + \Psi(\boldsymbol{u})_H, \end{aligned} \tag{13}$$

where Ψ_L and Ψ_H denote the low and high frequency components of Ψ. Decomposing ODF in such a manner, we can proceed by wavelet coefficient filtering, similar to what we did with wavelet coefficients of HARDI. This way, we obtain a sparse and denoised ODF. However, despite potentially high rate of ODF wavelet shrinkage, the low frequency component is still present. In our opinion, for the appropriately chosen resolution levels for ODF decomposition, this low frequency component may be limited to sufficiently low angular frequency band that effectively carries no relevant information on fibre bundle angular distribution. Our main goal is to extract a small number of interesting ODF components that would facilitate WM fibre tracking and similar applications. Thus, instead of presenting our sparse angular distribution function by both low and high frequency component, we rather focus on the “high” frequency part only, effectively neglecting the lowest frequency ODF contribution. In other words, we focus on sharp ODF, Ψ_H, as opposed to ODF Ψ in its entirety. In this respect, our sharp ODF is expected to resemble the FOD that is in essence a sort of a high-pass filtering adapted to data. For that reason, we compare our results with both the analytical SH q-balls method [7], and the FOD reconstructions from spherical deconvolution (SD) [8,9]. Note that for the ridgelet decomposition of the HARDI signal, the algorithm can no longer be recursive (due to cancellation of the $2\pi P_{l_n}(0)$ term). We thus modified the original recursive analysis scheme and employ the ridgelet/wavelet filters directly to the base-scale signal/ODF.

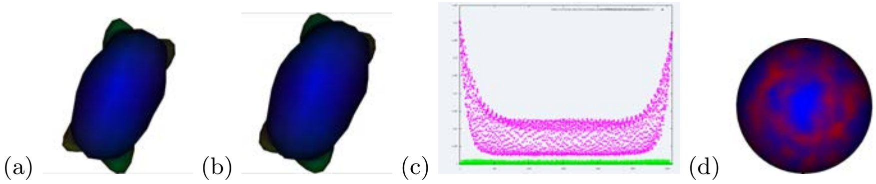

Fig. 2. Spherical wavelet compression of HARDI signal. (a) Original HARDI signal corresponding to a 45°-crossing voxel of the physical phantom shown in Fig. 1; (b) Synthesized and reduced HARDI signal after the wavelet analysis and hard thresholding of the wavelet coefficients at 95%, at each scale; (c) HARDI signal (magenta) and residuals (light green) per direction on the sphere; (d) Residuals on the sphere (higher values shown in red, lower in blue).

3 Experiments and Results

3.1 Spherical wavelet transform of HARDI: The method for wavelet decomposition, followed by the hard thresholding of the wavelet coefficients and synthesis upon the reduced wavelet basis, was applied to the HARDI signal of a central voxel of the 45°-crossing phantom (shown in Fig. 1). The cutoff frequency, l_c, was set to 12, and the analysis was performed at two scales. Fig. 2 depicts the result of the analysis. The magnitude and shape of the residuals indicate a reasonably good accord between the chosen wavelet basis and the data.

3.2 Spherical wavelet transform of ODF applied to physical phantoms: We applied our method for spherical wavelet decomposition of ODF to 45°- and 90°-crossing real physical phantoms. To enable the subsequent comparison of results with the results of similar analysis performed on the real data of a healthy volunteer, we subsampled the directions to the same set of 200 directions as our real dataset (Sec. 2.1). Also, to adapt our analysis frequency bands to the frequency content of the data, the original cubic B-spline kernel was twice dilated in the frequency space. The data were decomposed onto 2 resolution scales, and the cutoff frequency was set to $l_c = 12$. Figure 3 depicts the results for the 45° and 90° crossing phantom at different b-values. Note that the result in (g) was obtained on the 45°-crossing phantom that was resampled to 500 uniform directions. In that case, a cutoff frequency $l_c = 30$ was used to show the resolution necessary to resolve a 45° fibre crossing at $b = 2000smm^{-2}$ since it could not be resolved using lower frequencies. To employ such a high frequency, the number of directions had to be increased proportionally. For comparison purposes, we also reconstructed analytical q-ball as well as two types of FODs (following the algorithms of [8, 9]) with filtered spherical deconvolution (FSD) and with constrained spherical deconvolution (CSD), at different order l. The low-pass filter for FSD was [1 1 1 0.5 0.1 0.02 0.002] applied to SH order $l = [0\ 2\ 4\ 6\ 8\ 12]$. For CSD, the regularization parameter $\lambda = 1$, threshold for positivity constraint $\tau = 0.1$, and convergence was set to 10 iterations.

3.3 Spherical wavelet transform of ODF: Similar analysis was performed on a slice of a real data set, only for these experiments, the cutoff frequency was set to $l_c = 8$, to diminish the high-frequency noise as much as possible. After the sharp ODF is reconstructed, the negative values are hard thresholded to zero. The results are shown in figure 4.

4 Discussion

In this study, we employed the methods for HARDI and ODF mutliscale decomposition based on the spherical wavelet and rigdelet analysis. We tested the methods on real physical phantoms and real brain data. The experiments allowed us to demonstrate the algorithm efficiency to represent the relevant features with only scarce number of wavelet coefficients, thus providing a high level of data compression and denoising. For example, a reconstruction of the signal or ODF/FOD with a SH basis of order 12 required 91 coefficients whereas our reconstrustion used 20 spherical wavelet coefficients (10 per scale).

More importantly, our approach for wavelet-based ODF sharpening proves to be efficient in extracting pertinent angular information, concealed by signal spread out over relatively wide range of frequencies that cannot be seen with classical ODF alone. This may show valuable for WM fibre tracking. The results of FOD working on similar frequency bands resemble our ODF sharpening results. This is not surprising, since, as aforementioned, SD acts like a high-pass filter and in that sense approaches the philosophy of wavelet analysis. Some of the results on real physical phantoms suggest that SD outperforms wavelet-based decomposition and sharpening, but one must bear in mind that SD filters are derived directly from the data, which is much easier to do on physical phantoms, such the ones employed in this study, than on real data. This is why, the estimated kernel on real data may not be equally optimal for all the investigated regions. It is possible that it should be defined differently depending on the region of the brain. Hence, SD methods assume a deconvolution kernel that is data-dependent and thus, “b-value dependent”, whereas our approach does not. Perhaps more care needs also to be taken when defining wavelet scaling functions or rigdelet generating functions, and render them more adaptive to the data, which is one of the issue that we plan to address in future work. Finally, we find the tests on real data rather encouraging. It appears that the problem that SD experiences at high noise levels, does not affect wavelet analysis as much (despite the inherent “Bessel”-blurring). In fact, thanks to the multiscale approach and denoising at different resolution levels, our ODF sharpening technique outperforms SD, even when we deal drastically with the negative values for the latter, and even with no explicit constraints put on signal reconstruction from its significant wavelet coefficients. Incorporating data adapted constraints will also take part in our future work.

We would like to stress again that although there is a link between our work and the work in [11], the two studied were conducted independently, in parallel and towards somewhat different targets. However, because the ridgelet frame of [11] was well adapted to our approach, we adopted that part of the method, as aforementioned. In addition, we showed the spherical wavelet method on the real brain data for the first time (to our knowledge) and focused on the high frequency decomposition of the ODF, which reveals interesting angular structure. To conclude, this report was done with the aim of stressing the potential of spherical, localized, and multiscale bases in HARDI analysis.

References

1. Frank, L.: Characterization of anisotropy in high angular resolution diffusion-weighted MRI. Magnetic Resonance in Medicine **47**(6) (2002) 1083–1099
2. Tuch, D.: Q-ball imaging. Magnetic Resonance in Medicine **52**(6) (2004) 1358–1372
3. Basser, P., Mattiello, J., LeBihan, D.: Estimation of the effective self-diffusion tensor from the NMR spin echo. Journal of Magnetic Resonance **B**(103) (1994) 247–254
4. Alexander, D., Barker, G., Arridge, S.: Detection and modeling of non-gaussian apparent diffusion coefficient profiles in human brain data. Magnetic Resonance in Medicine **48**(2) (2002) 331–340
5. Descoteaux, M., Angelino, E., Fitzgibbons, S., Deriche, R.: Apparent diffusion coefficients from high angular resolution diffusion imaging: Estimation and applications. Magnetic Resonance in Medicine **56** (2006) 395–410
6. Hess, C., Mukherjee, P., Han, E., Xu, D., Vigneron, D.: Q-ball reconstruction of multimodal fiber orientations using the spherical harmonic basis. Magnetic Resonance in Medicine **56** (2006) 104–117
7. Descoteaux, M., Angelino, E., Fitzgibbons, S., Deriche, R.: Regularized, fast, and robust analytical q-ball imaging. Magnetic Resonance in Medicine **58**(3) (2007) 497–510
8. Tournier, J.D., Calamante, F., Gadian, D., Connelly, A.: Direct estimation of the fiber orientation density function from diffusion-weighted mri data using spherical deconvolution. NeuroImage **23** (2004) 1176–1185
9. Tournier, J.D., Calamante, F., Connelly, A.: Robust determination of the fibre orientation distribution in diffusion mri: Non-negativity constrained super-resolved spherical deconvolution. NeuroImage **35**(4) (2007) 1459–1472
10. Jian, B., Vemuri, B.C.: A unified computational framework for deconvolution to reconstruct multiple fibers from diffusion weighted mri. IEEE Transactions on Medical Imaging **26**(11) (2007) 1464–1471
11. Michailovich, O.V., Rathi, Y.: On approximation of orientation distributions by means of spherical ridgelets. In: IEEE International Symposium on Biomedical Imaging: from Nano to Macro. (2008)
12. J.-L Starck, Y. Moudden, P.A., Nguyen, M.: Wavelets, ridgelets, and curvelets on the sphere. Astronomy and Astrophysics **446** (2006) 1191–1204
13. Starck, J.L., Murtagh, F.: Astronomical Image and Data Analysis. Springer (2006)
14. Poupon, C., Rieul, B., Kezele, I., Perrin, M., Poupon, F., Mangin, J.F.: New diffusion phantoms dedicated to the study and validation of hardi models. Magnetic Resonance in Medicine – (2008) In press
15. Poupon, C., Poupon, F., Allirol, L., Mangin, J.F.: A database dedicated to anatomo-functional study of human brain connectivity. In: Twelfth Annual Meeting of the Organization for Human Brain Mapping (HBM). (2006)
16. Mallat, D.S.: A Wavelet Tour of Signal Processing. Academic Press (1999)

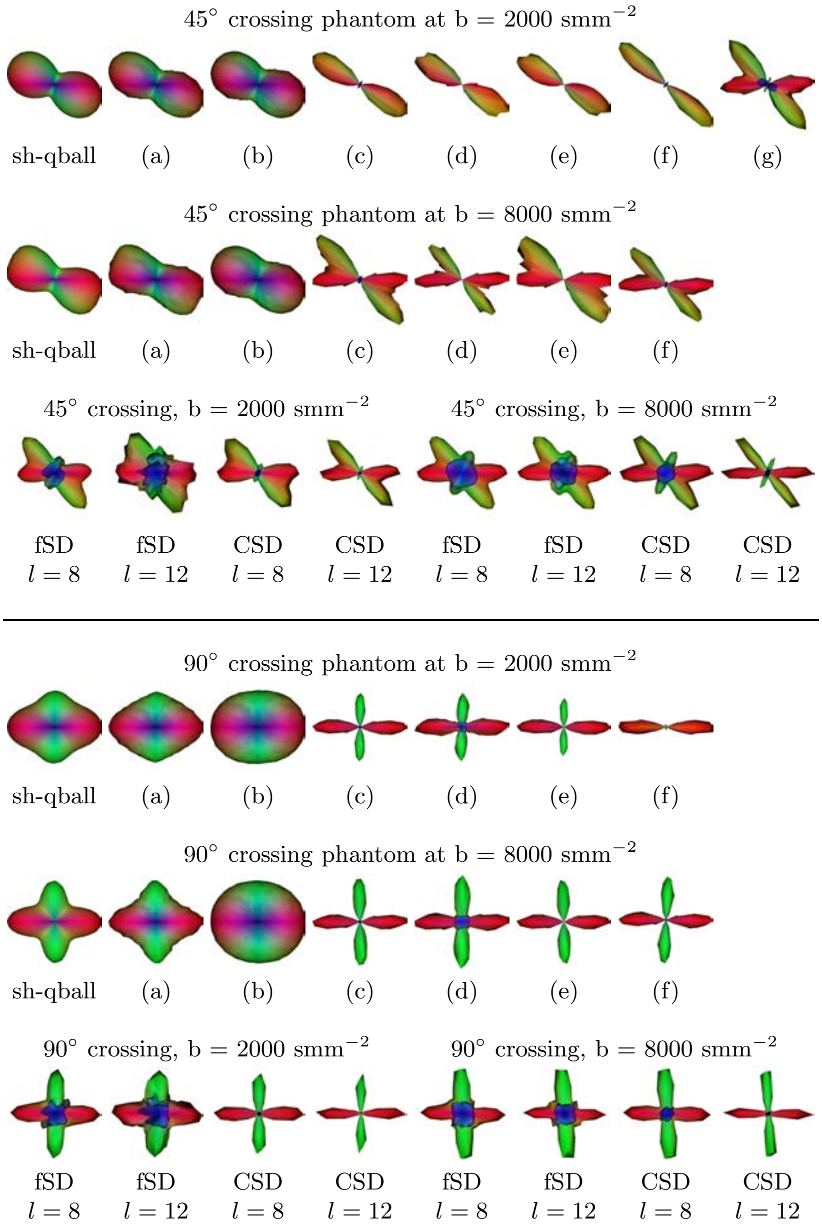

Fig. 3. ODF and FOD reconstruction for the 45° (rows 1-3) and 90° (rows 4-6) crossing phantom. Rows 3 and 6 illustrate the spherical deconvolution (SD) profiles, filtered (fSD) [8] and constrained (CSD) [9]. Shown are in rows (1, 2) and (4, 5): the full analytical ODF (sh-qball) at order $l = 12$; (a) the full ODF Ψ reconstructed as a sum of the Ψ_L and the thresholded Ψ_H (Eq. 13) (the maximum number of the significant coefficients was 10 at both scales); (b) the scaling (Φ) coefficients of lowest resolution (scale $j = 2$); (c) the sharp ODF reconstructed with wavelet coefficients at both scales after thresholding; (d) wavelet coefficients of the first resolution scale (highest frequencies) after thresholding; (e) wavelet coefficients of the second resolution scale after thresholding; (f) sharp ODF reconstruction using only the two highest magnitude coefficients at each scale; (g) the sharp ODF reconstructed from 20 largest magnitude wavelet coefficients at both resolution scales, for the HARDI signal subsampled to 500 uniformly distributed directions, and with $l_c = 30$ (see the text for the explanation).

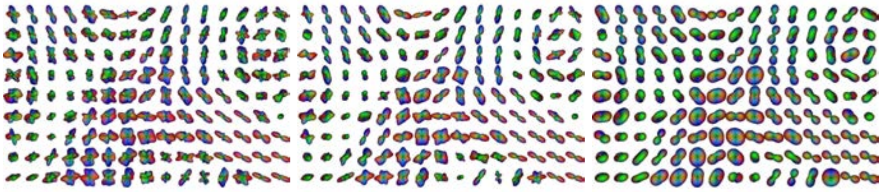

sh-qball, $l = 8$ (a) (b)

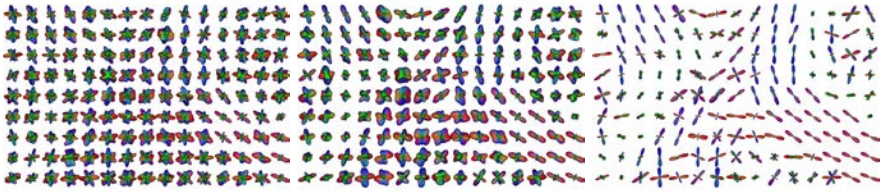

(c) (d) (e)

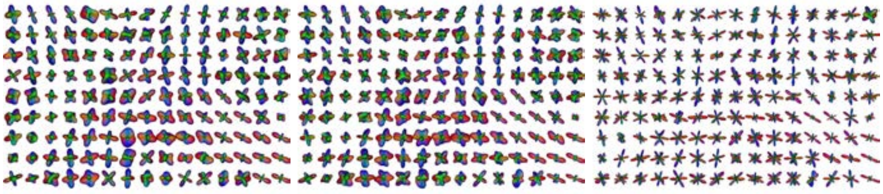

fSD $l = 4$ fSD $l = 6$ CSD $l = 6$ +ve

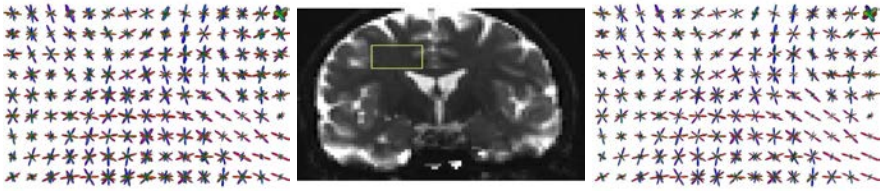

CSD $l = 12$ T2-weighted + ROI CSD $l = 12$ +ve

Fig. 4. ODF and FOD reconstructions on real data. From left to right, and from top to bottom: full ODF calculated analytically [7] in the SH space with $l = 8$; (a) full ODF Ψ reconstructed as a sum of the Ψ_L and the thresholded Ψ_H (the maximum number of the significant coefficients was 10 at both scales); (b) scaling coefficients at lowest resolution (scale 2); (c) wavelet coefficients of the first resolution scale (highest frequencies) after thresholding; (d) wavelet coefficients of the second resolution scale after thresholding; (e) the sharp ODF reconstructed with wavelet coefficients at both scales after thresholding. Last two rows illustrate filtered and constrained spherical deconvolution (fSD, CSD) for low and high order reconstructions. '+ve' indicates that the negative values were hard-thresholded to zero. The SNR of the real data diffusion acquisition is quite poor and is a challenge for SD methods.

A polynomial based approach to extract the maxima of an antipodally symmetric spherical function and its application to extract fiber directions from the Orientation Distribution Function in Diffusion MRI *

Aurobrata Ghosh[1], Elias Tsigaridas[2], Maxime Descoteaux[3], Pierre Comon[4],
Bernard Mourrain[2], and Rachid Deriche[1]

[1] Odyssee, INRIA Sophia Antipolis, France, `Aurobrata.Ghosh@sophia.inria.fr`,
[2] GALAAD, INRIA Sophia Antipolis, France,
[3] Neurospin, CEA Saclay, France,
[4] Laboratoire I3S, CNRS and the University of Nice, Sophia Antipolis, France.

Abstract. In this paper we extract the geometric characteristics from an antipodally symmetric spherical function (ASSF), which can be described equivalently in the spherical harmonic (SH) basis, in the symmetric tensor (ST) basis constrained to the sphere, and in the homogeneous polynomial (HP) basis constrained to the sphere. All three bases span the same vector space and are bijective when the rank of the SH series equals the order of the ST and equals the degree of the HP. We show, therefore, how it is possible to extract the maxima and minima of an ASSF by computing the stationary points of a constrained HP.
In Diffusion MRI, the Orientation Distribution Function (ODF), represents a state of the art reconstruction method whose maxima are aligned with the dominant fiber bundles. It is, therefore, important to be able to correctly estimate these maxima to detect the fiber directions. The ODF is an ASSF. To illustrate the potential of our method, we take up the example of the ODF, and extract its maxima to detect the fiber directions. Thanks to our method we are able to extract the maxima without limiting our search to a discrete set of values on the sphere, but by searching the maxima of a continuous function. Our method is also general, not dependent on the ODF, and the framework we present can be applied to any ASSF described in one of the three bases.

1 Introduction

In Diffusion MRI there exist numerous state of the art reconstruction algorithms which attempt to recover an integrated image by incorporating partial and directional information from diffusion weighted (DW) signals. The reconstructed

---

* Partially supported by the contracts ANR-06-BLAN-0074 "Decotes" and INRIA-ARC Diffusion-MRI.

and integrated image is often represented as values on a sphere at every voxel. The geometric characteristics of these antipodally symmetric spherical functions (ASSF) provide a sub-voxel resolution superior to the raw DW-MR images.

There are numerous aquisition schemes, and many reconstruction algorithms, that result in a number of distinct ASSFs, which represent different physical phenomena. For example there exist Diffusion Tensor Imaging (DTI) [1] which represents the Apparent Diffusion Coefficient (ADC), Generalized DTI (GDTI) [2–4] which also represents the ADC, Q-ball imaging (QBI) [5, 6] which represents the Orientation Distribution Function (ODF), Spherical Deconvolution (SD) which represents the fiber Orientation Density (fOD), and Maximum Entropy Spherical Deconvolution (MESD) [7] which is a generalization of the Persistent Angular Structure (PAS) method, and which recovers the angular structure of the particle displacement probability density function; to enumerate a few methods.

For certain of these ASSFs, their geometric characteristics have direct physical consequences. For example the maxima of the ODF and the fOD correspond to the fiber bundle directions. It is, therefore, important to be able to correctly estimate the maxima of these ASSFs to detect fiber directions (see Fig-1).

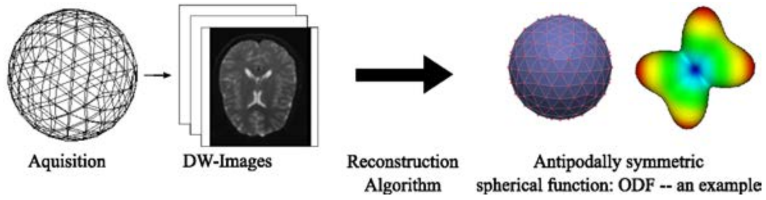

Fig. 1. An antipodally symmetric spherical function (ASSF) reconstructed from DWIs. The maxima of the ODF, for example, indicate fiber bundles. It is important to correctly estimate the maxima of these ASSFs.

It is common to analytically represent an ASSF in the Spherical Harmonic (SH) basis – analytical QBI for example, or in the Symmetric Tensor[5] (ST) basis constrained to the sphere – DTI or GDTI for example. These bases are bijective when the rank of the SH series equals the order of the symmetric tensor. The basis of Homogeneous Polynomials (HP) constrained to the sphere, is also bijective to the ST basis and spans the same vector space when the degree of the HP equals the order of the ST. It is, therefore, possible to represent an ASSF described in either the SH basis or the ST basis as a constrained HP.

In this paper, we take advantage of this constrained HP representation of an ASSF, to extract the maxima of the ASSF, by computing the stationary points of the constrained HP. We then rank the stationary points by their polynomial values to extract the maxima of the ASSF (see Fig-2).

---

[5] A symmetric tensor of any order requires that the coordinate array representating the tensor be invariant under all permutation of indices. It is often also referred to as a *supersymmetric* tensor.

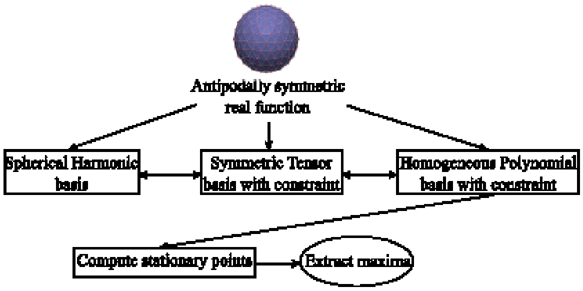

Fig. 2. An antipodally symmetric spherical function (ASSF) can be represented in three equivalent bases – spherical harmonics, symmetric tensor constrained to the sphere, or homogeneous polynomial (HP) constrained to the sphere. As a constrained HP it is possible to compute its stationary points to extract the maxima of the ASSF.

We illustrate our method on the ODF by computing its maxima, which correspond to fiber bundle directions. This method is, however, independent of the ODF, or of the ODF estimation process. It is, therefore, applicable to any ASSF that can be represented in either the SH, ST or HP basis. Also, since it is independent of the estimation process of the ASSF (ODF for example), this method, as we shall see, can be used to quantize the error of the estimation process of the ASSF. This can have important implications for evaluating the quality of the estimation process (ODF for example).

Another strength of our method, lies in the fact that it is not limited to searching for the maxima of the ASSF in a finite set of values on the sphere, but rather searches the maxima of a continuous function.

2 Methods

We begin the methods section by establishing the equivalence of the SH, ST and HP bases when describing an ASSF. First let us consider the ST and the HP bases, and then the HP and SH bases.

2.1 SH basis, constrained ST basis, constrained HP basis There is a useful connection between the space of STs and the space of HPs, e.g.[8, 9]. A symmetric tensor of dimension n and order d has a one-to-one correspondance with a homogeneous polynomial in n variables of total degree d. For example if we consider a 4-way array of dimension 3, then a tensor element $a_{ijk\ell}$, is associated to the monomial $a_{ijk\ell}x_i x_j x_k x_\ell$ and the whole tensor to the homogeneous polynomial $\sum_{i=1}^{3}\sum_{j=1}^{3}\sum_{k=1}^{3}\sum_{\ell=1}^{3} a_{ijk\ell}x_i x_j x_k x_\ell$. In other words, for an order d symmetric tensor of dimension n, an individual index i, j, $k, \ldots$, can take values from 1 to n, and the total number of indices qualifying a tensor element a (in the case of $a_{ijk\ell}$, it is four) has to be d. A similar construction exists for non-symmetric tensors and multi-homogeneous polynomials.

To illustrate this through an example, consider the $2 \times 2 \times 2$ tensor, i.e. order three symmetric tensor $\mathbf{A}$ of dimension two, with $a_{111} = 1$, $a_{121} = a_{211} = a_{112} = 2$, $a_{221} = a_{122} = a_{212} = 3$ and $a_{222} = 4$. The tensor consists of two 2×2 slices, i.e.

$$\mathbf{A}(::\ 1) = \begin{bmatrix} 1 & 2 \\ 2 & 3 \end{bmatrix} \quad \text{and} \quad \mathbf{A}(::\ 2) = \begin{bmatrix} 2 & 3 \\ 3 & 4 \end{bmatrix}.$$

The element a_{111} maps to the monomial x_1^3, the elements a_{121}, a_{211} and a_{112} map to the monomial $2x_1^2x_2$, the elements a_{221}, a_{122} and a_{212} map to the monomial $3x_1x_2^2$, and a_{222} maps to $4x_2^3$. Finally, $\mathbf{A}$ corresponds to the homogenous polynomial $f = x_1^3 + 6x_1^2x_2 + 9x_1x_2^2 + 4x_2^3$.

Now let us consider the SH basis and the HP basis. Spherical functions are naturally decomposed and expressed in a SH basis because SHs form an orthonormal basis for complex functions on the sphere and have many properties that facilitate computation [10, 11]. The correspondence between coefficients of the real and symmetric SH series and the coefficients of the HP constrained to the sphere are derived here.

In [2, 12], it was proved that both even order SHs up to rank d and the HPs of degree d restricted to the sphere are bases for the same vector space. It is, therefore, possible to define a general linear transformation $\mathbf{M}$ between the two bases which shall be recomputed here by expressing the coefficients of the modified SH series c_j in terms of the coefficients of the homogeneous polynomial.

Let an ASSF S be decomposed in the modified SH basis such that [10, 11, 2, 12],

$$c_j = \int_{\Omega} S(\mathbf{g}(\theta, \phi)) Y_j(\theta, \phi) d\Omega, \tag{1}$$

where $\mathbf{g}(\theta, \phi)$ is a normalized radial direction in spherical coordinates and Y_j is the jth coefficient of the real and symmetric SH basis [12].

Given a homogeneous polynomial P of degree d in three variables and constrained to the sphere

$$\mathrm{P}(\mathbf{x} = [x_1, x_2, x_3]^t) = \sum_{i_1=1}^{3} \sum_{i_2=1}^{3} \cdots \sum_{i_d=1}^{3} a_{i_1 i_2 \cdots i_d} x_{i_1} x_{i_2} \cdots x_{i_d}, \tag{2}$$

where $a_{i_1 i_2 \cdots i_d}$ are also the elements of the corresponding order d symmetric tensor $\mathbf{A}$ of dimension three, and $\mathbf{x}$ is of unit length to constrain P to the sphere; P can be rewritten in the form

$$\mathrm{P}(\mathbf{x}) = \sum_{k=1}^{N} \mu_k a_k \prod_{p=1}^{d} x_k(p), \tag{3}$$

where N are the number of independent elements of $\mathbf{A}$, a_k is the k^{th} independent element of $\mathbf{A}$, μ_k is its corresponding multiplicity, and $\prod_{p=1}^{d} x_k(p)$ is the corresponding monome (see[12]).

If P also describes the same ASSF S, then S in (1) can be replaced by (3) to obtain an expression in matrix form, where c_j is the jth element of the vector $\mathbf{C} = \mathbf{MA}$ and d is the number of elements in the SH basis:

$$c_j = \sum_{k=1}^{N} a_k \int_{\Omega} \mu_k \prod_{p=1}^{d} x_{k(p)}(\theta,\phi) Y_j(\theta,\phi) d\Omega \Longrightarrow \mathbf{C} = \mathbf{MA}\,, \text{ where} \tag{4}$$

$$\mathbf{M} = \begin{pmatrix} \mu_1 \int_{\Omega} \prod_{p=1}^{d} x_{1(p)}(\theta,\phi) Y_1(\theta,\phi) d\Omega & \ldots & \mu_N \int_{\Omega} \prod_{p=1}^{d} x_{N(p)}(\theta,\phi) Y_1(\theta,\phi) d\Omega \\ \vdots & \ddots & \vdots \\ \mu_1 \int_{\Omega} \prod_{p=1}^{d} x_{1(p)}(\theta,\phi) Y_N(\theta,\phi) d\Omega & \ldots & \mu_N \int_{\Omega} \prod_{p=1}^{d} x_{N(p)}(\theta,\phi) Y_N(\theta,\phi) d\Omega \end{pmatrix}. \tag{5}$$

It has been shown in [12] that the N x N square matrix $\mathbf{M}$ is a change-of-basis matrix, and is invertible. Therefore, given a vector $\mathbf{C}$ of SH coefficients, $\mathbf{M}^{-1}$ can be used to compute the coefficients of the constrained HP.

This establishes the bijectivity between the the SH basis, the constrained ST basis, and the constrained HP basis.

2.2 Constrained Polynomial maxima extraction Now that it is possible to express an ASSF in terms of a HP constrained to a sphere, the problem of determining the maxima of the ASSF reduces to computing the stationary points of the homogeneous polynomial P on the unit sphere. Once the stationary points are all computed, they can be sorted by their values in P to threshold and extract the maxima.

Therefore, to be more specific the following non-linear optimization problem has to be solved

$$\max_{\mathbf{x}} \mathrm{P}(\mathbf{x}) \text{ subject to } \|\mathbf{x}\|_2^2 - 1 = 0, \tag{6}$$

where $\mathbf{x} = (x_1, x_2, \ldots, x_n)$ are the variables and P is of degree d, i.e. $\mathrm{P} \in \mathbb{R}[\mathbf{x}]_d$. In our case, d is even and $n = 3$.

The size of the problem (6) (degrees of the polynomials involved, number of solutions) is relatively small, and thus there is no need to rely on general algorithms for polynomial optimization subject to constraints, e.g. [13]. Instead, we use the method of Lagrange multipliers for our problem. The reader may also refer to Karush-Kuhn-Tucker conditions [14] that provide the necessary conditions for the solution to (6) to be optimal.

We consider the polynomial $F(\mathbf{x}, \lambda) = \mathrm{P}(\mathbf{x}) - \lambda\,(\|\mathbf{x}\|_2^2 - 1)$. Then, the solution(s) of (6) is (are) among the solutions of the system

$$\frac{\partial F}{\partial x_1} = \frac{\partial F}{\partial x_2} = \cdots = \frac{\partial F}{\partial x_n} = \|\mathbf{x}\|_2^2 - 1 = 0. \tag{7}$$

It is easy to see that the equations in (7) are linear in λ. Thus one can be solved for λ and substituted in the others. The derived system is equivalent to the system obtained by requiring the vectors $\nabla \mathrm{P}$ and $\mathbf{x} = [x_1, x_2, \ldots, x_n]$, to be parallel. This yields the system

$$\begin{vmatrix} \frac{\partial \mathrm{P}}{\partial x_i} & x_i \\ \frac{\partial \mathrm{P}}{\partial x_j} & x_j \end{vmatrix} = 0 \text{ for } 1 \leq i < j \leq n \text{ and } \|\mathbf{x}\|_2^2 - 1 = 0.$$

This system describes the values $\mathbf{x}$ that maximize P on the unit sphere but also the other points where P has local extrema. For $n = 3$ variables and P a polynomial of degree $d = 4$, we obtain 3 equations of degree 4 and one of degree 2. One of them (of degree 4) being redundant, by Bezout's theorem this system has at most $4 \times 4 \times 2 = 32$ solutions. If $\mathbf{x}$ is a solution, them $-\mathbf{x}$ is also a solution. Thus the system defines at most 16 directions for the local extrema of P.

We choose to solve the corresponding systems combining two of the state of the art algorithms in polynomial system solving, i.e. subdivision methods and generalized normal forms algorithms. We solve the system using both methods and keep the best solutions by evaluating them in the polynomial system. The main virtue of both the algorithms is that they rely on algebraic techniques and thus unlike numerical iterative methods for polynomial system solving, they are neither slow, and nor do they diverge when dealing with ill conditioned systems.

Subdivision methods [15] approximate only the real solutions. Initialy, they consider a hyper-box where all the (real) solutions of the system are searched (here one can take the box $[-1, 1]^3$ which contains the unit sphere) and they subdivide it until a specified precision is reached, excluding boxes which do not contain roots. Preconditionning techniques are exploited to speed up the root approximation process. Bounding techniques are used to handle properly polynomials with approximate coefficients.

The other family of algorithms that can also be applied to polynomials with approximate coefficients is based on generalized normal form computations [16], which extend classical Gröbner basis methods [17]. Unlike Gröbner basis, this algorithm is numerical stable and thus suitable for solving polynomial systems with approximate coefficients. The method exploits the multiplicative structure of the quotient algebra of the polynomial ring by the (zero dimensional) ideal generated by a system of polynomial equations. Eventually, the resolution of the polynomial system is transformed into a generalized eigenvalue and eigenvector problem [18]. In practice, all the complex roots are computed within some tolerance, and those which are (almost) real are kept.

2.3 Analytical spherical harmonic estimation of the ODF Having established the theoretical framework of our method, we would like to illustrate it on a concrete example. We pick for that purpose the ODF computed analytically in the SH basis from QBI. The ODF is an ASSF. We, therefore, present for completeness, the analytical ODF estimation from High Angular Resolution Diffusion Imaging (HARDI) aquisitions. Our approach is, however, independent of the ODF or the ODF estimation process, and can be applied to any ASSF expressed in one of the SH, the ST or the HP bases.

The diffusion ODF is defined as the angular portion of the averaged diffusion PDF. It can be obtained from diffusion spectrum imaging (DSI) or from QBI. [5] showed that it was possible to reconstruct the diffusion ODF directly from raw HARDI measurements on a single sphere by the Funk-Radon transform (FRT). The ODF is intuitive because it has its maximum(a) aligned with the underlying population of fiber(s). [6, 19] proposed a simple analytical spherical harmonic (SH) reconstruction of the ODF. The FRT integral can be evaluated analytically which leads to a linear, robust and computationnally fast ODF reconstruction.

Letting Y_d^m denote the SH of rank d and degree m ($m = -d, ..., d$) in the standard basis and Y_j ($j(d, m) = (d^2 + d + 2)/2 + m$) be the SH in the modified real and symmetric basis [12, 6], the analytical ODF solution is

$$\Psi(\theta, \phi) = \sum_{j=1}^{N} \underbrace{2\pi P_{d(j)}(0) c_j}_{f_j} Y_j(\theta, \phi), \tag{8}$$

where $N = (d + 1)(d + 2)/2$, c_j are the SH coefficients describing the input HARDI signal [12], f_j are the SH coefficients describing the ODF Ψ, d_j is the rank associated with j^{th} SH basis element (for $j = \{1, 2, 3, 4, 5, 6, 7, ...\}$, $d_j = \{0, 2, 2, 2, 2, 2, 4, ...\}$) and P_{d_j} a Legendre polynomial.

3 Experiments

For our initial experiments, we test our method for a SH basis of rank-4, or equivalently a ST basis of order-4, or equivalently a HP basis of degree-4.

We test on synthetic data with known ground truth maxima directions. We perform two types of tests along similar lines. We consider an ASSF to be a set of scalar values defined on a sphere. In the first type of tests we generate a spherical function with four maxima (antipodally symmetric, therefore, we can consider the maxima to be along two distinct directions), to test our approach on a purely mathematical framework. We generate the spherical function by first randomly choosing the two maxima-directions separated by a pre-defined angle. Along these directions (and their opposite directions) we then set the function to have value 1, and everywhere else on the sphere to have value 0. Essentially we generate a spherical dirac function. We then fit a rank-4 SH function to this spherical data, for our maxima extraction tests. We call this the dirac test (section-3.1).

In the second type of tests, we use the multi-tensor model [12], to synthetically generate DW signals with fiber crossings. We simulate one and two fiber voxels with known ground truth directions. In the case of two fiber voxels, the two fibers have equal volume fractions are are separated by 90°. The diffusion tensor profile used for a fiber has diag($\mathbf{D}$) = [1390,355,355]x10^{-6} mm^2/s, FA = 0.7 which corresponds to our real dataset diffusion profile. This synthetic data generation is relatively standard and has the advantage of producing known ground truth ADC and ODF profiles as well as ground truth fiber orientations. We add no noise to the signal. We then estimate the analytical ODF in the SH basis with rank-4 from this signal, on which we perform the maxima extraction tests. We call this the ODF test (section-3.2).

Both tests, essentially involve three steps, which can be summarized as:

1. A set of ground truth directions $\{d_i\}$ are used to generate either a set of values on the sphere (section-3.1) or DW signals (section-3.2) such that the maxima of the set of values on the sphere or the ODF estimated from the DW signals respectively, have their maxima alligned with $\{d_i\}$.
2. In section-3.1 we estimate a rank-4 SH series to best fit the set of values on the sphere. In section-3.2 we estimate an ODF of rank-4 from the DW signals.
3. We then convert the SH coefficients to the HP basis (or the equivalent ST basis) and formulate the constrained polynomial problem, which we call $\mathcal{F}$. We compute its stationary points $\{R_j\}$, and sort them by their polynomial value, and then threshold the list to retrieve a set of computed maxima $\{d_k^{'}\}$.

We then proceed to compare $\{d_k^{'}\}$ to $\{d_i\}$. This is only possible when $k = i$. When the two sets are comparable, we pair the computed directions with the ground truth directions such that their difference is minimized. Then we first compute the angle between d_i and $d_i^{'}$ in degrees which we denote as $ang(d_i, d_i^{'})^o$. If this angle is non zero, we proceed to quantize the errors in steps 1, 2 and 3. Since, $\{d_i^{'}\}$ are the stationary points of $\mathcal{F}$, the value of $||\nabla\mathcal{F}(d_i^{'})||$ indicates the amount of error in step 3. Computing $||\nabla\mathcal{F}(d_i)||$ on the other hand indicates the amount of error in steps 1 and 2. In both the dirac tests and the ODF tests the error in step 1 can be considered to be nominal, since in the dirac tests the spherical function is analytically generated, and in the ODF tests we don't use any noise while generating the DW signals. So essentially $||\nabla\mathcal{F}(d_i)||$ is a measure of the error in step 2, which for the dirac tests is a truncated SH fit, and for the ODF tests is a truncated ODF estimation.

3.1 Dirac test In these tests we have four antipodally symmetric maxima, or two distinct maxima-directions (the two other are the opposites of these), separated by a pre-decided angle. We test our method for separation angles of 65^o and of 90^o. We construct one hundred test cases for each separation angle,

	$ang(d, d^{'})^o$		$\lVert\nabla\mathcal{F}(d^{'})\rVert$		$\lVert\nabla\mathcal{F}(d)\rVert$	
	m	v	m	v	m	v
65^o	0.281947	0.165978	4.70385e-11	2.91655e-21	5.00318e-05	3.28434e-10
90^o	0.0308949	0.0242211	4.00631e-11	2.82319e-21	1.09740e-05	1.55176e-11

Table 1. (m=mean, v=variance). The correct number of maxima were extracted. $||\nabla\mathcal{F}(d^{'})||$ gives a measure of the error in step 3, and $||\nabla\mathcal{F}(d)||$ gives a measure of the error in step 2. The error in step 3 is orders of magnitude smaller than the error in step 2. Our approach can be used to quantify the error in step 2 due to the truncation of SH series.

but randomly chosen maxima-directions, to compute the maxima directions and to compare the errors in steps 2 and 3. Since two maxima are extracted, for all the errors computed, such as $ang(d_i, d_i^{'})^o$, $||\nabla\mathcal{F}(d_i)||$, and $||\nabla\mathcal{F}(d_i^{'})||$ we keep the maximum of the two errors in each test (and remove the index i). The results are presented in Table-1.

In each of these tests we extract the correct number of maxima. We, however, notice that for a rank-4 SH estimation of the dirac spherical function, if we decrease the separation angle from 65^o, then the maxima were not prominently distinct any more, and we did come across cases when the number of estimated directions didn't match the number of ground truth directions. We suspect, therefore, that our approach can be also used to determine the angular resolution of a truncated SH series, depending upon the truncation length.

We also realise that the error in step 3: $||\nabla\mathcal{F}(d^{'})||$, is orders of magnitude smaller than the error in step 2: $||\nabla\mathcal{F}(d)||$. Again our approach can be useful in determining the goodness of fit of a truncated SH series to a set of scalars defined on a sphere.

3.2 ODF test In these tests we used the multi-tensor model [12] to generate DW signals, from where we estimate the ODF in the SH basis with rank-4.

We again construct one hundred test cases for both the one fiber and the two fiber simulations, and the ground truth directions are chosen randomly. The results are summarized in Table-2. Again in each of the tests we extract the correct number of maxima. We notice that the mean error in step 2 of the ODF tests: $||\nabla\mathcal{F}(d)||$ (Table-2), i.e. the ODF estimation in the truncated (rank-4) SH basis, entails an error that is orders of magnitude larger than the mean error in step 2 of the dirac tests: $||\nabla\mathcal{F}(d)||$ (Table-1). This can be explained by the fact that the ODF estimation is a much more complex process than a simple rank-4 SH fit. The error in the ODF estimation step is of course much larger than the error in step 3: $||\nabla\mathcal{F}(d^{'})||$ (Table-2), where we compute the maxima using the homogeneous polynomial representation. A graphical illustration of our approach from this test can be seen in Fig-3a.

We also tested our method on real data[20] and successfully extracted maxima from ODFs with various fiber configurations. We tested in a region of interest (ROI) of a coronal slice, where complex fiber structures are known to exist in

	$ang(d, d^{'})^o$		$\|\|\nabla\mathcal{F}(d^{'})\|\|$		$\|\|\nabla\mathcal{F}(d)\|\|$	
	m	v	m	v	m	v
1-Fib	0.0104625	4.22152e-05	2.07053e-11	1.49751e-21	0.000490269	9.16956e-08
2-Fib$_{90^o}$	0.0254106	3.85231e-05	5.5777e-11	1.7602e-21	0.0036013	2.4827e-06

Table 2. (m=mean, v=variance). The correct number of maxima were extracted from the ODF estimation. $||\nabla\mathcal{F}(d^{'})||$ gives a measure of the error in step 3, and $||\nabla\mathcal{F}(d)||$ gives a measure of the error in step 2 – the ODF estimation. The error in step 3 is orders of magnitude smaller than the error in step 2. Our approach can be used to quantify the error in the ODF estimation due to the truncation of SH series.

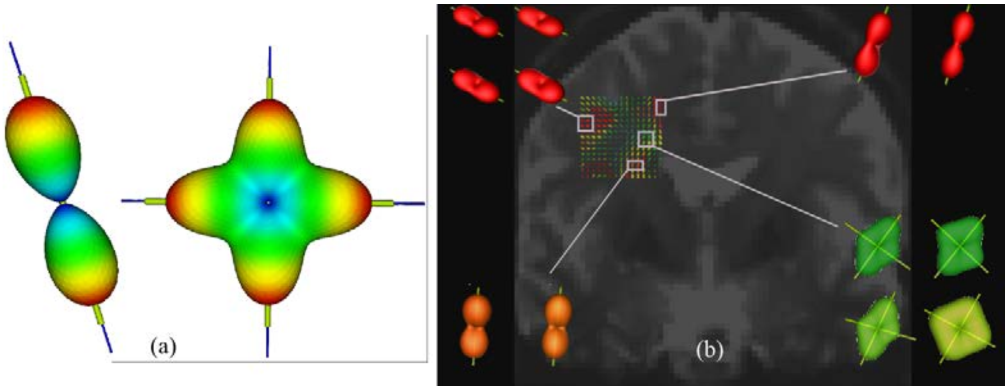

Fig. 3. Our approach applied to extract the maxima of an ODF in the SH basis with rank-4. **a)** We test on synthetic data, the dark blue lines are the ground truth directions. In the more prominent green are the computed directions. **b)** We test on a coronal slice of a real dataset within a region with complex fiber crossings. We see highlighted the fibers extracted by our method. We see that our approach can successfully extract the maxima of the ODF which are the fiber directions.

the white matter. The ROI contained fiber bundles from the cortico-spinal tract, superior longitudinal fibers (traversing the plane) and the corpus callosum (in the plane). The visual results can be viewed in Fig-3b.

Finally on the real dataset we compared our method against a discrete approach[6] which searches for the maxima on the discretized mesh of the ODF. For the discrete approach we used an icosahedron scheme on the sphere with tesselations of order 2, 3, 4, 5, 6 with 21, 81, 321, 1281, 5121 mesh-points respectively on a hemisphere. For the discrete method on each of these meshes and our approach, after extracting the maxima, we computed the error $||\nabla\mathcal{F}(d)||$ for each voxel and from there the mean and the variance. Figure-4 compares the mean error and the variance of the discrete approach on increasingly refined meshes to those of our method.

4 Discussion & Conclusion

We took advantage of the fact that an ASSF can be equivalently represented in any of three bijective bases – the SH basis, the ST basis constrained to the sphere, and the HP basis constrained to the sphere. This permitted us to extract the geometric characteristics, i.e. the maxima of an ASSF by computing the stationary points of a constrained homogeneous polynomial problem.

We tested this approach on synthetic tests, first on a purely mathematically generated dirac spherical function, and then on the ODF computed analytically in the SH basis. The ODF is a state-of-the-art reconstruction algorithm in diffusion MRI, who's maxima are aligned with the underlying dominant fiber bundles. Therefore, it is of utmost importance to be able to extract these maxima cor-

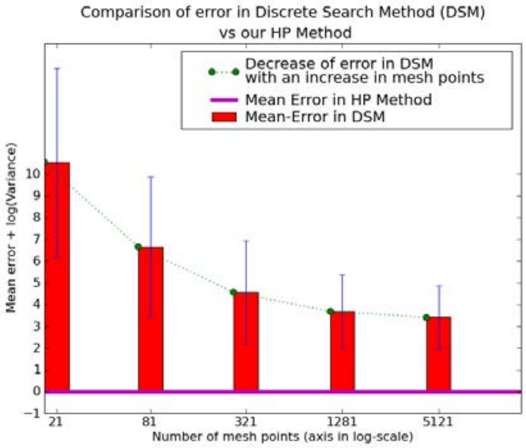

Fig. 4. Mean error ($||\nabla\mathcal{F}(d)||$: red bar) with ln of the variance (blue vertical intervals) of the discrete search method (DSM) plotted as a function of the mesh resolution, compared against our homogeneous polynomial (HP) method on a real dataset.

rectly. We took the ODF as an example, to concretely illustrate our method. But our method is independent of the ODF or of the ODF estimation process. It can be applied to any ASSF that can be written in either the SH basis, or the ST basis or the HP basis.

Our method has also the added strength of searching for the maxima of a continuous function, and is, therefore, not limited to searching for the maxima of an ASSF in a finite set of values on the sphere.

We tested our method with a rank-4 SH series, or equivalently order-4 ST, or equivalently a degree-4 HP. In the future we plan to test for greater values of rank/order/degree.

We also discovered that, using our polynomial approach, it was possible to quantify the error in the ODF estimation process that takes place due to the truncation of the SH basis to a finite rank. This interesting point could be further developed too.

References

1. Basser, P., Mattiello, J., LeBihan, D.: Estimation of the effective self-diffusion tensor from the NMR spin echo. Journal of Magnetic Resonance **B**(103) (1994) 247–254
2. Ozarslan, E., Mareci, T.: Generalized diffusion tensor imaging and analytical relationships between diffusion tensor imaging and high angular resolution imaging. Magnetic Resonance in Medicine **50** (2003) 955–965
3. Liu, C., Bammer, R., Acar, B., Moseley, M.E.: Characterizing non-gaussian diffusion by using generalized diffusion tensors. Magnetic Resonance in Medicine **51** (2004) 924–937

4. Barmpoutis, A., Jian, B., Vemuri, B.C.: Symmetric positive 4th order tensors & their estimation from diffusion weighted MRI. In: Information Processing in Medical Imaging (IPMI 2007). (2007)
5. Tuch, D.: Q-ball imaging. Magnetic Resonance in Medicine **52**(6) (2004) 1358–1372
6. Descoteaux, M., Angelino, E., Fitzgibbons, S., Deriche, R.: Regularized, fast, and robust analytical q-ball imaging. Magnetic Resonance in Medicine **58** (2007) 497–510
7. Alexander, D.C.: Maximum entropy spherical deconvolution for diffusion mri. In: Image Processing in Medical Imaging. (2005) 76–87
8. Comon, P., Mourrain, B., Lim, L., Golub, G.: Genericity and rank deficiency of high order symmetric tensors. Proc. IEEE Int. Conference on Acoustics, Speech, and Signal Processing (ICASSP) **31** (2006) 125–128
9. Comon, P.: Tensor decompositions. In McWhirter, J.G., Proudler, I.K., eds.: Mathematics in Signal Processing V. Clarendon Press, Oxford, UK (2002) 1–24
10. Frank, L.: Characterization of anisotropy in high angular resolution diffusion-weighted MRI. Magnetic Resonance in Medicine **47**(6) (2002) 1083–1099
11. Alexander, D., Barker, G., Arridge, S.: Detection and modeling of non-gaussian apparent diffusion coefficient profiles in human brain data. Magnetic Resonance in Medicine **48**(2) (2002) 331–340
12. Descoteaux, M., Angelino, E., Fitzgibbons, S., Deriche, R.: Apparent diffusion coefficients from high angular resolution diffusion imaging: Estimation and applications. Magnetic Resonance in Medicine **56** (2006) 395–410
13. Lasserre, J.: Global optimization with polynomials and the problem of moments. SIAM Journal on Optimization **11** (2001) 796–817
14. Karush, W.: Minima of functions of several variables with inequalities as side constraints. Master's thesis, Dept. of Mathematics, Univ. of Chicago, Chicago, Illinois (1939)
15. Mourrain, B., Pavone, J.P.: Subdivision methods for solving polynomial equations. Technical Report RR-5658, INRIA Sophia-Antipolis (2005)
16. Mourrain, B., Trébuchet, P.: Generalised normal forms and polynomial system solving. In Kauers, M., ed.: Proc. Intern. Symp. on Symbolic and Algebraic Computation, New-York, ACM Press. (2005) 253–260
17. Cox, D., Little, J., O'Shea, D.: Ideals, Varieties, and Algorithms: An Introduction to Computational Algebraic Geometry and Commutative Algebra. Undergraduate Texts in Mathematics. Springer Verlag, New York (1992)
18. Elkadi, M., Mourrain, B.: Introduction à la résolution des systèmes d'équations algébriques. Volume 59 of Mathématiques et Applications. Springer-Verlag (2007)
19. Hess, C., Mukherjee, P., Han, E., Xu, D., Vigneron, D.: Q-ball reconstruction of multimodal fiber orientations using the spherical harmonic basis. Magnetic Resonance in Medicine **56** (2006) 104–117
20. Anwander, A., Tittgemeyer, M., von Cramon, D.Y., Friederici, A.D., Knosche, T.R.: Connectivity-based parcellation of broca's area. Cerebral Cortex **17**(4) (2007) 816–825

A Simulation Environment for High Angular Resolution DTI

Gregory T. Balls[1] and Lawrence R. Frank[1,2,3]

[1] UCSD Center for Scientific Computation in Imaging
[2] UCSD Center for Functional MRI
[3] San Diego VA Healthcare System

Abstract. Simulations of diffusion in neural tissues have traditionally been limited to analytical solutions, to grid-based solvers, or to small-scale Monte Carlo simulations. None of these approaches has had the capability to simulate realistic complex neural tissues on the scale of even a single voxel of reasonable (i.e. clinical) size. An approach is described that combines a Monte Carlo Brownian dynamics simulator capable of simulating diffusion in arbitrarily complex polygonal geometries with a signal integrator flexible enough to handle a variety of pulse sequences. Taken together, this package provides a complete simulation environment for diffusion tensor MRI experiments. Results are shown for aligned fibers, varying packing density and permeability, and for crossing straight fibers.

1 Introduction

The sensitivity of MRI to the anisotropic diffusion of water within neural tissues provides some insight into the tissue structure. Spatial (diffusion tensor imaging, or DTI [1]) and spectral (q-space imaging [2]) variations of the diffusion weighted imaging (DWI) signal can be compared to the expected pulse signal response for simplified models of tissue structure. Analytical solutions are not available for structures with the complexity of real neural tissues, however. An alternative approach is to simulate the DWI experiment numerically, including diffusion, tissue effects, and the influence of the pulse sequence. Much work has already been done in this area, with simulations ranging from grid-based finite difference methods to smoothed particle hydrodynamics to Monte Carlo Brownian dynamics [3–8], but most simulations are limited to simplified geometries. For example, [3] is limited to diffusion within a sphere, [5] simulates the one dimensional problem between two plates, and [7] simulates random walks only in rectangular domains. Earlier related work by Frank and Rapp [9] modeled diffusion within tubes along splines, but could not model arbitrary geometries.

We have created a computational environment capable of simulating the entire DTI experiment by embedding MCell [10–12] , a sophisticated Monte Carlo simulator for cellular microphysiology, within an MRI simulator that tracks particle location, state, and signal amplitude and phase, and whose output is connected to a suite of analysis and visualization tools. The simulation environment is capable of modeling highly complex tissue structures, testing new pulse sequences, and developing new post-processing and analysis techniques. Here we demonstrate initial results testing the effects of fiber permeability and packing density on fractional anisotropy (FA).

2 Theory

2.1 Diffusion Weighted Imaging Simulation

For spins moving according to a time-dependent function $\mathbf{x}(t)$, the signal, S, generated by a standard spin echo or gradient echo sequence is given by the ensemble average of all the spins:

$$S = S_0 \left\langle e^{i\gamma \int_0^{\mathrm{TE}} a\mathbf{G}(t)\cdot\mathbf{x}(t)dt} \right\rangle . \tag{1}$$

In this equation S_0 is the echo amplitude in the absence of any gradient field; γ is the gyromagnetic ratio; a is $+1$ for gradient echo sequences while for spin echo sequences it is $+1$ before and -1 after the 180° RF pulse; $\mathbf{G}(t)$ is the applied diffusion weighting vector; and $\mathbf{x}(t)$ is the spin position.

By simulating the diffusion of N_p individual spins with MCell, we can calculate the integral in (1) numerically:

$$S = \frac{S_0}{N_p} \sum_{j=1}^{N_p} e^{i\gamma \sum_{i=0}^{N_t} a\mathbf{G}(t_i)\cdot\mathbf{x}_j(t_i)dt}, \tag{2}$$

where dt is the length of the time step used in the Monte Carlo simulation, N_t is the total number of time steps, and $\mathbf{G}$ and $\mathbf{x}$ are evaluated at each time step t_i.

The user interface to our simulation allows gradient directions which are defined by tessellating an icosahedron, as in [13]. Users may specify the tessellation level from 1 to 5 (12 to 2562 gradient directions). The methods within the simulator itself support arbitrary gradient directions. Our current implementation can model both gradient echo and spin echo pulse sequences. The user interface allows users to specify the diffusion time, $\mathit{\Delta}$, the gradient pulse duration, δ, and the gradient strength, G, as well as the gradient ramp time, t_r. The b-value is calculated automatically.

2.2 Simulating Diffusion by Monte Carlo Random Walk

Equation 2 allows us to calculate the signal given the diffusion gradient and spin locations. The spin locations are in turn computed by simulating particle diffusion. MCell [10–12] models diffusion of individual particles by a 3D Brownian-dynamics random walk. Time is discretized into time steps of length dt. The location of each diffusing particle is updated every time step by a random displacement vector (or ray). If the ray traced by the diffusing particle intersects a boundary, the particle is reflected.

For each type of diffusing molecule, random walk diffusion steps are scaled according to the associated diffusion coefficient, D. The fractional probability of finding a molecule between r and $r + dr$ at time t can be given as

$$p_r(r,t) = \frac{4\pi r^2 dr}{(4\pi Dt)^{3/2}} e^{-r^2/4Dt}, \tag{3}$$

or, when defined in terms of the dimensionless parameter $s = r/\sqrt{4Dt}$,

$$p_r(s) = \frac{4}{\sqrt{\pi}} s^2 e^{-s^2} ds. \tag{4}$$

MCell allows for much longer simulation time steps than simpler random walk algorithms using Cartesian lattices which require very small lattice sizes for accurate simulation of diffusion in the presence of small gaps and restrictions [11]. A look-up table containing a large number (1024 by default) of equally probable values of step length s is initialized using (4). MCell stores another look-up table of equally probable radial directions, constructed with symmetry properties necessary to avoid directional bias. For each simulated time step, dt, a step length and radial direction are chosen at random from these look-up tables. The diffusion step is scaled by the appropriate factor ($\sqrt{4Dt}$), and the ray describing the diffusing molecule's path for this time step is traced, reflecting elastically off any barriers in its path.

2.3 Tissue Generation

Geometry is represented by polygonal surfaces of arbitrary detail and complexity. A polygonal surface is defined, as in the MCell model description language, by listing the locations its vertices and the vertices for each face.

We model membrane permeability using MCell's support for chemical reactions. Diffusing particles that hit a surface may undergo a reaction (be transmitted) with a probability determined by the reaction rate for that particle and surface. Particles transported through a boundary continue on their original path; particles that are not transported reflect elastically off the boundary. The diffusion coefficient for a particle is updated as necessary when it is transmitted. We are thus able to create models with multiple diffusion coefficients, with, e.g. distinct diffusion coefficients for the axonal core, myelin sheathing, and extraaxonal (bath) fluid.

Users may design tissues using the bundle editor interface, shown in Fig. 1.A, which allows users to specify multiple fiber bundles according to fiber radius, bundle radius, and number of fibers per bundle. Each bundle may be curved along a spline.

Users may also generate simple bundles of straight, aligned fibers with a specified orientation and packing density. These bundles can be arranged with regular hexagonal packing as in Fig. 1.B, or regions can be filled with randomly placed fibers with sizes varying around a mean radius as in Fig. 1.C. For regular hexagonal packing, users specify the fiber radius and the center-to-center spacing between fibers. For randomly packed fiber bundles, users specify the mean fiber radius, the standard deviation of the the fiber radii, the desired filling fraction, and the maximum number of attempts to place a fiber. In addition to long, straight fibers, we can also fill surrounding and interstitial spaces with randomly placed and oriented ellipsoidal cells with axis lengths randomly distributed around a given mean, as in Fig. 3. The user again specifies the mean radius and standard deviation as well as the total voxel filling fraction.

2.4 Analysis and Visualization of Simulation Results

The simulation environment includes analysis tools for high angular resolution diffusion-weighted MRI [13] to compute the spherical harmonic decomposition (SHD) and quantities derived from it, such as the the q-ball orientation distribution function (ODF) [14] according to the method described by Anderson [15]. We have also developed a visualization package implemented with the Visualization Toolkit (VTK) [16]. The visualization package displays the fibers simulated, the computed signal, the SHD, and the ODF. Output from the simulation is also compatible with other analysis packages, such as AFNI [17], which can be used to calculate derived quantities such as fractional anisotropy (FA) and mean diffusion (MD).

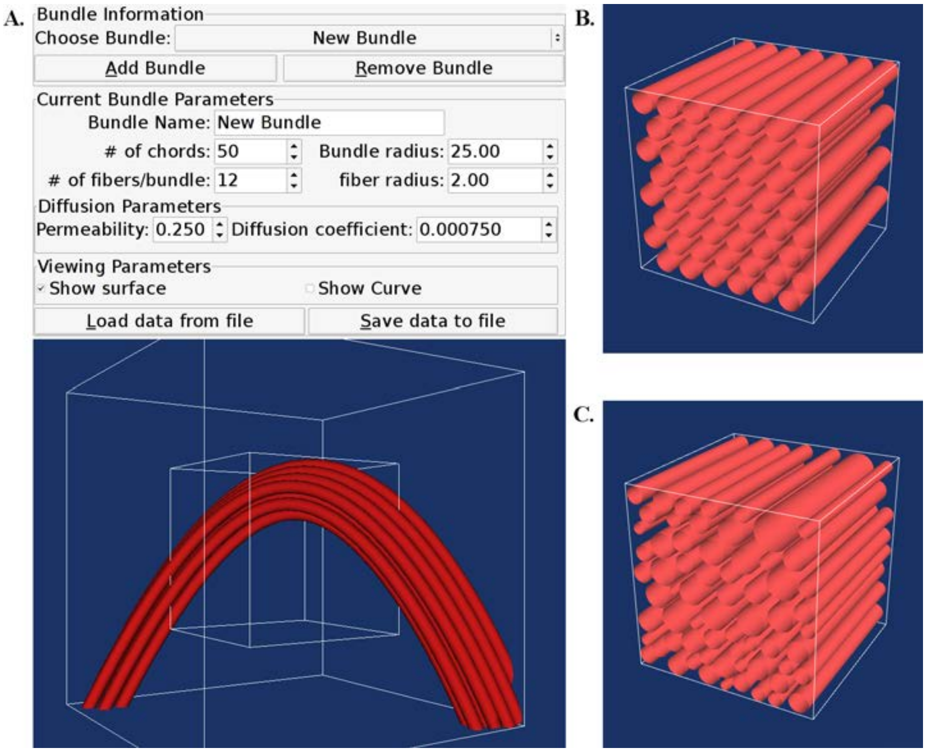

Bundle Information
Choose Bundle: New Bundle

Current Bundle Parameters
Bundle Name: New Bundle
# of chords: 50
Bundle radius: 25.00
# of fibers/bundle: 12
fiber radius: 2.00

Diffusion Parameters
Permeability: 0.250
Diffusion coefficient: 0.000750

Viewing Parameters
☑ Show surface
☐ Show Curve

Fig. 1. A. A snapshot of the bundle editor. A curved fiber bundle following a user designed spline crosses through the simulated volume (outer box) and measured voxel (inner box). B. A 200 μm^3 voxel filled with hexagonally packed fibers with a radius of 12 μm. Volume fraction filled is 0.54. C. A 200 μm^3 voxel filled with randomly packed fibers with a mean radius of 12 μm and a standard deviation of 2 μm. Volume fraction filled is 0.57.

3 Results

In order to demonstrate some of the features of our simulation environment, we have simulated diffusion experiments with straight hexagonally-packed cylindrical fibers. For all the results discussed here, we used the following parameters: $G = 4$ G/cm, $\Delta = 60$ ms, $\delta = 15.75$ ms, and $b = 2003\,\mathrm{s/mm}^2$. We chose to keep the diffusion coefficient uniform with $D = 0.75\,\mu\mathrm{m}^2/\mathrm{ms}$. We generated straight fibers with radii of 1.2 μm diameter. The signal was measured on a 100 μm^3 voxel centered in a 200 μm^3 simulated space, using 12 gradient directions oriented toward the vertices of a regular icosahedron. The motion of 4096 individual particles was simulated.

For our first simulation, we tested the sensitivity of permeability changes with fibers packed to a density of 80%. Fiber permeability was varied by varying the associated reaction rate on a logarithmic scale from $4.6 \times 10^{-9}\,\mathrm{M}^{-1}\mathrm{s}^{-1}$ to $2.2 \times 10^{-8}\,\mathrm{M}^{-1}\mathrm{s}^{-1}$. The calculated fractional anisotropy (FA) decreased as permeability increased, falling from a high of 0.65 for a reaction rate of $4.6 \times 10^{-9}\,\mathrm{M}^{-1}\mathrm{s}^{-1}$ to a low of 0.36 when the reaction rate was increased to $2.2 \times 10^{-8}\,\mathrm{M}^{-1}\mathrm{s}^{-1}$, as shown in Fig. 2.A.

Next, keeping the fiber permeability fixed with a reaction rate of $1.0 \times 10^{-9}\,\mathrm{M}^{-1}\mathrm{s}^{-1}$, the fiber density was varied from 50% to 90% (near the maximum for hexagonally packed cylinders). The calculated FA increased with increasing fiber density, from 0.51 to 0.65, as shown in Fig. 2.B.

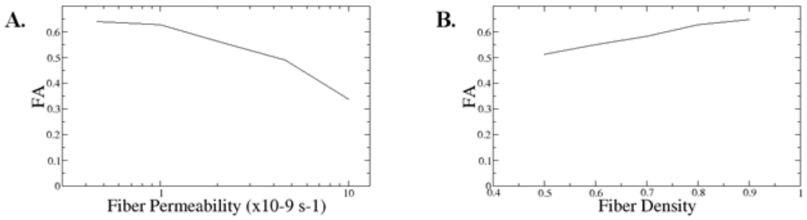

Fig. 2. A. FA as a function of the reaction rate defining fiber permeability. B. FA as a function of fiber density.

We simulated crossing fiber bundles, with fiber bundles placed perpendicular to one another and filling 80% of the voxel volume, with both bundles filling equal volume fractions of the voxel. The surrounding space was filled with randomly oriented ellipsoidal cells with an average diameter of $2.0\,\mu$m. Permeability of all the surfaces was kept fixed with a reaction rate set to $1.0 \times 10^{-9}\,\mathrm{M}^{-1}\mathrm{s}^{-1}$. The fibers and cells for this simulation are shown next to the resulting q-ball orientation distribution function (ODF) [14] in Fig. 3. The ODF was derived from the spherical harmonic decomposition [13] following the method described by Anderson [15].

4 Discussion

Our software allows researchers to simulate various MRI experiments (pulse sequences, gradient directions, b-values, etc.) and to understand better what features will can be detected before any MRI scans are even done. As a tool in experiment design, then, our software could be useful

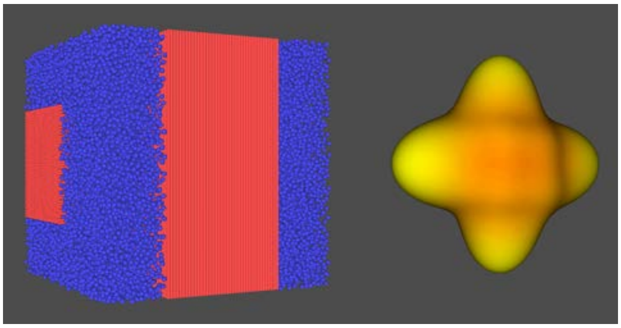

Fig. 3. Crossing packed fibers surrounded by randomly oriented ellipsoidal cells (left) and the resulting q-ball orientation distribution function (right).

in finding the most cost-effective MRI prescription capable of detecting changes of interest to a study.

The constructed geometry used in this initial demonstration is fairly simplistic, with straight, densely packed fibers, but the ability to vary packing density, fiber permeability, and both interior and exterior diffusion coefficients allows us to test a wide range of realistic models. The underlying support for complex geometries is quite flexible, and future work will include more realistic large scale models.

Our simulation environment is capable of modeling several structural sources of anisotropy in white matter, including variations in diffusion coefficients, particle concentrations, and membrane permeabilities. Beaulieu [18] provides a comprehensive revieiw of these sources of anisotropy and discusses several models of pathology that we believe are amenable to testing within our framework, such as demyelination and membrane degradation. In addition, other modes of water motion present in white matter, such as active transport due to molecular water pumps [19], should also be tractible with our simulation tools, and will be a focus of future work.

We are in the process of adding a more flexible model for pulse sequence specification to support other types of sequences (e.g. hyperecho sequences). We have also begun work on modeling the effects of T1 and T2 decay. Finally, we are extending the scale of possible models by using a parallelized version of MCell [10], allowing us to simulate much larger geometries.

References

1. Basser, P.J., Mattiello, J., LeBihan, D.: Estimation of the effective self-diffusion tensor from the NMR spin echo. J. Magn. Reson. **103** (1994) 247–254

2. Callaghan, P.: Principles of NMR Microscopy. Oxford (1993)
3. Kuchel, P.W., Lennon, A.J., Durrant, C.: Analytical solutions and simulations for spin echo measurements of diffusion of spins in a sphere with surface and bulk relaxation. J. Magn. Reson. B **112** (1996) 1–17
4. Stanisz, G.J., Wright, G.A., Henkelman, R.M., Szafer, A.: An analytical model of restricted diffusion in bovine optic nerve. Magnetic Resonance in Medicine **37** (1997) 103–111
5. Duh, A., Mohoric, A., Stepisnik, J.: Computer simulation of the spin echo spatial distribution in the case of restricted self diffusion. J. Magn. Reson. **148** (2001) 257–266
6. Meier, C., Dreher, W., Leibfritz, D.: Diffusion in compartmental systems. I. A comparison of an analytical model with simulations. Magnetic Resonance in Medicine **50** (2003) 500–509
7. Hall, M.G., Alexander, D.C.: Finite pulse widths improve fibre orientation estimates in diffusion tensor MRI. In: Proc. ISMRM 14th Scientific Meeting, Seattle, WA, International Society of Magnetic Resonance in Medicine (May 2006) 1076
8. Hwang, S.N., Chin, C.L., Wehrli, F.W., Hackney, D.B.: An image-based finite difference model for simulating restricted diffusion. Magnetic Resonance in Medicine **50**(2) (2003) 373–382
9. Frank, L.R., Rapp, J.L.: Smoothed particle hydrodynamic (SPH) simulation of diffusion in realistic neural tissue models. In: Proc. ISMRM 13th Scientific Meeting, Miami, FL, International Society of Magnetic Resonance in Medicine (May 2005) 839
10. Balls, G.T., Baden, S.B., Kispersky, T., Bartol, T.M., Sejnowski, T.J.: A large scale monte carlo simulator for cellular microphysiology. ipdps **01** (2004) 42a
11. Stiles, J.R., Bartol, T.M.: Monte carlo methods for simulating realistic synaptic microphysiology using mcell. In Schutter, E.D., ed.: Computational Neuroscience: Realistic Modeling for Experimentalists. CRC Press (2001) 87–127
12. Stiles, J.R., Van Helden, D., Bartol, T.M., Salpeter, E.E., Salpeter, M.M.: Miniature endplate current rise times $< 100\,\mu$s from improved dual recordings can be modeled with passive acetylcholine diffusion from a synaptic vesicle. Proceedings of the National Academy of Sciences of the United States of America **93** (1996) 5747–5752
13. Frank, L.: Characterization of anisotropy in high angular resolution diffusion weighted MRI. Magn Reson Med **47**(6) (June 2002) 1083–1099
14. Tuch, D.S., Reese, T.G., Wiegell, M.R., Wedeen, V.J.: Diffusion MRI of complex neural architecture. Neuron **40** (2003) 885–895
15. Anderson, A.W.: Measurement of fiber orientation distributions using high angular resolution diffusion imaging. Magnetic Resonance in Medicine **54** (2005) 1194–1206
16. Schroeder, W., Martin, K., Lorensen, B.: Visualization Toolkit: An Object-Oriented Approach to 3D Graphics. 4th edn. Kitware, Inc. (2006)
17. Cox, R.W.: AFNI: Software for analysis and visualization of functional magnetic resonance neuroimages. Computers and Biomedical Research **29** (1996) 162–173
18. Beaulieu, C.: The basis of anisotropic water diffusion in the nervous system - a technical review. NMR in Biomedicine **15** (2002) 435–455
19. Baslow, M.: Evidence supporting a role for N-acetyle-L-aspartate as a molecular water pump in myelinated neuon in the central nervous system: An analytical review. Neurochemistry International **40** (2002) 295–300

Tensor Interpolation by Concise Local Estimation of Anisotropy and Rotation

Bennett A. Landman[1], Pierre-Louis Bazin[2], and Jerry L. Prince[3]

Biomedical Engineering[1]; Radiology[2]; Electrical and Computer Engineering[3],
Johns Hopkins University, Baltimore, MD, USA, `landman@jhu.edu`. *

Abstract. In diffusion tensor imaging, tensors represent the oriented probability of intra-voxel water diffusion. These positive definite, symmetric matrices form a non-Euclidean space which poses challenges for interpolation and analysis. In particular, most tensor interpolation schemes have a non-linear effect on the clinically important tensor attributes of fractional anisotropy and mean diffusivity, resulting in tensor "swelling." We propose a new interpolation method that explicitly preserves user-specified interpolation of fractional anisotropy and mean diffusivity, while independently interpolating diffusion directions. The approach leads to an efficient technique that is practical for routine use.

1 Introduction

Diffusion tensor imaging (DTI) is widely used to characterize the structure and connectivity of white matter in health and disease [1]. In this context, tensors represent 3-D diffusion processes on a voxel-wise basis. DTI has been largely analyzed in medical studies in terms of the derived contrasts of anisotropy and diffusivity which have been shown to be sensitive to specific clinical findings. Mean diffusivity (average of the tensor eigenvalues) is acutely sensitive to edema in stroke, and anisotropy and orientation are essential for establishing local and global connectivity with fiber tracking [2, 3].

Previous investigations on tensor interpolation have focused on establishing metric spaces in which shortest paths lead to monotonic interpolation of important tensor contrasts. Positive definite tensors have been described as elements of a Riemannian manifold with an affine invariant metric [4–7]. Arsigny et al. [8] proposed the Log-Euclidean framework as a computationally efficient close approximation. Rohlfing et al. [9] derived a biophysically motivated approach based on Kullback-Leibler divergence. These approaches guarantee monotonic interpolation of tensor determinants, but not necessarily of anisotropy and diffusivity. Recently, Kindlmann et al. [10] proposed the geodesic-loxodrome framework in which shortest paths are determined with respect to orthogonal tensor invariants. This method ensures monotonic interpolation of diffusivity, anisotropy, and determinant. Furthermore, tensor directions are interpolated as rotation matrices. Despite its desirable mathematical properties, this approach is severely limited

---

* This project was supported by NIH/NINDS 1R01NS056307.

in practice by computational complexity, and extension from pairwise processing to 2-D or 3-D interpolation also appears to be a challenging obstacle. In this work, we present a novel closed-form tensor interpolation method, Concise Local Estimation of Anisotropy and Rotation (CLEAR), based on the requirement of preserving specific interpolation of the clinically significant tensor properties of fractional anisotropy (FA), mean diffusivity (MD), and determinant.

The strategy of CLEAR is to first interpolate the tensor contrasts—MD, FA, and determinant—and then determine a tensor that possesses these interpolated contrasts and whose eigenvectors represent an appropriate directional interpolation of the source tensor eigenvectors. In the following, we establish an exact, one-to-one correspondence between the tensor eigenvalues and the derived contrasts (MD, FA, determinant). With this result, we can interpolate monotonically the contrasts using any linear or nonlinear image interpolation method and recover the underlying tensor characteristics. The tensor orientations are interpolated separately. This approach leads to a computationally efficient procedure where tensor swelling is avoided and the regularity of derived clinical quantities is preserved.

2 Methods

In DTI, tensors (symmetric 3×3 matrices) represent 3-D Gaussian diffusion processes. A tensor, $\mathbf{D}$, may be diagonalized into eigenvectors ($\boldsymbol{v_1}$,$\boldsymbol{v_2}$,$\boldsymbol{v_3}$) and eigenvalues (λ_1,λ_2,λ_3), where the eigenvalues represent the diffusivity in each of the eigenvector directions. The diffusion process has been commonly investigated through scalar contrasts based on the eigenvalues, mainly mean diffusivity ($\mathrm{MD} = \frac{1}{3}(\lambda_1 + \lambda_2 + \lambda_3) = \frac{1}{3}\mathrm{tr}\mathbf{D}$) and fractional anisotropy ($\mathrm{FA} = \sqrt{\frac{3}{2}\frac{(\lambda_1 - \mathrm{MD})^2 + (\lambda_2 - \mathrm{MD})^2 + (\lambda_3 - \mathrm{MD})^2}{\lambda_1{}^2 + \lambda_2{}^2 + \lambda_3{}^2}}$). To represent a valid physical diffusion process, the tensor must have positive eigenvalues, and thus interpolation methods have to ensure they interpolate the determinant $|\mathbf{D}|$ monotonically. The orientation of the principal eigenvector, $\boldsymbol{v_1}$, (we assume $\lambda_1 \geq \lambda_2 \geq \lambda_3 > 0$) is also used to study local connectivity and reconstruct global fiber tracts.

Because of the importance of these tensor contrasts in situations where tensor interpolation is required—e.g., for atlas registration, data resampling, and fiber tracking—it is sensible to generate a linear or monotonic interpolation of the tensor contrasts rather than to interpolate the tensor matrix coefficients themselves. Assuming that the contrasts are each independently interpolated, we show here that the tensor associated with these contrasts can be (almost uniquely) determined. First, we show that there exists an exact, closed-form relation giving the tensor eigenvalues as a function of the target contrasts FA, tr$\mathbf{D}$, and $|\mathbf{D}|$. We have the following relations with the unknown eigenvalues:

$$\begin{aligned} |\mathbf{D}| &= \lambda_1\lambda_2\lambda_3 &&= a \\ \frac{\mathrm{tr}\mathbf{D}}{3} &= \tfrac{1}{3}(\lambda_1 + \lambda_2 + \lambda_3) &&= b \\ \frac{2}{3}\mathrm{FA}^2 &= \tfrac{(\lambda_1 - b)^2 + (\lambda_2 - b)^2 + (\lambda_3 - b)^2}{\lambda_1{}^2 + \lambda_2{}^2 + \lambda_3{}^2} &&= c \end{aligned} \tag{1}$$

This gives a nonlinear system of three equations with three unknowns that we would like to solve for λ_1, λ_2, and λ_3. We define the following complex-valued intermediate variables:

$$\begin{aligned}
\alpha &= (c-1)[b^3(2-5c)+2a(c-1)] \\
\beta &= (\alpha+\sqrt{\alpha^2+2b^6c^3})^{\frac{1}{3}} \\
\gamma &= b-2^{-\frac{1}{3}}\tfrac{b^2c}{\beta}+2^{-\frac{2}{3}}\tfrac{\beta}{c-1} \\
\delta &= \sqrt{9b^2+b^2\tfrac{12-18c}{c-1}+6b\gamma-3\gamma^2}
\end{aligned} \tag{2}$$

Algebraic manipulations of (1) and (2) yield:

$$\lambda_1 = \gamma \qquad \lambda_2 = \frac{1}{2}(3b-\gamma+\delta) \qquad \lambda_3 = \frac{1}{2}(3b-\gamma-\delta) \tag{3}$$

Eq. 3 is unique up to eigenvalue permutation and exists for all combinations of non-negative eigenvalues except when all three eigenvalues are equal. In that limit case, FA is zero and either the trace or determinant determine all three eigenvalues. While Eq. 3 identifies the eigenvalues that correspond to a particular set of target contrasts, it is possible that the interpolation kernel will result in a valid set of contrasts (i.e., FA $\in [0,1]$, tr$\mathbf{D} > 0$, and $|\mathbf{D}| > 0$) for which the corresponding eigenvalues are complex or negative. To ensure a physically plausible interpolation in this case, we project the eigenvalues into the domain of positive reals while minimizing the following mismatch energy term:

$$E=\left(\frac{\mathrm{FA}-\sqrt{\frac{3}{2}\frac{(\lambda_1-\mathrm{MD})^2+(\lambda_2-\mathrm{MD})^2+(\lambda_3-\mathrm{MD})^2}{\lambda_1{}^2+\lambda_2{}^2+\lambda_3{}^2}}}{\mathrm{FA}}\right)^2+\left(\frac{\mathrm{tr}\mathbf{D}-(\lambda_1+\lambda_2+\lambda_3)}{\mathrm{tr}\mathbf{D}}\right)^2+\left(\frac{|\mathbf{D}|-\lambda_1\lambda_2\lambda_3}{|\mathbf{D}|}\right)^2 \tag{4}$$

Minimization was achieved through Nedler-Mead simplex search. Projection was typically required when interpolating between rather isotropic tensors. To our knowledge, this is the first time that these formulae have been derived.

Now that we have a direct relation from contrasts to eigenvalues, we can perform a three-step interpolation procedure where we first interpolate the contrasts, recover the corresponding eigenvalues, and finally interpolate the tensor directions independently. Consider a set of N tensors, $\mathbf{D}_1$,...,$\mathbf{D}_N$ and a set of weights, w_1,...,w_N, with $\sum_1^N w_i = 1$. For the interpolation examples presented herein, the weights are chosen based on a trilinear interpolation kernel that uses the eight nearest neighbors (in 3-D). Nonlinear kernels, such as sinc or data adaptive interpolation (cf. [11]) could be substituted easily if deemed necessary.

We start by identifying the tensor contrasts for each voxel, i.e., FA_1,...,FA_N, tr$\mathbf{D}_1$,...,tr$\mathbf{D}_N$, and $|\mathbf{D}_1|$,...,$|\mathbf{D}_N|$. We interpolate each scalar contrast as follows:

$$\widehat{|\mathbf{D}|} = \exp\sum_{i=1}^{N} w_i \log|\mathbf{D}_i| \qquad \widehat{\mathrm{tr}\mathbf{D}} = \sum_{i=1}^{N} w_i \mathrm{tr}\mathbf{D}_i \qquad \widehat{\mathrm{FA}} = \sum_{i=1}^{N} w_i \mathrm{FA}_i \tag{5}$$

Here, FA and trace are linearly combined while the determinant is logarithmically combined (in analogy with the Log-Euclidean method). We then recover $\widehat{\lambda_1}, \widehat{\lambda_2}, \widehat{\lambda_3}$ using Eq. 3.

To completely specify the interpolated tensor, we must define its eigenvectors. Eigenvector matrices are orthonormal matrices, yet, diffusion eigenvectors are determined only up to a sign change because the diffusion process is symmetric. There are eight possible orthonormal matrices that explain the same physical diffusion process. Which eigenvector matrix is estimated for any particular set of observations is an artifact of the tensor estimation method, not a property of the physical system. Thus, averaging in rotation space as proposed in [12] would lead to different results based on the arbitrary choice of vector orientations. Instead, we use a simple iterative algorithm that minimizes the angular distance between the weighted mean vector and either each eigenvector or its reflection:

```
$\widehat{\boldsymbol{v}} \leftarrow \frac{\sum_{i=1}^{N} w_i v_i}{||\sum_{i=1}^{N} w_i v_{1,i}||}$    Normalize weighted mean coordinates.
while($\exists\, \boldsymbol{v}_i \cdot \widehat{\boldsymbol{v}} < 0$)    Iterate while any vectors are misoriented.
    $\forall\, \boldsymbol{v}_i \cdot \widehat{\boldsymbol{v}} < 0 : \boldsymbol{v}_i \leftarrow -\boldsymbol{v}_i$    Orient all vectors toward the weighted mean.
    $\widehat{\boldsymbol{v}} \leftarrow \frac{\sum_{i=1}^{N} w_i v_i}{||\sum_{i=1}^{N} w_i v_{1,i}||}$    Recompute weighted mean.
```

If the initial mean vector is zero, a random non-zero initialization is used. As the total angular distance between the putative weighted mean and the set of eigenvectors is bounded and strictly decreasing at each step, the algorithm will converge. In practice, convergence is rapid and typically within $N/2$ steps. Note that there are ambiguous configurations in regions where the interpolated directions are covering the entire angular domain, e.g. when interpolating two orthogonal directions or N coplanar directions separated by an angle of $\frac{\pi}{N}$. These configurations are intrinsic to the problem, but can be detected by measuring the angular variation between the eigenvectors and their mean. In practice, this problem will arise in areas with mostly isotropic or very noisy tensors, both cases where the actual main diffusion direction is likely to be unknown or irrelevant.

To obtain three orthonormal mean eigenvectors, we consider first the set of principal eigenvectors, $\boldsymbol{v}_{1,1}$,...,$\boldsymbol{v}_{1,N}$, which encode the main direction of diffusion. Using the method above, we identify the weighted mean principal eigenvector, $\widehat{\boldsymbol{v}_1}$. We then rotate each tensor around the axis formed by $\widehat{\boldsymbol{v}_1}$ and the respective $\boldsymbol{v}_{1,i}$ by the minimum angle such that $\boldsymbol{v}_{1,i}$ is aligned with the $\widehat{\boldsymbol{v}_1}$. Using the set of rotated tensors, we compute the weighted mean secondary eigenvector, $\widehat{\boldsymbol{v}_2}$, which must lie in the plane orthogonal to $\widehat{\boldsymbol{v}_1}$. The tertiary eigenvector is computed as the cross product of the weighted mean primary and secondary eigenvectors.

3 Experiments

Synthetic Data. Four prolate (i.e. with $\lambda_2 = \lambda_3$) tensors were placed at the corners of a grid and interpolated with linear (Euclidean), Log-Euclidean, and CLEAR interpolation. The interpolated tensor at each spatial location within the grid was determined with tensor averaging using four bilinear weights (see Fig. 1). Unlike the linear and Log-Euclidean methods, CLEAR interpolates the path between rotated tensors as a series of rotated tensors. There is no "squashing" effect on FA as can be appreciated by the blue areas indicating non-monotonic changes (Row D). CLEAR avoids the tensor "swelling" effect

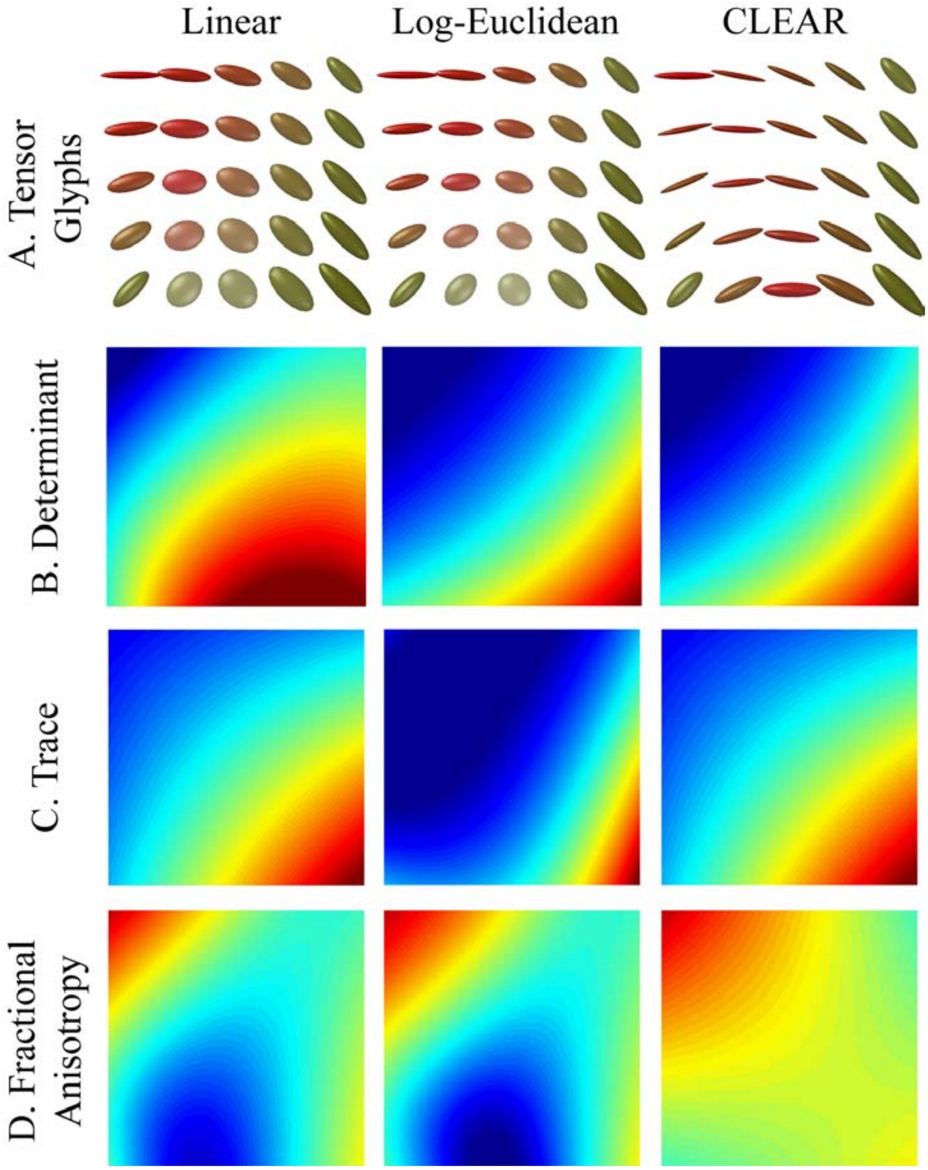

Fig. 1. Interpolation of simulated tensor fields. Results for linear (left), Log-Euclidean (center), and CLEAR (right) tensor interpolation methods are shown. Row A: Four 3-D prolate tensors located on the corners were bilinear interpolated. Rows B-D: Image intensities are proportional to the contrast indicated at left for the four corner tensors interpolated to a 100x100 grid. Log-Euclidean and CLEAR result in logarithmic determinant interpolation (Row B), while linear and CLEAR result in bilinear trace interpolation (Row C). Linear and Log-Euclidean result in non-monotonic decreases in FA, while CLEAR results in bilinear FA interpolation (Row D).

on the determinant as seen with linear interpolation (Row B) and non-linear changes in trace as with Log-Euclidean (Row C).

In Vivo Data. A representative region of interest from an axial slice of a diffusion tensor field was selected from a study of a young, healthy control. A multi-slice, single-shot EPI sequence achieved whole brain coverage (2.2 mm isotropic nominal resolution, k-space interpolated to 0.828 mm, three repetitions). Each sequence used 30 diffusion encoding directions (b-value of 700 s/mm^2) and five, averaged minimally weighted volumes on a 3T MR scanner (Intera, Philips Medical Systems, The Netherlands). Tensor estimation was performed offline with a custom, non-negative tensor estimator [13]. The reconstructed tensor field was upsampled by 4×4 with linear, Log-Euclidean, and CLEAR interpolation.

As an illustrative example, we demonstrate the benefits and pitfalls of the three interpolation techniques by examining an in vivo region of high curvature (Fig. 3). A quantitative comparison between the observed tensors (A-D) and each of the interpolated fields (E-M) is not straightforward, as different norms on tensor differences will favor different methods. Visually, the CLEAR method results in the smoothest interpolation over the field. The linear method results in abrupt changes in determinant (G). The Log-Euclidean results in block-like structure in the anisotropy of the longitudinal fasciculus (H). CLEAR provides a smooth interpolation of orientation (K), anisotropy (K), and diffusivity (L,M). The eigenvalue projection step (Eq. 4) was necessary in the gray matter and along the ventricular interface (Fig. 2). In regions where projection was necessary, contrasts were altered by a median of 0.05% (95$^{\text{th}}$ percentile=1.41%).

Performance. A prototype implementation of the proposed algorithm in Java on a 1.6 GHz Intel CPU run in 10 μs for arbitrary trilinear interpolation between eight tensors. The majority of time in the prototype is spent on matrix manipulation, which could be optimized. The eigenvalue determination described in (3) runs in 2.5 μs, while the weighted mean vector computation runs in 1.3 μs.

4 Discussion

This paper demonstrates that one can interpolate tensors by independently interpolating quantities of clinical and scientific interest–eigenvalue contrasts (FA, MD, and determinant) and eigenvectors. This work is the first to derive explicit formulae for computing eigenvalues from determinant, trace, and FA. The proposed interpolation method, CLEAR, preserves the intuitive behavior of contrasts and orientation. In simulations and in vivo, the results are visually intuitive and appealing. Regions of directional uncertainty are mostly located in the CSF, where the diffusion information is not clinically relevant. These singularities are the price to pay for separating eigenvector and eigenvalue interpolation, and the ultimate application or clinical goal will dictate if these few singularities are acceptable in exchange for a well controlled interpolation of the eigenvalues and preservation of the tensor main direction. One could also mitigate the issue by applying anisotropic filtering to the interpolation process [11]. Alternatively, the interpolation method could include a penalty term that balances modification of eigenvalues against angular rotation uncertainties.

References

1. Basser, P.J., Jones, D.K.: Diffusion-tensor MRI: theory, experimental design and data analysis - a technical review. NMR Biomed **15**(7-8) (2002) 456–67
2. Mori, S., van Zijl, P.C.: Fiber tracking: principles and strategies - a technical review. NMR Biomed **15**(7-8) (2002) 468–80
3. Le Bihan, D., Mangin, J.F., Poupon, C., Clark, C.A., Pappata, S., Molko, N., Chabriat, H.: Diffusion tensor imaging: concepts and applications. J Magn Reson Imaging **13**(4) (2001) 534–46
4. Fletcher, P.T., Joshi, S.: Riemannian geometry for the statistical analysis of diffusion tensor data. Signal Processing **87** (2007) 250–262
5. Pennec, X., Fillard, P., Ayache, N.: A riemannian framework for tensor computing. Int J Comp Vis **66**(1) (2006) 41–66
6. Batchelor, P.G., Moakher, M., Atkinson, D., Calamante, F., Connelly, A.: A rigorous framework for diffusion tensor calculus. Magn Reson Med **53**(1) (2005) 221–5
7. Lenglet, C., Rousson, M., Deriche, R., Faugeras, O.: Statistics on the manifold of multivariate normal distributions: Theory and application to diffusion tensor MRI processing. J Math Imaging Vis **25** (2006) 423–444
8. Arsigny, V., Fillard, P., Pennec, X., Ayache, N.: Log-Euclidean metrics for fast and simple calculus on diffusion tensors. Magn Reson Med **56**(2) (2006) 411–21
9. Rohlfing, T., Sullivan, E.V., Pfefferbaum, A.: Divergence-based framework for diffusion tensor clustering, interpolation, and regularization. In: IPMI. (2007) 507518
10. Kindlmann, G., Estepar, R.S.J., Niethammer, M., Haker, S., Westin, C.F.: Geodesic-loxodromes for diffusion tensor interpolation and difference measurement. In: MICCAI. Volume 4791. (2007) 1–9
11. Castaño Moraga, C.A., Rodriguez-Florido, M.A., Alvarez, L., Westin, C.F., Ruiz-Alzola, J.: Anisotropic interpolation of DT-MRI. In: MICCAI. (2004) 343–350
12. Maher, M.: Means and averaging in the group of rotations. SIAM J. Matrix Anal. Appl. **24**(1) (2002) 1–16
13. Landman, B., Bazin, P.L., Prince, J.L.: Diffusion tensor estimation by maximizing rician likelihood. In: International Conference on Computer Vision, Workshop on Mathematical Methods in Biomedical Image Analysis, Rio de Janeiro (2007)

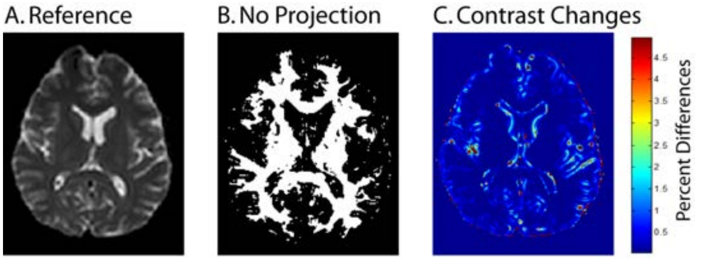

Fig. 2. Projection of non-physical solutions. The anatomic reference (A) shows that projection was not required in major white matter regions (B). In regions where projection was necessary (C), the percentage change in contrasts was small.

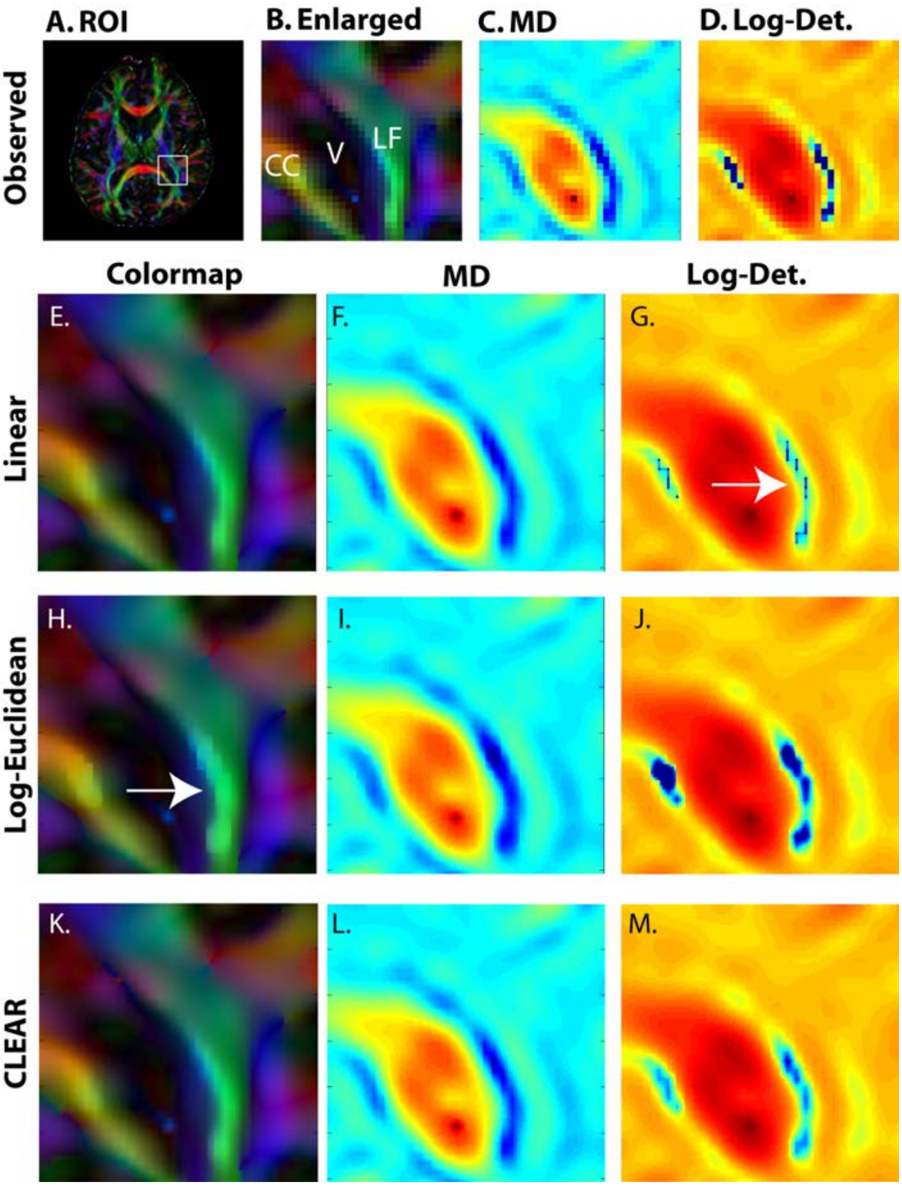

Fig. 3. Interpolation of the genu of the Corpus Callosum (CC) and longitudinal fasciculus (LF) near the lateral ventricle (V): region of interest (ROI) selected on an orientation color coded anisotropy map (A,B). MD (C) and log-determinant (D) are shown at the reconstructed resolution. Upsampled (4×4) and interpolated contrasts are shown for linear (E-G), Log-Euclidean (H-J), and CLEAR (K-M) tensor interpolation. While the linear interpolation has smooth FA and MD (E,F), it exhibits abrupt changes in the determinant (G). The Log-Euclidean interpolation exhibits FA artifacts in regions of high anisotropy and curvature (H). CLEAR avoids all these problems.

Tubular Fiber Bundle Segmentation for Diffusion Weighted Imaging

M. Niethammer[1,2], C. Zach[1], J. Melonakos[3], and A. Tannenbaum[3,4]

[1] Department of Computer Science
[2] Biomedical Research Imaging Center, School of Medicine
University of North Carolina, Chapel Hill, NC, USA
[3] School of Electrical and Computer Engineering
[4] School of Biomedical Engineering
Georgia Institute of Technology, Atlanta, GA, USA

Abstract. This paper proposes a methodology to segment tubular fiber bundles from diffusion weighted magnetic resonance images (DW-MRI). Segmentation is simplified by locally reorienting diffusion information based on large-scale fiber bundle geometry. Segmentation is achieved through simple global statistical modeling of diffusion orientation. Utilizing a modification of a recent segmentation approach by Bresson et al. [19] allows for a convex optimization formulation of the segmentation problem, combining orientation statistics and spatial regularization. The approach compares favorably with segmentation by full-brain streamline tractography.

1 Introduction

Diffusion weighted (DW) magnetic resonance imaging (MRI) allows for in-vivo measurements of water diffusion in tissues such as the human brain. While brain white matter appears uniform in structural MRI, DW-MRI measurements can provide estimates of macroscopic fiber bundle direction as well as indicate changes in tissue properties. However, the relation between DW-MRI signal and white matter ultra-structure is only known partially. For example, how axonal organization and geometry relates to a measured diffusion profile in general remains an open question. Fiber bundle direction correlates with the major diffusion direction in fiber bundle areas comprised of large numbers of approximately unidirectional axons [1]. This allows for the estimation of distinct fiber bundles from DW-MRI measurements.

A variety of approaches to extract white matter bundles from diffusion weighted images exist. They may be classified into streamline-based approaches and voxel-based approaches. The streamline-based approaches utilize streamline tractography to come up with bundle segmentations. This can for example be direct voxelization of the streamlines, voxelization preceded by streamline clustering [21], or stochastic tractography [16, 11]. Voxel-based approaches aim at extracting white matter bundles directly from the voxel data without using streamline tractography. Approaches include voxel-based clustering [18], surface-evolution using global statistics [6, 23] or local similarity terms [10], optimal connectivity methods [17], region-growing [9], hidden Markov measure fields [15] and fuzzy segmentation [14].

This paper proposes a segmentation approach based on reorienting the diffusion measurements. Reorientation information is derived from large-scale fiber bundle geometry; it facilitates region-based fiber bundle segmentation with global statistics. The approach is computationally efficient, is simple, allows for reliable optimization, and is robust to local noise effects.

Briefly summarizing the remainder of this paper, in Sec. 2, we give an overview of the system. Sec. 3 introduces the *local* coordinate system used for the reorientation of diffusion information. Sec. 4 describes how to extend the local coordinate system to the complete image volume. The reorientation of diffusion data is described in Sec. 5. Sec. 6 and 7 describe the statistical modeling of fiber bundle direction and its use for bundle segmentation respectively. Results are given in Sec. 8. Sec. 9 concludes the paper with a discussion of the approach, and an outlook on possible future work.

2 System Overview

This section summarizes the key steps in the proposed segmentation approach. The overall goal of the method is to be able to segment tubular fiber bundles from diffusion weighted images. Segmentation requires a suitable similarity measure for voxel grouping into object foreground and object background. While a multitude of segmentation methods for diffusion weighted images exists (see Sec. 1) arguably the methods used in practice are based on streamlining: direct voxelization of streamlining results, clustering of streamlines, or stochastic tractography. This is surprising, because (i) streamlining approaches are sensitive to noise and (ii) volumetric segmentation algorithms developed outside the area of diffusion weighted imaging have either not been applied to DW-MRI or only with limited success. A major impediment to adopting existing volumetric segmentation approaches for DWI segmentation is the nature of DWI data. DWI data is (i) vector-valued (tensor-valued if diffusion tensors are computed), is (ii) axial (identifying antipodal directions), typically has (iii) low signal to noise ratio and is of relatively low resolution, and is (iv) spatially non-stationary (i.e., large scale orientation changes are expected to occur within individual fiber bundles).

Fig. 1 illustrates diffusion tensors changing direction along a fiber bundle and the same set of diffusion tensors when realigned relative to a representative fiber tract. This realignment process is at the core of the approach proposed in this paper. Realignment simplifies the original problem by making it spatially stationary. Segmentation methods for vector-valued images can then be employed for fiber bundle segmentation. Note that standard streamline tractography usually incorporates a weak, implicit form of spatial realignment by disallowing orientation changes considered too drastic.

The proposed approach is:

1) For every candidate point in the image volume, find the *closest* point on the representative fiber tract.

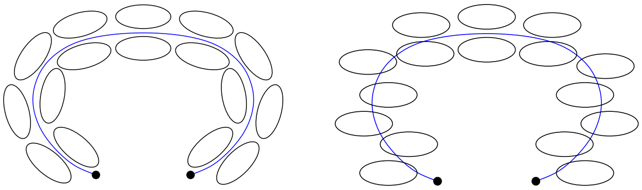

(a) Original fiber bundle. (b) Realigned fiber bundle.

Fig. 1. Tensor reorientation concept. The spatially varying tensor orientation can largely be removed by reorientation with respect to a representative fiber tract (blue).

2) Regard the candidate point as part of the fiber bundle if its diffusion information is *similar* to the diffusion information at the closest point.
3) Create a *spatially consistent* segmentation based on the similarities of 2).

The key questions are, what is meant by "closest," "similar," and "spatially consistent." The direct approach to measure closeness is to look at Euclidean distance. Euclidean distance typically does not yield unique point to point correspondences. Sec. 4 thus proposes a method based on frame diffusion. Since the focus of this paper is the segmentation of tubular fiber bundles, the overall fiber bundle geometry can be approximately described by the space curve given by a representative fiber tract. The (regularized) Frenet frame of the space curve can then be used as a local coordinate frame and as the basis for frame diffusion; see Sec. 3.

Many probabilistic and deterministic similarity measures have been proposed for diffusion weighted imaging (in particular, for diffusion tensor imaging; see for example [6, 10]). One of the simplest measures of diffusion similarity is to measure angular deviations of the major directions of diffusion. This is in line with streamline tractography which typically uses only the principal diffusion direction for streamline propagation[5] and will be used in a probabilistic formulation in this paper as discussed in Sec. 6. To achieve spatial consistency, which cannot be achieved by local segmentation decisions based on directional statistics and reorientation of diffusion measurements alone, regularization is necessary. Sec. 7 describes the proposed segmentation approach based on a slight modification of the convex optimization formulation by Bresson et al. [19].

3 The Regularized Axial Frenet Frame

To parameterize tubular fiber bundles, a suitable coordinate system is necessary. For space-curves, the Frenet frame can be used. Given a parameterized curve $\mathcal{C}(p) : [0,1] \mapsto \mathbb{R}^3$, such that $\mathcal{C}_{ss} \neq 0$, $\mathcal{C}_s \neq 0$ (i.e., without singular points of order 0 and 1 [4]) the Frenet frame is given by

$$\mathcal{T}_s = \kappa\mathcal{N}, \quad \mathcal{N}_s = -\kappa\mathcal{T} - \tau\mathcal{B}, \quad \mathcal{B}_s = \tau\mathcal{N}, \quad \frac{\partial}{\partial s} = \frac{1}{\|\mathcal{C}_p\|}\frac{\partial}{\partial p}.$$

---

[5] Tensor derived measures other than principal diffusion direction are typically only used as tract termination criteria.

$\mathcal{T} = \frac{\mathcal{C}_p}{\|\mathcal{C}_p\|}$ is the unit tangent vector, $\mathcal{N}$ and $\mathcal{B}$ are the normal and the binormal, κ and τ denote curvature and torsion respectively, and s denotes arc-length. See Fig. 2 for a depiction of the Frenet frame. Computing $\mathcal{T}$ from $\mathcal{C}$ is immediate. Computing $\mathcal{N}$ yields $\mathcal{B} = \mathcal{T} \times \mathcal{N}$ and thus the desired local coordinate frame.

In this paper the space curve is given by a representative fiber tract. For the experiments of Sec. 8 streamline tractography was used to compute the representative fiber. For a more robust approach, streamlining should be replaced by an optimal path method [8]. In what follows, a known representative fiber tract is assumed.

Since the Frenet frame is based on differential properties of the space curve it is sensitive to noise. Instead of using the Frenet frame directly, the frame diffusion is instead based on a regularized version of the Frenet frame. Fig. 2 (right) shows a progressively more regularized Frenet frame. Note that for the reorientation of diffusion information (see Sec. 5) the Frenet axes can be flipped. All computations in this paper identify antipodal directions; derivatives are computed by prealigning all vector-valued quantities locally before derivative computation.

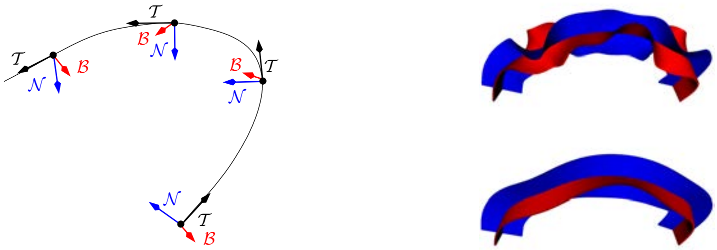

Fig. 2. The Frenet frame $\{\mathcal{T}, \mathcal{N}, \mathcal{B}\}$ consisting of tangent, normal, and binormal to $\mathcal{C}$. Regularization helps to obtain smoothly varying frames from noisy data (right).

4 Frame Diffusion

Instead of declaring a point in space to correspond to its closest point (measured by Euclidean distance) on the representative tract, here, correspondence is established implicitly through a diffusion process. This allows for smoother correspondences avoiding orientation jumps which occur at shock points for the Euclidean distance map. Since orientation is the quantity of interest, the orientation information is diffused *away* from the representative tract. Tschumperle and Deriche [22] regularize diffusion tensor fields by evolutions on frame fields. This can be used to define the diffusion of the frame field off the reference tract. Formally,

$$\mathbb{F}_\theta(\boldsymbol{x}, \theta) = \Delta_{\boldsymbol{x}} \mathbb{F}, \ \boldsymbol{x} \in \Omega \setminus \mathcal{C}, \quad \mathbb{F}(\boldsymbol{x}, \theta) = \mathbb{F}_b, \ \boldsymbol{x} \in \mathcal{C}, \tag{1}$$

where $\mathbb{F} = \{\mathcal{T}^a, \mathcal{N}^a, \mathcal{B}^a\}$ is the set of the axes implied by the regularized Frenet frame, $\mathbb{F}_b$ denotes the boundary condition given by the Frenet-frame-implied axes on the tract, $\boldsymbol{x} \in \mathbb{R}^3$ denotes spatial position, θ artificial evolution time, and $\Delta_{\boldsymbol{x}} = \frac{\partial^2}{\partial^2 x} + \frac{\partial^2}{\partial^2 y} + \frac{\partial^2}{\partial^2 z}$ the spatial Laplacian operator. The frame diffusion problem (1) can be solved [22] by evolving a set of three coupled vector diffusions:

$$\begin{cases} \mathcal{T}_\theta &= \Delta\mathcal{T} - (\Delta\mathcal{T}\cdot\mathcal{T})\mathcal{T} - (\Delta\mathcal{N}\cdot\mathcal{T})\mathcal{N} - (\Delta\mathcal{B}\cdot\mathcal{T})\mathcal{B}, \\ \mathcal{N}_\theta &= \Delta\mathcal{N} - (\Delta\mathcal{T}\cdot\mathcal{N})\mathcal{T} - (\Delta\mathcal{N}\cdot\mathcal{N})\mathcal{N} - (\Delta\mathcal{B}\cdot\mathcal{N})\mathcal{B}, \\ \mathcal{B}_\theta &= \Delta\mathcal{B} - (\Delta\mathcal{T}\cdot\mathcal{B})\mathcal{T} - (\Delta\mathcal{N}\cdot\mathcal{B})\mathcal{N} - (\Delta\mathcal{B}\cdot\mathcal{B})\mathcal{B} \end{cases}$$

which may be rewritten [22] as the rotations

$$\mathcal{T}_\theta = R\times\mathcal{T}, \quad \mathcal{N}_\theta = R\times\mathcal{N}, \quad \mathcal{B}_\theta = R\times\mathcal{B},$$

where $R = \mathcal{T}\times\Delta\mathcal{T} + \mathcal{N}\times\Delta\mathcal{N} + \mathcal{B}\times\Delta\mathcal{B}$ and $\mathbb{F} = \{\mathcal{T}^a, \mathcal{N}^a, \mathcal{B}^a\}$ is given by identifying antipodal directions. While the statistics used for the segmentation in Sec. 7 only use directional information, diffusing the complete frame information specifies a local rotation. This allows for easy extension of the methodology to formulations using for example the full tensor information or orientation distribution functions. Fig. 3 shows two 2D examples of frame diffusion. The resulting diffused frame field is smoother. Interestingly, the partial half-circle example shows that, to a limited extent, frame diffusion can be used to fill in missing information. This is a useful feature in case it is not possible to obtain one connected representative fiber tract.

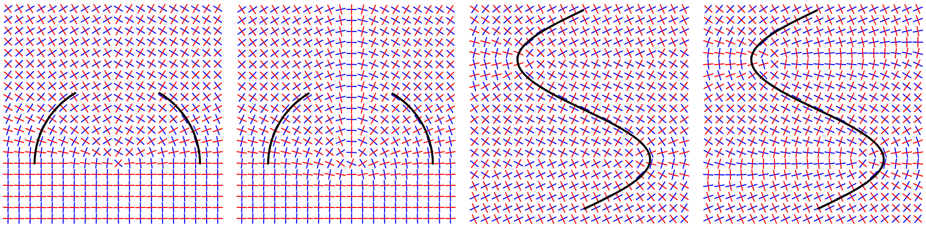

(a) Initialization. (b) Diffused. (c) Initialization. (d) Diffused.

Fig. 3. Frame diffusion yields smooth frame fields and thus smooth reorientations. Initializations using Euclidean distance point correspondences show frame discontinuities.

5 Frame Reorientation

The diffused frames can be used to reorient diffusion measurements locally to a canonical frame M[6]. This reorientation can be applied to any representation of diffusion information, e.g., the diffusion tensor, orientation distribution functions, etc. For clarity, reorientation is explained here for the case of diffusion tensors T. Given the diffused frame $\{\mathcal{T}, \mathcal{N}, \mathcal{B}\}$ and the associated rotation matrix $F = [\mathcal{T}, \mathcal{N}, \mathcal{B}]$ a tensor T is reoriented by applying the relative rotation MF^T, i.e., by

$$T^r = MF^T T F M^T.$$

The tensor reorientation yields tight tensor statistics while allowing a segmentation algorithm to apply spatial regularizations in the original space. It greatly simplifies computations by avoiding an explicit warping to straighten a curved fiber bundle.

---

[6] See Sec. 6 for a way to determine the canonical frame automatically

6 Orientation Statistics

We now describe the probabilistic modeling of fiber bundle orientations.

6.1 Watson Distribution

The Watson distribution is one of the simplest distributions for directional random variables [24, 2, 20]. It is radially symmetric around a mean direction μ, with a spread controlled by the concentration parameter k.

The Watson distribution on the unit sphere S^2 has probability density

$$p_w(q|\mu,k) = \frac{1}{4\pi \; {}_1F_1(\frac{1}{2};\frac{3}{2};k)} e^{k\left(\mu^T q\right)^2}, \quad p_w(q|\mu,0) = \frac{1}{4\pi},$$

where μ is the mean direction vector, k the concentration parameter[7], $q \in S^2$ is a direction represented as a column vector, and ${}_1F_1(\cdot;\cdot\cdot)$ denotes the confluent hypergeometric function. The Watson distribution is bipolar for $k > 0$, with maxima at $\pm\mu$ and uniform for $k = 0$. To model the interior of a fiber bundle, μ is set to the tangential direction of the canonical frame M. Reorienting diffusion information results in a tight Watson distribution with large concentration parameter k. The statistics outside the fiber bundle are modeled using the uniform distribution, since no preferred direction can be assumed in general in the fiber exterior.

While it is possible to use more complicated probability distributions (e.g., the Bingham distribution, or distributions on the diffusion tensor directly) to model a fiber tract orientation distribution, the Watson distributions chosen (in conjunction with the reorientation scheme) have the advantage of modeling the interior and the exterior of the fiber bundle with only one free parameter, the concentration k, greatly simplifying the estimation task and allowing for an easy interpretation of the estimated probability distribution.

6.2 Parameter estimation for the Watson distribution

The distribution parameters k and μ are easy to estimate. Given a set of N points $\boldsymbol{q}_i \in S^2$ (written as column vectors and representing spatial directions), the maximum likelihood estimate of μ is the major eigenvector of the sample covariance [5] $C = \frac{1}{N}\sum_{i=1}^{N} \boldsymbol{q}_i \boldsymbol{q}_i^T$ and $1 - \lambda_1$ (with λ_1 the largest eigenvalue of C) is the maximum likelihood estimate of $\frac{1}{k}$. Estimation of μ is performed only as a means of estimating the canonical frame direction and computed only on the representative tract. It is assumed fixed throughout the segmentation process described in Sec. 7. Only the concentration parameter k is estimated during bundle segmentation. For increased estimation robustness, robust estimators for the concentration parameter k may be used to account for cases where orientation measurements are either incorrect or cannot be reliably determined (as for example for isotropic tensors).

---

[7] To avoid ambiguities the concentration is denoted as k; κ denotes curvature in this paper.

7 Segmentation

We now integrate the diffusion data reorientation method and the statistical modeling described in Sec. 6 within a probabilistic version of the Chan-Vese [3] segmentation framework [7] using the probability distributions of Sec. 6.

7.1 Optimization Problem

The probabilistic Chan-Vese segmentation approach [3] is a piecewise-constant approximation problem, minimizing the energy functional

$$E_{cv}(\Omega_i, p_1, p_2) = \int_{\partial\Omega_i} ds + \lambda \int_{\Omega_i} (-\log p_1(f(x))\, d\Omega + \lambda \int_{\Omega \setminus \Omega_i} (-\log p_2(f(x))\, d\Omega, \tag{2}$$

where $f(\cdot)$ denotes an image feature (here, direction), p_1 and p_2 are the likelihoods for the interior and the exterior of the segmentation respectively, Ω is the computational domain and Ω_i is the interior domain. Choosing

$$p_1(q) = p_w(q|\mu, k), \quad p_2(q) = p_w(q|\mu, 0) = \frac{1}{4\pi},$$

constitutes the segmentation approach. See Sec. 6.1 for a discussion of this choice.

7.2 Numerical Solution

According to a slight modification of the solution approach in [19], the *probabilistic* Chan-Vese energy minimization problem 2 (on log-likelihood functions instead of image intensities) can be recast as the minimization of

$$E_{cvb}(u, c_1, c_2) = \int_{\Omega} \|\nabla u(x)\|\, d\Omega + \int_{\Omega} \lambda r_1(x, c_1, c_2) u + \alpha\nu(u)\, d\Omega \tag{3}$$

where

$$\nu(\zeta) = \max\{0, 2|\zeta - \frac{1}{2}| - 1\}, \quad \text{(the exact penalty function)},$$

$$r_1(x, c_1, c_2) = \log \frac{p_2(f(x))}{p_1(f(x))} = \log \left({}_1F_1(\frac{1}{2}; \frac{3}{2}; k) \right) - k \left(\mu^T q\right)^2.$$

The boundary is recovered as $\Omega_i = \{x : u(x) > \xi\}$, $\xi \in [0, 1]$. Eq. 3 can be solved efficiently through a dual formulation of the total-variation norm [19]:

1) Solve for u keeping v fixed:

$$\underset{u}{min} \left\{ \int_{\Omega} \|\nabla u\|\, dx + \frac{1}{2\theta} \|u - v\|^2_{L^2} \right\} \tag{4}$$

2) Solve for v keeping u fixed:

$$\underset{v}{min} \left\{ \frac{1}{2\theta} \|u - v\|^2_{L^2} + \int_{\Omega} \lambda r_1(x, p_1, p_2) v + \alpha\nu(v)\, dx \right\} \tag{5}$$

3) Repeat until convergence.

Eq. 5 has the solution $v = min\{max\{u(x) - \theta\lambda r_1(x, p_1, p_2), 0\}, 1\}$ and Eq. 4 can be solved using a fixed-point iteration

$$u = v - \theta div\ p, \quad p^{n+1} = \frac{p^n + \delta t \nabla(div(p^n) - \frac{v}{\theta}}{1 + \delta t|\nabla(div(p^n) - \frac{v}{\theta}|}, \quad p = (p^1, p^2, p^3), \quad \delta t \leq \frac{1}{6}.$$

To enforce segmenting a bundle containing the representative tract set

$$\begin{cases} v = 1 & \text{for all points on the representative tract,} \\ v = 0 & \text{for all points at a distance } d \geq d_{max} \text{ from the representative tract.} \end{cases}$$

The segmented fiber bundle is the set of voxels with $u \geq \frac{1}{2}$ which are contained in the connected component containing the voxels of the representative tract. This is also the volume which is used throughout the evolution to update the estimation of the concentration k of the fiber bundle's Watson distribution.

8 Results

This section gives results for the proposed segmentation approach. Synthetic examples are discussed in Sec. 8.1. Sec. 8.2 presents results for a real DW-MRI of the brain and compares them to segmentation results obtained through streamline tractography.

8.1 Synthetic example

A synthetic tensor example was generated. Tensors are assumed of uniform shape with eigenvalues $(1.5, 0.5, 0.5)e-3$ oriented along a circular path to model a fiber bundle. Tensors oriented orthogonally to the circular path model the outside. Diffusion weighted images were generated using the Steijskal Tanner equation $S_k = S_0 e^{-b\boldsymbol{g}_k^T T \boldsymbol{g}_k}$, where S_k denotes the diffusion weighted image acquired by applying a gradient direction $\boldsymbol{g}_k$ with b-value b, and T the diffusion tensor. Parameters were $S_0 = 1000$, $b = 1000$ with 46 gradient directions equally spaced on the unit sphere. Rician noise of $\sigma = 70$ was introduced to the baseline image S_0 (non-diffusion weighted) and the diffusion weighted images S_k. Fig. 4 shows the original data and the resulting segmentation on the top row (with the streamline indicating the computed representative tract) and the reoriented data with associated segmentation on the bottom row. For this synthetic example, reorientation results in an almost perfectly uniform tensor distribution on the inside and the outside of the simulated fiber bundle. Consequently, while the proposed approach fails at segmenting the original data, it segments the reoriented data well. Note, that the failure to segment the original data is not merely a result of the segmentation method employed. Any segmentation relying purely on region-based statistics will either have to include some of the background in its bundle segmentation or will severely under-segment the bundle itself, since background and foreground are not clearly separable based on global statistics. While including edge-based terms may improve the segmentation of the original data, regional terms will be of limited use and will locally counteract the edge influence requiring a delicate balance between region-based and edge-based energies to faithfully segment the simulated fiber bundle.

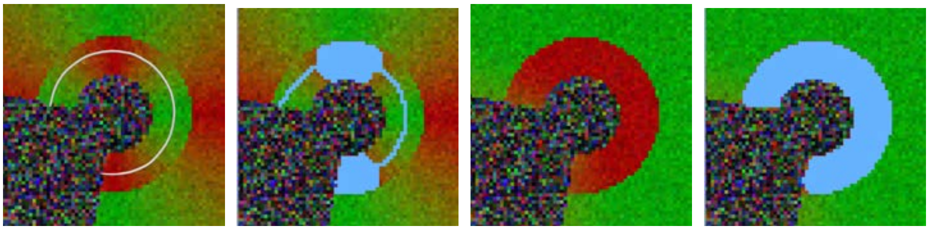
(a) Original. (b) Original. (c) Reoriented. (d) Reoriented.

Fig. 4. Synthetic segmentation example overlaid on a color by orientation representation. Reorientation results in a successful segmentation ($k = 10$, $\theta = 0.01$, $\lambda = 0.7$).

8.2 Real example

The real example was computed for the cingulum bundle using a 3T DW-MRI upsampled to isotropic resolution (0.93 mm^3) with 8 baseline images and 51 uniformly distributed gradient directions (b=586). The representative tract was computed using streamline tractography.

Fig. 5 shows color by orientation representations for a sagittal slice through the brain with the cingulum bundle (mainly in green) before and after reorientation. The reoriented image shows a consistently green cingulum bundle, whereas in the original image the cingulum bundle is colored blue when wrapping posteriorly around the corpus callosum, indicating a change of orientation from anterior-posterior to superior-inferior. Example segmentation results of the proposed approach are shown for the reoriented and the original data. Algorithm parameters were set to $\theta = 0.01$, $\lambda = 0.5$. The concentration parameter was set to $k = 100$ and converged to $k = 19.5$ throughout the evolution for the reoriented dataset. The surface models generated from the computed segmentations show that the segmentation for the reoriented data approximates the cingulum bundle more faithfully.

Finally, to demonstrate the strength of the reorientation approach, Fig. 6 gives an example for the cingulum bundle segmentation at a posterior slice of the cingulum bundle where the cingulum bundle wraps around the corpus callosum. While in the reoriented case the segmentation is successful and the direction of the cingulum bundle is uniform (green), the segmentation on the original data fails in this part of the fiber bundle.

To compare the proposed methods to alternative segmentation approaches, the cingulum bundle was segmented using a region of interest based approach (the same regions of interest used to generate the representative fiber tract for reorientation). Two small axial regions of interest were defined for the cingulum bundle (superiorly to the corpus callosum). Streamline tractography with

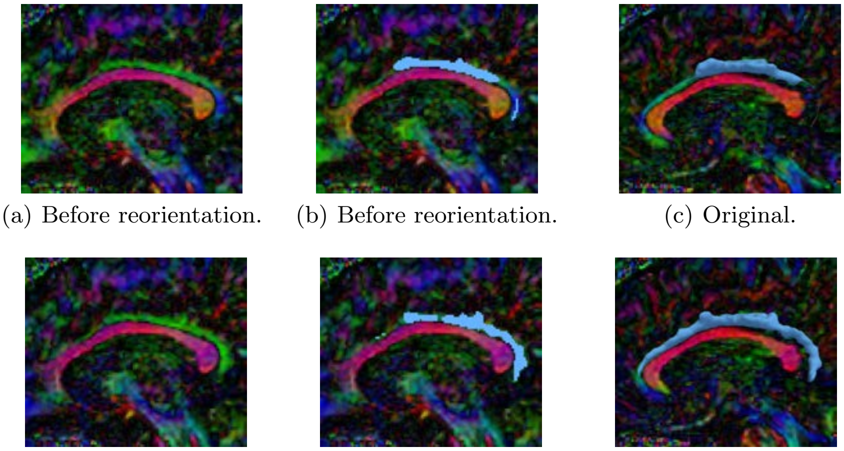

(a) Before reorientation. (b) Before reorientation. (c) Original.

(d) After reorientation. (e) After reorientation. (f) Reoriented.

Fig. 5. Sagittal slice of the cingulum bundle, before and after tensor reorientation. The cingulum bundle appears more uniform in direction (green) after reorientation. Reorientation greatly improves the segmentation result of the proposed approach.

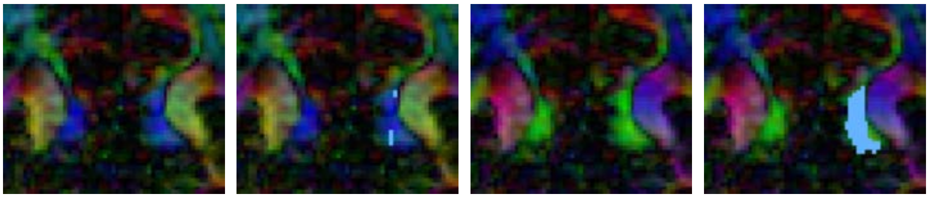

(a) Original (O). (b) Segmented (O). (c) Reoriented (R). (d) Segmented (R).

Fig. 6. Posterior coronal slice: Color by orientation shows advantage of reorientation.

voxelization, full brain streamline tractography with voxelization, as well as segmentation on the original and reoriented data using the proposed approach was performed. Fig. 7 illustrates segmentation results for these methods for coronal slices in the superior part of the cingulum bundle (where the cingulum bundle is *not* strongly curved). As expected streamline tractography and full brain streamline tractography mainly capture the interior of the fiber bundle, with full brain tractography performing qualitatively better than standard region of interest based streamline tractography (streamlines were seeded one per voxel in the regions of interest). The proposed segmentation approach captures the cingulum bundle well for the reoriented and for the original data, showing the utility of segmenting in orientation space. However, the reoriented segmentation results are better where the cingulum bundle curves strongly, as shown in Fig. 6.

9 Conclusion and Discussion

This paper proposed a new segmentation method for tubular fiber bundles. It is based on reorientation of diffusion measurements resulting in more uniform data

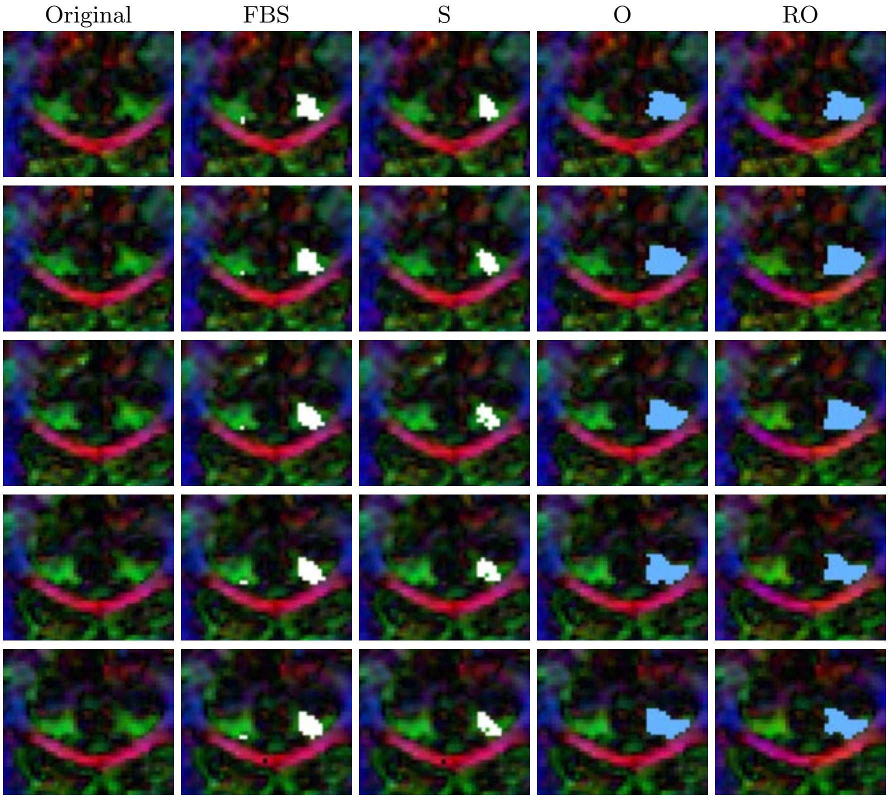

Fig. 7. Superior coronal slices: Original data; results for streamline (S) and full brain streamline (FBS) tractography, for the proposed segmentation on original data (O) and on reoriented data (RO). Only the proposed approach segments up to the perceived bundle boundary in orientation space.

distributions inside the fiber bundle of interest. Segmentation is performed by an efficient convex approximation of the probabilistic Chan-Vese energy using region-based directional statistics. The approach compares favorably to streamline approaches for bundle segmentation. However, since no realistic ground-truth for DW-MRI is available to date quantitative analysis is difficult. Extensions to sheet-like structures are conceivable, where the representative tract would be replaced by a representative sheet [12, 13] (using the major diffusion direction combined with the normal to the medial sheet to define a frame for reorientation). Population studies could be performed by either performing segmentation in atlas space, or by using an atlas defined representative tract and subject-specific bundle segmentations.

Acknowledgments This work is part of the National Alliance for Medical Image Computing (NAMIC), funded by the National Institutes of Health through the NIH Roadmap for Medical Research, Grant U54 EB005149. Information on the National Centers for Biomedical Computing can be obtained from `http://nihroadmap.nih.gov/bioinformatics`.

References

1. D. Le Bihan. Looking into the functional architecture of the brain with diffusion MRI. *Nature Neuroscience*, 4(6):469–480, 2003.
2. C. Bingham. An antipodally symmetric distribution on the sphere. *The Annals of Statistics*, 2(6):1201–1225, 1974.
3. T. F. Chan and L.A. Vese. Active contours without edges. *TIP*, 10(2):266–277, 2001.
4. M. P. do Carmo. *Differential Geometry of Curves and Surfaces.* Prentice Hall, 1976.
5. A. Schwartzman et al. False discovery rate analysis of brain diffusion direction maps. *Annals of Applied Statistics*, 2(1):153–175, 2008.
6. C. Lenglet et al. DTI segmentation by statistical surface evolution. *TMI*, 25(6):685–700, 2006.
7. D. Cremers et al. A review of statistical approaches to level set segmentation: Integrating color, texture, motion and shape. *IJCV*, 72(2):195–215, 2007.
8. E. Pichon et al. A Hamilton-Jacobi-Bellman approach to high angular resolution diffusion tractography. In *MICCAI*, pages 180–187, 2005.
9. J. Melonakos et al. Locally-constrained region-based methods for DW-MRI segmentation. *ICCV*, pages 1–8, 2007.
10. L. Jonasson et al. White matter fiber tract segmentation in DT-MRI using geometric flows. *MEDIA*, 9(3):223–236, 2005.
11. O. Friman et al. A Bayesian approach for stochastic white matter tractography. *TMI*, 25(8), 2006.
12. P. A. Yushkevich et al. Structure-specific statistical mapping of white matter tracts using the continuous medial representation. In *ICCV*, pages 1–8, 2007.
13. S. M. Smith et al. Tract-based spatial statistics: Voxelwise analysis of multi-subject diffusion data. *Neuroimage*, 31:1487–1505, 2006.
14. S. P. Awate et al. A fuzzy, nonparametric segmentation framework for DTI and MRI analysis: With applications to DTI-tract extraction. *TMI*, 26(11):1525–1536, 2007.
15. T. McGraw et al. Segmentation of high angular resolution diffusion MRI modeled as a field of von Mises-Fisher mixtures. *ECCV*, pages 463–475, 2006.
16. T.E.J. Behrens et al. Characterization and propagation of uncertainty in diffusion-weighted MR imaging. *MRM*, 50(5):1077–1088, 2003.
17. W. K. Jeong et al. Interactive visualization of volumetric white matter connectivity in DT-MRI using a parallel-hardware Hamilton-Jacobi solver. *TVCG*, pages 1480–1487, 2007.
18. Wiegell et al. Automatic segmentation of thalamic nuclei from diffusion tensor magnetic resonance imaging. *Neuroimage*, 19(2):391–401, 2003.
19. X. Bresson et al. Fast global minimization of the active contour/snake model. *Journal of Mathematical Imaging and Vision*, 28(2):151–167, 2007.
20. K. V. Mardia. Statistics of directional data. *Journal of the Royal Statistical Society. Series B.*, 37(3):349–393, 1975.
21. L. J. O'Donnell and C.F. Westin. Automatic tractography segmentation using a high-dimensional white matter atlas. *TMI*, 26(11):1562–1575, 2007.
22. D. Tschumperle and R. Deriche. Diffusion tensor regularization with constraints preservation. In *CVPR*, volume 1, pages 948–953, 2001.
23. Z. Wang and B. C. Vemuri. DTI segmentation using an information theoretic tensor dissimilarity measure. *TMI*, 24(10):1267–1277, 2005.
24. G. Watson. Equatorial distributions on a sphere. *Biometrika*, 52:193–201, 1965.

An Unbiased Non-Local Means Scheme for DWI Filtering

S. Aja-Fernández[1], Karl Krissian[2]

[1] LPI, ETSI Telecomunicación, Universidad de Valladolid (Spain)
[2] CTM, Universidad de las Palmas de Gran Canaria (Spain)

Abstract. The Non-Local means algorithm has been introduced recently in image processing and its application to denoising in Magnetic Resonance Imaging is an active field of research. Recent publications proposed a fast implementation suited for three-dimensional filtering and also applied it to Diffusion Tensor MRI. However, the Rician noise that affects this acquisition modality introduces a bias of the local intensity mean which could lead to wrong interpretation of the images. We propose two simple extensions to the NL-means algorithm to deal with this bias, one recursive and one based on the conventional approach. We also present a new, simpler, and fast implementation of the algorithm which performs as well as the original NL-means algorithm in our context.

1 Introduction

Noise in magnitude Magnetic Resonance (MR) images is usually modeled by a Rician distribution, due to the existence of uncorrelated Gaussian noise with zero mean and the same variance σ_n^2 in both the real and imaginary parts of the complex k-space data. If no phase errors are considered, the magnitude signal can be represented as $M(\mathbf{x}) = \sqrt{(A+n_r)^2 + (n_i)^2}$, where $A = A(\mathbf{x})$ denotes the original signal level if no noise is present, and n_r and n_i are the real and imaginary components of the noise, each of them following a Gaussian distribution with zero mean and the same standard deviation σ_n. Several filtering methods to improve Signal-to-Noise Ratios in MRI have been proposed in literature, like the *conventional approach* (CA) [1], maximum likelihood based methods [2], maximum a posteriori estimation [3], Linear Minimum Mean Square Error (LMMSE) based schemes [4], wavelet-based methods for noise removal [5], Perona and Malik's anisotropic diffusion, non-parametric neighborhood statistics [6, 7] techniques, or filtering using log-Euclidean space [8]. Other classes of algorithms are based on the redundancy of local patches in the images to remove the noise. Recently, the Non-Local means (NLM) was introduced in [9] and performs very well in removing the noise. However, the initial algorithm is computationally heavy especially for 3D images and a fast version was proposed in [7] and especially applied to 3D MRI data sets, and to 3D DT-MRI [10]. According to these last publications, the NLM algorithm outperforms previous techniques such as the anisotropic diffusion and total variation techniques. In the context of DT-MRI [10], three variants of the NLM algorithm have been proposed and compared and

Algorithm 1 NL-means algorithm. The parameters are: - the input n-dimensional image denoted I, - the window size $t \in \mathbb{N}$, - the pattern window size $f \in \mathbb{N}$, and - the pattern similarity threshold $h \in \mathbb{R}$.

```
for each voxel $p$ do
    for each voxel $q \in \mathcal{N}_{2t+1}(p), q \neq p$ do          ▷ window centered on $p$
        $d_f(p,q) = \frac{1}{(2f+1)^n} \sum_{\delta \in [-f,f]^n} \|I(p+\delta) - I(q+\delta)\|^2$
        $w_p(q) = e^{-\frac{d_f(p,q)}{h^2}}$
    end for
    $w_p(p) = \max_{q \neq p} w_p(q)$
    $I_{res}(p) = \frac{1}{\sum w_p(q)} \sum_{q \in \mathcal{N}_{2t+1}(p)} w_p(q).I(q)$
end for
```

the best results have been obtained by applying separately the NLM to each of the directional diffusion weighted images (DWI) and by estimating the DT-MRI from the denoised DWI. However, these previous works don't take into account the specific characteristics of the Rician noise that corrupts magnetic resonance images, and in particular affects their mean intensities. As a result, the filtered image may be biased with respect the original one, which is a major drawback for instance when filtering DWI for tensor estimation. In this paper, we propose a new NLM scheme to deal with the bias in the image after filtering Rician noise. We show how the original image intensity can be better recovered, and in diffusion tensor images we show how this correction improves the estimated eigenvalues of the diffusion tensor.

2 Unbiased Non-Local Means for Rician data

2.1 Non-Local means algorithm

The NLM algorithm is based on the idea that the intensity of a pixel in a noisy image can be recovered by averaging the set of pixels that share a similar local pattern in the whole image. This simple idea is intuitively very well suited to texture denoising, where the direct neighbors of a pixel can have very different intensities and a few patterns or patches are repeated many times. However, in practice, it gives very good results even in non-textured images where the image intensity can be considered as a continuous function. One reason to the efficiency of the NLM algorithm is that it is able to shape any kind of local vicinity when defining the averaging weights. The NLM algorithm is described by the algorithm 1. The central voxel p is given as weight the maximal distance found with all the other voxels of the searching window, preventing the preservation of isolated points. The pattern similarity threshold is typically chosen as proportional to the standard deviation of the noise. In [7], the authors use $h^2 = 2\beta\sigma_n^2$, where β is a coefficient between 0.5 and 1.

2.2 Unbiasing the NLM algorithm

Regardless of the method used to calculate the local mean, a window around the voxel or a non-local means algorithm, we are estimating the mean of parameter $M(\mathbf{x})$, i.e. $E\widehat{\{M(\mathbf{x})\}} = \langle M(\mathbf{x})\rangle$. In a Rician distribution, the value of $E\{M(\mathbf{x})\}$ is not the original signal value, denoted $A(\mathbf{x})$. Accordingly, the volume $\langle M(\mathbf{x})\rangle$ will be biased with respect to the original volume. The mean of a Rician distribution is defined as $E\{M\} = \sigma_n\sqrt{\frac{\pi}{2}}e^{-\frac{A^2}{4\sigma_n^2}}\left[\left(1+\frac{A^2}{2\sigma_n^2}\right)I_0\left(\frac{A^2}{4\sigma_n^2}\right)+\frac{A^2}{2\sigma_n^2}I_1\left(\frac{A^2}{4\sigma_n^2}\right)\right]$, and after some algebra

$$A^2 = 2\langle M(\mathbf{x})\rangle\sigma_n\sqrt{\frac{2}{\pi}}\frac{\exp\left(\frac{A^2}{4\sigma_n^2}\right)}{I_0\left(\frac{A^2}{4\sigma_n^2}\right)+I_1\left(\frac{A^2}{4\sigma_n^2}\right)} - 2\sigma_n^2\frac{I_0\left(\frac{A^2}{4\sigma_n^2}\right)}{I_0\left(\frac{A^2}{4\sigma_n^2}\right)+I_1\left(\frac{A^2}{4\sigma_n^2}\right)} \tag{1}$$

being $\langle M(\mathbf{x})\rangle$ the output of the NLM algorithm. The unbiased Non-Local Means (UNLM) for a Rician distribution is defined as

$$I_{ub}(\mathbf{x}) = \sqrt{\max(A^2(\mathbf{x}),0)} \tag{2}$$

where $A^2(\mathbf{x})$ is estimated from eq. (1). This may be done following an iterative fixed point method. To avoid the iterative method, an alternative based in the Rician second order moment is proposed. In a Rician distribution $E\{M^2\} = A^2 + 2\sigma_n^2$, so we can average the squared image intensities instead of the original intensities. Combined with a robust estimation of the noise standard deviation σ_n, we can remove the bias from the squared intensity average by subtracting $2\sigma_n^2$ before applying the square root to obtain the estimated denoised intensity. The modified algorithm is almost the same as the original one, where line 7 is replaced by:

$$I_{res}(p) = \sqrt{\max\left(\frac{\sum_{q\in\mathcal{N}_{2t+1}(p)} w_p(q).I^2(q)}{\sum w_p(q)} - 2\,\sigma_n^2,\ 0\right)}, \tag{3}$$

the weights $w_p(q)$ being still computed from the original image I. As the formulation is similar to the *conventional approach* [1], we will call it Non-Local Conventional Approach (NLCA).

2.3 On the distance measure between local patches

If we consider the two local patches as the observation of random variables A and B, the weights of the NLM algorithm are calculated as:

$$d(A,B) = E((A-B)^2) = (E(A)-E(B))^2 + Var(A) + Var(B) + Cov(A,B) \tag{4}$$

The terms $E(A)$, $E(B)$, $Var(A)$ and $Var(B)$ can be pre-computed very fast in a recursive separable way, for example using Gaussian smoothing if we define a Gaussian weighting window. The term $Cov(A,B)$ requires more processing,

Algorithm 2 Modified unbiased NLM algorithm, denoted NLCA (Non-Local Conventional Approach). The parameters are: - the input n-dimensional image denoted I, - the window size $t \in \mathbb{N}$, - the standard deviation of the Gaussian smoothing kernel σ, and - the pattern similarity threshold $h \in \mathbb{R}$.

```
Precompute $I_\sigma = I * G_\sigma$
for each voxel $p$ do
    for each voxel $q \in \mathcal{N}_{2t+1}(p)$ do                ▷ window centered on $p$
        $w_p(q) = e^{-\frac{(I_\sigma(p)-I_\sigma(q))^2}{h^2}}$
    end for
    $I_{res}(p) = \sqrt{\max\left(\frac{\sum_{q\in\mathcal{N}_{2t+1}(p)} w_p(q).I^2(q)}{\sum w_p(q)} - 2\,\sigma_n^2,\ 0\right)}$
end for
```

but could be speed-up using Fourier Transform. However, we argue that the distance between two patches should be rotational invariant to allow more efficient smoothing. In fact, the level of noise reduction will depend on the uniformity of the weights within voxels of same intensity values in the non-noisy image, if $X_i, i \in [1,k], k \in \mathcal{N}$ are all random variables of zero-means and standard deviation σ, and w_i are averaging weights, $Var(\sum_i w_i X_i) = \sum_i w_i^2 \sigma^2$ which means that we can approximate at each point the reduction in the noise variance as the sum of the square of the averaging weights applied in the local window. Since a rotation in the local patch will not change the intensity of its center, using a measure that is not rotational invariant will limit the denoising performance of the filter. Thus, we propose a modification of the NLM algorithm, which is based only based on the local intensities of the smoothed image to define the distance between patches. Smoothing is performed by Gaussian convolution as a preprocessing step. In practice, we get the same denoising efficiency as equation (4) at a much lower computational cost: the complexity is divided by $(2f+1)^n$. The parameter f is replaced by the standard deviation σ of the Gaussian smoothing which is directly related to the size of the smallest size of the structures we would like to preserve, as described by algorithm 2. The only drawback of the modified version is that it does not preserve as well very small texture elements, but this kind of texture is not present in conventional brain MRI.

2.4 Comparison of the standard and modified NL-means

In this section, we evaluate the effect of the new pattern distance measure by comparing two versions of the unbiased NLM: one using the original distance and one using the new proposed distance. We use two synthetic 2D images of size 50×50 pixels represented in fig. 1. The first image is a disk with simulated partial volume effect, and object intensity 140 with background intensity 40. The second image is a smooth star with 2 level of intensities 120 and 160 and a background of intensity 40, and simulated partial volume effects. Both images are corrupted with a Rician noise of standard deviation 15. We ran the two versions of the unbiased NLM filter, both are unbiased using equation (3), one uses the

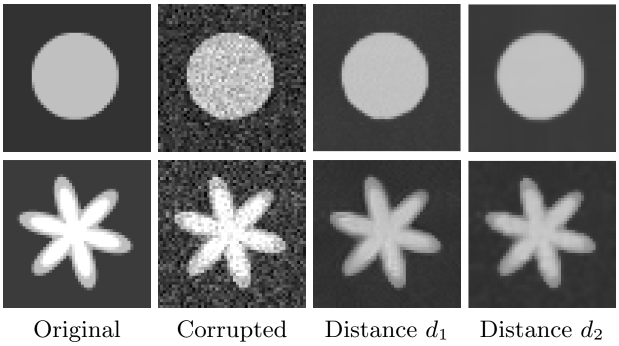

Fig. 1. Two synthetic 2D images of 50 × 50 pixels, corrupted with Rician noise.

distance defined as in algorithm 1, denoted d_1, and the other uses the distance defined as in algorithm 2, denoted d_2. We looked for the optimal parameters of the Mean Square Error measure based on the following sets of values: for both d_1 and d_2, $t \in [3, 12]$ and $h \in [10, 30]$; for d_1, $f \in [1, 7]$. and for d_2, σ from 0.8 to 1.5 with a step of 0.1. The following table show the best MSE obtained from both methods and the corresponding best set of parameters. The denoising level of each approach is similar, with a slightly better result for the proposed distance in the case of the star synthetic image.

	Standard distance d_1					Proposed distance d_2				
	t	f	h	MSE	time	t	σ	h	MSE	time
disk	12	3	28	6.63	0.429 sec	12	1	24	6.65	0.121 sec
star	6	4	17	29.02	0.216 sec	6	0.8	17	27.17	0.039 sec

3 Validation

Synthetic experiments have been carried out to validate the unbiased NLM scheme previously introduced. First, a synthetic image from the BrainWeb database has been corrupted with Rician noise with different values of σ_n. The image is filtered using either the NLM, the UNLM or the NLCA algorithms. Although the purpose of this paper is to compare the unbiased algorithms with the original one, to provide a wider reference, two well-known methods have also been used: (i) Anisotropic Diffusion filtering, using a Green diffusion function with a threshold $K = 5$, and 30 steps with a time-step $\Delta t = 0.1$, and (ii) The Conventional Approach by McGibney et al. [1], using $3 \times 3 \times 3$ windows and manually setting the value of σ_n. It is an unbiased method, defined as $\hat{A}_c(\mathbf{x}) = \sqrt{\max(\langle M^2(\mathbf{x})\rangle - 2\sigma_n^2, 0)}$. To compare the filtering performance of the different methods, two quality indexes are used: the Structural Similarity (SSIM) index [11] and the Quality Index based on Local Variance (QILV) [12]. Both give a measure of the structural similarity between the ground truth and the estimated images. However, the former is more sensitive to the level of

	$\sigma_n = 5$			$\sigma_n = 7$			$\sigma_n = 10$		
	SSIM	QILV	MSE	SSIM	QILV	MSE	SSIM	QILV	MSE
Noise	0.9470	**0.9955**	25.33	0.9037	**0.9872**	50.25	0.8320	0.9535	103.95
CA	0.9417	0.7062	69.75	0.9382	0.7079	70.87	0.9310	0.7117	73.40
AD	0.9202	0.8257	72.60	0.9098	0.8221	77.05	0.8937	0.8164	87.18
NLM	0.9641	0.9566	26.33	0.9532	0.9538	30.35	0.9347	0.9484	40.14
UNLM	**0.9728**	0.9593	24.28	**0.9719**	0.9588	25.11	**0.9698**	**0.9583**	26.71
NLCA	0.9721	0.9576	**23.02**	0.9709	0.9577	**23.67**	0.9678	0.9573	**25.30**

	$\sigma_n = 15$			$\sigma_n = 20$			$\sigma_n = 25$		
	SSIM	QILV	MSE	SSIM	QILV	MSE	SSIM	QILV	MSE
Noise	0.7190	0.8611	237.16	0.6274	0.7114	424.83	0.5563	0.5485	666.50
CA	0.9139	0.7197	80.21	0.8924	0.7311	90.5	0.8676	0.7436	104.99
AD	0.8707	0.8087	115.30	0.8520	0.8041	160.86	0.8327	0.8051	229.59
NLM	0.9051	0.9359	68.91	0.8791	0.9212	115.92	0.8551	0.9031	184.50
UNLM	**0.9633**	0.9572	31.32	**0.9508**	0.9574	38.89	**0.9307**	0.9574	**51.15**
NLCA	0.9576	**0.9577**	**29.86**	0.9379	**0.9581**	**38.11**	0.9071	**0.9586**	52.16

Table 1. Quality measures: SSIM, QILV and MSE for the 3D volume experiments. The best value of each column is highlighted.

noise in the image and the latter to any possible blurring of the edges. Both indexes are bounded; the closer to one, the better the image. The mean square error (MSE) is also calculated. These three quality measures are only applied to areas of the original image of strickly positive intensities to avoid taking into account the background area. The average measure over 10 experiments is considered for each σ_n and each filter. Results are presented in Table 1 and illustrated in Fig. 2. Proposed unbiased schemes show the better and similar results, even for high noise levels. When working with DT-MRI, some scalar measures are directly related to the eigenvalues of the diffusion tensors. Since tensor estimation results are noise-dependent, noise removal before tensor estimation should lead to an improved tensor estimation. However, using a biased filtering method leads to a bias in the estimated tensors. To study the effect of bias and unbiased schemes over the tensors eigenvalues, a 128 × 128 synthetic 2D tensor field has been created, as shown in Fig. 3-(a), where tensors are depicted using ellipses. For better representation, ellipses are represented every few pixels. Tensors with three different eigenvalue combinations were chosen $\boldsymbol{\lambda}_a = [1.9\ 10^{-3}, 0.4\ 10^{-3}]$ $\boldsymbol{\lambda}_b = [2\ 10^{-3}, 0.1\ 10^{-3}], \boldsymbol{\lambda}_c = [2\ 10^{-3}, 1.25\ 10^{-3}]\}$. The field was created with the same number of tensors of each kind. Afterwards, the diffusion weighted images (DWI) were simulated using the Stejskal-Tanner equation [13] with a constant baseline with a level of 1000. The DWI and the baseline are corrupted with Rician noise and the tensors are re-estimated, using a Least Squares approach, Fig. 3-(b). To better illustrate the effect of the bias over the estimated Tensors, as the bias depends on σ_n, we have selected a scenario with high level of noise ($\sigma_n = 175$) and a moderate-high number of gradients ($N = 15$), to assure a good estimation. Results are presented in Fig. 3 (tensor field) and in Fig. 4 where the distribution of the eigenvalues is depicted in a 2D histogram for 20 experiments. The original sets of eigenvalues are de-

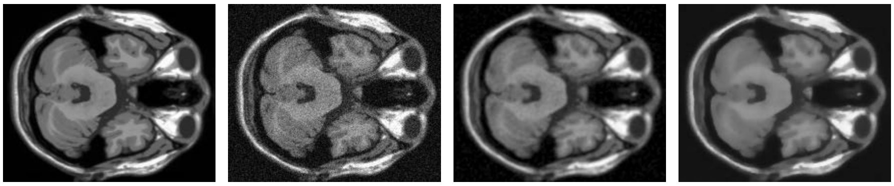

(a) Original (b) Noisy (c) CA (d) AD

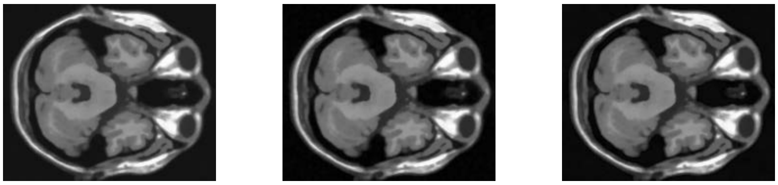

(e) NLM (f) UNLM (g) NLCA

Fig. 2. Slice of the volume in the experiments for $\sigma_n = 15$.

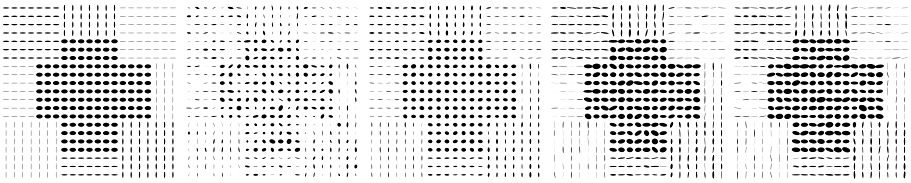

(a) Original (b) Noisy (c) NLM (d) UNLM (e) NLCA

Fig. 3. Synthetic tensor field used in the experiments. $\sigma_n = 175$, 15 different gradients.

picted as black dots. Notice that the NLM filter is able to reduce considerably the effect of noise in the estimation, but the estimated eigenvalues are still biased in relation with the original ones, see Fig. 4-(b). As a result, the tensor field depicted in Fig. 3-(c) is more homogeneous than the noisy one, but the tensor are also smaller. The UNLM and NLCA are both able to correct this bias, see Fig. 4-(c-d) where the maxima of the histogram are placed in the original values. However, the price to pay is an increased variance of the estimation. Although the performance of both unbiased methods is very similar, NLCA is faster than UNLM, since no iterative method is needed to remove the bias.

4 Conclusions

Two different methods to effectively remove the bias in NLM schemes for MRI have been proposed. They are based on moments of the Rician distribution. In addition, a new fast implementation of the NLM algorithm is also proposed. The experimental results show a good quantitative performance in terms of noise removal, edge preservation, and minimization of the error. Experiments also show that, when working with DWI, a reduction of the bias of the images induces a reduction on the bias of the estimated eigenvalues of the diffusion tensor.

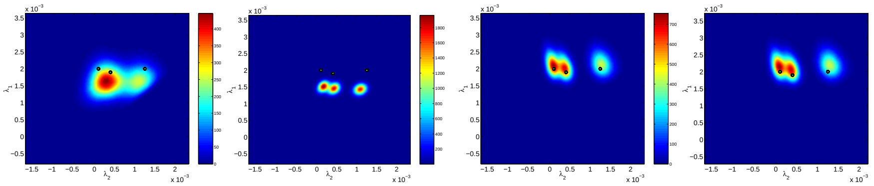

(a) Noisy (b) NLM (c) UNLM (d) NLCA

Fig. 4. Two dimensional histograms of the distribution of the estimated eigenvalues. $\sigma_n = 175$, 15 different gradients. In black the original eigenvalues. The proposed methods (UNLM and NLCA) show a smaller bias in the estimation.

References

1. McGibney, G., Smith, M.: Unbiased signal-to-noise ratio measure for magnetic resonance images. Med. Phys. **20**(4) (1993) 1077–1078
2. Sijbers, J., *et al.*: Maximum-likelihood estimation of Rician distribution parameters. IEEE Trans. Med. Imaging **17**(3) (1998) 357–361
3. Basu, S., Fletcher, T., Whitaker, R.: Rician noise removal in diffusion tensor MRI. In: Proceedings of MICCAI. Volume 1. (2006) 117–125
4. Aja-Fernández, S., Alberola-López, C., Westin, C.F.: Signal LMMSE estimation from multiple samples in MRI and DT-MRI. In: Proceedings of MICCAI 07. Lecture Notes on Computer Science. Volume 4792. (2007)
5. Nowak, R.: Wavelet-based Rician noise removal for Magnetic Resonance Imaging. IEEE Trans. Image Proccess. **8**(10) (1999) 1408–1419
6. Awate, S., Whitaker, R.: Nonparametric neighborhood statistics for MRI denoising. In: Information Processing in Medical Imaging. Volume 3565 of Lecture Notes in Computer Science., Springer (2005) 677–688
7. Coupé, P., Yger, P., Prima, S., Hellier, P., Kervrann, C., Barillot, C.: An optimized blockwise non local means denoising filter for 3D magnetic resonance images. (IEEE Trans. Med. Imaging) In press.
8. Fillard, P., Pennec, X., Arsigny, V., Ayache, N.: Clinical dt-mri estimation, smoothing, and fiber tracking with log-euclidean metrics. IEEE TMI **26**(11) (2007) 1472–1482
9. Buades, A., Coll, B., Morel, J.: A review of image denoising algorithms, with a new one. Multiscale Modeling and Simulation **4**(2) (2005) 490–530
10. Wiest-Daesslé, N., Prima, S., Coupé, P., Morrissey, S., Barillot, C.: Non-local means variants for denoising of diffusion-weighted and diffusion tensor MRI. In: Proc. of MICCAI 2007. Volume 4792 of Lec. Notes in Comp. Sci. (2007) 344–351
11. Wang, Z., Bovik, A.C., Sheikh, H.R., Simoncelli, E.P.: Image quality assessment: from error visibility to structural similarity. IEEE Trans. Image Proccess. **13**(4) (2004) 600–612
12. Aja-Fernández, S., San-José-Estépar, R., Alberola-López, C., Westin, C.F.: Image quality assesment based on local variance. In: Proc of the 28th EMBC, New York (2006) 4815–4818
13. Stejskal, E.O., Tanner, J.E.: Spin Diffusion Measurements: Spin Echoes in the Presence of a Time-Dependent Field Gradient. Journal of Chemical Physics **42** (1965) 288–292

Visualization Tools for High Angular Resolution Diffusion Imaging

David W. Shattuck[1], Ming-Chang Chiang[1], Marina Barysheva[1],
Katie L. McMahon[2], Greig I. de Zubicaray[2], Matthew Meredith[2],
Margaret J. Wright[3], Arthur W. Toga[1], and Paul M. Thompson[1]

[1] Laboratory of Neuro Imaging, Dept. of Neurology, UCLA, Los Angeles, CA, USA
[2] Centre for Magnetic Resonance, University of Queensland, Brisbane, Australia
[3] Queensland Institute of Medical Research, Brisbane, Australia

Abstract. There is a major effort in medical imaging to develop algorithms to extract information from DTI and HARDI, which provide detailed information on brain integrity and connectivity. As the images have recently advanced to provide extraordinarily high angular resolution and spatial detail, including an entire manifold of information at each point in the 3D images, there has been no readily available means to view the results. This impedes developments in HARDI research, which need some method to check the plausibility and validity of image processing operations on HARDI data or to appreciate data features or invariants that might serve as a basis for new directions in image segmentation, registration, and statistics. We present a set of tools to provide interactive display of HARDI data, including both a local rendering application and an off-screen renderer that works with a web-based viewer. Visualizations are presented after registration and averaging of HARDI data from 90 human subjects, revealing important details for which there would be no direct way to appreciate using conventional display of scalar images.

1 Introduction

Diffusion magnetic resonance imaging [1] applies gradient fields during image acquisition, allowing local measures of water diffusion preferences to be made. In diffusion tensor imaging (DTI), a reference image and at least six diffusion images are acquired with non-collinear gradients and used to reconstruct a volume of rank-2 tensor models [2]. The shapes of these tensors provide information about the underlying structure within the biological sample. For brain imaging, DTI provides valuable insight into the white matter architecture, with a distinct advantage over traditional MRI structural imaging where this architecture is not well-resolved.

While the 2nd-order tensor model is capable of describing regions of the brain that have consistent structure, the model breaks down in voxels that contain multiple fibers. To address this problem, Tuch et al. proposed High Angular

---

Funding: Grants P41-RR013642, RO1-HD050735, and NHMRC496682 (Australia)

Resolution Diffusion Imaging (HARDI) [3]. HARDI uses larger numbers of directions, often 100 or more, to acquire measurements of the diffusion. The sampled data can be used to estimate the orientation distribution function (ODF), which gives the probability of directional water diffusion within each voxel. One representation of the ODF is in the form of a spherical harmonic basis [4], allowing the shape at each voxel to be compactly represented by a truncated set of spherical harmonic coefficients (SHCs). While HARDI presents several advantages over DTI, it significantly raises the complexity of data processing and visualization.

A number of other packages support display and processing of DTI data, e.g., SCIRun (http://www.sci.utah.edu), TrackVis (http://www.trackvis.org), DTIStudio (http://www.dtistudio.org), Slicer (http://www.na-mic.org/Wiki/index.php/Slicer), and MedINRIA (http://www-sop.inria.fr/asclepios/software/MedINRIA). Camino (http://www.cs.ucl.ac.uk/research/medic/camino) can fit 2 and 3-tensor models to HARDI data, and it exports models for viewing in other programs; however it has limited capabilities for display. None of these tools specifically support visualization of spherical-harmonic-based ODF models. While there have been various published works [5, 6] that make use of these types of data, the customized tools used to explore these data do not appear to have reached the neuroimaging community yet.

There is a clear need for visual methods to evaluate the results of image processing operations on HARDI data or to investigate features in the data. One important application for visualization of ODFs is in the interpretation of HARDI registration results. Techniques have been developed for the registration of DTI [7–9] that account for the inherently non-Euclidean nature of DTI, which requires that the tensors be reoriented during spatial normalization and averaging. HARDI further complicates this problem, as it allows for more detailed shapes that may represent, for example, the crossing of two nerve tracts. The rotational approach, which can be determined if we compute a registration using a tensor model, may be insufficient to account for the distortions required to match the ODF across subjects.

In this paper, we present a set of tools for producing interactive visualization of HARDI ODF models based on the modified spherical harmonic basis presented by Descoteaux et al. [4]. We demonstrate their capabilities using individual and averaged HARDI data.

2 Methods

HARDI data from 90 subjects were acquired on a 4T Bruker Medspec MRI scanner using an optimized diffusion tensor sequence [10]. These data included both 30-direction (HARDI30) and 105-direction (HARDI105) diffusion imaging. For the HARDI30 data, imaging parameters were: 21 axial slices (5 mm thick), FOV = 23 cm, TR/TE 6090/91.7 ms, 0.5 mm gap, with a 128x100 acquisition matrix. The reconstruction matrix was 128x128, yielding a 1.8x1.8 mm^2 in-plane resolution. The total scan time was 3.05 minutes. For the HARDI105 data, 105 images were acquired: 11 baseline (b0) images with no diffusion sensitization and 94 diffusion-weighted images (b-value 1159 s/mm2) in which gradient directions were evenly distributed on the hemisphere [10]. Imaging parameters were: TR/TE 92.3/8250 ms, 55 x 2mm contiguous slices, FOV = 23 cm. The reconstruction matrix was 128x128, yielding a 1.8x1.8 mm^2 in-plane resolution. The total scan time was 14.5 minutes. For each subject, rank-2 diffusion tensor images were computed from the HARDI signals using MedINRIA software. The first component of the diffusion tensor (D_{xx}) was manually stripped of non-brain tissues to produce a brain mask for the subsequent processing and display.

Orientation distribution functions (ODF) for water diffusivity were estimated voxel-wise from the HARDI signals using the Funk-Radon Transform (FRT). The HARDI measurements were expanded as a spherical harmonic (SH) series, which simplified the FRT to a linear matrix operation [5]. The estimated ODF was normalized to unit mass, creating a diffusion probability density function (PDF) parameterized by spherical angle. The representation for the ODF followed the model described in [4], using the modified spherical harmonic basis

$$Y_j = \begin{cases} \frac{1}{\sqrt{2}}((-1)^m(Y_l^m) + Y_l^{-m}) & -l < m < 0 \\ Y_l^0 & m = 0 \\ \frac{i}{\sqrt{2}}((-1)^{m+1}(Y_l^m) + Y_l^{-m}) & 0 < m <= l \end{cases}, \tag{1}$$

where $\theta \in [0, \pi]$, $\phi \in [0, 2\pi]$, $j(l, m) = (l^2 + l + 2)/2 + m$. Y_l^m is the standard spherical harmonic basis function

$$Y_l^m(\theta, \phi) = \sqrt{\frac{2l+1}{4\pi}\frac{(l-m)!}{(l+m)!}} P_l^m(cos\theta)e^{im\phi} \tag{2}$$

where P_l^m is the associated Legendre polynomial. The modified SH basis takes advantage of the symmetries in the spherical harmonics to produce a real-valued set of basis functions, simplifying computation for data pre-processing and rendering. The diffusion ODF at each voxel is then represented by

$$ODF[k](\theta, \phi) = \sum_{j=1}^{N} ODFC_j[k]Y_j(\theta, \phi) \tag{3}$$

where $ODFC_j[k]$ is the j-th coefficient of the spherical harmonic transform for the k-th voxel. $N = (l + 1)(l + 2)/2$, and can be truncated at different levels. Higher orders of coefficients correspond to higher frequencies on the sphere, thus truncating at higher orders allows the shape of the ODF to be more complicated, while truncating at lower levels will produce much smoother shapes.

We aligned and averaged the HARDI30 datasets for 90 subjects using a non-linear fluid registration approach. An initial affine transformation was computed to produce a suitable initial alignment for the fluid method. The masked D_{xx} image was registered to the ICBM53 average brain template using an affine 9-parameter transformation produced by the software FLIRT [11] and resampled to isotropic voxel resolution (dimension: 128x128x93 voxels, resolution: 1.7x1.7x1.7

mm^3). The resulting transformation parameters were used to rotationally reorient the tensor at each voxel and then affine align the tensor-valued images based on trilinear interpolation of the log-transformed tensors. All affine-registered DT images were then registered to a randomly selected subject's image, using an inverse-consistent fluid registration algorithm that minimized the symmetrized Kullback-Leibler divergence of the two tensor-valued images [12]. This minimization allows us to achieve better correspondence in the white matter structures than would be achieved with scalar image matching. We note that DT data are not available from the ICBM53 template, hence we are not able to apply tensor-matching directly to the template. The images of the diffusion ODFs were resampled to the target space by applying the corresponding DTI mapping. To keep the direction of the diffusion ODFs oriented with the direction of the underlying fibers, the ODFs were reoriented using the Preservation of Principal Direction (PPD) method [7], where the principal direction of the ODF was determined based on principal component analysis of the ODF [12].

We developed a Windows-based interactive software package for 3D visualization of the ODF shapes using OpenGL and C++. Each shape is represented as a glyph based on a sampling of the values of $ODF[k](\theta, \phi)$. The software can load a series of SHC volumes and display orthogonal views of slices through the coefficient data, as well a 3D view of the reconstructed glyph shapes. Its graphical user interface (GUI) provides controls to adjust the number of coefficients (N), the number of samples for θ and ϕ, as well as a window size for how many voxel ODFs are displayed at once. When the parameters are adjusted, a new series of glyphs are computed and the display is updated. The software can also display additional volume files in register with the HARDI data, as well as surface models of other anatomical structures, such as the cortex or streamline models of fiber tracts, and tensor glyphs for analyzing DTI data. Because each voxel is represented by a detailed shape model, we note that the rendering time for high levels of detail can be prohibitive for interaction. Thus, the software allows the user to navigate using a lower-fidelity set of glyphs and produce the detailed rendering when an appropriate view has been selected.

The software provides user-selectable color models for the ODF glyphs, including the R_2 measure proposed in [13],

$$c = \frac{\sum_{j:l=2} |c_j|}{\sum_{\forall j} |c_j|} \tag{4}$$

where c_j is the j-th SHC. This represents the fraction of energy in the $l = 2$ components and is an indicator of structural content. We implemented other measures described in [4] and a color model that shades each glyph according to the direction of the maximum in the ODF. The latter uses an encoding similar to DTI, where red corresponds to left-right directions, green corresponds to anterior-posterior directions, and blue corresponds to superior-inferior directions.

We also developed an off-screen renderer that can generate slice views of the ODFs. This renderer provides a command-line interface with all the parameters of the GUI, but it can produce images with dimensions as high as 16K by 16K

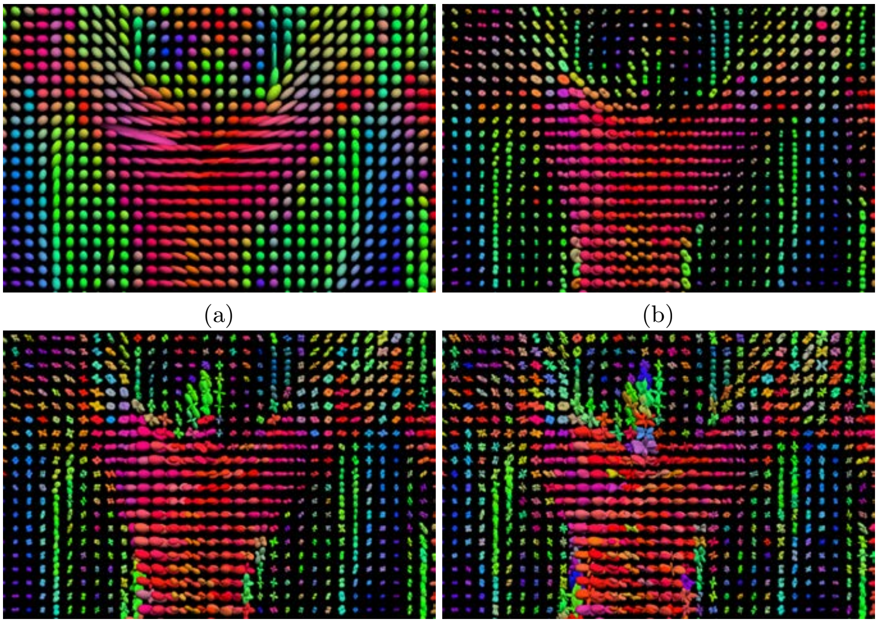

(a) (b) (c) (d)

Fig. 1. Glyphs computed from a HARDI105 data set. (a) DTI ellipsoid glyphs (b) HARDI ODF (6 SHCs) (c) HARDI ODF (15 SHCs) (d) HARDI ODF (28 SHCs).

pixels. Images can be produced in JPEG format, as well as the Zoomify format (Zoomify, Inc., Santa Cruz, CA), which produces a multi-resolution pyramid decomposition of the image into tiles of smaller images. We applied this rendering package using a clustered-computing environment, allowing us to send each slice in the HARDI volume to a different compute node. The resulting images were stored directly into a web-accessible directory, with an automatically constructed web-interface that allowed navigation through each slice of data, zooming to any level of detail, and switching among axial, coronal, and sagittal views of the HARDI data. This allows for convenient sharing of research results online, obviating the need for special hardware and allowing for rapid display of results without downloading the entire set of volumetric data.

3 Results

We applied the methods described in the previous section. The results were displayed using a notebook computer with an Intel Centrino Duo 2.16Ghz processor and an NVidia 7950GTX graphics card. We observed that frame rates suitable for interaction (approximately 10 frames / second) were achieved for whole-slice masked data with 15×15 samples in (θ,ϕ), which were represented by approximately 2 million triangles per slice.

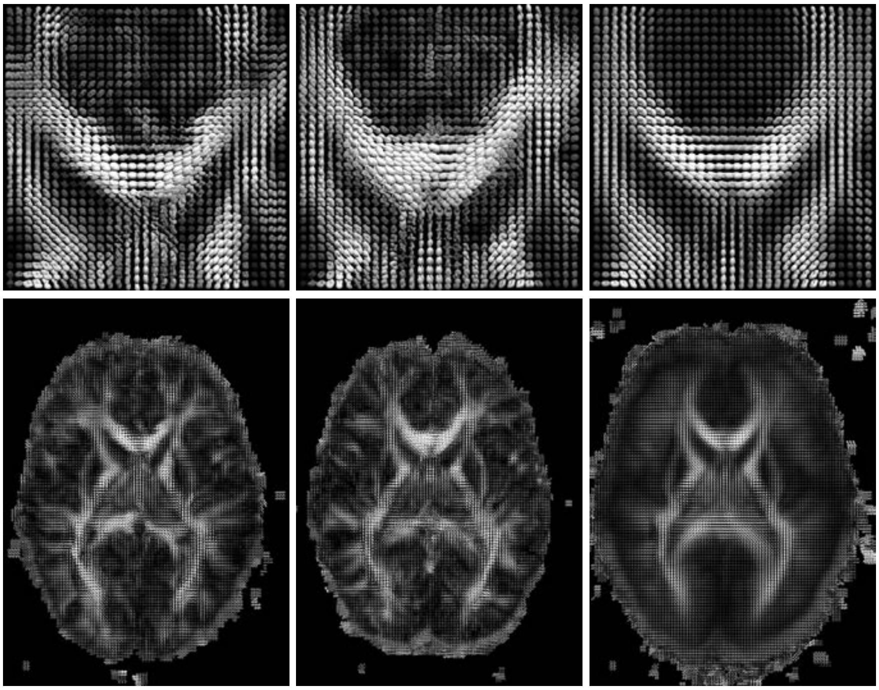

Fig. 2. Visualization of orientation distribution functions. (left) Data from a single subject. (middle) Data from a second subject, resampled after alignment to match the first subject. (right) An average map of orientation distribution functions for 90 subjects. Each image is colored using the R_2 measure. The top row is a set of zoomed views of the images beneath them. The white matter structure is readily apparent in these images. We note that the group average image demonstrates visually that the averaged ODF for each voxel retains significant shape characteristics.

Figure 1 shows renderings of a region near the corpus callosum in a slice of DTI and ODF data from a single subject. The first view shows the DTI glyph model, normalized to unit mass to be consistent with the ODFs. The other views show the SH representation of the ODF, with $N = 6$, $N = 15$, and $N = 28$. These correspond to increasing values of the l-parameter, i.e., $l \in \{2, 4, 6\}$. The sampling in (θ,ϕ) was 50×50. The color encoding scheme for each frame indicates the maximum direction for the tensor or ODF. We observe that, as expected, the ODF representation provides significantly more detail than the DTI version. This is seen, e.g., in the upper left corner of the images where the corticospinal tracts (blue) and the corpus callosum (red) meet. The tensors in this region are fairly isotropic, making their direction ambiguous. In the ODF models, the crossings become more apparent as there are multiple local maxima. As we move to higher numbers of coefficients ($N = 28$), we see what appears to be an increase in the noise in the image. Selection of an appropriate level at which to truncate

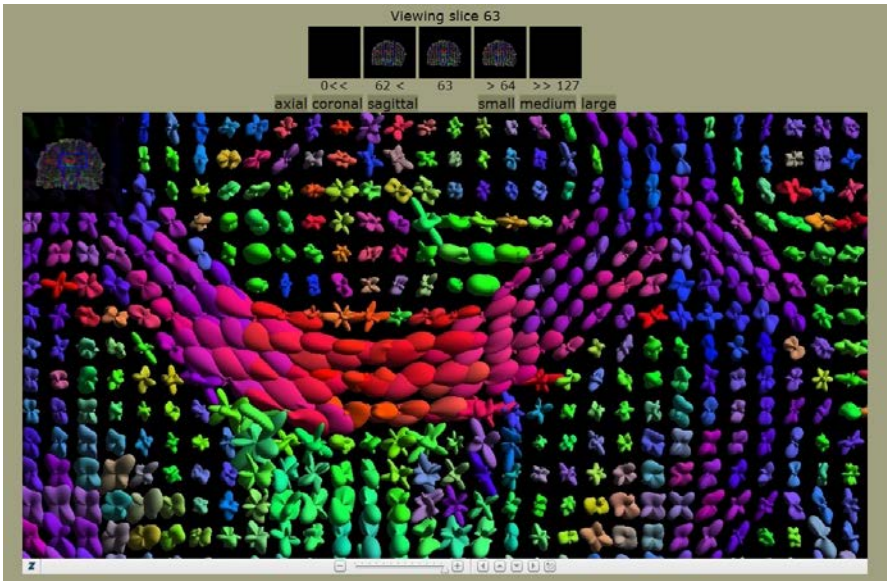

Fig. 3. The zoomify-enabled web-view of a HARDI dataset, produced automatically by our software. The user can navigate to different slices and orientations, and zoom to high levels of detail. The image being viewed is 8192 x 8192 pixels.

the SH series remains an open area of research; visualizations such as these may assist in better understanding the impact of the coefficients.

Figure 2 shows the results of the registration of the HARDI30 data for 90 human subjects, as described in the previous section. These visualizations indicate the transformations that are induced upon the ODF model and demonstrate the process that occurs as the spherical harmonic representations of the ODF are averaged. Orientations of the second subject (middle panel) can be seen to closely match those of the first subject (left panel) in many regions. The 90-subject average (right panel) clearly preserves many of the features of the individual brains, though much of the higher order detail has been smoothed by the averaging process. We note that the shapes of the ODFs in the average map are similar to those in Fig. 1.b., where $N = 6$ SHCs were used.

We also applied the off-screen renderer to the HARDI105 data. Figure 3 shows the resulting web interface, which provides access to 2GB of pre-rendered image data. The images were computed with a 75×75 sampling of (θ, ϕ) space with an image resolution of 8192×8192 pixels. The total wall-clock time to compute this collection was less than 10 minutes using a 111-node 2.4GHz Opteron cluster. We note that the cluster is a shared resource, and its load may vary greatly. Renderings of individual slices at this resolution required less than one minute of compute time. We were able to use the web-based interface to share results directly among collaborators, including ones on different continents. In the rendering shown in Fig. 3, we observe features that would not normally be detectable with DTI. For example, on the upper right that corpus callosum fibers become interspersed with other white matter tracts orthogonal to them. We also observe spatially varying contrast inside the striatum.

4 Discussion

We have introduced a new set of tools for the visualization of ODF models computed from HARDI. These tools allow the display of intricate details, and we applied them to produce novel views of averaged multi-subject HARDI data. The visualizations reveal that the continuum-mechanical HARDI registration method applied in this paper, based on fluid convection of HARDI functions, does in fact preserve, and even enhance, key features in population studies of HARDI. We believe these tools will be of practical use to the neuroimaging community, and we will be distributing them online. We will be applying these visualization tools to understanding aspects of HARDI imaging to examine disease characteristics. We will use these visualization tools to understand features of the ODF data acquired at 3T and 7T in patients with Alzheimer's disease. We will also explore improving the rendering capabilities through the use of GPU programming.

References

1. LeBihan et al.: MR imaging of intravoxel incoherent motions: application to diffusion and perfusion in neurologic disorders. Radiology **161**(2) (1986) 401–407
2. Basser et al.: Estimation of the effective self-diffusion tensor from the NMR spin echo. J Magn Reson B **103**(3) (1994) 247–254
3. Tuch et al.: High angular resolution diffusion imaging reveals intravoxel white matter fiber heterogeneity. Magn Reson Med **48**(4) (2002) 577–582
4. Descoteaux et al.: Apparent diffusion coefficients from high angular resolution diffusion images: Estimation and applications. Research Report 5681, INRIA (2005)
5. Descoteaux et al.: A linear and regularized odf estimation algorithm to recover multiple fibers in q-ball imaging. Research Report 5768, INRIA (2005)
6. McGraw et al.: Von Mises-Fisher mixture model of the diffusion ODF. In: ISBI 2006. (April 6, 2006) 65 – 68
7. Alexander et al.: Spatial transformations of diffusion tensor magnetic resonance images. IEEE Trans Med Imaging **20**(11) (2001) 1131–1139
8. Xu et al.: Spatial normalization of diffusion tensor fields. Magn Reson Med **50**(1) (2003) 175–182
9. Zhang et al.: Deformable registration of diffusion tensor MR images with explicit orientation optimization. Med Image Anal **10**(5) (2006) 764–785
10. Jones et al.: Optimal strategies for measuring diffusion in anisotropic systems by magnetic resonance imaging. Magn Reson Med **42**(3) (1999) 515–525
11. Smith et al.: Advances in functional and structural MR image analysis and implementation as FSL. NeuroImage **23 Suppl 1** (2004) S208–S219
12. Chiang MC et al.: Fluid registration of diffusion tensor images using information theory. IEEE Trans Med Imaging **27**(4) (2008) 442–456
13. Chen et al.: Estimation, smoothing, and characterization of apparent diffusion coefficient profiles from high angular resolution DWI. In: CVPR. (2004) 588–593